Superconductivity, Insulation and Metallicity in the Vicinity of the Superconductor-Insulator Transition in Ultra-Thin Granular Aluminum

DISSERTATION ZUR ERLANGUNG DES DOKTORGRADES DER NATURWISSENSCHAFTEN (DR. RER. NAT.) DER FAKULTÄT FÜR PHYSIK

DER UNIVERSITÄT REGENSBURG

vorgelegt von

THOMAS HUBER
aus Laaber

im Jahr 2022

Das Promotionsgesuch wurde am 02.05.2022 eingereicht.
Die Arbeit wurde von Prof. Dr. Christoph Strunk angeleitet.

Prüfungsausschuss:

Vorsitzender:	Prof. Dr. G. Bali
1. Gutachter:	Prof. Dr. C. Strunk
2. Gutachter:	Prof. Dr. D. Bougeard
weiterer Prüfer:	PD Dr. A. Weymouth

Das Promotionskolloquium fand statt am: 21.12.2022

Contents

1. Introduction

In former times materials were more or less categorized by their electrical properties into conductors and insulators. The discovery of the proportionality of voltage and current in conductors (Ohm's Law) and the introduction of the electrical conductivity led to the possibility of more differentiation.
Afterwards additional classes of materials were found, e.g. semiconductors and superconductors. The latter received special attention as by decreasing the temperature below a material specific critical temperature T_c the resistance dropped to an unmeasurable low value. This superconducting state can be destroyed by an external magnetic field once it exceeds a critical value B_c.
It took until the 1960s to find theoretial descriptions for superconductivity by theories of Bardeen, Cooper and Schrieffer (BCS theory) [1] and Ginzburg and Landau (GL theory) [2].

A new class of superconductors was discovered accidentally by the group of Abeles [3] in 1967. Their aim was to grow thin homogenous aluminum films. However, their thin films revealed a granular structure with grain sizes from nanometers up to 10 nm and more [4]. It turned out that granular aluminum had a much higher critical temperature and critical magnetic field than bulk aluminum. The grain size distribution in those films was found to depend on oxigen concentration. It could be narrowed down to 2nm $\pm$ 1nm by optimizing process parameters [4, 5]. In their films the thickness exceeded the grain size by several times and therefore can be treated as three dimensional films, which have been studied since. Deutscher [6] reviews the most important findings over the last decades.
It was Anderson [7], who first came up with the idea, that materials that show Cooper pairing can be transformed from a superconductor to an insulator, when considering small superconductors coupled by Josephson coupling. Abeles further applied this idea to granular systems [8].

In the end of the 1980s and in the beginning of the 90s two-dimensional superconducting systems were studied. The focus was set on thin granular films, thin homogenous films and Josephson junction arrays (JJA), which showed similar behaviour at low temperatures [7].
Experiments on ultra-thin films (2D) showed that the thickness, which is connected to the normal state sheet resistance, controls a transition from a superconducting to an insulating state [9, 10]. The latter was found for R_N above a value close to the quantum resistance of Cooper pairs $R_Q = 6.45\text{k}\Omega$, while a state with global phase coherence was seen for R_N smaller, but close to R_Q.

JJAs comprise an array of defined, periodical superconducting islands coupled by Josephson links and are accessible experimental systems with easily controllable properties. In the critical regime ($R_N \leq R_Q$) the superconductor to insulator transition (SIT) can be induced by an external magnetic field.

In this thesis two (ultra-thin) granular aluminum films have been characterized for its electrical transport properties. The investigated samples have a normal state sheet resistance tuned to a value close to R_Q. The sample with $R_N(4K) < R_Q$ shows a zero resistive state at the lowest temperatures, while the sample with $R_N(4K) > R_Q$ behaves insulating without magnetic field. This is consistent with a disorder induced SIT.
A magnetic field induced SIT is found in the lower resistance sample ($R_N(4K) < R_Q$) as well. A perpendicular magnetic field $B_\perp < 50$mT is sufficient to switch from state with zero resistance to an insulating behaviour at the lowest temperatures.
In addition, in two samples a high resistive state arises by applying a higher perpendicular magnetic field. This magnetoresistance can be separated into a positive magnetoresistance for magnetic fields $B_\perp < B_{max} \approx 2$T and a negative magnetoresistance for higher fields. The high resistive state is not present in parallel magnetic fields up to $B_\parallel = 2.5$T.
In the vicinity of the magnetic field induced SIT we find signatures for an anomalous metallic state, as we see a low temperature saturation of the resistance.

The work starts with chapter 2, giving theoretical background information on superconductivity in general, followed by effects specific to two dimensions and at the end discusses the properties of disordered and granular systems.
Chapter 3 focuses on low temperature filtering and the used measurement setups for DC and AC characterization.
After that, the characterization (material, morphology, dimensions) of our samples is described in chapter 4.
Chapter 5 deals with our experimental results of ultra-thin granular aluminum, which have been put in perspective to earlier findings on JJA, ultra-thin granular films and three dimensional homogenous granular films.
Additional results on niobium-silicon are presented in chapter 6.
Chapter 7 summarizes the findings and discusses open questions and further experiments.
Further information on cryogenic engeneering, including a more detailed description of our home-made low temperature filters and their implementation, can be found in the appendix A.

2. Theoretical Background

2.1. Superconductivity

The two most prominent properties of superconductors are the perfect electrical conductivity, i.e. zero resistive charge transport and the perfect diamagnetism, i.e. the expelling of magnetic flux lines from the interior of the superconductor, below a critical temperature T_c. The first was discovered by Kamerlingh Onnes in 1911, who had successfully liquified helium three years before. Using the liquid helium to cool down mercury, lead and tin he found a vanishing electrical resistance in a small temperature range around a critical temperature T_c specific for each corresponding material [11][12]. The second hallmark is known as the Meissner-Ochsenfeld-Effect after W. Meissner and R. Ochsenfeld [13]. They had found that an external magnetic field was not only screened by the superconductor, but is expelled when cooling down a superconducting material from its normal state $T > T_c$ to the superconducting state $T < T_c$. While the screening effect can also be achieved by a "simple" ideal conductor, the expulsion can not be attributed to ideal conduction, but has to originate from superconductivity. Materials with a perfect diamagnetic response to an external magnetic field have a magnetic susceptibility χ = -1.

London Equations

In 1935 the two brothers F. and H. London described the electrodynamic properties by deriving the following two London equations [14].

$$\frac{\partial j_s}{\partial t} = \frac{n_s e_s^2}{m} E \tag{2.1a}$$

$$\nabla \times j_s = -\frac{n_s e^2}{m_s} B \tag{2.1b}$$

with j_s being the supercurrent density, n_s the charge carrier density, e_s the charge, m_s the mass, E the electric field and B the magnetic field. The subscript "s" is used to divide between "normal" and "superconducting" electrons referring to a two-fluid model by Gorter and Casimir in 1934 [15][16]. Later, in the BCS theory (see section 2.1.1), the charge, mass and carrier density has been attributed to Cooper-Pairs, formed by two interacting electrons due to an attractive force.
From Eq. 2.1b it becomes clear, that there should be a critical current density connected to a critical magnetic field as both values are directly connected. Silsbee had already predicted in 1926 [17] that superconductivity should break down for a current density larger than a critial value, independent of the origin of the current.

The prefactor $\Lambda = \frac{m_s}{n_s e_s^2}$ is the London parameter and can be rewritten as $\Lambda = \mu_0 \lambda_L^2$. λ_L is the London penetration depth for which an external magnetic field decreases exponentially from its surface to its center.

$$\lambda_L(T) = \sqrt{\frac{m_s}{\mu_0 n_s e_s^2}} \tag{2.2}$$

Since the Cooper pair density near T_c varies with temperature as $n_s \propto 1 - \frac{T}{T_c}$ [15], the temperature dependence of the penetration depth follows

$$\lambda_L(T) = \frac{\lambda_L(0)}{\sqrt{1 - (\frac{T}{T_c})^4}} \tag{2.3}$$

No complete picture for the field of superconductivity had been accomplished until the 1960s [18]. Two publications turned this unsatisfactory state around. In 1950 Ginzburg and Landau presented their macroscopic Ginzburg-Landau-theory (GL-theory) [2, 19] and 7 years later Bardeen, Cooper and Schrieffer brought up their microscopic BCS-theory [1]. It was in 1986 Bednorz and Müller [20] found a new class of superconductors, namely High-Temperature-Superconductors (High-T_c-S.C.), which could not fully be understood with the two mentioned theories. The research in the field of superconductivity started to grow again and is still a big and vivid field covering multiple different directions.
The following pages deal with the basic concepts of the BCS- and the GL-theory before turning to more specific topics, e.g. two dimensional charge transport and disordered systems. [16, 18]

2.1.1. BCS Theory

Cooper-Pairing due to Attractive Interaction

Cooper had already predicted that a weak attractive force between two electrons may destabilize the ground state of a Fermi gas in 1956 [21]. The mechanism leading to the attractive interaction had already been proposed in 1950 by Fröhlich [22] and Bardeen [23], independently. The attractive interaction manifests itself in an exchange of "virtual" phonons and can be viewed as follows: one electron with momentum k_1 emits a phonon with wave vector q and second electron with momentum k_2 absorbs that phonon (see Fig. 2.1a).

Due to momentum conservation

$$k_1 + k_2 = k_1' + k_2' = K \tag{2.4}$$

the matrix element in the second-order perturbation theory reads as

$$\nu(k_1, k_2, q) = \frac{g^2 \hbar \omega_q}{(\epsilon_{k_1+q} - \epsilon_{k_1})^2 - (\hbar \omega_q)^2)} \tag{2.5}$$

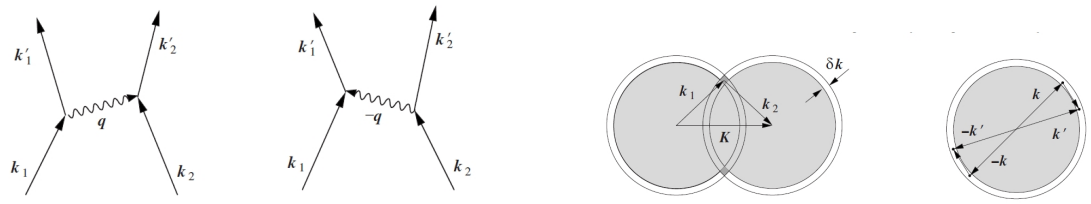

Figure 2.1.: Virtual phonons and Fermi sphere. Figures taken from [16].

with g being the coupling constant for the electron-phonon interaction, ϵ_{k_1} the energy of the electron with momentum k_1 and $\hbar\omega_q$ the energy of the exchange phonon. For the interaction to be attractive the matrix elements has to be negative and it follows:

$$|\epsilon_{k_1+q} - \epsilon_{k_1}| < \hbar\omega_q \tag{2.6}$$

From Eq. 2.5 one can see, that a stronger coupling between electrons and phonons favors superconductivity. Therefore, highly conducting metals do not become superconducting as g is very small and the repulsion due to Coulomb effects is bigger than the attractive force [16].

At $T = 0$ all single electron states are occupied up to the Fermi energy E_F and only states $\epsilon(k)$ in between $E_\mathrm{F} \leq \epsilon(k) \leq E_\mathrm{F} + \hbar\omega_\mathrm{D}$ contribute to electron-phonon interactions, where ω_D is the Debye frequency.
When converted into the k-space the location of those state is a thin shell located around the Fermi surface with δk, which can be see in Fig. 2.1b).

The two-particle wavefunction can be written as

$$\psi(r_1, r_2) = \frac{1}{V} e^{ik_1 r_1} e^{ik_2 r_2} = \frac{1}{V} e^{ikr} = \psi(r) \tag{2.7}$$

where $r = (r_1 - r_2)$ is the relative coordinate and V the sample volume. As the two electrons are permanentely scattered and recombined to states with different k, the wavefunction of a Cooper-Pair can be rewritten as

$$\psi(r) = \sum_k A_k e^{ikr} \tag{2.8}$$

where $|A_k|^2$ is the probability for an electron pair to be in the state of $(k, -k)$.
One may derive the eigenvalue E of a Cooper-Pair with the following Schrödinger equation

$$\left[-\frac{\hbar^2}{2m}(\Delta_1 + \Delta_2) + \nu(r_1, r_2) \right] \psi(r_1, r_2) = E\psi(r_1, r_2) \tag{2.9}$$

with potential $\nu(r_1, r_2)$, that includes effects of attractive interaction as well as repulsive. After some math and assumptions, that can be found in various textbooks as well [16, 18], one ends up with the following expressions

$$E = 2E_F - \delta E \tag{2.10}$$

$$\delta E = \frac{2\hbar\omega_{\mathrm{D}}}{1 - e^{\frac{4}{\nu_0 D(E_{\mathrm{F}})}}} \tag{2.11}$$

δE can be understood as the binding energy, when pairing two electrons to form a Cooper-Pair. From Eq. 2.10 it follows that the energy of the Cooper-Pair is indeed smaller than $2E_{\mathrm{F}}$ corresponding to two single electrons.

BCS-Groundstate, Energy Gap and Excited States

Cooper-Pairs with angular momentum $L = 0$ and total spin $S = 0$ behave bosonic. This configuration is called spin-singlet state. Cooper-Pairs therefore do not have to obey the Pauli-Exclusion-principle for fermions and the wavefunction of the Cooper-Pair groundstate is a superposition of all the states

$$|\Psi\rangle = \prod_k |\psi\rangle_k = \prod_k \left(u_k |0\rangle_k + v_k |1\rangle_k\right) \tag{2.12}$$

where $|1\rangle_k$ denotes an occupied state with ($k \uparrow$,-$k \downarrow$) and $|0\rangle_k$ refers to an unoccupied state. The arrows indicates the opposite orientaton of the spins of the electrons and u_k, v_k are real probability coefficients. The ground state energy $W_0 = \langle\Psi| H |\Psi\rangle$ can be derived with the Hamiltonian

$$H = \sum_k 2\eta_k \sigma_k^+ \sigma_k^- - \frac{\nu_0}{V} \sum_{k,k'} \sigma_k^+ \sigma_{k'}^- \tag{2.13}$$

with $\eta = \frac{\hbar^2 k^2}{2m} - E_{\mathrm{F}}$ (the first term is the kinetic energy of a single electron), σ_k^+ and σ_k^- are the occupied and unoccupied states rewritten as Pauli spin matrices, respectively.

Finally, the value of W_0 can be written as

$$W_0 = \sum_k \eta_k \left(1 - \frac{\eta_k}{E_k}\right) - \frac{\Delta_0^2}{\nu_0} \tag{2.14}$$

where the probability coefficients were replaced by

$$u_k^2 = \frac{1}{2}\left(1 + \frac{\eta_k}{E_k}\right), \tag{2.15}$$

and

$$v_k^2 = \frac{1}{2}\left(1 - \frac{\eta_k}{E_k}\right) \tag{2.16}$$

together with the relation

$$E_k^2 = \eta_k^2 + \Delta_0^2 \tag{2.17}$$

Important to note is that Δ_0 is the energy gap for elementary excitations at $T = 0$ and given by

$$\Delta_0 = \frac{\hbar\omega_{\mathrm{D}}}{\sinh[\frac{2}{\nu_0 D(E_{\mathrm{F}})}]} \tag{2.18}$$

To excite a Cooper-Pair a minimum energy of $\delta E_{\min} = 2\Delta_0$ is required. The excitations are called "quasiparticles" or "Bogoliubov quasiparticles" and are a linear combination of electrons and holes. The excitation spectrum for the quasiparticles following Eq. 2.17 can be seen in Fig. 2.2.

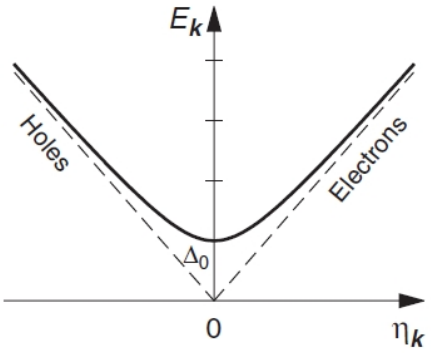

Figure 2.2.: Excitation spectrum. Figure taken from [16].

The energy gap is connected to the critical temperature by the simple, but important form

$$\Delta_0 = 1.76 k_{\mathrm{B}} T_{\mathrm{c0}} \tag{2.19}$$

where $\mathrm{k_B}$ is the Boltzmann constant and $\mathrm{T_c}$ the critical temperature of the material. Nevertheless, Eq. 2.19 does not necessarily hold for every material and/or configuration as some of the made assumptions might not be true for real metals, e.g. we assumed a single phonon exchange mechanism and a spherical Fermi surface.

Near the critical temperature T_{c} the energy gap follows

$$\frac{\Delta(T)}{\Delta_0} = 1.74\sqrt{1 - \frac{T}{T_{\mathrm{c0}}}} \tag{2.20}$$

2.1.2. Ginzburg-Landau Theory

The Ginzburg-Landau theory is another milestone for the understanding of the experimentally observed properties of superconductivity. The GL-theory is based on the theory for second-order phase transitions proposed by Landau himself. In this "classical" Landau theory the free energy is expanded into a power series of an order parameter Φ. Argumenting that the equilibrium phase is achieved by minimizing g_s, then $\alpha\Phi_0+\beta\Phi_0^3=0$ and g_s can be written as

$$g_\mathrm{s} = g_\mathrm{n} + \alpha(T)\Phi^2 + \frac{1}{2}\beta(T)\Phi^4 \tag{2.21}$$

$\Phi_0 = 0$ can be connected to the disordered phase for $T > T_\mathrm{c}$ and the solution

$$\Phi_0^2 = -\frac{\alpha}{\beta} \tag{2.22}$$

with an ordered phase for $T < T_\mathrm{c}$. For this conditions to hold true β must be positive for all temperatures and

$$\frac{\alpha}{\beta} = \begin{cases} \text{positive} & \text{for} \quad T > T_\mathrm{c} \\ \text{negative} & \text{for} \quad T < T_\mathrm{c} \end{cases}$$

GL Free Energy and GL Equations

Up to now the order parameter Φ was treated as spatially invariant. This is one of the changes that were made in deriving the GL theory. Here the order parameter is associated with a macroscopic wavefunction for the superconducting state

$$\Psi(r) = \Psi_0(r)e^{-i\varphi(r)} \tag{2.23}$$

where $|\Psi_0|^2 = n_\mathrm{s}$ is the density of the superconducting particles.
The Gibbs free energy density can then be formulated to

$$g_\mathrm{s} = g_\mathrm{n} + \alpha|\Psi(r)|^2 + \frac{1}{2}|\Psi(r)|^4 + \frac{\hbar^2}{2m}|\nabla\Psi(r)|^2 \tag{2.24}$$

By taking the external magnetic field into account Eq. 2.24 translates to

$$g_\mathrm{s} = g_\mathrm{n} + \alpha|\Psi(r)|^2 + \frac{1}{2}|\Psi(r)|^4 + \frac{1}{2\mu_0}|B_\mathrm{a} - B_\mathrm{i}|^2 + \frac{1}{2m}|(-i\hbar\nabla + 2eA)\Psi(r)|^2 \tag{2.25}$$

One sees that two additonal terms popped up. The first one accounts for the expulsion energy needed to change the magnetic field from $\mathrm{B_a}$ to $\mathrm{B_i}$ and the second term takes into account additional magnetic field effects, where ∇ was replaced with $\nabla - \frac{2ieA}{\hbar}$, together with $-e$ being replaced with $-2e$ due to the double charge of Cooper-Pairs [16].

From Eq. 2.25 the two important Ginzburg-Landau equations can be derived

$$\frac{1}{2m}(-i\hbar\nabla + 2eA)^2\Psi + \alpha\Psi + \beta|\Psi|^2\Psi = 0 \tag{2.26}$$

$$j_s = \frac{ie\hbar}{m}(\Psi^*\nabla\Psi - \Psi\nabla\Psi^*) - \frac{4e^2}{m}|\Psi|^2 A \tag{2.27}$$

together with the boundary condition

$$n(-i\hbar\nabla + 2eA)\Psi = 0 \tag{2.28}$$

which accounts for the current perpendicular to the sample surface to vanish.

Important GL parameters

The GL-theory features two important parameters, namely the penetration depth λ and the Ginzburg-Landau coherence length ξ_{GL}.
The penetration depth λ can be deduced by considering a sample much larger than the penetration depth. Then Ψ is constant and only the last two terms of Eq. 2.26 do matter and lead to $|\Psi|^2 = -\frac{\alpha}{\beta}$. Inserting into Eq. 2.27 gives the expression for the current density

$$j_s = \frac{4e^2}{m}\frac{|\alpha|}{\beta}A \tag{2.29}$$

with A being the London gauge fixed vector potential. Eq. 2.29 is identical to the second London equation Eq. 2.1b.
The penetration depth then can be written as

$$\lambda = \sqrt{\frac{m\beta}{4\mu_0 e^2|\alpha|}} \tag{2.30}$$

The second important parameter, the coherence length ξ_{GL} corresponds to the distance over which the wavefunction Ψ, hence the Cooper pair density $n_s = |\Psi^2|$, changes from zero at a phase boundary, e.g. a surface between a normal and a superconductor, to its bulk value $n_s(x = \infty) = |\Psi^2(\infty)|$ reads as

$$\xi_{GL} = \frac{\hbar}{\sqrt{2m|\alpha|}} \tag{2.31}$$

Fig. 2.3 presents a schematical visualization of the dependencies for the different parameters at the interface between a normal conductor and a superconductor in presence of an external magnetic field B_a, where the x-direction indicates the direction from the interface to the center of the superconductor.

For bulk superconductors one can express the thermodynamical critical magnetic field B_c as the difference in the Gibbs free energies of the normal and the superconducting state.

$$G_n(T) - G_s(T) = \frac{B_c^2(T)}{2\mu_0} \tag{2.32}$$

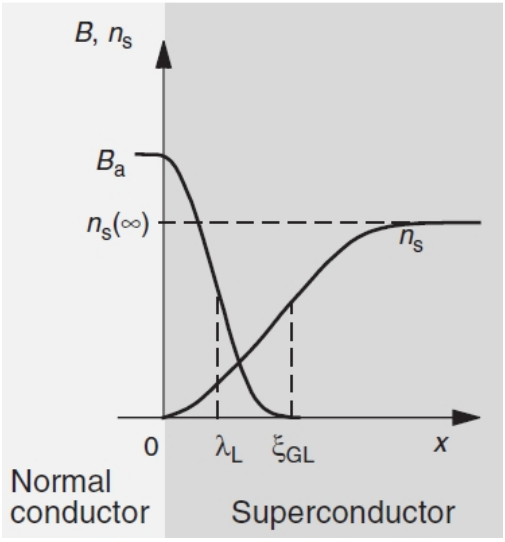

Figure 2.3.: Visualization of the GL parameters at the normal conductor/superconductor interface. Figure taken from [16].

This thermodynamical critical field can be expressed in terms of the GL prefactors in the following way

$$\frac{B_c^2(T)}{2\mu_0} = \frac{\alpha^2}{2\beta} \tag{2.33}$$

and the temperature dependence follows

$$B_c(T) \approx B_c(0)\left[1 - \left(\frac{T}{T_c}\right)^2\right] \tag{2.34}$$

Ginzburg-Landau Parameter κ

The ratio of the two parameters is called Ginzburg-Landau parameter κ, which separates two types of superconductors.

$$\kappa = \frac{\lambda}{\xi_{GL}} = \begin{cases} < \frac{1}{\sqrt{2}} & \text{Type 1} \\ > \frac{1}{\sqrt{2}} & \text{Type 2} \end{cases} \tag{2.35}$$

The threshold value of κ as well as the distinction between two types of superconductors was first discussed by Abrikosov in 1957 [24, 25]. He investigated what would happen if κ would be large, i.e. $\lambda > \xi_{GL}$ instead of the reverse case. Contrary to Type 1 superconductors, which favor to expell the magnetic field below B_c (Meissner-Ochsenfeld effect) and turn normal conducting above, Type 2 superconductors generate phase-boundaries by partly letting the external magnetic field penetrate. This mechanism is energetically favorable due to a negative surface energy [18]. Single flux lines penetrate

through the superconductor by increasing the external magnetic field from B_{c1} to B_{c2}. This mixed state is called Shubnikov phase. For $B < B_{c1}$ Type 2 superconductors behave as Type 1 and for $B > B_{c2}$ superconductivity is destroyed.
In the center of the flux lines the order parameter/Cooper-Pair density is zero, i.e. a normal conducting area is generated at the location of the maximum magnetic field. To shield that normal conducting area from the superconducting surrounding supercurrents are induced and that configuration is called Abrikosov vortex. This is sketched in Fig. 2.4.

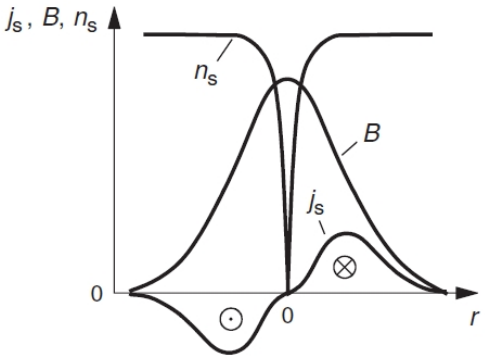

Figure 2.4.: Visualization of an Abrikosov vortex. Figure taken from [16].

Assuming that each Abrikosov vortex consists of one flux quantum, the number of vortices increases with increasing external magnetic fied. By finally crossing B_{c2} global superconductivity is destroyed as the vortices do overlap, cutting off the last superconducting path. Abrikosov predicted a square configuration for the vortices called "Abrikosov lattice". Later it was shown that a triangular lattice should be more favorable. The latter was confirmed by scanning electron mircoscopy [26] and later by scanning tunneling microscopy [27, 28].

The upper critical field associated with the destruction of superconductivity may be expressed in forms of the thermodynamical critical magnetic field and in terms of the coherence length

$$B_{c2}(T) = \sqrt{2}\kappa B_c(T) = \frac{\Phi_0}{2\pi\xi(T)^2} \tag{2.36}$$

It is noteworthy, that the GL-theory at first was not commonly accepted and appreciated until in 1959 Gor'kov [29] showed that in fact the GL-theory is a special, limiting case of the BCS theory, when focusing on spatial variations [18]. It is only truely valid near the critical temperature T_c, where the wavefunction Ψ is directly proportional to the energy gap Δ. Nowadays the GL-theory is commonly accepted and the wavefunction Ψ can be related to the center-of-mass motion of a Cooper pair.

Non locality and different limits

Experimentally it was found that the penetration depth λ is bigger than the theoretically expected values. Pippard followed that the second London equation Eq. 2.1b needed a correction, namely a nonlocal expression, when the electron mean free path is comparable or greater than the skin depth in his nonlocal theory [30]. He further proposed that the current density j_s is then given by an average electrical field in the environment connected to the mean free path, instead of the local electric field connected with skin depth. The important parameter ξ_{em} is called the electromagnetic coherence length and connects to the BCS coherence length and the mean free path of normal conducting electrons.

$$\xi_{\mathrm{em}} = \frac{1}{\xi_0} + \frac{1}{\ell} \tag{2.37}$$

ξ_0 can be derived from BCS theory and is given by

$$\xi_0 = \frac{\hbar v_{\mathrm{F}}}{\pi \Delta_0} \approx 0.18 \frac{\hbar v_{\mathrm{F}}}{k_{\mathrm{B}} T_{\mathrm{c0}}} \tag{2.38}$$

with v_{F} being the Fermi velocity.

In the so called London limit with $\lambda, \ell \gg \xi_0$ the above mentioned corrections due to non locality and electron scattering are very small and the penetration depth is given by the London penetration depth $\lambda = \lambda_{\mathrm{L}}$.

The Pippard limit accounts for $\lambda \ll \xi_0$ and $\ell \gg \xi_0$. The correction to the penetration depth is given by

$$\lambda \approx (0.28 \lambda_{\mathrm{L}}^2 \xi_0)^{\frac{1}{3}} \tag{2.39}$$

Most of the classical superconductors are part of this limitation, e.g. pure aluminum. The measured penetration depth is therefore way larger than the one predicted by London.

If $\ell \ll \lambda$, which is called the dirty limit, the penetration depth is modified to

$$\lambda = \lambda_{\mathrm{L}} (1 + \frac{\xi_0}{\ell})^{\frac{1}{2}} \tag{2.40}$$

For this case, the relation gives an increasing penetration depth by decreasing the mean free path. That can be achieved by alloying the superconductor or by increasing disorder.

Flux Pinning and Flux Flow

As mentioned above, Type 2 superconductors with $B_{\mathrm{c1}} < B < B_{\mathrm{c2}}$ are penetrated by vortices, where each vortex carries one magnetic flux quantum Φ_0. We concluded in the previous sections, that the onset of resistance is given by B_{c2}. However, by applying a current to a Type 2 superconductor in the Shubnikov phase, there will be a force, the Lorentz force, acting on the vortices. The vortices start to move perpendicular to

the current flow and thus create an electric field. That electric field is then parallel to the current flow and effectively creates a voltage along the current path. Thus, for $B > B_{c1}$ there should be a finite resistance, in contrast to the assumed zero bias state. That "problem" is solved by taking into account a pinning force, which effectively cancels out the Lorentz force. Such a pinning results from inhomogeneities or impurities in the material at which the vortices are pinned, until the Lorentz force overcomes the pinning force. It is that point that marks the onset of resistance. As the resistance is governed by the flux flow, it is called flux flow resistance ρ_F and is proportional to it. When the external magnetic field reaches B_{c2} $\rho_F = \rho_N$, where the latter denotes the resistance in the normal conducting state.

$$\rho_F = \frac{E}{J} = B\frac{\Phi_0}{\eta} \tag{2.41}$$

where E is the electric field and J the current density. η is called the viscous drag coefficient, independent on magnetic field.
By having a linear slope in the $R(B)$ curve one may therefore deduce η by

$$\eta = \frac{\Phi_0}{\left(\frac{dR}{dB}\right)} \tag{2.42}$$

and the upper critical magnetic field B_{c2}

$$B_{c2} = \frac{\eta\rho_N}{\Phi_0} \tag{2.43}$$

Using the relation $B_{c2} = \frac{\Phi_0}{2\pi\xi^2}$ for dirty superconductors

$$\xi = \sqrt{\frac{\Phi_0}{2\pi B_{c2}}} \tag{2.44}$$

one may deduce the Ginzburg-Landau coherence length ξ_{GL} by investigating the flux flow resistance. [16, 18]

2.1.3. Josephson Effect

Let us now consider two superconductors separated by, e.g. an insulating barrier of thickness d. For the case of sufficiently small d Josephson predicted that Cooper-Pairs may tunnel from one superconductor to the other through that barrier [31]. It is today clear, that the effects predicted by Josephson occur whenever two superconducting reservoirs are coupled by a weak link [18]. The most common weak links are the originally proposed insulating barrier (S-I-S junction), a normal conducting metal that is proximitized to be weakly superconducting (S-N-S junction) or a constriction, i.e. a narrowing in an otherwise continuous geometry (S-c-S junction).

Josephson Equations

The effects can be described by the following two expressions

$$I_\mathrm{s} = I_\mathrm{c} \sin(\Delta\varphi) \tag{2.45}$$

and

$$\frac{d(\Delta\varphi)}{dt} = \frac{2eV}{\hbar} \tag{2.46}$$

where $\Delta\varphi = \varphi_1 - \varphi_2$ is difference of the phases of the GL wavefunctions of the two superconductors. The first Josephson equation Eq. 2.45 relates the supercurrent across the junction with the phase difference, while the second Josephson equation Eq. 2.46 takes into account time varying phase differences.

DC Josephson Effect

If we do not apply an external voltage across the junction, then the phase difference $\Delta\varphi$ is constant in time and Eq. 2.45 leads to a direct current given by the critical current I_c, which is the maximum supercurrent the junction is able to carry, and the phase difference. This effect is called the DC Josephson effect.

AC Josephson Effect

Things turn, by either applying a small voltage across the junction or by sending an external current I above the critical current I_c through it for which the voltage across the weak link jumps to a finite value given by its quasiparticle characteristics. In that case the phase difference starts to oscillate in time as Eq. 2.46 predicts with frequency

$$\omega_\mathrm{J} = \frac{2eV}{\hbar} \tag{2.47}$$

The supercurrent flowing through the junction is then given by

$$I_\mathrm{s} = I_\mathrm{c} \sin(\omega_\mathrm{J} t + \varphi_0) \tag{2.48}$$

The oscillating supercurrent is known as the AC Josephson effect.

In the zero magnetic field case the critical current the junction may carry is given by material properties and is temperature dependent.

Ambegaokar-Baratoff Relation

Ambegaokar and Baratoff [32] calculated the temperature dependence of the $I_c R_N$ product for tunnel junctions

$$I_c(T)R_N = \frac{\pi\Delta(T)}{2e}\tanh\frac{\Delta(T)}{2k_B T} \tag{2.49}$$

which for $T = 0$ simplifies to

$$I_c(0)R_N = \frac{\pi\Delta(0)}{2e} \tag{2.50}$$

where R_N is the junction normal resistance and Δ the BCS energy gap. Later on we use the definition $I_{c0} = I_c(0)$.

Josephson Inductance and Josephson Energy

Two important parameters linked to the time dependence of the Josephson phase difference and the critical current are the Josephson inductance and the Josephson energy [33]. By rewriting the first Josephson equation to $\frac{\partial I}{\partial \varphi} = I_c \cos\varphi$, using $\Phi_0 = \frac{h}{2e}$ and applying the chain rule one can express the relation as

$$V = \frac{\Phi_0}{2\pi I_c \cos\varphi}\frac{\partial I}{\partial t} = L(\varphi)\frac{\partial I}{\partial t} \tag{2.51}$$

The inductance is associated with the inertia of charge carriers (Cooper-Pairs) in alternating electrical fields and $L(\varphi) = \frac{\Phi_0}{2\pi I_c \cos\varphi}$ is called kinetic inductance. Characteristic for the Josephson junction is the Josephson inductance given by

$$L_J = \frac{\Phi_0}{2\pi I_c} \tag{2.52}$$

The energy stored within the junction due to the time varying current and voltage can be calculated to

$$E(\varphi) = -\frac{\Phi_0 I_c}{2\pi}\cos\varphi \tag{2.53}$$

with the characteristic Josephson energy

$$E_J = -\frac{\Phi_0 I_c}{2\pi} \tag{2.54}$$

The Josephson inductance and energy are related by

$$E_J = L_J I_c^2 \tag{2.55}$$

It should be noted, that by **including an external magnetic field**, the phase difference $\Delta\varphi$ has to be replaced with the gauge-invariant phase difference

$$\gamma = \Delta\varphi - \frac{2\pi}{\Phi_0}\int A ds \tag{2.56}$$

where A is the vector potential and the integral is along the distance s from one electrode of the weak link to the other.

The external magnetic field therefore affects the Josephson junction in two ways. First it can be seen from Eqs. 2.49 2.50 that the temperature dependent critical current $I_c(T)$ is proportional to the BCS energy gap. For high magnetic fields the critical current and, as Eq. 2.54 states, the Josephson energy will be affected and reduced by a decreasing energy gap. On the other hand Eq. 2.53 relates the energy stored within the junction with the phase difference across the junction. That phase difference is replaced by a magnetic field dependent term, which means that the energy stored oscillates with a cosine with magnetic field and differs from the Josephson energy. Examplarily for that is the Fraunhofer diffraction pattern of the critical current in an extended Josephson junction. Furthermore it is the basis for DC-SQUID devices. [18, 34]

RCSJ Model

To describe the behaviour of a true Josephson junction, where finite voltages have to be included, the RCSJ (resistively and capacitively shunted junction) model can be used [18]. As the name indicates an ideal Josephson junction following

$$I_s = I_{c0} \sin(\gamma) \tag{2.57}$$

is shunted in parallel by a resistor R and a capacitor C. The resistor causes dissipation for the finite voltage case, while the capacitor corresponds to the geometric capacitance between the electrodes of the junction.

The total current is the sum of the three parallel channels given by

$$I = I_{c0} \sin(\gamma) + \frac{V}{R} + C\frac{dV}{dt} \tag{2.58}$$

and after rewriting V in terms of γ one ends with a second order differential equation

$$\frac{d^2\gamma}{d\tau^2} + \frac{1}{Q}\frac{d\gamma}{d\tau} + \sin\gamma = \frac{I}{I_{c0}} \tag{2.59}$$

Here $\tau = \omega_p t$ with ω_p being the plasma frequency of the system and Q the quality factor.

Qualitatively the RCSJ model and its solution can be visualized by the tilted-washboard model, which is an mechanical analog. A particle with mass $M = (\frac{\hbar}{2e})^2 C$ and damping $\eta = (\frac{\hbar}{2e})^2 \frac{1}{R}$ is affected by the potential

$$U(\gamma) = -E_J \cos\gamma - \left(\frac{\hbar I}{2e}\gamma\right) \tag{2.60}$$

with $E_J = \frac{\hbar}{2e} I_{c0}$ the Josephson coupling energy. The total current I modifies the potential in the following way. For $I < I_{c0}$ the particle is trapped inside a minimum of the cosine

and $V = 0$. By increasing I the slope is tilted and at $I = I_{c0}$ the minima turn into inflection points. For $I > I_{c0}$ only time dependent solutions are possible creating a voltage drop across the junction.

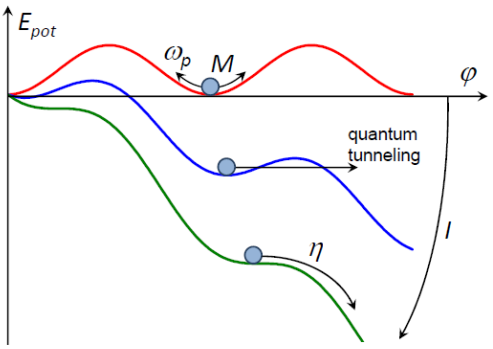

Figure 2.5.: Tilted washboard model. Here the effects of an external magnetic field, $E_J(B)$, are not included. The phase difference is given by φ. Figure taken from [35].

For **overdamped junctions** (C small, $Q \ll 1$) Eq. 2.59 simplifies to

$$\frac{d\gamma}{dt} = \frac{2eI_{c0}R}{\hbar}\left(\frac{I}{I_{c0}} - \sin\gamma\right) \tag{2.61}$$

with the solution for the voltage given by

$$V = R(I^2 - I_{c0}^2)^{\frac{1}{2}} \tag{2.62}$$

For $I < I_{c0}$ the voltage $V = 0$, while for very high currents it translates into Ohm's law with $V = IR$.

In the **underdamped** case (C large and $Q > 1$) the current voltage relation is hysteretic showing a zero voltage branch and a finite voltage branch with $V \approx I_{c0}R$ in the RCSJ model. For a real tunnel junction the voltage is given by the BCS energy gap $V = 2\Delta/e$, before approaching Ohm's law at high currents. In addition, the critical current is separated into an escaping current I_{c0} for increasing current from zero to infinite and a retrapping current I_{r0} for decreasing current from infinite to zero. Thermal fluctuations may decrease the separation of the two critical currents and even completely destroy the hysteretic behaviour. Then the value of the critical current $I_c < I_{c0}$ is independent on the sweeping direction.[18]

2.2. Superconductivity in Two Dimensions

By decreasing the thickness one approaches the 2D limit, where $d < \lambda$. In this regime the properties of superconductors are different to the bulk properties. In the **parallel magnetic field** configuration one has to replace the London penetration depth by an effective penetration depth λ_{eff} given by

$$\lambda_{\mathrm{eff}} \approx \lambda_{\mathrm{L}} \left(\frac{\xi_0'}{d} \right)^{1/2} \tag{2.63}$$

where ξ_0' is the modified Pippard coherence length for nonlocal electrodynamics [18]. The critical parallel field for a thin film can then be written as

$$B_{\mathrm{c}\parallel} = \sqrt{24} B_{\mathrm{c}} \frac{\lambda_{\mathrm{eff}}}{d} \tag{2.64}$$

where $\mathrm{B_c}$ denotes the thermodynamical critical field as defined in Eq. 2.32 and 2.33. In **perpendicular magnetic field** configuration the critical magnetic field is approximated by $\mathrm{B_{c2}}$ as defined in Eq. 2.36 and replacing λ by λ_{eff} [18]. For very thin films $d \ll \lambda_{\mathrm{eff}}$ Pearl [36] has shown, that

$$\lambda_{\perp} \approx \frac{\lambda_{\mathrm{eff}}^2}{d} \tag{2.65}$$

is a better description as it properly describes the screening length for the supercurrent. The upper critical magnetic field for ultra-thin films is then given by

$$B_{\mathrm{c}\perp} = \sqrt{2} B_{\mathrm{c}} \frac{\lambda_{\mathrm{eff}}^2}{d\xi} \tag{2.66}$$

2.2.1. Berezinskii-Kosterlitz-Thouless Transition

In section 2.1.2 the intermediate state of Type 2 superconductors $B_{\mathrm{c1}} < B < B_{\mathrm{c2}}$ was connected to single vortices, which can be viewed as flux penetrating through the material, surrounded by a screening supercurrent. In thin superconducting films with $d \ll \xi$ a magnetic vortex may spontanously be generated for $T \ll T_{\mathrm{c0}}$ even at $B = 0$. This leads to a finite resistance even below the critical mean field temperature T_{C0}. The vortex shape resembles a pancake for which the magnetic field penetrates perpendicular to the plane of the film.

The concept bases on a model by Kosterlitz and Thouless [37, 38] originally introduced for the phase transition of a liquid without long range order to a state with long range order. It is based on the XY-model and liquid helium. The KT-transition or BKT-transition (Berezinskii had already described vortex-anti-vortex pairs earlier [39, 40]) is associated with the creation of vortices at a temperature T_{BKT}. Below that temperature a vortex is not thermodynamically favoured. For $T > T_{\mathrm{BKT}}$ however it is and can live as an excited state. This theory was not applicable to superconductors, which is a charged superfluid.

The creation of one single vortex comes with a finite magnetic field and is not allowed as an excited state in such a charged superfluid. In 1979 Halperin and Nelson [41] reworked the theory and extended it to describe thin superconducting films by considering not single vortices, but vortex-anti-vortex pairs with a net magnetic field that cancels out to zero, i.e. vortex and anti-vortex show an opposite circulation sense. The nobel prize in physics was awarded to Kosterlitz and Thouless in 2016 for their theoretical discoveries of topological phase transitions and topological phases of matter [42].

The energy cost of a single vortex is given by

$$E_{\mathrm{V}} = \left(\frac{\Phi_0^2}{4\pi\lambda_\perp\mu_0}\right)\ln\left(\frac{\lambda_\perp}{\xi}\right) \tag{2.67}$$

where $\lambda_\perp$ is the Pearl penetration depth and ξ the GL-coherence length. For the case that the sample size R is smaller than the Pearl penetration depth, it has to be substituted with R in the argument of the logarithm.
In the BKT regime vortex-anti-vortex pairs are created in a distance R_{12} separating the vortex and the anti-vortex. The total energy of such a pair is not two times the energy of a single vortex, but set by the inter vortex separation R_{12}.

$$E_{\mathrm{V,pair}} = 2\left(\frac{\Phi_0^2}{4\pi\lambda_\perp\mu_0}\right)\ln\left(\frac{R_{12}}{\xi}\right) \tag{2.68}$$

The energy of the pair increases with increasing intervortex separation and acts as an attractive force between the two components of the pair. By decreasing the distance R_{12} to $\approx \xi$ the vortex and the anti-vortex touch and annihilate each other.
The unbinding temperature $T_{\text{V-BKT}}$ separates two regimes. Below $T_{\text{V-BKT}}$ only pairs do exist, while in the temperature region $T_{\text{V-BKT}} < T < T_{\mathrm{c0}}$ the pairs are broken up due to thermal activation. This creates independently moving single vortices.
The transition temperature is found by comparing the energy cost to create a vortex-anti-vortex pair ($T < T_{\mathrm{BKT}}$) with the gained entropy for two independently moving vortices ($T > T_{\mathrm{BKT}}$)

$$k_{\mathrm{B}}T_{\text{V-BKT}} \approx \frac{\Phi_0^2}{8\pi\lambda_\perp\mu_0} \tag{2.69}$$

A current passing through the sample creates a resistance only in the BKT phase with free single vortices. Due to opposite circulation sense the vortices and anti-vortices move into opposite directions and disappear at the edges of the sample. The resistance given by flux flow as presented in section 2.1.2 follows a square root form [41, 43] as

$$R(T) \propto \exp\left(\frac{-b}{(\frac{T}{T_{\text{V-BKT}}}-1)^{1/2}}\right) \tag{2.70}$$

Experimentally the transition temperature may be found by studying current-voltage characteristics. Above $T_{\text{V-BKT}}$ the voltage linearly depends on the current $V \sim I$. Below

$T_{\text{V-BKT}}$ there are no free vortices at $I = 0$, i.e. no linear resistance. The only vortices generated are those from the current, which come in pairs. Therefore right below the transition temperature the number of vortices increases with I^2 and $V \sim I^{\alpha}(T)$ with $\alpha(T_{\text{V-BKT}}) = 3$. The jump from $V \sim I$ to $V \sim I^3$ right at $T_{\text{V-BKT}}$ was confirmed by [44] and is a hallmark of the BKT transition.

2.2.2. Superconducting Fluctuations

Thin disordered films do not show an abrupt jump to the zero resistive state at the BCS mean field T_{c0}, but rather a decrease until the temperature decreases below the vortex BKT transition temperature $T_{\text{V-BKT}}$. However, for temperatures $T > T_{\text{c}}(B)$ with $B > B_{\text{c2}}(T)$ the conductivity is influenced by superconducting fluctuations connected to a fluctuating finite amplitude of the order parameter.
There are two separate contributions to the conductivity for T > T_C. The above mentioned superconducting fluctuations, represented by a charge transport channel for Cooper-Pairs (Cooper channel) and electron localization effect (diffusive channel).

An overview of the different contributions can be found in [45], where ultra-thin disordered TiN films were analyzed by taking quantum contributions to the conductivity into account.

The diffusive channel takes into account weak localization (WL) and interelectron interferences due to Aronov-Altshuler effect (AA) [46].

Weak localization is generated by the interference of an electron with itself. If an electron passes the same place twice for $t < \tau_{\Phi}$ (τ_{Φ} is the time after which the electron loses its phase memory due to inelastic scattering in the classical case), then the probability to find that electron in that place is double the classical value. This leads to an effective decrease in conductivity.
The Aronov-Altshuler term concerns two electrons that interfere with each other twice. This leads to a constructive interference in case the two electrons exhibit the same phase at a given time $t = 0$. The impact on conductivity is negligible for disordered films, but the interelectron interaction reduces the densitity of states around the Fermi level.
A distinction of both effects is only possible in magnetic field, where the WL contribution vanishes while the AA contribution is independent on magnetic field.

$$\Delta G^{AA} = \Delta G^{WL} + \Delta G^{ID} = G_{00} A \ln\left(\frac{k_{\text{B}} T \tau}{\hbar}\right) \tag{2.71}$$

where $A = \alpha p + B$ (αp originates from WL and B corresponds to AA), $\text{G}_{00} = \frac{e^2}{2\pi^2\hbar} \approx (81k\Omega)^{-1}$ and the time τ is given by the mean free path $l = \nu_F \tau$ for an elastic scattering event.
B is in the order of unity and depends on Coulomb screening. α should be taken as 1 for potenital, -1/2 for orbital and 0 for scattering interactions. p is connected to $1/\tau_{\Phi}$.

The Cooper channel governs the effects due to creation of Cooper pairs, i.e. interacting electrons with nearly oppsite momenta, due to fluctuations and the resulting consequences. The Aslamazov-Larkin (AL) term [47] is directly connected to the increase of conductivity due to the creation of Cooper pairs.

$$\Delta G^{\mathrm{AL}} = \frac{e^2}{16\hbar}\frac{T}{(T-T_{\mathrm{c}})} \tag{2.72}$$

As Cooper pairs are created above the critical temperature T_{c} the effective number of normal electrons decreases, which leads to a decrease of conductivity given by the Drude formula, (DOS-term) [48].

$$\Delta G^{\mathrm{DOS}} = G_{00}\ln\left(\frac{\ln\left(T/T_{\mathrm{c}}\right)}{\ln\left(k_{\mathrm{B}}T_{\mathrm{c}}\tau/\hbar\right)}\right) \tag{2.73}$$

The third term is due to renormalization of the single-particle diffusion coefficient in presence of fluctuations (DCR)

$$\Delta G^{\mathrm{DCR}} = \frac{4}{3}G_{00}\left(\ln\ln\left(1/T_{\mathrm{c}}\tau\right) - \ln\ln\left(1/T_{\mathrm{c}}\right)\right) \tag{2.74}$$

and the last considered term originates from the coherent scattering of electrons on impurites. This term is referred to as Maki-Thompson (MT) term [49–51] and can be positive or negative depending on the conventional pair breaking parameter $\delta = (\pi\hbar)/(8k_{\mathrm{B}}T\tau_{\Phi})$.

$$\Delta G^{\mathrm{MT}} = G_{00}\beta(T)\ln\left(\frac{T\tau_{\Phi}}{\hbar}\right) \tag{2.75}$$

where $\beta(T)$ is the Larkin factor.

Superconducting fluctuations may play an important role even at low temperatures $T < T_{\mathrm{c}}$ for magnetic field exceeding B_{c2}. The total conductivity is given by

$$\Delta G(T,B) = G_0 + \Delta G^{\mathrm{ID}} + \Delta G^{\mathrm{SF}} \tag{2.76}$$

The correction ΔG^{ID} reads as

$$\Delta G^{\mathrm{ID}} = G_{00}B\ln\left(\frac{k_{\mathrm{B}}T\tau}{\hbar}\right) \tag{2.77}$$

as shown in Eq. 2.71. The corrections above B_{c2} at $T \ll T_{\mathrm{c0}}$ due to superconducting fluctuations were calculated by [52]. The contributions AL, MT and DOS in the dirty limit $T_{\mathrm{c0}}\tau \ll 1$ can be written in a first loop approximation as

$$\Delta G^{\mathrm{SF}} = \frac{2e^2}{3\pi^2\hbar}\left[-\ln(\frac{r}{h}) - \frac{3}{2r} + \psi(r) + 4[r\psi'(r) - 1]\right] \tag{2.78}$$

Here $r = (1/2\gamma)h/t$ with $\gamma = 1.781$ Euler's constant. $h = (B - B_{\mathrm{c2}}/B_{\mathrm{c2}}(0))$ and $t = T/T_{\mathrm{c0}}$. ψ is the digamma function and ψ' is the trigamma function.

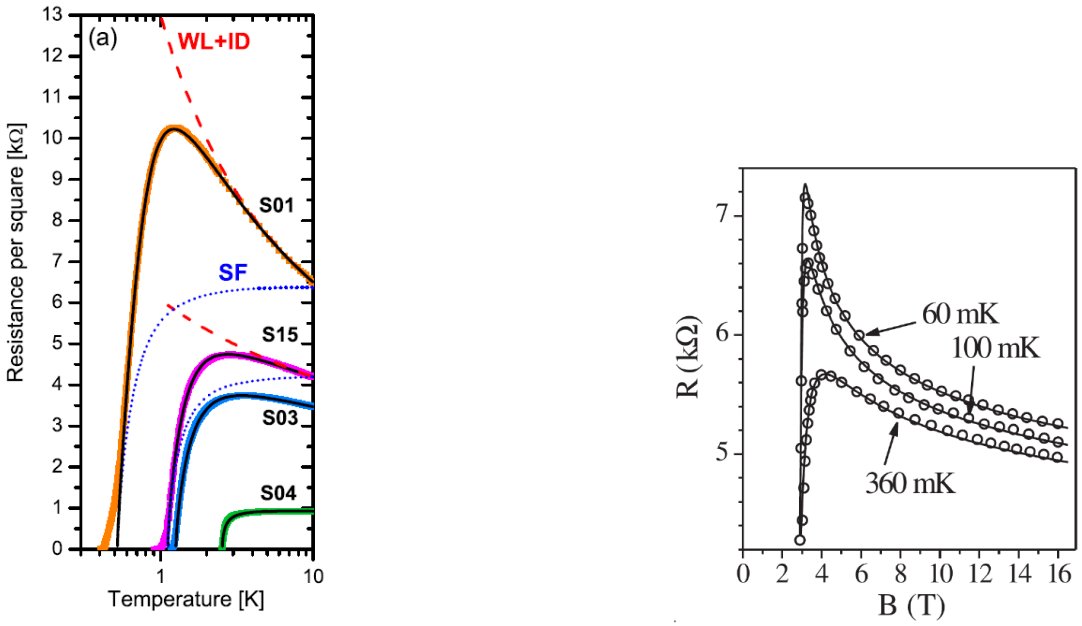

Figure 2.6.: a) Sheet resistance of 4 TiN samples fitted with all quantum fluctuation contributions. Contributions of diffusive channel and superconducting fluctuations are separately shown by red and blue dotted lines, respectively.
b) Fits of the Galitski-Larkin formula Eq. 2.78 for $T_c = 2$K and $B_c(0) = 2.8$T. a) taken from [45], b) taken from [53]. Orig. [54].

2.2.3. Superconductor-Insulator Transition (SIT)

In three dimensional (3D) systems two distinct transitions separate the superconducting state from a metallic state (SM transition) and the metallic state from an insulating state (MI transition). Those transitions are reviewed in [55, 56].

In the two dimensional (2D) case, Refs. [7, 57] and [58] review the most important results on the theoretical side and findings on the experimental side of the SIT.

It was Anderson who first came up with the idea that it should be possible to turn a superconductor into an insulator in case it consists of superconducting islands connected by (normal or insulating) Josephson weak links. The insulating state would then result from localized Cooper pairs on the islands, decoupled from each other [7]. His work was transfered onto granular systems by Abeles [8] and the theoretical proof of existence of such a phase transition in granular superconductors was given by Efetov [59]. Fisher predicted in 1986 [60] that the disorder induced transition should exactly happen at or very close to the quantum resistance for Cooper pairs $R_Q = \frac{\hbar}{(2e)^2} = 6.45\text{k}\Omega$ after evaluating data of granular Sn [61, 62]. This was supported by measurements on granular Pb, Al, In and Ga [10].

In 1989 Haviland [63] presented measurements on homogenously disordered bismuth films grown onto germanium, which revealed a transition from a superconducting state to an insulating state with decreasing film thickness as well. In addition, the resistance separating the superconducting and the insulating side is approximately R_{Q} as predicted for granular systems. However, it was also found that in lead films the separation resistance was at a higher value i.e. differed from R_{Q}.
In homogenously disordered thin films the origin of the transition is often referred to self-granularity indicating a self-ordering into superconducting islands in a spatially homogenous film [64, 65].
It was confirmed by simulations, that for sufficiently high disorder homogenously disordered films break into superconducting islands separated by an insulating sea [66]. Measurements on local density of states by scanning tunneling spectroscopy on TiN and InOx films support this hypothesis [67].

The transition is referred to as disorder-driven superconductor insulator transition (D-SIT) and has been found in various superconductors. There are amorphous e.g. InOx [68] and Ga [9], polycristalline e.g. TiN [69] and granular e.g. Pb [70] films. Disorder may be tuned in various ways, e.g. by thickness variation [71], thermal treatment [72] or a variation of stochiometric concentration in relatively thick superconducting alloys [73]. In the latter case for NbSi the SIT transition comes with an intermediate metallic phase as predicted for the transition in 3D. That intermediate metallic phase can be seen in Fig. 2.7a) for truely 2D amorphous lead films, where the transition was tuned by thickness variation. However, such an intermediate metallic state is not always observed. For example it is absent in case of TiN as seen in Fig. 2.7c).
Fig. 2.7 shows the thickness induced SIT for amorphous lead and lead grains with diameter $\approx$ 20nm and height $\approx$ 5-8nm. Clearly visible is the temperature dependence of the transition temperature in homogenously disordered films a), whereas the transition temperature is independent on the film thickness for Pb grains in b).

The origin of the SIT is still debated and there are more than one scenario that give rise to a superconductor insulator transition. In homogenous systems the mechanism may be of **fermionic** or **bosonic** nature. The third model is based on the physics of granular superconductors and is built on resistively shunted **Josephson junction arrays**. This model can be applied to granular and homogenous 2D superconductors. Another model involves **percolation**. In this model the superconductor has to be either naturally inhomogenous or homogenous with order parameter amplitude fluctuations, making it quasi-inhomogenous. That effect may play a role for the other three models as in reality inhomogeneity is unavoidable.[58]

The superconducting state is characterized by an order parameter (see GL theory 2.1.2)

$$\Psi(r) = \Delta(r) \exp\left(i\varphi(r)\right) \tag{2.79}$$

where Δ is the superconducting gap amplitude and φ the phase. The Cooper pair density

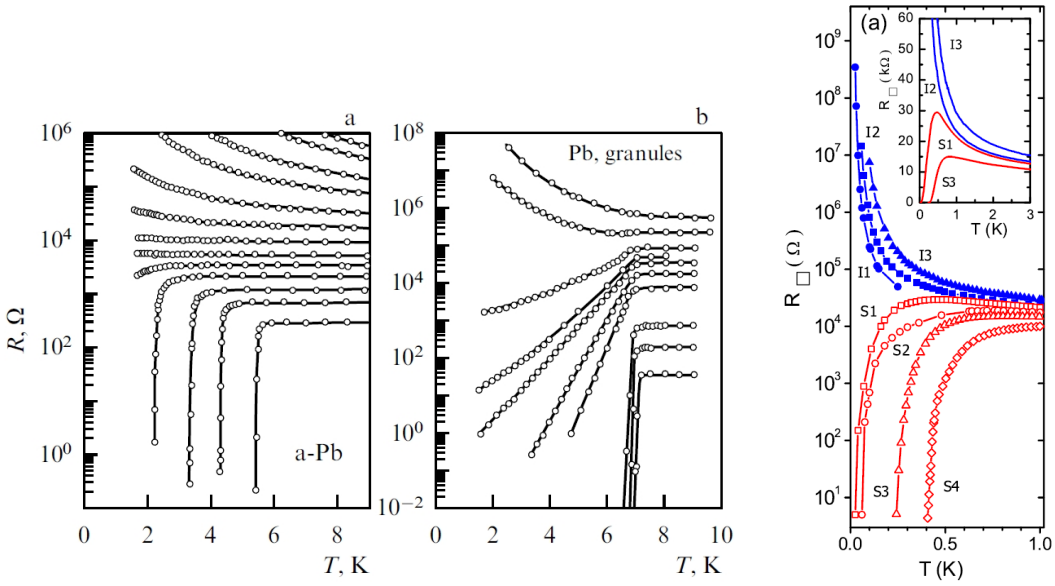

Figure 2.7.: SIT in a) amorphous and b) very small grains of Pb induced by thickness variation. Thickness increases from top to bottom. Adapted from [57]. Data from [71].
c) D-SIT without intermediate metallic phase in TiN tuned by thickness reduction using plasma etching. Figures taken from [69].

is given by

$$n_s = |\Psi|^2 = \Delta^2 \tag{2.80}$$

The particle density n_s and the phase are conjugate variable and are connected by the uncertainty principle

$$\Delta n_s \Delta\varphi \geq \hbar \tag{2.81}$$

Global phase coherence is achieved when the correlator

$$G(r) = \langle \Psi(r)\Psi(0) \rangle \tag{2.82}$$

remains finite at a long distance.

The **fermionic scenario of localization** is based on the work of Finkel'stein [74]. In this scenario the superconducting order parameter is suppressed by disorder in a homogenously disordered system. The competition between attractive and repulsive forces determines the low temperature behaviour. If attractive forces dominate, then Cooper pairs are created, i.e. a superconducting state emerges. In case of strong repulsive forces Cooper pairing is suppressed. Coulomb repulsion may be increased with increasing disorder due to a reduced electron mobility originating from impurity scattering. Hence, a superconductor-metal transition can be induced as for sufficiently high disorder Cooper pairing is unfavoured. The suppression of the transition temperature T_c from the bulk

T_{c0} value should follow

$$\frac{T_c}{T_{c0}} = \exp\left(-\frac{1}{\gamma_\tau}\right)\left[\left(1+\frac{(t_{00}/2)^{1/2}}{(\gamma_\tau - t_{00}/4)}\right)\cdot\left(1-\frac{(t_{00}/2)^{1/2}}{(\gamma_\tau - t_{00}/4)}\right)\right]^{1/\sqrt{2t_{00}}} \tag{2.83}$$

with $\gamma_\tau = 1/\ln(k_B T_{c0}/\hbar) < 0$ and $t_{00} = (e^2/2\pi^2\hbar)/R_\square(300K) = G_{00}R_\square(300K)$. Here the sheet resistance at room temperature is used as a measure of the disorder.
In this scenario the insulating state evolves by Anderson localization of electrons after the destruction of superconductivity. The intermediate metallic state between superconducting phase and insulating phase arises because the raising disorder leads to a reduction of Cooper pairs and an increase of single electrons until the breakdown of superconductivity. However, this disorder is not yet sufficient to localize normal charge carriers. At higher levels of disorder Anderson localization leads to an insulating state. The fermionic transition is rather a Superconductor-Metal-Insulator (SMI) transition than a direct Superconductor-Insulator (SI) transition.
The predicted suppression of T_c given by Eq. 2.83 was found to be in good agreement with experimental findings in homogenous thin films like TiN in the vicinity of the SIT [67], but no intermediate metallic phase has been found (see Fig. 2.7c)).

Another explanation for a SIT is the **bosonic scenario of localization**. We have already seen in Eq. 2.81 that phase and particle density are conjugate variables. In the superconducting state the phase of the macroscopic wavefunction is well defined and the particle number remains unknown. The opposite case is given when the particle number is fixed and the phase is fluctuating. This corresponds to localized Cooper pairs, i.e. local superconductivity is present, but global phase coherence is not achieved. Hence the system behaves insulating as the superconducting gap amplitude remains finite indicating Cooper pairing, but the correlator in Eq. 2.82 is suppressed.

For two dimensional, disordered superconducting films, the groundstate is composed by Cooper pairs. However, due to the disordered nature of the film, global phase coherence may not be established and an insulator should emerge without an intermediate metallic phase [75–77]. Local superconductivity may exist in some areas, but no global superconductivity is found. The small superconducting islands may be effectively disconnected from each other depending on external tuning parameters [75, 78]. Larkin [79] developed a theory for the suppression of the vortex-BKT transition temperature in uniformly disordered superconductors based on a bosonic approach. His idea is closely related to the JJA model. The superfluid density is reduced by classical and quantum fluctuations. A reduction of the superfluid density supresses the vortex-BKT transition temperature. That means at a sufficient strong disorder the superfluid density as well as $T_{\text{V-BKT}}$ approach 0, however the BCS critical temperature T_{c0} is changed only insignificantly. As the global superconducting state is absent due to the suppression of $T_{\text{V-BKT}}$, but a finite superconducting gap amplitude is present, this resembles superconducting islands decoupled from each other.

In case of a granular superconductor the scenario of superconducting islands in a normal or insulating matrix is naturally realized. Therefore granular superconductors are natural model objects to study the bosonic scenario for a SIT. However, true granular systems are very complicated objects. Related systems are artifical Josephson junction arrays [80, 81] and ultra-thin amorphous films patterned with a honeycomb lattice [82].
Historically, artifical Josephson junction arrays and granular superconductors were studied in parallel and showed similar effects. JJAs offer the possibility of an experimentally accessible system, where the two tuning parameters E_J (Josephson coupling) and E_C (charging energy of a single junction) may be easily controlled [7]. Due to features of JJAs, which they share with homogenously disordered and granular films, including a phase transition from superconducting state to an insulating state with disorder, JJAs are treated as a generic model for the latter two systems. The JJA model will be shown in the next section 2.2.4.
We will capture some of the essential properties of granular metals and superconductors in section 2.3.

In case the sample is in the vicinity of the disorder induced SIT ($R_N \approx R_Q$, $E_J \approx E_C$), then the transition may be induced by an applied magnetic field. This transition is called B-SIT and is accompanied by the creation of a highly insulating state by a small magnetic field in case the sample is still at the superconducting side for $B = 0$T. If it is on the insulating side already, then a small magnetic field further increases the resistance (see Fig. 2.8). This positive magnetoresistance (PMR) is followed by a negative magnetoresistance (NMR) for higher fields.

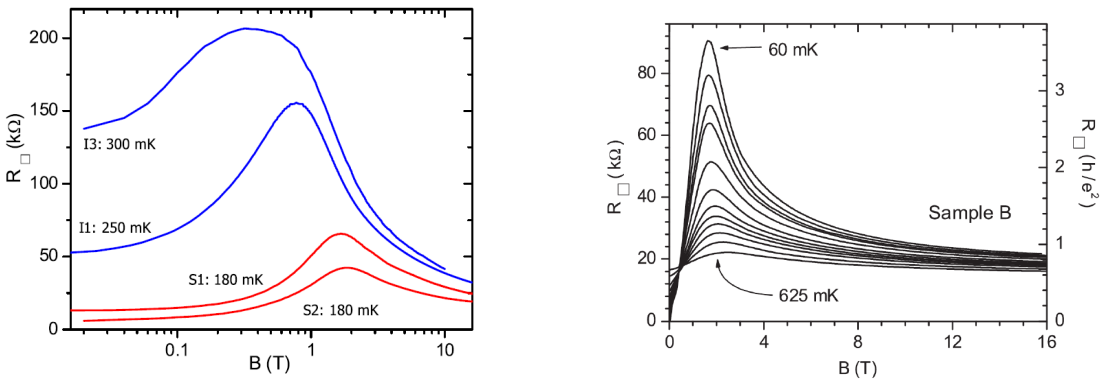

Figure 2.8.: a) Magnetoresistance isotherms of four samples. The red curves correspond to superconducting samples at $T, B = 0$ and blue curves to insulating samples at $T, B = 0$.
b) Magnetoresistance isotherm of a sample on the superconducting side of the SIT for various temperatures.
Material: TiN. Figures taken from [69] and [83].

SIT as Quantum Phase Transition

In context of the bosonic mechanism, Fisher [84] pointed out in 1990, that the Superconductor-Insulator transition in thin metal films may be associated with a continuous quantum phase transition (QPT) and is nowadays accepted as one of the prime examples [85]. QPTs occur between competing groundstates of many-body systems and result from quantum fluctuations near critical points [86]. At $T = 0$ a quantum phase transition arises as a parameter in the Hamiltonian of the quantum system is changed. The two groundstates are separated by a quantum critical point.

$R(T)$ curves measured for thin Bismuth films [63] showed a separation into superconducting $R(T)$s (positive temperature coefficient) and insulating $R(T)$ (negative temperature coefficient) around a fixed point without an intermediate metallic regime. The value of the critical resistance coincided approximately with the quantum resistance for Cooper pairs $h/4e^2$. However, this critical value was found to be non-universal in later studies. Nevertheless, a dual picture for the superconducting phase and the insulating phase was applied to describe the SIT with Boson physics. In case of the B-SIT a critical magnetic field B_c separates the superconducting side from the insulating side, while in D-SIT it is a critical disorder Δ_c for the critial point.
The superconducting side of the B-SIT consists of Bose condensed Cooper pairs and vortices are localized in a vortex glass. On the insulating side, vortices are delocalized by Bose condensation and Cooper pairs are localized in a Cooper pair glass. Right at the critical point there is no Bose condensation at all and both vortices and Cooper pairs diffuse with a finite resistance. Experimentally, that critical point with a metallic behaviour may not be observed as it is an unstable point.
The D-SIT shows a similar picture but with critical disorder Δ_c.

Near a quantum phase transition there are two correlation length, ξ and ξ_τ, which diverge by approaching the critical point at $T = 0$. The first one accounts for spatial dimension, while the latter accounts temporal dimensions. The transition happens at a critical value $g = g_c$, where g is a measure of disorder, magnetic field, etc. and enters a control parameter $\delta = \frac{g-g_c}{g_c}$. As $\delta \to 0$ at $T = 0$, both correlation length diverge following

$$\xi(g) \propto |\delta|^{-\nu} \tag{2.84}$$

$$\xi_\tau(g) \propto \xi^z \tag{2.85}$$

where ν is the correlation length exponent and z the dynamical critical exponent. The two exponents then represent universal behaviour.
As in experiments $T = 0$ is never reached, a modified model called finite-size scaling is introduced. In this model the critical exponents may be determined even at a finite temperature. In two dimension the resistance near the QPT is given by

$$R(B, T, E) = R_c \cdot F\left(\frac{\delta}{T^{1/z\nu}}, \frac{\delta}{E^{1/\nu(z+1)}}\right) \tag{2.86}$$

with B - magnetic field, T - temperature, E - electric field and R_c a resistance prefactor. The function F is system dependent, but does not have to be known for analysis.
A finite-size scaling leads to a collapse of $R(T)$ curves for exponents $z\nu$. This is examplarily shown in Fig. 2.9, where calculated $R(T)$ curves in a) collapse in b) using finite-size scaling. The two branches indicate the superconducting and the insulating side of the QPT. For a more detailed description of continuous quantum phase transitions, a deeper in-

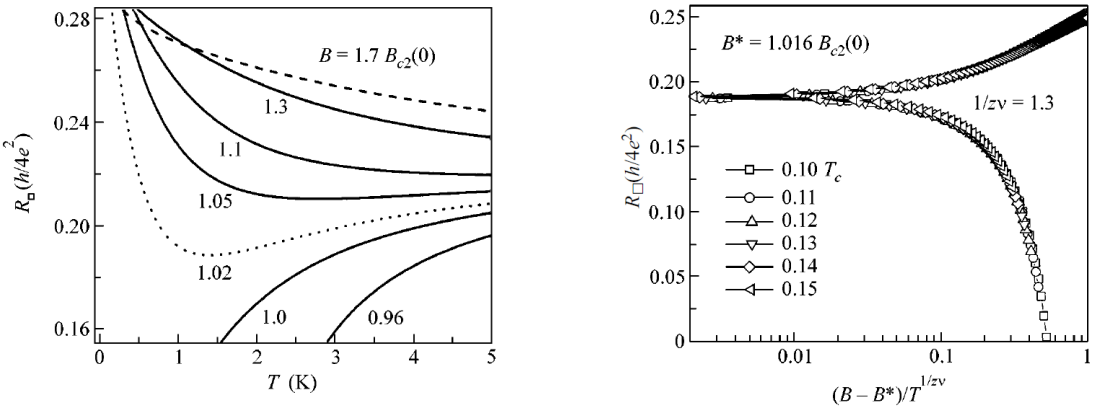

Figure 2.9.: Theoretical, calculated $R(T)$ curves shown for various ratios of $B/B_{c2}(0)$. Calculations included corrections to the conductivity due to Aronov-Altshuler interelectron interference effects as presented in section 2.2.2. The $T^* = 20$K. b) Finite size scaling for the theoretical curves in a). Figures taken from [87].

sight to the theoretical background and finite-size scaling, please refer to Refs. [84, 86, 88].

Percolative Scenario

Shimshoni [89] and Sheshadri [90] suggested that the superconductor insulator transition could be percolative. That idea would be applicaple to films, which are naturally inhomogenous, or to homogenous films, in case they are transformed into inhomogenous films by order parameter amplitude fluctuations [91]. In 2007 Strelniker [92] set up a percolation model for SIT in granular films. They modelled the granular superconductor by a two-dimensional random resistor network, which might be dominated by Josephson coupling by Cooper pair tunneling or by quasiparticle tunneling. In their modelling they found good agreement with the temperature dependence found in various granular films, e.g. Pb [71, 93], Al, Pb, In,Ga [10].

In those measurements the $R(T)$ curves followed an inverse activation law

$$R(T) \sim \exp\left(T/T_0\right) \tag{2.87}$$

in a wide temperature range below the critical transition temperature T_c as seen in Fig. 2.7 and 2.10a).

The percolative scenario for the SIT involves inhomogeneities in the coupling strength between the superconducting grains. On the superconducting side the path for the charge transport is governed by islands coupled with a different critical current I_c. On the insulating side the percolation path involves islands coupled with a different threshold voltage V_T. By crossing the SIT from the superconducting side to the insulating side the number of superconducting paths approaches zero and the system is determined by the weakest insulating paths.

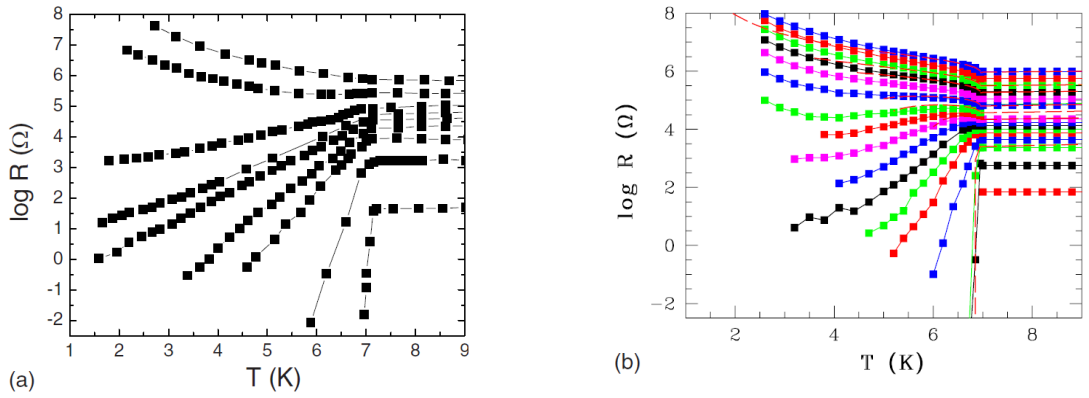

Figure 2.10.: a) $R(T)$ curves in granular Pb with grain sizes $\sim$ 5-10nm measured by [94] for different intergrain coupling strength. b) Theoretical plots to the model of [92]. Figures taken from [92].

2.2.4. Josephson Junction Array Model

A regular network of superconducting islands weakly coupled by tunnel junctions is referred to as a quantum Josephson junction array. Such arrays are an ideal model to study a variety of phenomena, e.g. phase transitions, frustration effects and vortex dynamics and offer the possibility to be accessible in case of artificially produced arrays. In such artificial JJAs those phenomena may be tuned by different parameters in a controlled way [95].

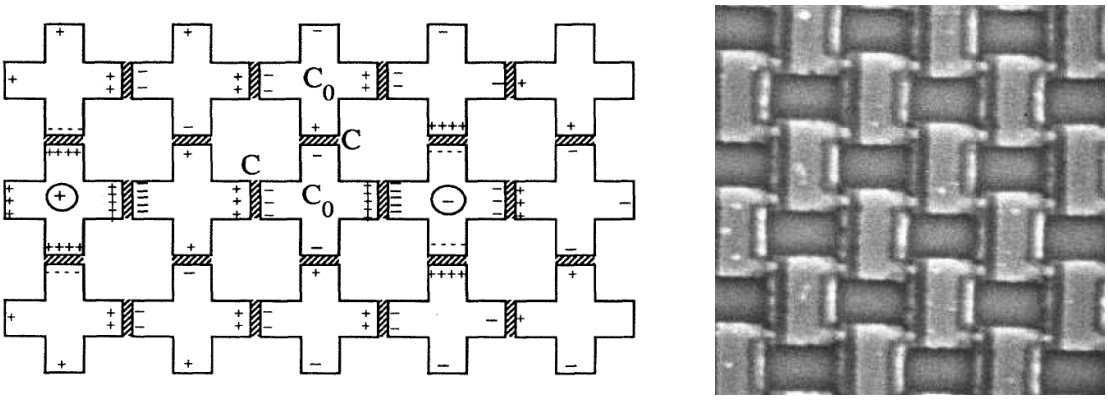

Figure 2.11.: a) Sketch of an array of tunnel junctions with capacitive couling C between the islands and C_0 to ground. Encircled + and - signs depict a local excess and a deficit of charge. Islands may be normal conducting or superconducting. In the latter the coupling is due to Josephson tunneling E_J. Figure taken from [96].
b) SEM image of a part of an array: islands are 0.5μm x 1μm. Figure taken from [81].

For Josephson junction arrays the interplay between the Josephson energy E_J and the charging energy E_C, given by the capacitance between two neighbouring electrodes, controls the low temperature behaviour of the array. For arrays with $E_\mathrm{J} \gg E_\mathrm{C}$ the array turns superconducting, while in the opposite case the array shows an insulating behaviour due to Coulomb blockade of Cooper pairs. If $E_\mathrm{J} \approx E_\mathrm{C}$, $R_\mathrm{N} \approx R_\mathrm{Q}$ then an external magnetic field may induce the B-SIT. Fazio and van der Zant [95] presented a good overview for quantum phase transitions in superconducting networks.

The Josephson energy (see section 2.1.3), related to the tunneling of Cooper pairs between the islands, is given by

$$E_\mathrm{J} = \frac{\Phi_0 I_\mathrm{c}}{2\pi} \tag{2.88}$$

with the magnetic flux quantum $\Phi_0 = h/2e$ and $\mathrm{I_c}$ the maximum critical current of the junction in absence of thermal fluctuations and charging effects. The critical current can be estimated from the superconducting energy gap Δ and the normal state resistance R_N of the junction using the formula proposed by Ambegaokar and Baratoff, Eq. 2.49.

As an array consists of a number of Josephson junctions in series and in parallel, each island is capacitively coupled to other islands denoted as C_{ij} for island i coupled to island j. In addition each island is capacitively coupled to ground with a capacitance C_0.
In the nearest neighbour approximation, that problem simplifies as only directly connected neighbouring islands are taken into account together with the coupling to ground. The resulting approximation of the charging energy gives

$$E_C = E_C^{(e)} = \frac{e^2}{2C} \qquad \text{for electrons} \tag{2.89}$$

For Cooper pairs with a charge 2e the charging energy is four times higher, i.e. $E_C^{(CP)} = 4E_C^{(e)}$. The electrostatic screening length takes into account the capacitance to ground as is given by

$$\Lambda = \sqrt{C/C_0} = \sqrt{E_0/E_C} \tag{2.90}$$

and measured in units of the lattice spacing/unit cell/plaquette.
In a distance up to Λ the Cooper pair interaction is logarithmically increasing and exponentially decreasing for larger distances. Quantum effects play a crucial role when $E_J \approx E_C$.

The Hamiltonian for such a quantum system is considered in the Quantum Phase Model (QPM). In this model quasi-particle tunneling is ignored and only Cooper pair tunneling in the superconducting quantum network is taken into account. The most general form of the Hamiltonian reads

$$H = H_C + H_J \tag{2.91}$$

$$= \frac{1}{2}\sum_{i,j}(Q_i - Q_{x,j})C_{ij}^{-1}(Q_j - Q_{x,j}) - E_J \sum_{<i,j>}\cos(\phi_i - \phi_j - A_{ij}) \tag{2.92}$$

and can be approximated by

$$H \sim \frac{1}{2}\sum_{i,j} Q_i C_{ij}^{-1} Q_j - E_J \sum_{<i,j>}\cos(\phi_i - \phi_j - A_{ij}) \tag{2.93}$$

in case the effects $Q_{x,i} = 2eq_x = \sum_j C_{ij}V_{x,j}$ of an external gate voltage $V_{x,i}$ is omitted.
The first term is the charging energy, where C_{ij}^{-1} is the capacitance matrix of the system, and the second term describes the Josephson tunneling with ϕ_i, ϕ_j the phases of the corresponding superconducting islands i, j, respectively.

Eqs. 2.92 and 2.93 include the effect of a perpendicular magnetic field with vector potential A. It enters the Hamiltonian by $A_{ij} = 2e\int_i^j Adl$, where the relevant parameter is the magnetic frustration f.

$$f = (1/2\pi)\sum_P A_{ij} = \frac{\Phi}{\Phi_0} \tag{2.94}$$

where P denotes the plaquette over which is summed.

Zero Magnetic Field

In case the Josephson tunneling dominates ($E_\mathrm{J} \gg E_\mathrm{C}$) then the energy minimum is found for aligned phases and a global superconducting phase emerges at low temperatures. In the opposite limit ($E_\mathrm{C} \gg E_\mathrm{J}$) the islands of the array are superconducting, but the array in total is insulating as the islands are effectively decoupled from each other due to the large energy cost needed to transfer an extra charge onto an island.

By tuning the ratio of $E_\mathrm{J}/E_\mathrm{C}$ the system undergoes a superconductor to insulator transition. A prominent picture of the SIT is the dual picture of vortices in the vortex-BKT regime on the superconducting side (see section 2.2.1) and charges in the so-called charge-BKT regime on the insulating side.
In the vortex-BKT regime a finite resistivity arises for $T > T_{\text{V-BKT}}$ as vortex-antivortex pairs are broken up. In the charge-BKT regime a finite conductivity is generated for $T > T_{\text{C-BKT}}$ as Cooper-pair/anti-Cooper-pair pairs (local excess and local deficit in the Cooper pair density), referred to as Cooper-pair dipoles, are broken up. The transition between the two low temperature phases was found to occur at $E_\mathrm{J}/E_\mathrm{C} = \mathrm{a}(2/\pi^2)$, where the parameter a is slightly larger but close to 1. This is depicted in Fig. 2.12. The

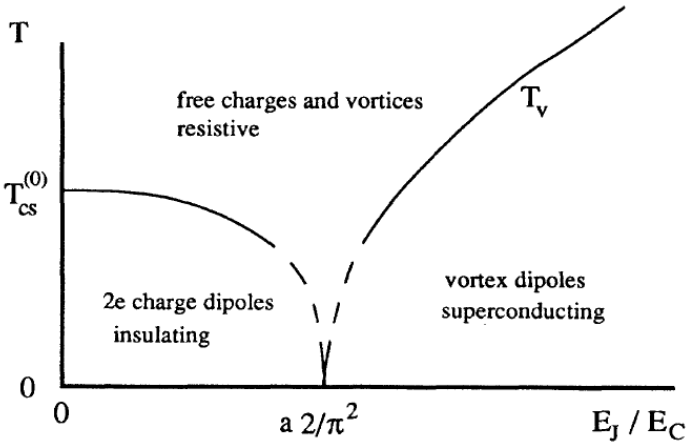

Figure 2.12.: Phase diagram for vortex- and charge-unbinding transition in a superconducting JJA depending on the ratio of $E_\mathrm{J}/E_\mathrm{C}$. Quasi-particle tunneling is ignored. Figure taken from [96].

transition temperatures in the classical limits are given by

$$k_\mathrm{B} T_{\text{V-BKT}} = \frac{\pi}{2\epsilon_\mathrm{v}} E_\mathrm{J} \quad \text{for} \quad E_\mathrm{C} = 0 \tag{2.95}$$

and

$$k_\mathrm{B} T_{\text{C-BKT}} = \frac{1}{\pi\epsilon_\mathrm{q}} E_\mathrm{C} \quad \text{for} \quad E_\mathrm{J} = 0 \tag{2.96}$$

ϵ_v and ϵ_q usually differ from each other, but are both in the order of unity [96].

However, for superconducting arrays in the vortex-BKT regime increasing capacitances between the islands leads to a suppression of the transition temperature

$$k_{\mathrm{B}}T_{\text{V-BKT}} = \begin{cases} \dfrac{\pi E_{\mathrm{J}}}{2}\left(1 - \dfrac{4}{3\pi}\dfrac{E_0}{E_{\mathrm{J}}}\right) & \text{for} \quad C_0 \gg C \\ \dfrac{\pi E_{\mathrm{J}}}{2}\left(1 - \dfrac{1}{3\pi}\dfrac{E_{\mathrm{C}}}{E_{\mathrm{J}}}\right) & \text{for} \quad C_0 \ll C \end{cases} \tag{2.97}$$

with E_0 being the self charging energy [96, 97].
On the insulating side in the charge-BKT regime a finite value of the Josephson coupling leads to a suppression of the transition temperature

$$k_{\mathrm{B}}T_{\text{C-BKT}} = \frac{1}{\pi}E_{\mathrm{C}} - 0.31\frac{E_{\mathrm{J}}^2}{E_{\mathrm{C}}} \quad \text{for} \quad E_{\mathrm{J}} \ll E_{\mathrm{C}} \tag{2.98}$$

It is interesting to note, that the charge-BKT mechanism is achieved in arrays of normal tunnel junctions as well. Here instead of Cooper-pair dipoles, single electron dipoles (charge/anti-charge) are responsible for the transition into the insulating state. Due to the reduced charge $2e^- \rightarrow e^-$, the charging energy E_{C} is reduced to $E_{\mathrm{C}}/4$, which leads to

$$k_{\mathrm{B}}T_{\text{C-BKT,N}} = \frac{1}{4\pi\epsilon_{\mathrm{c}}}E_{\mathrm{C}} \quad \text{for} \quad E_{\mathrm{J}} = 0 \tag{2.99}$$

Below $T_{\text{C-BKT,N}}$ solitons of e^-/e^+ (excess and deficit of charge) are logarithmically bound, while above the transition temperature free charges of $\pm e$ move independently.

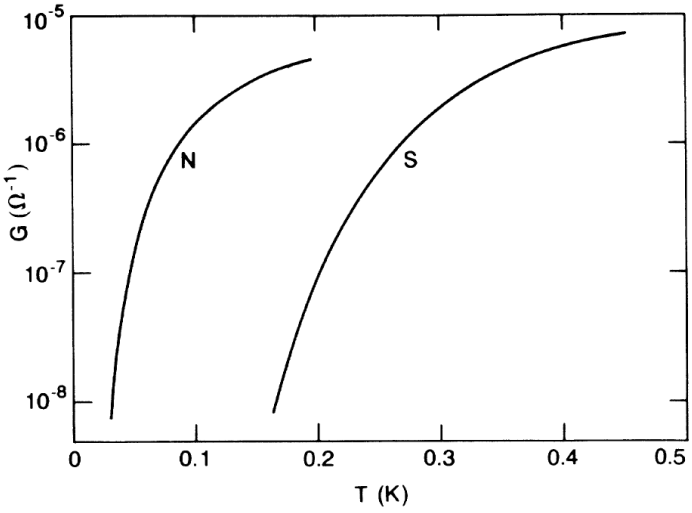

Figure 2.13.: Comparison of the conductance of an array consisting of 190x60 plaquettes of aluminum tunnel junctions. S denotes the islands to be superconducting, N denotes the islands to be in the normal state (B = 3T). Visible is the impact of superconductivity on the transition temperature $T_{\text{C-BKT}}$ due to the increase of E_{C}. Figure taken from [98].

The conductivity in the insulating state should vanish with the same dependence as the resistivity in the superconducting state, i.e. with a square root dependence on temperature. Instead an activated behaviour was found with

$$\sigma \propto \exp\left[-\frac{E_\mathrm{A}}{k_\mathrm{B}T}\right] \tag{2.100}$$

where the activation energy was approximated by $E_\mathrm{A} \sim \Delta + 0.24E_\mathrm{C}$ [80, 99].

Finite Magnetic Fields

The second term in Eq. 2.92 periodically oscillates with magnetic field. Its periodicity is determined by integer values of f, which corresponds to the case when an integer number n = f vortices penetrates one plaquette of the lattice. The Josephson coupling for integer values of f is exactly the same as in the $f = 0$ case for zero magnetic field. Due to the periodicity the behaviour with increasing magnetic field reduces to $0 \leq f \leq 1$. In the

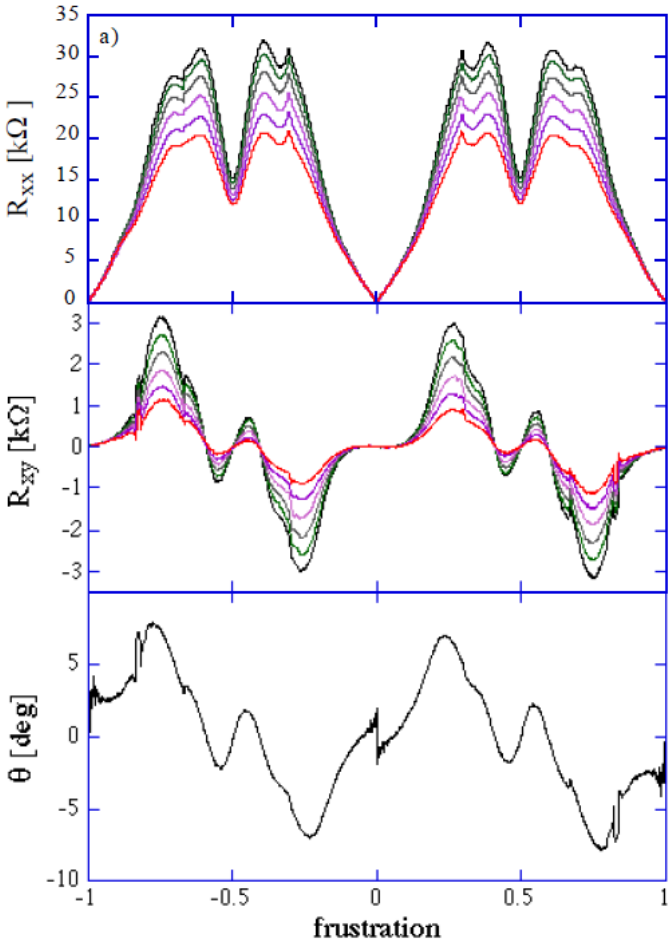

Figure 2.14.: Longitudinal resistance R_{xx}, Hall resistance R_{xy} and Hall angle θ shown for frustrations $-1 < f < 1$ and various temperatures between 20mK (top) and 175mK (bottom). The longitudinal resistance shows minima at $f \pm 1/2$ embedded in the expected peak for maximum frustration. Smaller dips in side lobes correspond to other values of p/q. Figure taken from [81].

special case $f = 1/2$, the array is at its maximum frustration, where the groundstate is constructed by alternating plaquettes of currents with opposite circulation sense. The

Josephson coupling then is suppressed. This leads to oscillations in the resistance versus magnetic field curves $R(B)$ as seen in Fig. 2.14. In addition, that manifests in highly non-linear current voltage characteristics (IVs) at the lowest temperatures (see Fig. 2.15). For f = n, n integer, critical current I_c features are present indicating a current flow of Cooper-pairs. Theoretically, for f = n + 1/2, n integer, the shape is represented by a threshold voltage V_T indicating a blockade for Cooper pair tunneling due to the maximum frustration. However, for f = p/q with p and q integer, there might be many different groundstates and their combined effect can lead to a shift of the critical (maximum) frustration f_c.

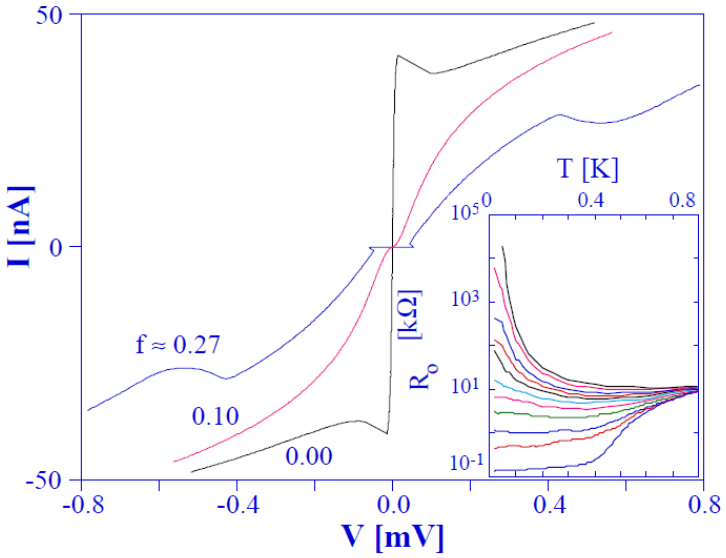

Figure 2.15.: Three selected low temperature (T = 15mK) IVs for f = 0, 0.1 and 0.27. Zero bias regime exhibits a critical current feature (vertical line) in the non-frustrated case f = 0 and a threshold voltage feature (horizontal line) for frustration f = 0.27. Intermediate frustration f = 0.1 shows a finite slope. Inset shows the corresponding $R(T)$ curves in the interval $0 < f < 0.27$. The values of the sheet resistance varies by a factor 10^4, while the magnetic field was changed by 0.44mT only. Figure taken from [81].

By further increasing the magnetic field, the prefactor E_J in Eq. 2.92 will be affected by the decreasing value of the superconducting gap Δ as Cooper pairs are broken up. This effectively drives the JJA into the insulating side by decreasing the ratio E_J/E_C and hence the overall resistance will increase (positive magnetoresistance). The resistance peaks in the $R(B)$, where the suppression of the conductivity associated by the suppression of E_J is equaled out by the increasing impact of single electron transport on the conductivity (negativ magnetoresistance).

As mentioned in the previous section, granular superconducting thin films are closely related as they naturally consist of superconducting islands (sizes may be relatively uniform or show a broad distribution) connected by various coupling energies given by island size and interisland separation). In such granular systems disorder plays a crucial role, while it is either absent in JJAs or may be induced by external parameters. Due to striking similarities to granular films and even homogenously disordered films ("self-induced granularity" in the vicinity of the SIT) JJAs can be used as a model capturing the most essential features for a wide class of systems [7]. However, the ratio $E_\mathrm{J}/E_\mathrm{C}$ is replaced by the dimensionless conductance g (measured in $\frac{e^2}{h}$) for thin films. Large values of g corresponds to superconductivity, small g to insulating behaviour and g_c denotes the critical conductance separating both regimes.

2.3. Disordered and Granular Systems

2.3.1. Conduction in Disordered Solids

Disordered solids may be categorized into a) amorphous and polycristalline solids, b) granular metals, c) doped semiconductors and d) two-dimensional electron gases (2DEGs). Ref. [100] gives a very broad overview about the physics and conduction mechanisms of those disordered electronic systems. The materials may behave metallic or insulating depending on the locations of the Fermi energy. If the material behaves insulating, then at higher temperatures the conduction follows an Arrhenius behaviour attributed to thermal excitation of charge carriers (activated behaviour).

$$\sigma \propto e^{-\frac{E_\mathrm{G}}{2k_\mathrm{B}T}} \tag{2.101}$$

where E_G is the energy gap between the bands of a doped semiconductor.

For lower temperatures it was found that the activation energy deviates from that behaviuor and decreases with temperature, which was first explained by Mott [101] and Conwell [102]. The mechanism was called "hopping" and attributed to transitions between impurities. Miller and Abrahams [103] showed that it can be viewed as a series of resistors in a network connecting impurities.

Following the ideas of Anderson [104], Mott and Twose [105] came up with the idea, that electronic systems may be described by localized wavefunctions with a sharp energy boundary, called mobility edge. This energy separates localized states from delocalized (extended states), where the transition is governed by the density of states and the localization length. It was proposed by Mott that if the electrons around the Fermi energy are localized, then the material would become insulating at low temperature, while it would become metallic if the states are delocalized. This transition is called Anderson transition. The minimum value for the metallic conductivity in 2D is given by $\frac{e^2}{h}$.

The DC conductivity on the insulating side was described by Mott [106] in 1968. He proposed a mechanism called Variable Range Hopping (VRH), where the charge carriers may hop over larger distances, compared to the Miller Abrahams approach.

For non-interaction systems the temperature dependence of the conductivity follow Mott's law

$$\sigma = \sigma_0 \exp\left[-\left(\frac{T_1}{T}\right)^{\frac{1}{d+1}}\right] \tag{2.102}$$

with d being the dimensionality of the system. Hence, for the case of a 2D film the temperature dependence follows $\sigma \propto \exp\left(-T^{-\frac{1}{3}}\right)$.

For interacting systems however, Efros and Shklovskii [107] derived the VRH by replacing the constant Mott density of states by the Coulomb gap density of states.

$$\sigma = \sigma_0 \exp\left[-\left(\frac{T_0}{T}\right)^{\frac{1}{2}}\right] \tag{2.103}$$

The conductivity in granular metals is often found to follow Efros-Shklovskii law with s $= \frac{1}{d+1} = \frac{1}{2}$ [108]. Nevertheless, s has also been found to be bigger than 0.5. For highly insulating granular aluminum films Delahaye [109] reported s = 1.

That behavior resembles the classical activated behavior governed by an activation energy due to thermal activation of charge carriers and the conductivity can be written as

$$\sigma = \sigma_0 \exp\left[-\left(\frac{T_0}{T}\right)\right] = \sigma_0 \exp\left[-\left(\frac{E_\mathrm{A}}{k_\mathrm{B}T}\right)\right] \tag{2.104}$$

2.3.2. Conduction in Granular Systems

True granular systems can be further devided into granular metals and granular superconductors. Granular metals can be viewed as a random array of N-I-N junctions, where the insulation layer may be either vacuum (free standing metallic islands) or an insulating material (metallic islands in an insulating matrix). The transport properties are determined by the tunneling conductance g between the grains, the charging energy E_C for a single grain, the mean level spacing for a grain δ and the mean electronic lifetime $\hbar/g\delta$.
For the case that the grains turn superconducting the granular system may be treated as a random array of S-I-S (Josephson junctions) in the simplest way and adds another tuning parameter to the system, namely the energy parameter Δ.
In reality one might have a broad set of different types of junctions coupled to each other as some grains may be superconducting while others may be normal conducting. The ratio of superconducting grains and normal conducting grains may depend on temperature, grain size, external magnetic field, etc. A review of the properties of granular electronic systems can be found in Ref. [110].

Granular Metals

Let us first examine the case without superconductivity. The coupling parameter $g = G/G_0$, $G_0 = \frac{2e^2}{h}$, determines the transport properties. For $g \gg 1$ (strong coupling) the granular material behaves metallic, while for $g \ll 1$ it behaves insulating. To understand the insulating state one has to take into account not only Coulomb effects (blockade of electron transport at low T) but also quantum interference effects leading to localization of electrons, as mentioned in the section above.

In the metallic regime and at high temperatures Coulomb and interference effects can be neglected and the conductivity can be written as the classical Drude formula. An

important parameter is the characteristic energy Γ, which corresponds to the invers of the life time of an electron inside a single grain.

$$\Gamma = g\delta \tag{2.105}$$

It becomes clear from Eq. 2.105 that the characteristic energy is connected to the grain coupling g and the mean energy level spacing inside a grain.
After taking into account corrections due to Coulomb effects and interference effects the critical conductance can be rewritten as

$$g_{\mathrm{c}} = (\frac{1}{2\pi d}) \ln(E_{\mathrm{C}}\delta) \tag{2.106}$$

with d being the dimension of the system.
In the 3D case the system behaves metallic for $g > g_{\mathrm{c}}$. For $g < g_{\mathrm{c}}$ it develops a Coulomb blockade for which, below a certain temperature, insulating behaviour takes over. Therefore g_{c} separates superconducting and insulating state for $T \to 0$.
In 2D there is no sharp transition from metal to insulator as low temperature conductivity corrections (electron-electron interactions and localization) have to be taken into account. For $g < g_{\mathrm{c}}$ the system exhibits a strong Coulomb blockade, while for $g > g_{\mathrm{c}}$ the system is only weakly insulating at the lowest temperatures without a clear separation from the metallic regime.

In the insulating regime, i.e. weak coupling, a periodic system becomes a Mott insulator at the lowest temperatures. The transport is mediated due to electron hopping from grain to grain and blocked due to the Coulomb gap at the lowest tempratures $T \ll \Delta_{\mathrm{M}}$. The Mott gap is then given by the charging energy $\Delta_{Mott} = E_{\mathrm{C}}$ and the conductivity is given by the Arrhenius form

$$\sigma \propto e^{-\frac{\Delta_{\mathrm{M}}}{T}} \tag{2.107}$$

However, in most real granular samples the activated behaviour is not seen at the lowest temperatures, but it is replaced by the Efros-Shklovskii law Eq. 2.103. This can not be explained by a periodic model and suggests that disorder plays a crucial role in the insulating regime. The deviation remained unexplained for a long time. Averin and Nazarov [111] considered two tunneling processes through single grains, elastic and inelastic co-tunneling. In the first case, an electron tunnels through a grain and has the same energy before and after the process. In the ineleastic case the ingoing and outgoing energies are different, therefore the grain is left behind with an electron-hole excitation. Both mechanisms base on virtual states, that are inaccessible in a classical descripton. Beloborodov [112] and Feigel'man [113] independently generalized the two processes to the case of multiple co-tunneling processes through several grains. As the tunneling probability decreases exponentially with distance or number of grains they argue that this is equivalent to the Efros-Shklovskii behaviour, where the tunneling probability between states near the Fermi surface does as well fall off exponentially.

In granular metals a crossover is expected at a temperature T^*, where the low temperature Efros-Shklovskii law translates into a simple activated dependence at higher T.

Granular Superconductors

Granular superconductors are heavily influenced by the properties of the grains, e.g. size, distance, etc.. This disorder, due to inhomogeneities exceeding the atomic level, may be controled by the resistance of the interlayer (normal conducting or insulating). Another important aspect is related to the question, whether superconductivity may exist on the grains itself. [57, 110]

In 1959 Anderson concluded that the critical temperature for superconductivity of small grains should be comparable or close to the bulk BCS T_c [114] and predicted that the average mean level spacing δ should be smaller than the BCS energy gap Δ for this arguement to hold.

$$\delta \ll \Delta \tag{2.108}$$

If on the other hand this condition is not fullfilled, conventional BCS theory is no longer applicable and the grains can not get superconducting by themselves. Experimentally it was found that below $\approx$ 5nm the electron spectrum of aluminum grains did not show any features of superconductivity [115].

The transport properties of granular superconductors are very rich, vary for different material systems and far from being understood. The most common model used is the JJA model as discussed in section 2.2.4 based on superconducting networks reviewed by Fazio and van der Zant [95].
In absence of magnetic field granular superconductors show a non-monotonic temperature dependence. By decreasing temperature their resistivity increases due to enhancement of Coulomb correlations, which decreases the current. Closer to the transition temperature the resistivity starts to decrease and vanishes for even lower temperatures (see Fig. 2.16). In addition, granular films with a normal state sheet resistance close to the critical value R_Q often exhibit a complicated reentrant behaviour, where the resistance first drops as it would go superconducting but then increases for lower temperatures. This effect can be seen in Fig. 2.17 and is attributed to be a consequence of the competition between the conductance increase due to Cooper pairing and freezing of excitations due to the opening of the superconducting gap in the density of states [110].

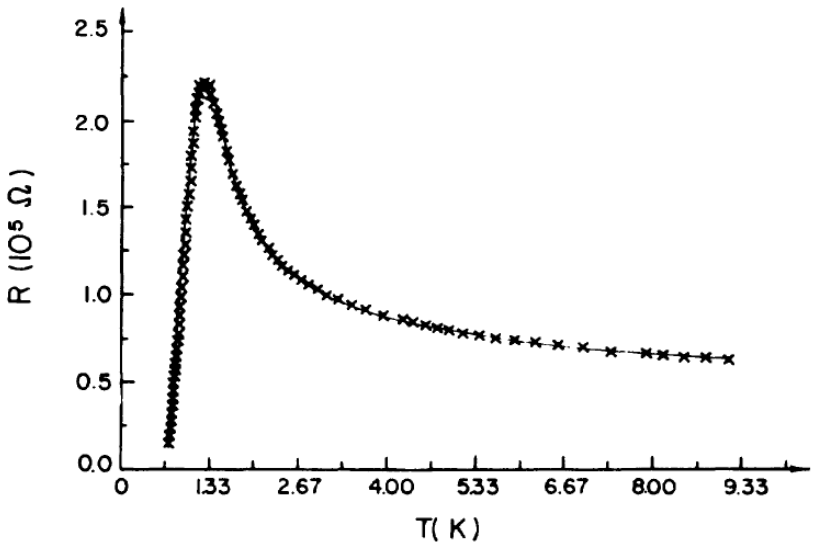

Figure 2.16.: $R(T)$ curve of a granular aluminum film on germanium. An increase in resistance is clearly visible until the grains turn superconducting and a finite Josephson coupling E_J leads to a vanishing resistance below the critical temperature. Figure taken from [116].

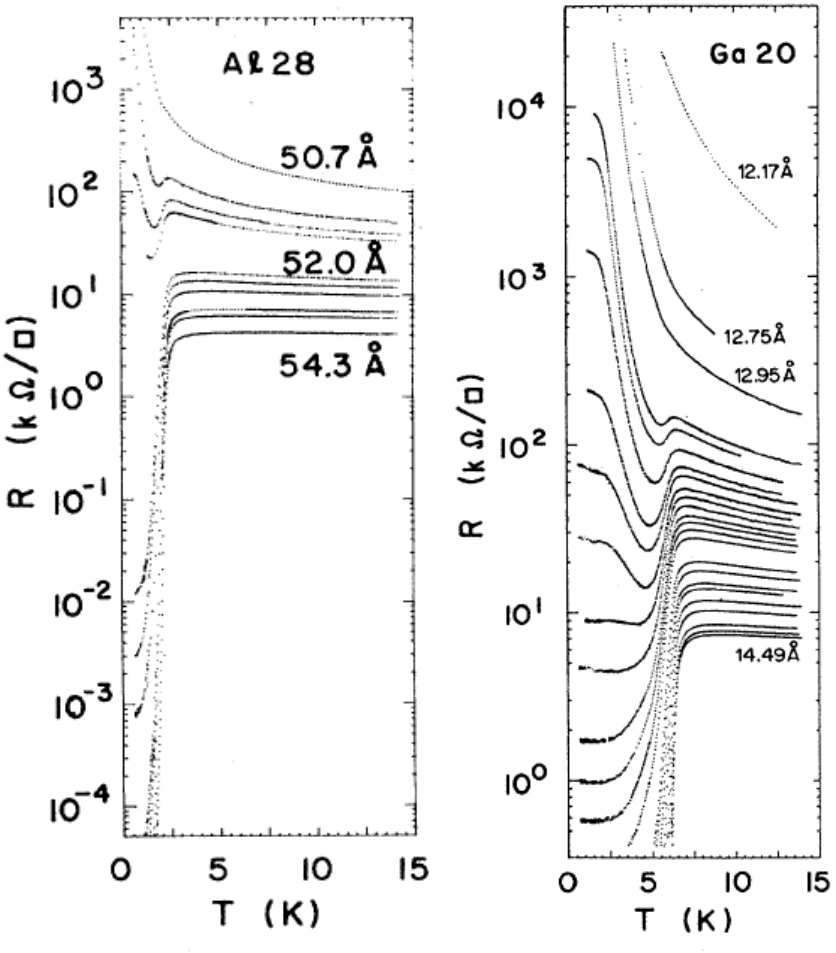

Figure 2.17.: Thickness dependent $R(T)$ curves for granular aluminum and gallium films. Superconductor to insulator transition happens in a small range of a few nm only. Reentrant behviour is seen in both materials, but more pronounced in gallium data set. Figure taken from [10].

Upper Critical Field

We now turn to the behaviour in an applied magnetic field [18, 110]. For small tunneling conductances the critical magnetic field of the sample is close to the critical field of a single grain

$$B_{\mathrm{c}}^{\mathrm{gr}} = \mu_0 H_{\mathrm{c}}^{\mathrm{gr}} = \sqrt{\frac{5\Delta_0}{2R^2 D}} \tag{2.109}$$

where Δ_0 is the BCS energy gap for $T = 0$, $R = a/2$ the grain radius and D the diffusion coefficient in the grain.
However, for sufficient large tunneling conductances the critical field is rather given by the bulk value

$$B_{\mathrm{c}}^{\mathrm{bulk}} = \mu_0 H_{\mathrm{c}}^{\mathrm{bulk}} = \frac{\Phi_0}{2\pi}\frac{\Delta_0}{D_{\mathrm{eff}}} \tag{2.110}$$

with Φ_0 the magnetic flux quantum and D_{eff} being an effective diffusion coefficient for the array given by $D_{\mathrm{eff}} = g\delta a^2$.

The conductance separating the two regimes is given by a new characteristic conductance value

$$g^\star \approx 0.16(a\delta)^{-1}\sqrt{\Delta_0 D} \tag{2.111}$$

The mechanism leading to Eq. 2.109 and 2.110 was first considered by Larkin [117] and is known as the orbital mechanism. However, as grain sizes shrink the Zeeman mechanism becomes more and more important [18, 118].
In case the Zeeman mechanism dominates the orbital one, the critical magnetic field is given by the Clogston value [119, 120]

$$B_{\mathrm{c}}^{\mathrm{z}} = \mu_0 H_{\mathrm{c}}^{\mathrm{z}} = \frac{\Delta_0}{\sqrt{2}\mu_{\mathrm{B}}} \tag{2.112}$$

The critical size of a grain a_c below which the Zeeman term dominates, can be estimated by

$$a_{\mathrm{c}} \approx \sqrt{\frac{5}{D\Delta_0 m^2}} \sim \frac{1}{k_{\mathrm{F}}}\frac{E_{\mathrm{Th}}}{\Delta_0} \tag{2.113}$$

where k_{F} is the Fermi momentum, m denotes the mass and $E_{\mathrm{Th}} = \hbar D/a^2$ is the Thouless energy.

2.3.3. Anomalous Metallic State in the Vicinity of the Superconductor-Insulator Transition

Measurements taken over the last decades in two dimensional systems, which have been declared by theory to exhibit a direct SIT, may be reinterpreted as they show signs of an indirect transition with an intermediate metallic regime, i.e. the resistances saturate at the lowest temperatures and can be continuously tuned by an external parameter. An example are the thickness dependent $R(T)$ curves in Ref. [10]. Those curves have been attributed to exhibit a true thickness/disorder driven SIT. While the thinner films follow an insulating trend down to the lowest temperatures, thicker films show a low temperature saturation of resistance (see Fig. 2.17). By further increasing the thickness a true superconducting state is approached at low temperatures. The saturation value is smaller than predicted by the Drude model for metals.
Similar saturations at values, up to orders of magnitude smaller than the Drude value, have been found in other material systems, e.g. in two dimensional Josephson junctions arrays [121], gated two dimensional semiconductor-superconductor arrays [122], In-InOx composites [123], ultrathin amorphous gallium films [9] and in amorphous NbSi thin films [124].
The intermediate metallic state in the vicinity of the SIT is referred to as anomalous metallic state (AMS) and has been reviewed recently by Ref. [125], where the focus was set on the transition from a true superconducting state to the anomalous metallic state. The transition is referred to as superconductor to quantum metal transition, SQMT.

Most of the evidences for an AMS have been found in 2D systems. Observations of the anomalous metal include a decreasing resistance with decreasing temperature, i.e. the system behaves as it would approach a superconducting groundstate with zero resistance, followed by a saturation at the lowest temperatures. The non-thermal parameters used to tune the transition from superconducting to non-superconducting are manifold. Examples for tuning parameters are microscopic or macroscopic disorder, charge carrier density (modified by a gate voltage V_g), screening properties by a nearby groundplane and magnetic field. Those experimental results are presented and discussed in Kapitulnik et al. [125].
An AMS has been found in metal films with a normal state conductivity $\sigma_D^{(2\mathrm{D})} \gg \frac{e^2}{h}$ and appears as an intermediate state. Tuning further away from the SQMT leads either to a crossover to a normal metallic state or to a transition to an insulating state (metal-insulator transition - MIT). No obvious dependence of the disorder of film morphology has been found as an AMS has been seen in strong non-uniform systems, e.g. in naturally granular films or in artificially prepared arrays of superconducting islands, as well as in homogenous films, e.g. crystalline and amorphous. In some cases of strong disorder a true, direct SIT is observed. The anomalous metal does indeed behave as it would be a failed superconductor, instead of a normal metal.[125]

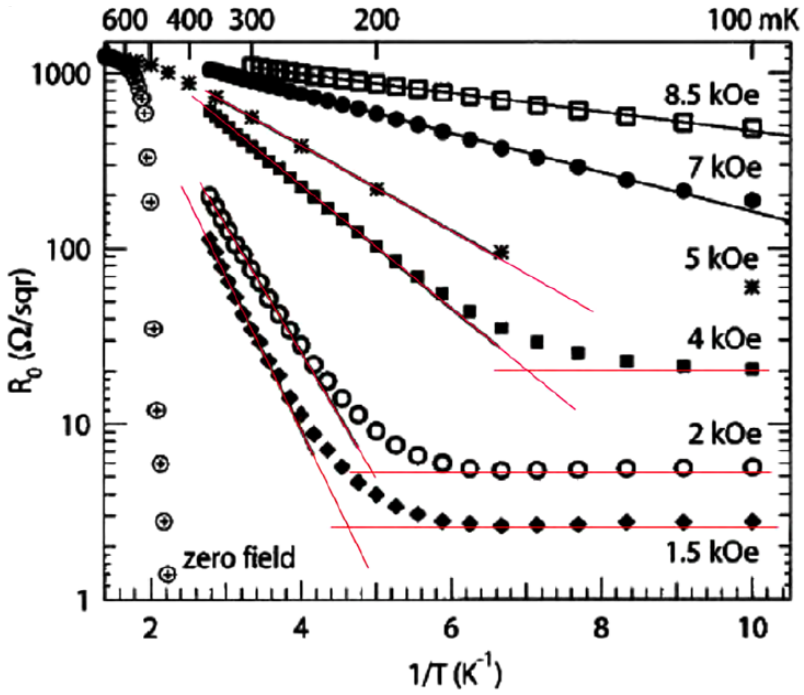

Figure 2.18.: Data set of $R(T)$s of MoGe films presented in an Arrhenius plot for various magnetic fields. The high temperature activated behaviour indicated by the linear curvature is followed by a low temperature saturation of resistance. This saturation was taken as indicator for the failed superconducting state. Figure taken from [125]. Data from [126].

A recent example of a magnetic field driven SQMT, i.e. the transition from the superconducting state to the failed superconducting state of the anomalous metal, in amorphous MoGe is presented in Fig. 2.18. The low temperature saturation has been attributed to the anomalous metallic state. With increasing magnetic field the saturation resistance increases [126]. The B-SQMT in highly metallic a-MoGe has been further studied by Refs. [127, 128].

Ref. [125] argues that the electronic properties found for the anomalous metal can not be understood on the basis of the standard paradigms for transport in disordered two dimensional systems. There is up to date no satisfactory theory for the AMS and Ref. [125] views this as one of the major open questions in condensed matter theory. The authors of Ref. [125] argue that theories, e.g. classical percolation theory or fluctuation superconductivity, as well as local bosonic theories inadequately describe the observed phenomena in the anomalous metallic state.

It was only recently, that the low temperature saturation of resistance on the insulating side has received more attention. Ref. [123] studied the magnetic field induced SIT in a random array of indium islands grown onto a gateable layer of InOx. By tuning the intergrain coupling the authors find a wide range of magnetic fields, for which a low temperature saturation of the resistance is found. The resistance saturates at values higher then R_Q and R_N and the saturation value R_{QF} increases with increasing magnetic field. The continuous transition from the superconducting state to an insulating state with an intermediate regime, which shows a low temperature saturation of resistance, is referred to as an avoided SIT by the authors of [123]. Zhang et al. [123] find a failed superconducting regime ($R_{QF} < R_Q$) for low magnetic fields and a failed insulating regime ($R_{QF} > R_Q$) for higher magnetic fields. The transition from the superconducting state through the two phases of the AMS to the insulating state is referred to as an avoided magnetic field induced SIT. In addition, a logarithmic temperature dependence for the resistivity and the conductivity on the superconducting and the insulating side, respectively, of the avoided SIT has been found.

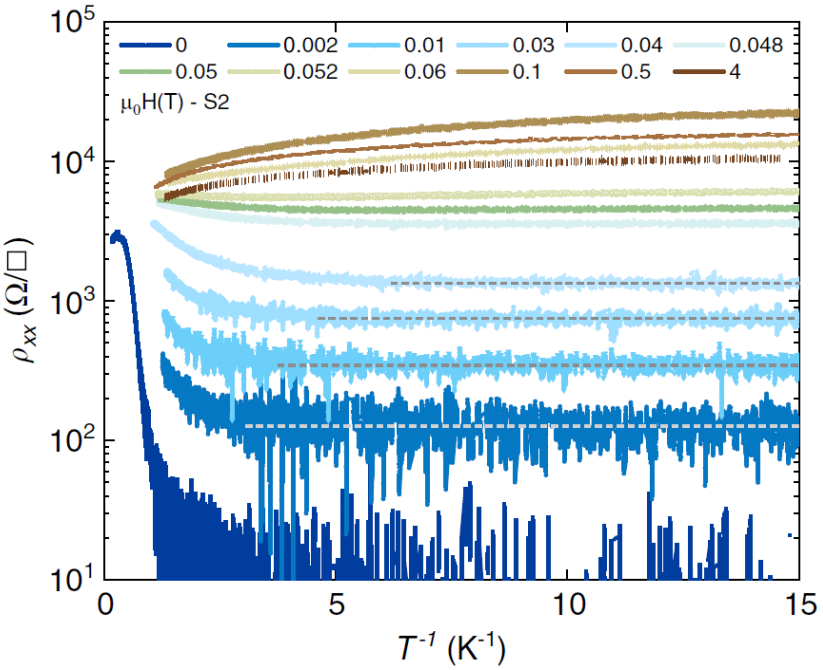

Figure 2.19.: Data set of $R(T)$s presented in an Arrhenius plot for various magnetic fields. For magnetic fields below B ∼55mT the resistivity decreases with temperature and saturates at $R_{QF} < R_Q$. For magnetic fields above B ∼55mT the resistivity increases with decreasing temperature and shows a low temperature saturation with $R_{QF} > R_Q$. Above a maximum in resistance at $B \sim 0.5$T the a negative magnetoresistance is observed. The highest field shown $B = 4$T shows an overall smaller resistance. Figure taken from [123].

Ref. [123] obtained the anomalous metallic phase under conditions of carefull electromagnetic filtering. Exposure to external broadband noise or microwave excitation leads to a superconducting tendency ruling out the origin of the AMS to be connected to improper filtering or external irradiations. The authors conclude that the AMS is directly linked to the granular/inhomogenous nature of the system and highlight the duality of the resistivity and conductivity on the different sides of a true SIT.

In a follow-up paper Zhang et al. [129] further studied the transition from superconductor to insulator through an AMS in granular In/InOx composite tuned by an external magnetic field. For this composite Ref. [130] had already shown a direct SIT with magnetic field. The findings by the authors of Ref. [129] suggest that the AMS can be separated into failed superconductor and failed insulator, where the first lives on the superconducting side and the latter on the insulating side of the avoided B-SIT. The saturation resistance separating the two regimes, failed superconductor and failed insulator, is found to be $\sim 6.5\text{k}\Omega/\square$ in Refs. [123, 129]. In Fig. 2.20 the phase diagram proposed by the authors of Ref. [129] for two tuning parameters (intergrain coupling and magnetic field) is shown.

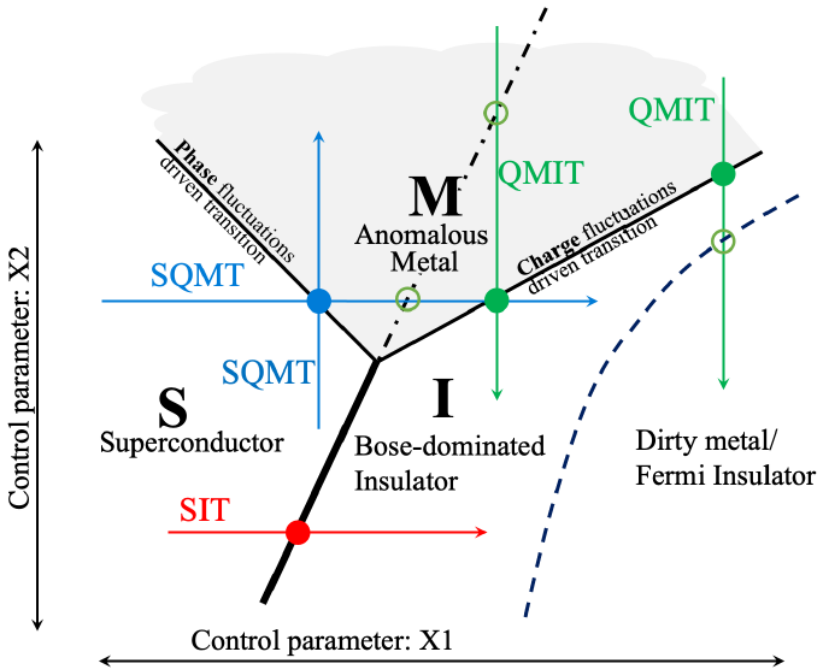

Figure 2.20.: Proposed phase diagramm by [129] for disordered granular films. The two tuning parameters are intergrain coupling strength X2 (depending on E_J/E_C) and magnetic field B, X1. Figure taken from [129].

The phase diagram consists of a superconducting region with global phase coherence (S), a Bose-dominated insulator (I) (local superconductivity without global phase coherence), and an anomalous metal (M) (regime with quantum fluctuations which lead to finite resistances at $T = 0$K). Depending on the intergrain coupling (X2), a magnetic field (X1) tuned transition may either be a direct SIT (red arrow) or a transition from superconducting state to the Bose-insulating state with an intermediate metallic state. The AMS is further separated into failed superconductor and failed insulator. By increasing the magnetic field first the superconductor exhibits a superconductor to quantum metal transition (SQMT) to the failed superconducting state. The transition is driven by phase fluctuations (blue arrows). Further increasing the magnetic field leads to a crossover to the failed insulating regime of the AMS. This is indicated by the black dash-dotted line. Applying the duality of phase and charge there is a charge fluctuation driven transition to the Bose-dominated insulator, referred to as Quantum-Metal-to-Insulator-Transition (QMIT). For high magnetic fields the Bose-dominated insulator is transformed into a Fermi-insulator as Cooper pairs are broken up. Above the critical magnetic field B_c superconductivity is completely gone and localization of single electrons due to disorder and Coulomb interactions lead to an insulating behaviour.

Ref. [129] argues that due to the granular nature of their film, the material can be modelled by superconducting grains embedded in a tunable intergrain matrix, where the superconducting transition is dominated by phase fluctuations ($E_\mathrm{J} \gg E_\mathrm{C}$) [131–133]. In that model local pair amplitude fluctuations depend on grain size [134] and global phase coherence is established by percolation along a path with intergrain phase coherence [93, 135–137]. For a given pair of neighbouring grains ij, the Josephson coupling E_ij is given by the local superconducting gaps, Δ_i and Δ_j, and the normal state intergrain resistance R_N^ij. Due to the granular nature intergrain and self capacitances C_ij and C_0 have to be taken into account. The intergrain charging energy $E_\mathrm{C,ij}$ depends on local charge carrier density, n_i and n_j, and the intergrain dielectric constant $\chi_\mathrm{N}^\mathrm{ij}$. The insulating state in that model is a result of Coulomb blockade for Cooper pairs, which prevents Cooper pair tunneling between adjacent grains. In granular films the coupling strength $\gamma = E_\mathrm{J}/E_\mathrm{C}$ determines the occurence of the SIT [8, 59, 96]. In single resistively-shunted JJs with $E_\mathrm{J} \gg E_\mathrm{C}$ phase coherence is established for small bias currents. This leads to a zero voltage supercurrent. At low temperatures activation is exponentially small and quantum fluctuations of phase leads to quantum tunneling of the phase variable [138]. Hence, a finite voltage state is established [139, 140].
There is a dual picture for $E_\mathrm{C} \gg E_\mathrm{J}$. Electric charge, which is the conjugate to the phase, on the junction capacitance, results in a Coulomb blockade, hence an insulating state. However, at small bias voltages quantum fluctuations of charge lead to a coherent current of Cooper pairs, but also to dissipation due to single electron tunneling [141].
Ref. [129] transfers this model onto random arrays of JJs resulting from the random nature of the granular film. The similarity of granular films and JJAs is supported by the fact that the $R(T)$ curves can both be nicely fitted by empirical formulas 5.15 and $R_\square = R_0 \exp\left(\frac{-E_\mathrm{A,S}}{k_\mathrm{B}T}\right) + R_\mathrm{QF}$ for JJAs. This agrees with the assumption of a duality

picture with interchanging roles of number of charge carriers N and the phase Φ, strenghtened by the similar dependence in transport when exchanging resistivity and conductivity.

3. Low Temperature and Measurement Setups

Data presented in chapter 5 and chapter 6 were measured in a He3/He4-dilution refrigerator designed by Oxford Instruments (Kelvinox 400HA) with a specified base temperature of 10mK (see Tab. A.1). The insert, which includes the most important parts of the cooling system, is combined with a low-loss dewar, including an outer-vacuum-chamber (OVC) and a liquid nitrogen shield surrounding the liquid He4-bath. The dewar is connected to a pipe, transporting the evaporated He4 to the faculty helium liquification plant. Inside the dewar there is a 2D vector magnet. The magnets Z-Axis can reach a maximum field of 7T, while the X-axis is limited to 3T. In addition, the Z-axis magnetic field is compensated by compensation coils to shield the mixing chamber plate from the magnetic field.
The insert consists of the dilution unit, 5 thermometers and 3 heaters. At the 1K-plate, still plate and the mixing chamber plate heater and thermometer are combined so the user may operate in different modes (open loop, PID-loop, etc.). There are measurement (2x 24-way phosphor-bronze wiring) and additional thermometry (24-way constantan wiring) lines from room temperature to the mixing chamber plate. As those lines were delivered with the system they are properly laid and thermalized on each of the different temperature stages.
The bottom part, mainly on or below the mixing chamber plate, received home-made additions. This includes a coldfinger reaching down to the center of homogenous magnetic field/sample space, a Magnicon SQUID-thermometer sitting next to the mixing chamber, a calibrated germanium thermometer next to sample space as well as an ruthenium-oxide thermometer, which was calibrated against the germanium/SQUID (see Tab. A.1). To reduce noise and heating, the measurement lines and the thermometry lines are heavily filtered using cold RC and silver-epoxy filters sitting on the mixing chamber plate.
In the next pages the home-made filtering, thermalization and thermometry is presented. The last part then covers the measurement setups, including devices and electrical circuits.

3.1. Filtering, Thermalization and Thermometry

As mentioned above He3/He4 dilution refrigerators are able to continuously cool down to temperatures around 10mK at the mixing chamber plate. Nevertheless, experiments require additional electronical components to be implemented affecting the base temperature T_{base} of the operating system. Such elements may be separated into active and passive.
Active elements rely on a source of energy, usually a DC source, and can inject power into a circuit, e.g. transistors or diodes. Passive elements do not rely on a power source and can not actively amplify the power of a signal. Such elements are resistors, capacitors and inductors. However, they may increase a voltage or a current. Active elements therefore continuously alter the temperature of the surroundings, which is not necessarily true for passive elements as the signals passing through them are usually very small.

Assuming that the temperature of the cooling system is not altered by the above mentioned devices, then the temperature of a device under test (DUT) is ideally given by $T_{\text{el}} = T_{\text{bath}}$. The latter is the temperature of the mixing chamber and at the lowest temperature coincides with T_{base}, the minimum temperature accessible in the system.

In reality, the electronic temperature T_{el} in the device under test can be significantly higher than the bath temperature T_{bath} due to insufficient thermalization (thermally decoupling of the DUT from the surroundings at T_{bath}) or inproper filtering of high frequency radiation [142, 143]. Not ony should the DUT be very well thermally coupled to the bath, the same holds for the sample holder, wires and other heat generating elements. However, at very low temperatures thermalization becomes challenging as the electron-phonon coupling decreases with T^5 [144, 145]. The dominant cooling mechanism is then eventually given by the Wiedemann-Franz cooling via the wires, which decreases with T^2 [144]. Obviously, the measurement lines connected to the DUT (as well as low temperature thermometers) need to be very well thermalized and filtered.

Thermalization

Achieving thermal equilibrium between two materials in contact requires a heat flow $\dot{Q}$ from one to the other. The temperature step between the materials can be calculated by

$$\Delta T = R_{\text{K}} \dot{Q} \tag{3.1}$$

where R_{K} denotes the thermal boundary resistance known as Kapitza resistance. R_{K} should be kept reasonable small to decrease thermalization times. The surfaces of the two materials should be pressed together with relatively high force. That increases the effective area for the heat flow and increases thermal conductance. In addition, the surfaces should be clean and ideally gold-plated to prohibit surface oxidation.[145]
Experimentally, proper thermalization can be achieved in different ways. Unshielded wires (simple metallic wires with a thin insulation or coaxial wires) may be wound around

a cyclindrical copper anchor, which is screwed into the corresponding temperature stage. To increase the effective area one needs to increase the number of windings and/or glue the wire to the anchor with a thermally very good conducting material, e.g. silver epoxy. Another possibility is to solder the inner conductor to a metallic strip, which is electrically disconnected, but thermally connected to the thermal anchor. For coaxial cables the outer conductor should be in direct contact to the thermal anchor.
For multi-wires with a shielding one could for example use metallic clamps that generate force and press together the shielding and the outer conductors inside. Care must be taken as too much force might break the insulation. A general other option is to use a copper braid, tighten it around the wire and cover the contact area with a very good thermally and electrically conducting material. The copper braid then should be screwed to the thermal bath using high pressure.

Filtering

Noise may come in all kind of forms, ranging from frequency independent noise, e.g. thermal noise and shot noise, to frequency dependent noise types, e.g. 1/f-noise [146]. All types/sources of external noise decrease measurement resolution as it shifts the signal to noise ratio (SNR) to lower values.
The frequency independent thermal noise (Johnson-Nyquist noise [147, 148]) is always present in resistors and therefore it has to be taken into account in our measurement setup. The power spectral density is given by

$$\bar{\nu}_{\mathrm{n}}^2 = 4k_{\mathrm{B}}TR \tag{3.2}$$

and scales with temperature T and resistance R. This can be rewritten as the root mean square of the voltage fluctuations

$$\nu_{\mathrm{n}} = \sqrt{4k_{\mathrm{B}}TR\Delta f} \tag{3.3}$$

where Δf is the bandwidth. This may expressed in term of a current noise simply by dividing with the resistance R

$$i_{\mathrm{n}} = \sqrt{\frac{4k_{\mathrm{B}}T\Delta f}{R}} \tag{3.4}$$

As temperature decreases both voltage and current noise decrease. However, the voltage noise increases with increasing resistance whereas the current noise decreases with increasing resistance. Most importantly, by decreasing the bandwidth Δf by high frequency filtering and shielding the measurement lines the thermal as well as extrinsic noise may be significantly reduced.

Depending on the frequency of operation, low pass, band pass or high pass filters may be used [149]. A comparison of filters operating in the microwave regime can be found in [150].

In the following we focus on the low pass filtering as measurements here were performed either with direct current or alternating current with very small frequencies (below a few Hz).
Signals with frequency ω fed into a low pass filter may pass below a certain cutoff frequency ω_c and are attenuated for frequencies above. The cutoff frequency depends on the filter design and usually denotes the frequency at which the power of the input signal is reduced to its half, i.e. $P_{out} = 0.5\ P_{in}$. That corresponds to an attenuation of -3dB when expressing the power in decibel. In that case the voltage ratio V_{out}/V_{in} drops to $\sqrt{1/2}$. The cutoff frequency is the invers of the time constant τ, which denotes the time for a step-like signal to decay to a value of 1/e.

The final filtering implemented to gather the data presented in the next chapters consisted of 3 different filter types: a) room temperature π filters b) cold RC filters and c) cold Ag-epoxy filters. b),c) were located on the mixing chamber plate. All three types of filters are passive, i.e. consist of combinations of resistances, capacitances and inductances and do not require an external powersupply.

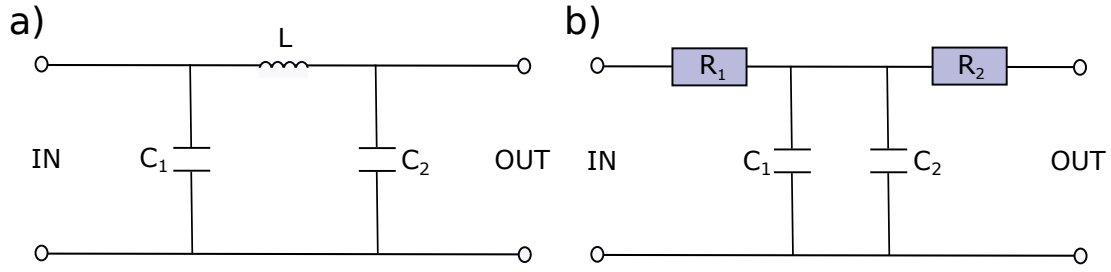

Figure 3.1.: a) Low-pass π filter circuit. b) Low-pass RC filters circuit. L denotes an inductance, C a capacitance and R a resistance.

a) Each room-temperature π filter (see Tab. A.4) has its own small metal box. It can be connected to the desired measurement line with a standard SMA connector. The counterpart of the SMA connector is located in a breakout box, which splits the 25-way Fischer connector at the head of the insert into 25 single SMA-connectors. This creates variability in choosing the desired lines and the possibility to work with filtered or unfiltered lines depending on the requirements of the measurement.

Fig. 3.1a) shows the circuit diagram of that low pass π filter. It consists of one inductance in series and two capacitances parallel to the load. The cutoff frequency of that simple low pass filter is given by

$$\omega_c = \frac{1}{\sqrt{LC}} \tag{3.5}$$

The total capacitance is at least 5500pF and the cutoff frequency $\omega_c = 10$MHz. The filters used were commercial π filters by Tusonix.

b) Cold RC filters (see Tab. A.4) were connected to the measurement lines as well as to the thermometry lines at the mixing chamber plate.

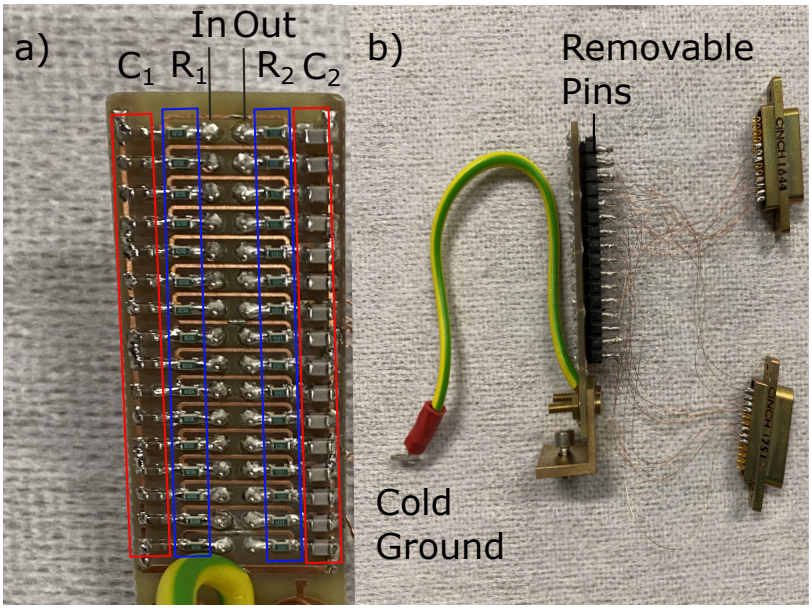

Figure 3.2.: RC-Filters: a) front view containing throughputs for input and output together with the input resistances R_1 and output resistances R_2 and the capacitors to ground C_1 and C_2. There is no direct electrical connection of the front side to ground. The only connection to ground is through the capacitors, which are connected to a ground plane on the backside via metallic feedtroughs. The ground plane is shorted to insert ground with a copper braid. b) side view: Micro-D connectors (one for input and one for output) soldered to removable pins connected to feedthroughs from the rear side of the PCB to its front side. There is no electrical connection from the pins/feedthroughs to the groundplane located on the rear side.

A sketch can be seen in Fig. 3.1b). The filter consists of two resistors in series and two capacitors parallel to the load between the two resistors. The general cutoff frequency of an RC filter is given by

$$\omega_c = \frac{1}{RC} \tag{3.6}$$

In our case Eq. 3.6 rewrites as

$$\omega_{c,1} = \frac{1}{R_1(C_1 + C_2)} \tag{3.7}$$

and

$$\omega_{c,2} = \frac{1}{R_2(C_1 + C_2)} \tag{3.8}$$

for the different current directions, where R_1 and R_2 are the input and output resistances as shown in Fig. 3.1b).
The designed filter board has 16 filters in parallel, see Fig. 3.2. Each has an input resistance of $R_1 = 820\Omega$ and and output resistance of $R_2 = 1.2\text{k}\Omega$. The latter is irrelevant for most applications. Inbetween, a total capacitance 27.1nF to ground is added consisting of two parallel capacitors with $C_1 = 18\text{nF}$ and $C_2 = 9.1\text{nF}$. The capacitors are connected on the grounding side to a metal plate covering the rear side of the filter board. That metal plate is then cold grounded with a low resistance copper braid to the insert ground. To avoid ground loops, the PCB board is electrically disconnected from the gold-plated copper anchor, which can be screwed to the mixing chamber plate.
The corresponding cutoff frequencies are both in the low kHz regime $\omega_{c,1} = 7.2\text{k}\Omega$ and $\omega_{c,2} = 4.9\text{k}\Omega$.

Below, in Fig. 3.3 the impact of the RC filters is presented. a) shows two base temperature IVs for $B = 0\text{T}$ and b) $R(B)$s at base temperature for the same NbSi sample measured with an AC setup (see Fig. 3.12). The green curves were measured with π filters at room temperature and low temperature Ag-epoxy filters (see below) as the Ag-epoxy filters were implemented before the RC filters. The red curves corresponds to the final filter setup, including the low temperature RC filter.

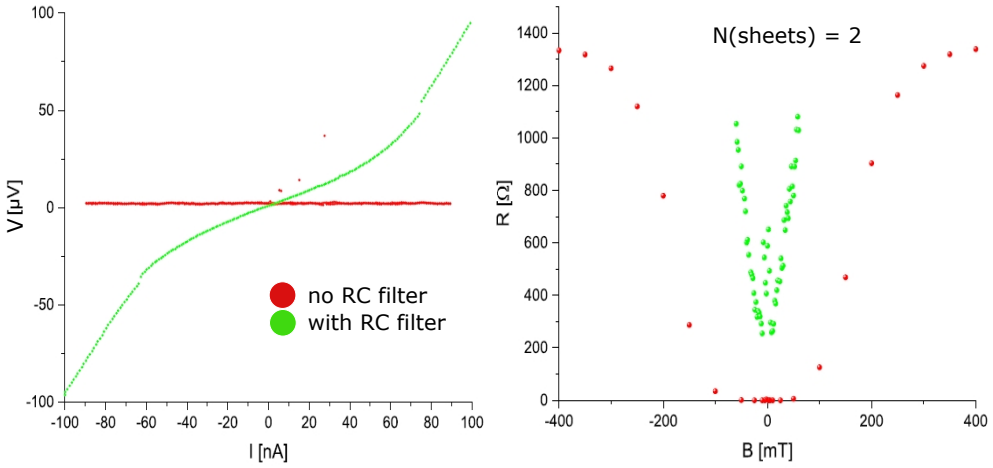

Figure 3.3.: Impact on measurements by RC filters. a) shows a comparison of two IV characteristics. The green curve is measured without RC filter. The same measurement is repeated with RC filters. The red curve shows a broad zero resistive state, while the green curve exhibits a finite differential resistance around zero bias. In b) the same impact is presented in comparison of two a $R(B)$ measurements. The data were collected together with two bachelor students, [151] and [152]. The figure is adapted from [152].

Without RC filters (green curve) a clear deviation (finite slope) from the superconducting

state (red curve) is visible in Fig. 3.3a). The non-RC filtered measurements did not show superconducvitity at all. This is presented in Fig. 3.3b) for a set of magnetic fields. The $R(B)$ curve of the non-RC filtered measurement (green) shows a minimum of resistance with $R \sim 200\ \Omega$ around $B = 0$T, while for the RC filtered (red) measurement the resistance drops down to zero. The shape of the curves are similar, however the onset of resistance takes place at higher magnetic fields with RC filters.

c) The Ag-epoxy filters acting as the third filtering stage are taking care of the very high frequencies of 100MHz and above. Those filters are home made following some ideas of Ref. [153] and modified to fit the measurement requirements. To make full use of the filtering, they were combined with a shielded measurement environment reaching down from the mixing chamber to the sample space.
A more detailed description on how the filters were built, placed into a filter-box and combined with the coldfinger can be found in the appendices A.1 and A.2. A later bachelor work, partly supervised by the author, followed the same approach for a different low temperature system. A detailed summary of the working principle [153, 154] and a description of the production process for the Ag-epoxy filters can be found there [155]. In the following the most important parts are presented.

The Ag-epoxy filters are designed to heavily attenuate signals with frequencies in the microwave regime, i.e. between 150MHz and 10GHz. They are robust against thermal cycling, i.e. cooling down and warming up between base temperature of a dilution refrigerator and room temperature, and are designed to effectively take away energy generated by resistive elements. Hence, they show a very good thermalization and are quite simple to fabricate.
The filters are made of an insulated copper wire wound around a silver epoxy rod. The rod has 4 chambers in series, where each chamber has 5 layers of 21 windings, i.e. 105 windings. This segmentation reduces parasitic or stray capacitances, that could severely lower high frequency attenuation. The direction of winding is inverted for each segment to cancel out induced magnetic fields due to the coil-like geometry. The insulated copper wire is constantly covered with silver epoxy during winding. Therefore it is very well embedded in an highly electrically and thermally conducting matrix.

Theoretical description

The filter geometry can be thought of as a coaxial cable and the filter attenuation can be modelled by a distributed transmission line with skin-effect.
Consider a copper wire with diameter D, then a DC current may flow using the whole crosssection with area $A = \frac{D\pi}{4}$, while due to the skin effect an AC current with frequency ω is forced to flow in an annulus with width δ only.

$$\delta = \frac{1}{\sqrt{\sigma_{\mathrm{Cu}}\mu_{\mathrm{Cu}}\omega\pi}} \tag{3.9}$$

δ is the skin depth, σ_{Cu} the conductivity of copper and μ_{Cu} magnetic permeability.

Therefore the effective crosssection for AC currents rewrites as

$$A = D\pi\delta \tag{3.10}$$

By modelling the filter as a coaxial cable, consisting of an inner copper wire separated from the outer silver epoxy conductor by an insulating layer (see Fig. 3.4a)) then the skin effect also applies to the outer conductor. The resistance seen by an AC current therefore increases with frequency and the total resistance can be written as

$$R_{\mathrm{tot}}(\omega) = R_{\mathrm{IC}}(\omega) + R_{\mathrm{OC}}(\omega) \tag{3.11}$$

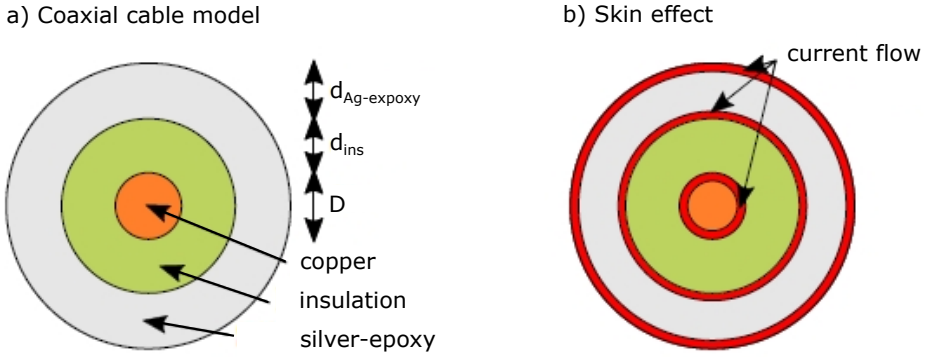

Figure 3.4.: Sketch of a) coaxial cable model and b) skin effect. Figure adapted from [155]

The attenuation of a coaxial cable can be calculated by transmission line theory [149].

$$\mathrm{Attenuation}(\omega) = 20\log|\exp(-\gamma z)| \tag{3.12}$$

where z is the length of the wire and γ reads as

$$\gamma = \sqrt{(R_{\mathrm{tot}} + 2\pi i\omega L)(G + 2\pi i\omega C)} \tag{3.13}$$

where L is the inductance per meter and C the capacitance per meter.
Ref.[153] found an attenuation of 100dB for frequencies above 150MHz for their filter design. Our filters are not identical and show less, but still good attenuation.
One of our filters can be seen in Fig. 3.5a) and a corresponding attenuation characterisation measurement in b).

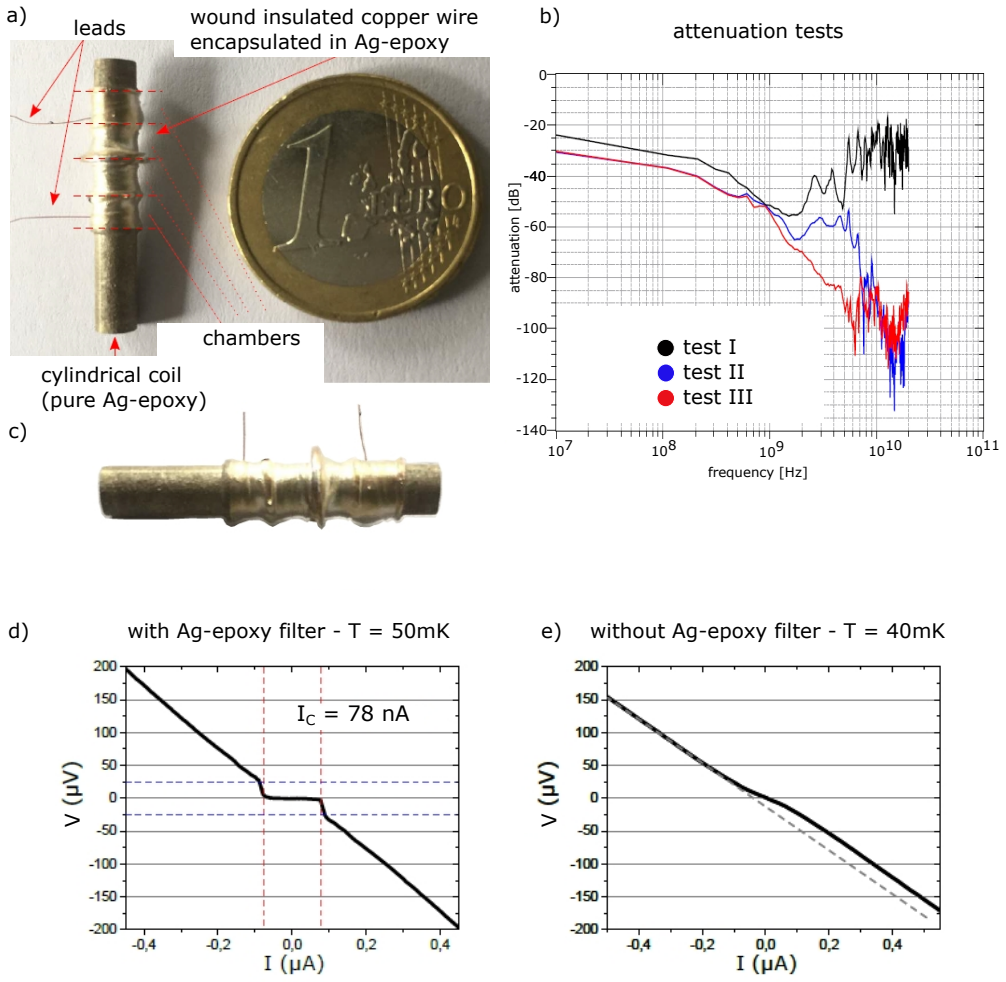

Figure 3.5.: a) Completed Ag-Epoxy filter with its components compared to a 1 Euro coin. b) Damping characteristics for three different tests, where the attenuation has been measured in reference to the frequency in a single Ag-epoxy filter. c) Larger picture of an Ag-epoxy filter. d) and e) Impact of the Ag-epoxy filtering on measurement: only with Ag-epoxy filter a critical current I_c is resolved. Data were collected by [155] and adapted.

The filter performance was tested at room temperature. A small metal test box was designed, where a metallic dividing wall separated input and output side. The different curves in Fig. 3.5b) correspond to different approaches (See Fig. A.3 in appendix A.1). In test I the filter was measured in an empty, but closed metal box. Then the output side was filled with Eccosorb for test II. The final test III, the slits between cap and box were sealed with silver epoxy.

The attenuation between 10MHz and 1GHz slighty increases from 30dB to 50 dB. Above 1GHz it only further increases when shielding the filter by closing the test box output side (blue curve). By adding a frequency damping Eccosorb in the output side and closing it, the damping increases at 1GHz to values of approximately 100dB (red curve).
The impact of the filter in a measurement can be seen in Fig. 3.5d) and e). The data were collected in a bachelor thesis [155]. The critical current in the IV curve is only sharply defined with Ag-epoxy filters.
Finally, as the frequency range between 10kHz and 100MHz is covered with the room temperature π filters and the low- temperature RC-filters, the overall attenuation should be sufficient for our purpose.

Filterbox

The results of the filter performance measurements suggested to use an electrically shielded output that includes a volume of high-frequency damping Eccosorb. Therefore a box has been designed, where 31 of those filters are implemented, see Fig. 3.6. The filterbox follows the same design as the test box. Input and output are separated by a metallic interlayer with drilled holes. The filters are placed into the holes. One half of the filter reaches into the input side, the other into the output side. Both sides are sealed with silver epoxy hermetically and electrically. Therefore no signals may enter the output side, but only by passing through the filters.

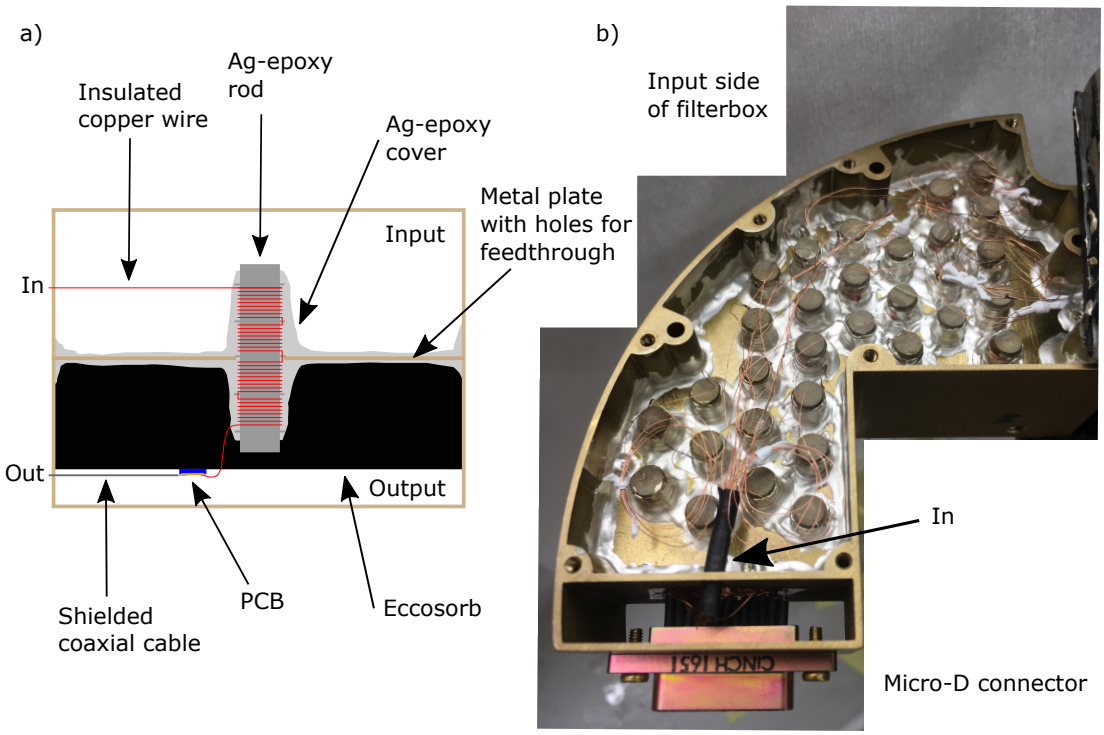

Figure 3.6.: a) A vertical cut through the filterbox is sketched. A brass plate separates the input from the output side. The Ag-epoxy filters reach half way from the inut into the output. Both sides are covered with Ag-epoxy to increase thermal coupling to the environment. The output side is in addition filled with high frequency damping Eccosorb. b) Optical image of the input side. The Ag-epoxy filters, the Ag-epoxy cover as well as copper wires and input micro-D connector can be seen.

To keep noise signals from coupling in after the filterbox, the electrically shielded environment is extended down to sample space by using shielded coaxial cables with a CuNi inner and outer conductor (see Tab. A.3).

The setup below the mixing chamber stage can be seen in Fig. 3.7a), while b) shows the final sample space, including sample holder, thermometers, etc..

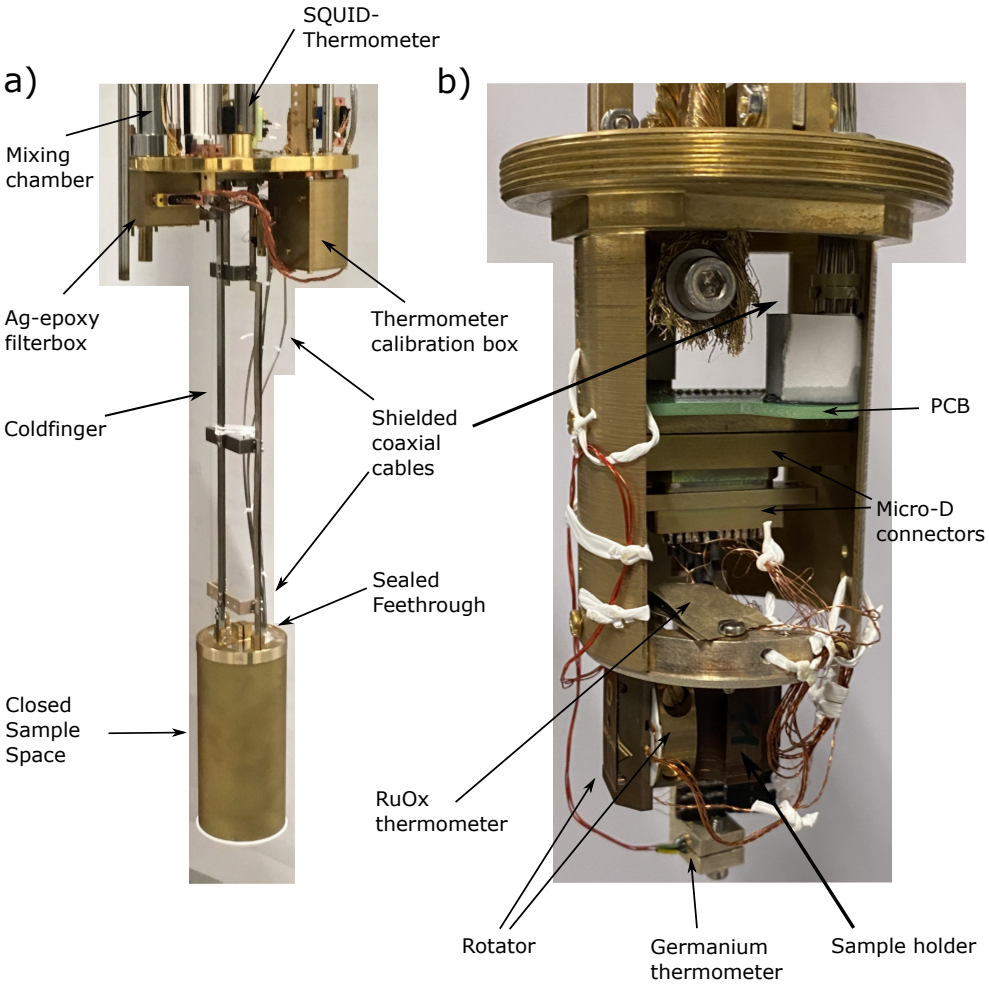

Figure 3.7.: a) Coldfinger connected to the mixing chamber plate of our He3/He4 dilution refrigerator. The coldfinger puts the sample space in the correct distance to the mixing chamber, so it is in the central, homogenous magnetic field of the two axis magnet located in the dewar. b) The sample space, i.e. the volume where temperature and sample are characterized, is presented. It includes thermometers, thermalizations, sample holder and the wiring needed for read out.

Thermometry and Temperature Control

To make full use of the system, the AC resistance bridge and temperature controller (Lakeshore Model 372) is combined with a scanner (Model 3726), which gives access to 16 independent 4-point resistance measurement channels. The Kelvinox 400HA provides 5 thermometers, two on the 1K-plate (1K-pot and sorb/charcoal trap for He4-exchange gas), one for the still, coldplate and the mixing chamber. Those thermometers are resistors with a negative temperature coefficient (RuOx, Cernox) and are accompanied by 3 heaters, sorb heater (warm-up heater), still heater and mixing chamber heater (sample heater).
The combination of heater and thermometer next to each other may be used for powerful control options, e.g. closed-loop-PID-control or temperature ramping.

Fig. 3.8 shows a sketch of the combination of the Lakeshore, scanner and the dilution refigerator, where blue lines correspond to thermometry channels (input of resistance bridge) and red to heater channels (output of resistance bridge). The advantages of

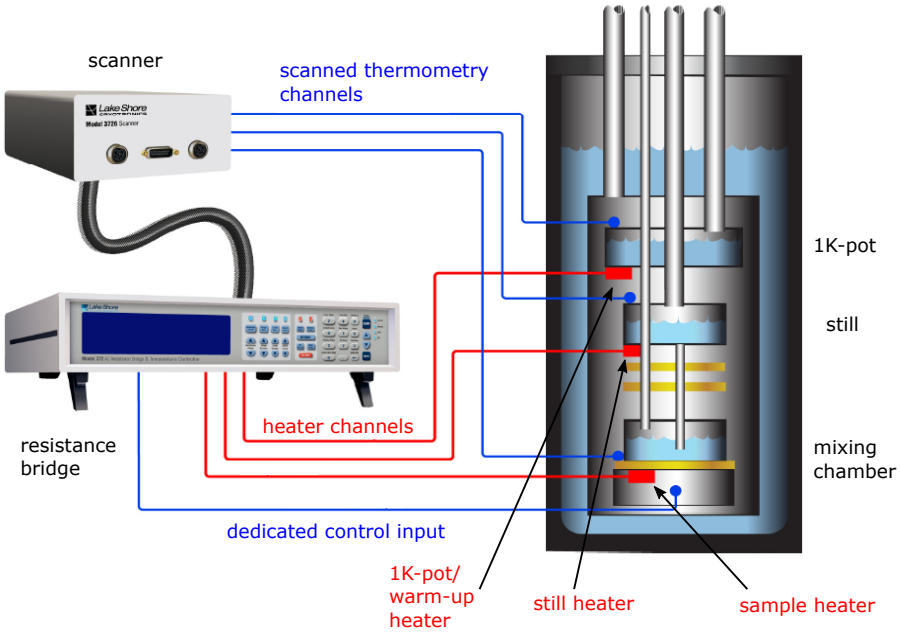

Figure 3.8.: Combination of AC resistance bridge for readout, scanner for channel switching and dilution refigerator to provide low temperatures. Figure adapted from [156].

the Model 372, an overview over the broad set of applications, physical background informations and operation instructions, when combined with a dilution refrigerator, are provided in [156].

The most used mode of operation in this thesis was the closed-loop-PID-Control, which allows to keep a stable temperature, e.g. at the mixing chamber/sample, for a very long time while performing electrical measurements (current-voltage-characteristics) or while sweeping the magnetic field ($R(B)$-curves). In addition it allows the user to change the temperature setpoint and approach it safely without overheating or dramatic temperature oscillations.
This mode is often referred to as feedback control and is commonly associated with tempeature control. It uses the control sensor (of the dedicated input) to monitor the temperature while actively adjusting the control heater output.
The heater output is given by

$$\mathrm{HeaterOutput} = \mathrm{P}\left[(\mathrm{e}) + \frac{1}{\mathrm{I}}\int(\mathrm{e})\mathrm{dt} + \mathrm{D}\frac{\mathrm{d(e)}}{\mathrm{dt}}\right] \tag{3.14}$$

P denotes a **(P)**roportional factor called gain, the **(I)**ntegral is referred to as reset term and D as **(D)**erivative or rate. The error (e) is given by the difference of the setpoint and the feedback readout value. The value P is mostly found by trial and error as it is connected to the properties of the load, sensor and controller. It therefore may be found in a very broad range of values. The I part monitors the change of the error in time, is given in seconds and acts as counterpart to the gain. The derivative part takes into account very fast changing error signals and is usually turned off for steady state operations. The impact of the different inputs of the PID-loop control by approaching a new setpoint and its stability are shown in Fig. 3.9.

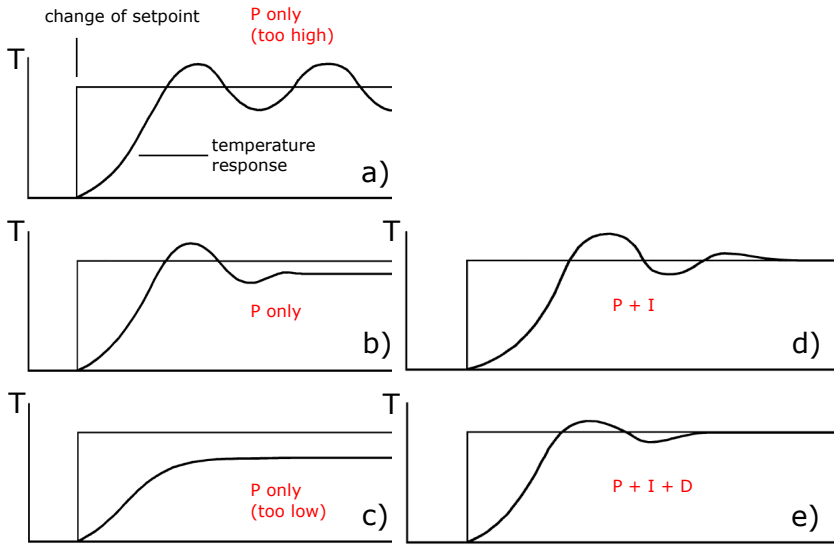

Figure 3.9.: Response of temperature after a setpoint change. Presented are different settings and combinations of the parameters P, I, and D. Figure adapted from [156].

As the negative resistance coefficient thermometers come with a generic calibration curve one has to actively check the actual temperature at the desired place, which usually is the mixing chamber. We implemented additional thermometry, a SQUID-thermometer (calibrated down to 6mK) next to the mixing chamber as well as a germanium thermometer (calibrated down to 40mK) at the sample space.
Ideally, the temperature of the mixing chamber and the sample space should be equal. However, in reality it may take a while until sample temperature approaches mixing chamber temperature, especially when ramping to a new setpoint. By probing the sample or due to external interferences sample temperature might be increased compared to the mixing chamber temperature. The calibrated germanium thermometer is a reference value to cross check deviations. We also calibrated a RuOx thermometer against the germanium and the SQUID and placed it at a different location in the sample space.
The germanium and the RuOx thermometers were read out by the resistance bridge via the filtered lines explained above. The SQUID thermometer was read out by a separate hardware and converted into a temperature by a software delivered by Magnicon. The principle of operation of the SQUID-thermometer is presented in [157–160]. The SQUID gradiometer is glued onto a copper foil, which produces a temperature dependent magnetic noise due to Johnson-Nyquist noise. It inductively measures the magnetic noise and analyses its power spectral density (PSD), which is proportional to the temperature. The shape of the PSD, however, is temperature independent. The thermometer is calibrated by the empirical equation

$$S_\Phi(f,T) = \frac{S_0(T)}{\left(1+(\frac{f}{f_c})^{P_1}\right)^{P_2}} \tag{3.15}$$

where f_c, P_1 and P_2 are fit parameters at the reference temperature T_{ref} using a Levenberg-Marquardt algorithm. The measured temperature is then found by using

$$T = T_{ref}\frac{S_0(T)}{S_0(T_{ref})} \tag{3.16}$$

3.2. Measurement Setups

Having discussed the cooling mechanism of the He3/He4 dilution refrigerator, temperature control, thermalization and filtering, we finally turn to the measurement setups for probing the samples. While most of the data is obtained from direct current (DC) measurements, a small part is accumulated with alternating current (AC). Due to the heavy filtering as presented in the last section as well as due to residual capacitances to ground, care has to be taken when measuring at a finite frequency (RC-time). This is even more important for high resistive samples. The frequencies used for the AC measuremements are below a few Hertz, most of the time even below 1Hz, and the integration times are long approx. a few seconds. The high resistances are therefore measured using DC-current-voltage characteristics, while some of the lower resistive measurements were performed using an AC technique.

By crossing the SIT from the superconducting regime to the highly insulating regime the resistances cover a broad range from zero to above GΩ. Such a measurement can not be accomplished by a single setup. To measure superconductivity a four-point measurement should be used, where current and voltage may be measured independently. In addition, wire resistances and contact resistances are excluded as no current flows through the voltage probes. For low resistive samples the setup should be current biased, while for high resistive samples a voltage bias setup is recommended. That is because the Joule power generated by a fixed current through a resistor is given by

$$P_{\mathrm{J}} = R \cdot I^2 \tag{3.17}$$

while in case of a voltage biased resistor it writes as

$$P_{\mathrm{J}} = \frac{V^2}{R} \tag{3.18}$$

However, a true four point measurement was not possible for the granular aluminum samples due to a lack of working contacts at low temperatures. Either the number was insufficient or their geometric position did not allow measurements in a four-point geometry. We therefore adapted a voltage bias setup used for measurements of high resistances in TiN samples [53] and added a preresistor R_{P}. The value was varied for different sets of measurements and/or temperature/magnetic field ranges. The lowest preresistor was 17.9kΩ and the highest 1MΩ. It allows to extract resistances from as low as $\approx 100\Omega$ up to high resistances $\approx$ GΩ, depending on the state of the sample, by two-point measuring the current only and calculating the voltage drop across the sample V_{S} by

$$V_{\mathrm{S}} = V_{\mathrm{B}} - I_{\mathrm{M}} \cdot R_{(\mathrm{P+W})} \tag{3.19}$$

Here V_{B} is the bias voltage, I_{M} the measured current and $R_{(\mathrm{P+W})}$ is the series resistance consisting of the preresistor and the resistance of the wiring.

From that current-voltage characteristic one may extract differential resistance $R_S = \frac{dV_S}{dI_M}$. The zero bias resistance is the differential resistance around zero bias and given by

$$R_{S,0} = \left(\frac{dV_S}{dI_M}\right)|_{I=0} \tag{3.20}$$

Another way to find the zero bias resistance from the raw current-bias-voltage curve is given by $R_{tot} = R_P + R_W + R_{S,0}$ and

$$R_{S,0} = \frac{dV_B}{dI_M}|_{I=0} - R_P - R_W \tag{3.21}$$

By using an additional preresistor one effectively sets an upper limit for the current. This can be important in case of a superconducting sample, when measured with a voltage bias setup. The generated current may exceed low critical currents. In case of a superconducting or low resistive sample the adapted setup does rather behave current biased, where the sample resistance accounts for the deviation of current from the theoretical maximum $I_{max} = V_B/R_{(P+W)}$. This setup is not ideal for low resistive samples, but the best we can achieve considering a two point geometry.

For high resistive samples ($R_S \gg R_P$) it is a true voltage bias setup as basically the total bias voltage drops across the sample and the current is determined by the sample resistance.
In some cases we measure the voltage drop V_M across sample and measurement lines with a Femto DLPVA voltage amplifier (amplification 10^0-10^4) in combination with an Agilent HP458A voltmeter. This is indicated by the dotted box on the right in Fig. 3.11. The voltage amplifier has a very high input resistance in the order of TΩ to prevent current flow along the voltage wiring in case of a very high sample resistance. As the ideal case of two separate voltage drops was not possible, this quasi-four-point geometry is the closest we can get to a four point measurement. The minimum resistance that can be measured is given by the resistance of the measurement wiring R_W, which is known to be approx. 4.5kΩ. The sample resistance is then given by V_M/I_M - R_W.

In Fig. 3.10 and 3.11 the two most used setups for the IV characteristics are presented. For high temperatures and/or relatively high currents/voltages the current was measured after the sample in a double-ended configuration. For the lowest temperatures and very small currents/voltages a single-ended approach was used. Tests had shown a smaller current noise compared to the double-ended setup. The two setups were used for the characterization of the granular aluminum samples. The measured samples are denoted in the figures with device under test (DUT).

1. Double-Ended DC Setup

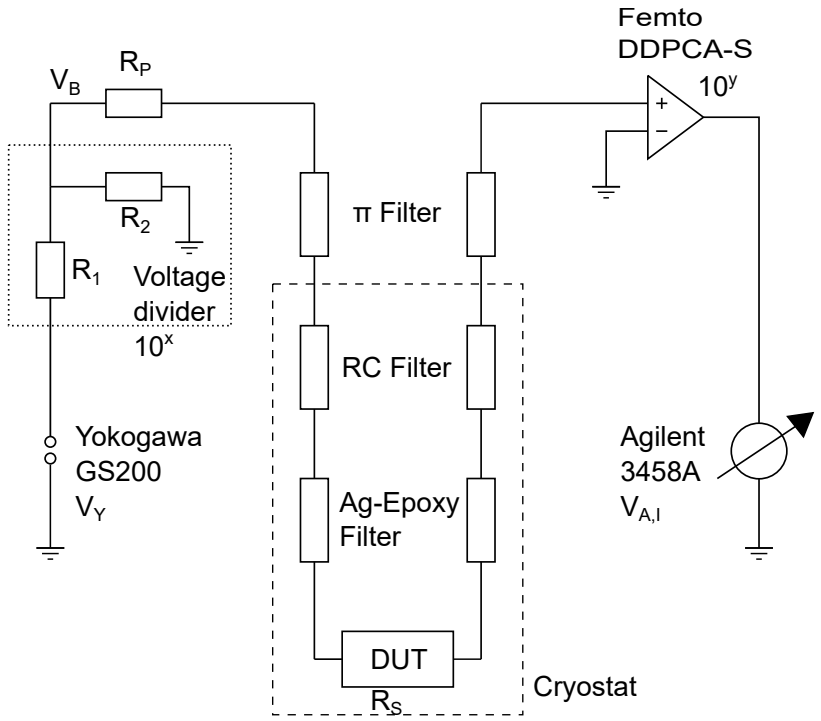

Figure 3.10.: Double-ended DC setup used for high temperature IVs and for low temperature IVs with relatively high bias.

A DC voltage source (Yokogawa GS200) provides a voltage V_Y, which might be downconverted by an optional voltage-divider by a factor 10^x. In some measurements x = 2 in others x = 3. The corresponding resistances were $R_1 = 10\mathrm{k}\Omega$ combined with $R_2 = 100\Omega$ or $R_2 = 10\Omega$, i.e. conversion factors of 10^{-2} or 10^{-3}. That voltage V_B is applied over a total resistance $R_\mathrm{tot} = R_\mathrm{P} + R_\mathrm{W} + R_\mathrm{S}$. R_W, the resistance of the wires, does include filter resistances. The current I_M is measured between sample/DUT and ground using a transimpedance amplifier (Femto DDPCA-S). That device sets the ground potential and transduces the flowing current into a voltage with a variable factor 10^y, i.e. $V_\mathrm{A,I} = 10^\mathrm{y}$ I_M, where y ranges inbetween 8 and 13.
That voltage is then read out by Agilent 458A voltmeter and the sample zero bias resistance $R_{\mathrm{S},0}$ is given by Eqs. 3.19 and 3.20.

2. Single-Ended DC Setup

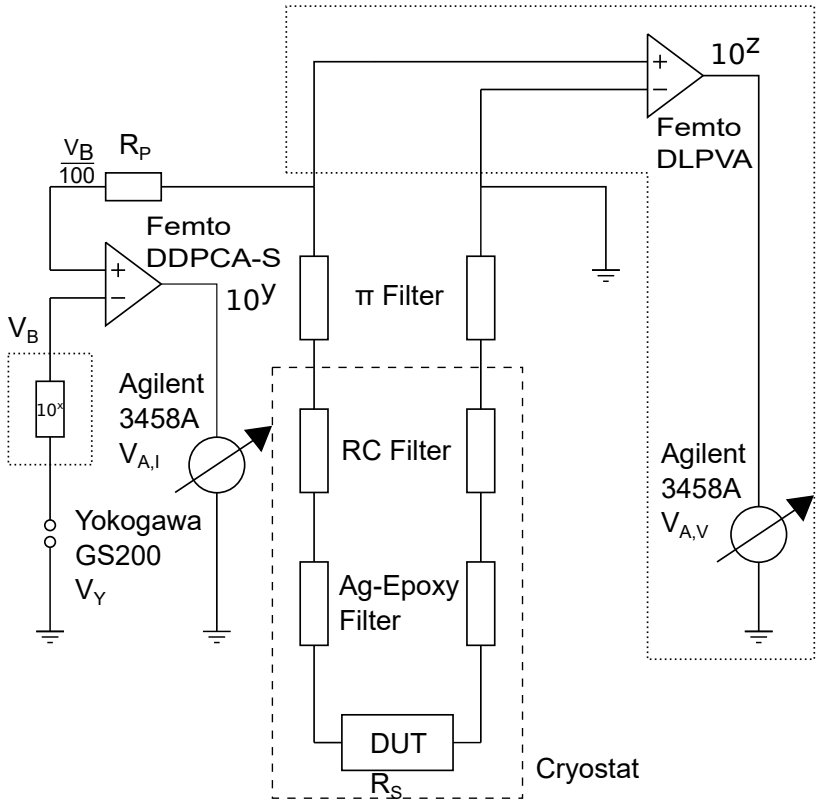

Figure 3.11.: Single-ended DC Setup used for IV characteristics in the zero bias regime with low excitation.

In contrast to Setup 1, one side of the sample is connected to ground. This increases measurement resolution by decreasing current noise. The current has to be measured on the ungrounded side.
The DDPCA-S therefore is biased at its bias port, which in normal operation is shorted to ground. The input port is then connected to the sample. This allows to use a single measurement line, while the second measurement line is shorted to ground at room temperature. The biasing of the sample and conversion of the measured current into a voltage is done by the same device. It should be noted that by using the bias port in that configuration a built-in voltage-divider reduces the voltage by a factor 10^2.
V_Y is first divided by the optional voltage-divider with 10^x. The resulting bias voltage V_B is then again divided by a factor 100. That bias voltage V_B is in addition multiplied by factor of -1, indicating a reverted current flow, i.e. the charge is pulled from ground through the sample. This $V_\mathrm{B}/100$ is applied to the series of resistances $R_\mathrm{tot} = R_\mathrm{P} + R_\mathrm{W} + R_\mathrm{S}$. The current, measured by the DDCPA-S, is transduced to a voltage and multiplied

by a factor 10^y. The voltage $V_{A,I}$ is read out by an Agilent voltmeter connected to the DDPCA-S read out port.

A set of variations (different preresistors and/or voltage dividers) of the two setups were used for different resistance and temperature regimes. For example, at the lowest temperatures around zero bias the following combination is used for the single-ended setup. The maximum voltage applied by the source is e.g. 5V. It is downconverted to $V_B = 5 \cdot 10^{-4} V_S$ by the optional voltage divider with 1/100 and reverse mode operation with 1/100. A 1MΩ preresistor limits the current to $I_{max} \approx 5 \cdot 10^{-10}$A. The voltage/current ratio of 10^{10}V/A at the DDPCA-S accounts for the read out voltage to stay below the 10V input voltage range of the voltmeter.
For the double ended setup e.g. a 1/1000 voltage divider was used in combination with a 100kΩ preresistor and the DDPCA-S operation in normal mode with a ratio of 10^8V/A. With this combination one keeps the signal high at the source but stays at relatively low bias values applied to the sample. The read out voltage is kept below 10V at the voltmeter again.
The DC voltage at the source is swept by a list of predefined voltage values. To take into account large RC times generated by the high sample resistance in combination with the capacitance to ground, e.g. from measurement lines, as well as the low-pass filter of the DDPCA-S of 0.7Hz, we use a waiting time of 2s after each voltage step before readout. After that relaxation time the signal at the DDPCA-S should be at least 90% of its saturation value at t = ∞. In addition, the integration time of the voltmeter input was set to 20 number of power lines cycles (NPLC) to further reduce current noise by averaging over a relatively long time of 400ms.

3. AC Setup

The AC setup (see Fig. 3.12) is used for the two niobium silicon samples as well as for some measurements on granular aluminum, where the overall resistances ranged from zero to a few ten kΩs. As the resistances are much smaller than in most measurements of the granular aluminum, the RC times are significantly reduced allowing to measure AC with very low frequencies.

Two different approaches to deduce the resistance are applied. In case of granular aluminum the AC setup was used for a set of $R(B)$ curves at temperatures $T > 1$K. Sweeping the magnetic field with a rate of 50mT/min for a continuous $R(B)$ curve does not heat up the sample or surroundings. The AC resistance is continuously probed measuring current and voltage while sweeping the magnetic field. For this type of measurement the frequency is set to $f = 0.4755$Hz and the time constant to 10s.
For the granular aluminum there is no four-point measurement possible, therefore the same optional voltage probe as shown in Fig. 3.11 is utilized.
For the niobium silicon the $R(T, B)$ was measured with a different approach. As all those measurements are carried out below a few hundreds of mK, a relatively fast continuous

sweep with 20mT/min or more, leads to a constant elevation of sample temperature. We therefore set a fixed temperature, e.g. 50mK, and stepsweep the magnetic field with a rate of 25mT/min. After each step we let the temperature thermalize back to the set temperature for 1 hour. During this time we monitored the resistance continuously versus time. The saturation value of resistance at the end of the hour has been extracted and assigned to the corresponding magnetic field and temperature. The frequency is set to be $f = 11.267$Hz or $f = 17.329$Hz with time constants of 3s or 1s.

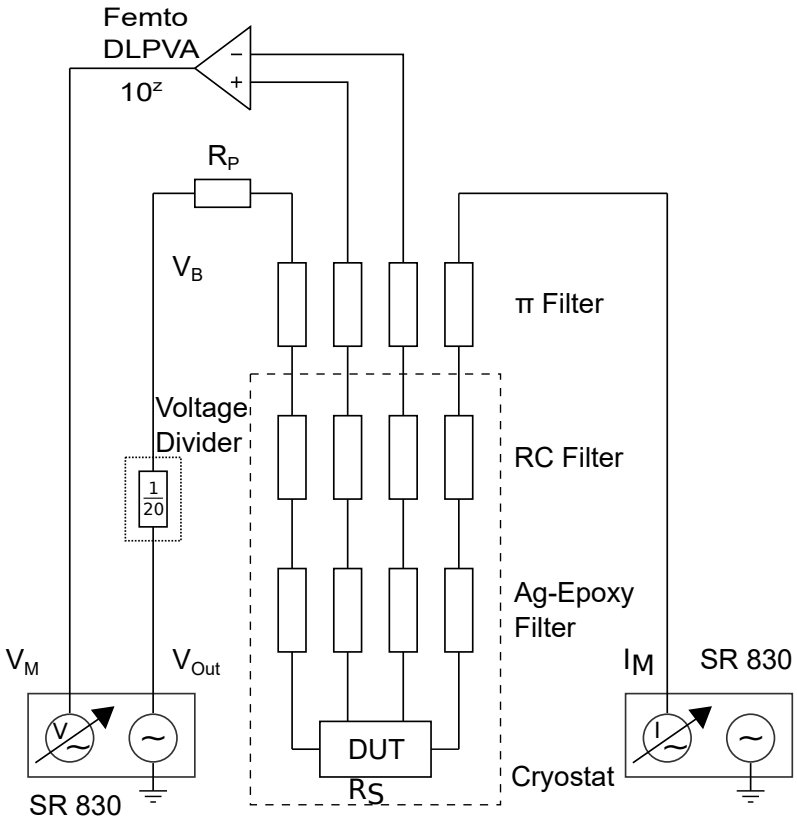

Figure 3.12.: Setup used for AC measurements of the zero bias differential resistance in NbSi and selected measurements in grAl.

The AC setup consists of two Stanford lock-in amplifiers, locked onto the same frequency. The first provides an output voltage V_{Out} with frequency f. In some cases it is downconverted by a voltage divider with a factor $\approx 1/20$ (the corresponding resistances are $R_1 = 100\Omega$ and $R_2 = 4.7\Omega$). The V_{B} is applied to a preresistor, which is much larger than the sample resistance R_{S} by at least a factor 1000, e.g. 1MΩ. The measurements are therefore current biased. The voltage drop V_{M} is measured by the input of the master in a four point geometry excluding measurement wiring and contact resistances after it is amplified by a DLPVA with a factor 10^{z}. z is in the range of 1-4. The corresponding AC

current is measured either directly by the input of the second lock-in amplifier or it is converted into a voltage by a DDPCA-S transimpedance amplifier. The corresponding voltage is then measured by the input of the second lock-in amplifier. The latter case is not shown in Fig. 3.12.

For all measurement setups the wiring at room temperature between the measurement equipment and the insert is done with coaxial cables that end with BNC connectors. The devices are plugged into electrical power points and each device receives its own insulating transformer. A star-shaped like grounding scheme is established via the shielding of the coaxial cables to the top part of the insert. A thick copper-braided cable connects the top part of the insert to laboratory ground.
The measurements are automated using scripts based on Lab::Measurement [161]. The measurement computer and the devices are connected with GPIB cables, but are electrically disconnected by an optocoupler.

4. Material and Sample Characterization

4.1. Overview on the 3D Granular Aluminum Material System

Our two dimensional ultra-thin films are provided by the group of Guy Deutscher[1] and were grown by Aviv Glezer Moshe. They used the same growth mechanism as for their 3D samples. Here we present an overview on their 3D material system.
In this growth process samples are prepared by thermally evaporating clean aluminum pallets under controlled oxygen pressure onto a cold, liquid nitrogen cooled, or room temperature substrate. A very narrow grain size distribution in the low nanometer regime can be achieved, where the temperature of the substrate controls the grain size, its distribution and the maximum critical temperature T_c. For room temperature substrates the grain size is about 3nm ± 1nm [4] and the maximum critical temperature in those films was found to be 2.2K [5, 162, 163]. By cooling the substrate to liquid nitrogen temperatures the maximum transition temperature could be increased to 3.2K and the narrow grain size distribution further decreased to 2nm ± 0.5nm [5, 164]. The increased

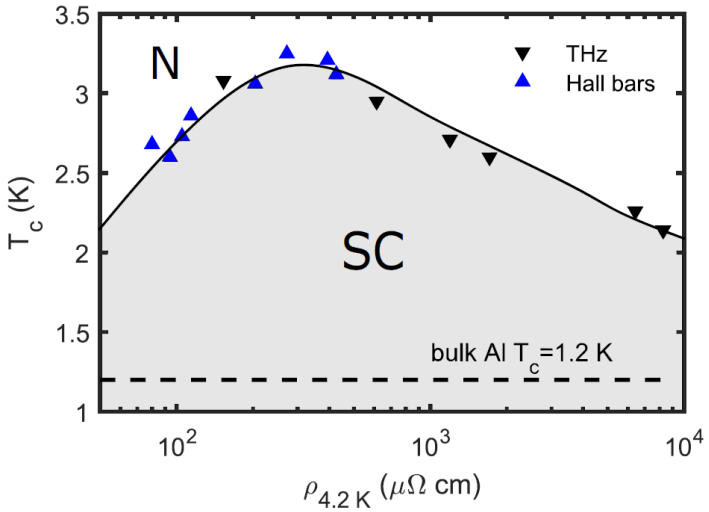

Figure 4.1.: Critical temperature plotted against resistivity in films with average grain size of 2nm. Black triangles: T_c extracted from measurements of the energy gap by THz spectroscopy. Blue triangles: T_c directly measured by probing the resistivity in a standard four-probe hallbar geometry. Figure taken from [165].

[1] Raymond and Beverly Sackler School of Physics and Astronomy, Tel Aviv University, Tel Aviv 6997801, Israel

critical temperature of granular aluminum compared to bulk aluminum is known for a very long time and has been observed first by Abeles [166] in 1966. The origin of the enhanced T_c and its dome-like shaped dependence on normal state resistivity is still debated (see Fig. 4.1).
Due to their narrow grain size distribution films grown as presented above can be treated as homogenously disordered films. Over the last years they have been studied extensively for their transport properties and optical conductivity [163, 165, 167–172]. A possible application for quantum circuits are superconducting microwave resonators [173, 174] due to the high and tunable kinetic inductance in granular aluminum. The films studied were all relatively thick, i.e. at least 20-30nm up to $\sim$ 100nm. As the grain sizes are in the order of 2-3nm, the films can be considered three dimensional and no high resistive state has been found.

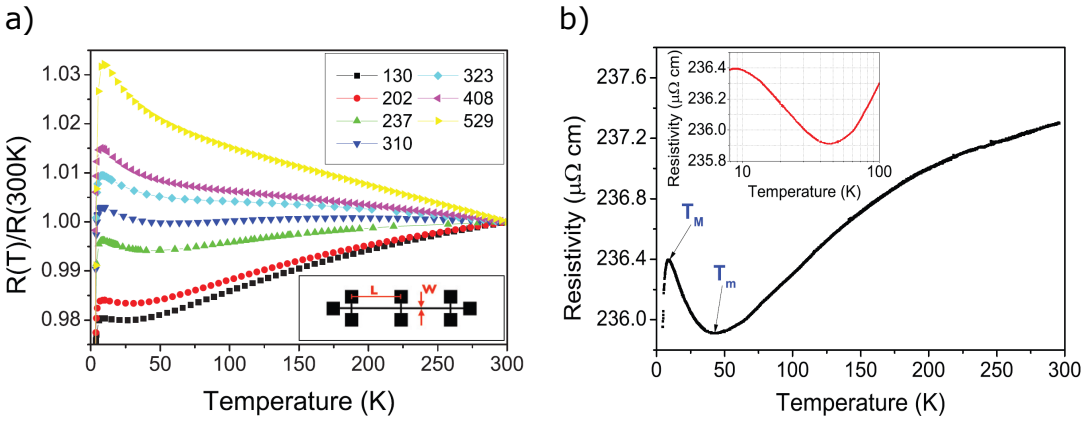

Figure 4.2.: a) Relativ resistance $R(T)/R(300\text{K})$ plotted against the temperature. Curvature changes with increasing 300K-resistivity from a positive TCR to a negative TCR. b) $R(T)$ of a low resistive sample, showing a negative curvature at high temperature, a minimum of resistance at T_m and an increase to a maximum at T_M. The inset shows the logarithmic increase at low temperatures. Figure taken from [167].

In 2013 Ref. [167] reported results of transport measurements on thin granular films with a grain size of 2nm close to the metal to insulator transition. As the films are about 100nm thick they are treated as three dimensional, because their thickness is more than one order of magntiude larger than the grain size. By measuring the $R(T)$ curves of the zero bias resistance they find transition temperatures T_c consistent with the dome like shape in Fig. 4.1. Above the individual critical temperature they find, that the normal state properties near the metal to insulator transition show striking similarities to systems, like CuMn and CuFe [175, 176]. Due to scattering of conduction electrons in a metal due to magnetic impurities this dilute alloys show a negative magnetoresistance in samples with a high resistivity, a minimum in the $R(T)$ at a temperature T_m followed by a logarithmic increase of resistivity below T_m in samples with lower resistivity (metallic behaviour). This behaviour is known as the Kondo effect [177]. The metallic samples in addition show

a negative curvature with a positive TCR, i.e. the resistance decreases with decreasing temperature, while the insulating samples show a negative TCR, i.e. an increasing resistance with decreasing temperature. Fig. 4.2a) presents the $R(T)$ curves in reference to the resistance at 300K. The room temperature resistivities increase from small (black) to large (yellow) and are listed in the upper right corner. The lower right inset depicts the used hallbar geometry. The above mentioned behaviour of positive TCR for low resistivity samples towards a negative TCR for samples with high resistivity is visible. In addition, in Fig. 4.2b) a single $R(T)$ is shown for a metallic sample. It exhibits a negative curvature at high temperatures, a resisitivity minimum T_{m} and a log(T) dependence at low temperatures. At a temperature T_{M} the resistivity has a maximum below which the resistivity starts to decrease towards the superconducting transition at a temperature $T_{\mathrm{c}} < T_{\mathrm{M}}$. The properties of the normal state above T_{c} are interpreted in terms of spin-flip scattering of conduction electrons by local magnetic moments, which possibly are located at the interface between metal and oxide of the grains. The theoretical description as well as experimental findings have also been published in Ref. [168] and [169]. In the latter a Mott transition [178, 179] is observed by probing the increase of the spin-flip scattering rate of the conduction electrons as the grains inside the granular film are decoupled (increasing ρ_{N}). The coupling strength is measured in terms of the room temperature resistivity. The findings suggest, that the scattering of the conduction electrons by free spins increases by several orders of magnitude. The increase of the normal state resistivity is attributed to a decrease of the effective Fermi energy. Once the effective Fermi energy approaches the electrostatic charging energy E_{C} of a single grain at high resistivities, a Mott transition to an insulating state is likely to occur. The critical resistivity observed at the transition $\rho_{\mathrm{c}}(300\mathrm{K}) \sim 50000\mu\Omega\mathrm{cm}$ is in agreement with previous measurements in 3D granular films close to the metal to insulator transition [169].
In Ref. [170] signatures for unconventional superconductivity, i.e. not in agreement with predictions by the BCS theory, have been found in 3D granular aluminum films. By measuring the complex transmission of superconducting granular aluminum films in the THz optical range accompanied by measurements of the temperature dependence of the BCS energy gap, they find good agreement with BCS predictions as long as the grains are well coupled. However, for fairly decoupled grains they find an enhanced absorption for frequencies lower than the energy gap. The absorption at sub-gap frequencies is not in agreement with BCS predictions. Ref. [170] argues that the found deviations can not be explained by thermally excited quasiparticles nor by inhomogeneity effects despite of the granular nature of their samples.
A further study of the optical conductivity using THz spectroscopy near the Mott metal to insulator transition by Ref. [165] indicates a crossover from BCS regime to a Bose-Einstein-condensate (BEC). In the BCS regime the number of pairs in a coherent volume is very large. In a BEC this number is in the order of unity. It was only recently theoretical predictions regarding the evolution of strong- coupling ratio and the crossover from BCS to BEC became availabe [180, 181]. Ref. [165] find an increase of the coupling strength $2\Delta(0)/k_{\mathrm{B}}T_{\mathrm{c}}$ up to 4.51 by comparing the value of the optical gap determined by fitting the conductivity data to the Mattis-Bardeen theory [182] to the BCS energy gap

extracted from their tunneling data. The increase above the value of $2\Delta(0)/k_{\mathrm{B}}T_{\mathrm{c}} = 3.5$, as predicted by BCS theory, by increasing the room temperature resistivity, while the critical temperature is not found to be strongly reduced by the grain decoupling, is again consistent with a Mott transition. Ref. [165] argues that the good performance of high kinetic granular aluminum resonators by Ref. [173] may in fact originate from the Mott like metal to insulator transition instead of an Anderson like transition. A granular system exhibiting a Mott type transition may be viewed as a network of Josephson junctions between well defined aluminum grains, rather than as a highly disordered superconductor [173]. Ref. [171] studied the temperature dependence of the upper critical

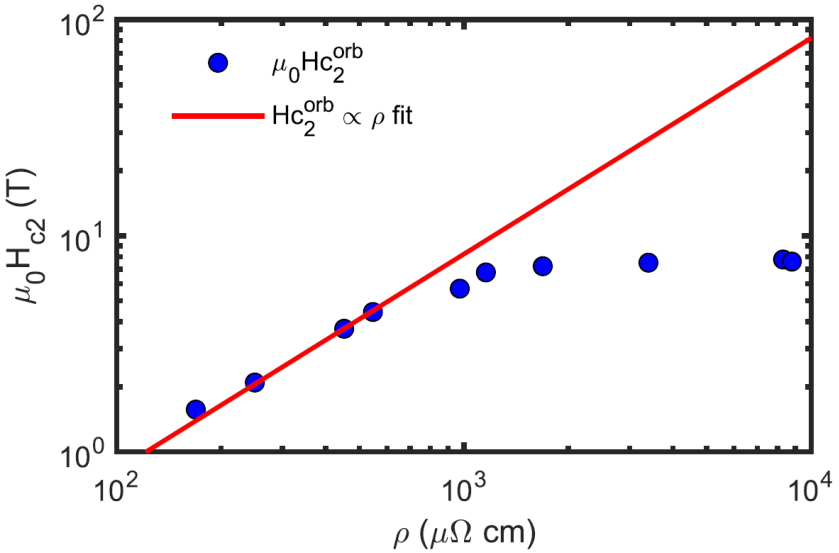

Figure 4.3.: Orbital critical field $H_{\mathrm{c2,orb}}$ plotted against 4.2K resistivity. Blue dots are measurement data and the red line corresponds to the prediction by WHH theory. For resistivities above 1000$\mu\Omega$cm the critical fields deviate from the prediction and saturate at value of B = 7-8T. The deviation from the red curve is attributed to the crossover to a Pauli limitation of the upper critical field. Figure taken from [171].

field of superconducting granular aluminium films with resistivities close to the metal to insulator transition. They find a shift from orbital (low normal state resistivity at 4.2K) to Pauli limited (high normal state resistivity at 4.2K) critical field (see Fig. 4.3) and argue that this is due to a renormalization of the electron mass. In the regime of Pauli limited critical fields the transition becomes of first order as predicted by [183, 184].

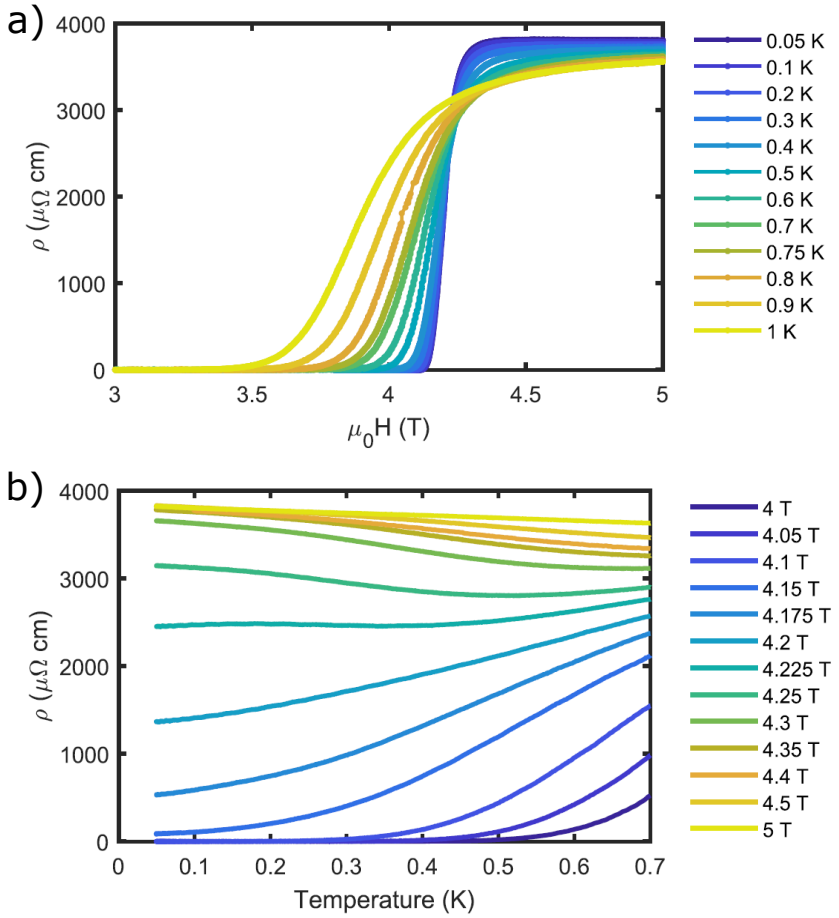

Figure 4.4.: a) and b) present $R(B)$ and $R(T)$ curves for a sample with $\rho_{4.2K} = 3400\mu\Omega$cm. a) With decreasing temperature the transition to the normal conducting state gets very narrow. b) In between 4T and 5T the $R(T)$s display a non zero saturation resistance smaller than $\rho_{4.2K}$. Interestingly, there is a minimum in the $R(T)$ around B = 4.25T and $T \sim 500$mK. Figure taken from [171].

In Fig. 4.4 the $R(B)$ and $R(T)$ curves are presented for a sample having a normal state resistivity of $\rho_{4.2K} = 3400\mu\Omega$cm, i.e. a high enough resistivity to be in the Pauli limited regime as shown in Fig. 4.3. For low temperatures the $R(B)$ curves show a very narrow transition, while in the $R(T)$ curves around B = 4.25T the resistivity goes through a minimum. The minimum occurs at a temperature compatible with the occurence of the maximum in the upper critical field. To fit the temperature dependence of the upper critical field of samples with $\rho_{4.2K} > 1000\mu\Omega$cm to the Werthamer-Helfand-Hohenberg (WHH) theory [185], the authors of Ref. [171] had to use Maki parameters $\alpha > 1$. For that case, the WHH theory predicts that the upper critical field, connected to a second order transition, should decrease at lower temperatures.

Fig. 4.5 shows the extracted upper critical fields for the corresponding temperatures of the same sample as shown in Fig. 4.4. To do so, the resistivity versus magnetic field curves were fitted to the theory of Fulde and Maki [186]. The upper critical field increases

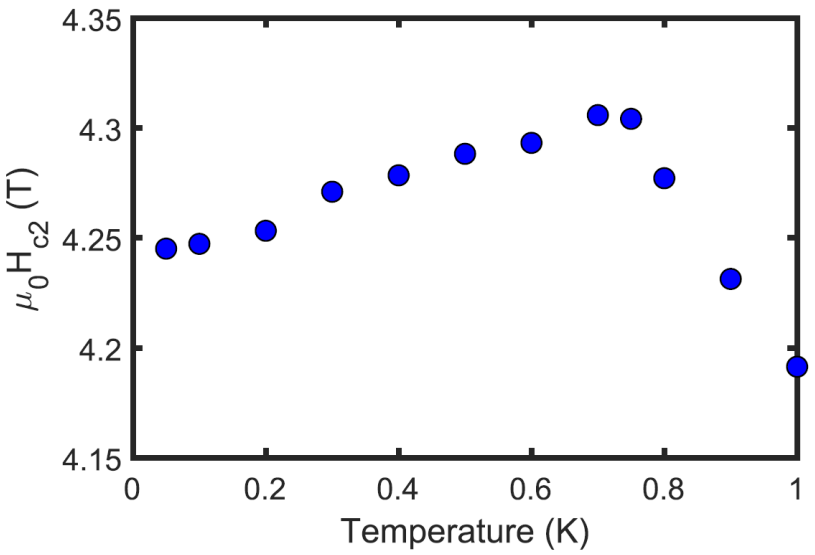

Figure 4.5.: Low temperature part of the upper critical field versus temperature plot. The critical field reaches a maximum at $T \sim 750$mK and decreases for lower temperatures. Figure taken from [171].

for decreasing temperatures until it reaches a maximum. For even lower temperatures there is a downturn of the critical magnetic field as predicted by WHH theory for a Maki parameter $\alpha > 1$. Above the maximum the transition is a second-order transition, while below the maximum it is a first order transition.
Ref. [171] argues that at the Mott transition, the effective Fermi energy reaches zero and therefore at some point has to become equal to the energy gap. Then the number of Cooper pairs in the coherence volume is in the order of unity and this can be treated as a BCS to BEC crossover. For that crossover it is predicted, that the phase coherence length ξ_{phase} and with it the orbital critical field saturates [187]. This is what has been found in their measurement. In addition the found strong coupling of $2\Delta(0)/k_{\text{B}}T_{\text{c}} \sim 5$ does as well agree with the prediction of a BCS-BEC crossover.
Recent measurements of the evolution of the superconducting energy gap Δ with THz spectroscopy further support the approach of a BCS-BEC crossover, which is proposed to be induced by the vicinity of a Mott transition [172].

4.2. 2D Granular Aluminum - Sample Characterization

Our goal is to study films in the true two dimensional limit. We aim at the SIT and transport properties in the insulating state. Hence, the requirements for our films were a further decrease of thickness, designed to 5nm, combined with a sheet resistance in the vicinity of the quantum resistance of Cooper pairs $R_Q = 6.45\text{k}\Omega$. Fig. 4.6 shows

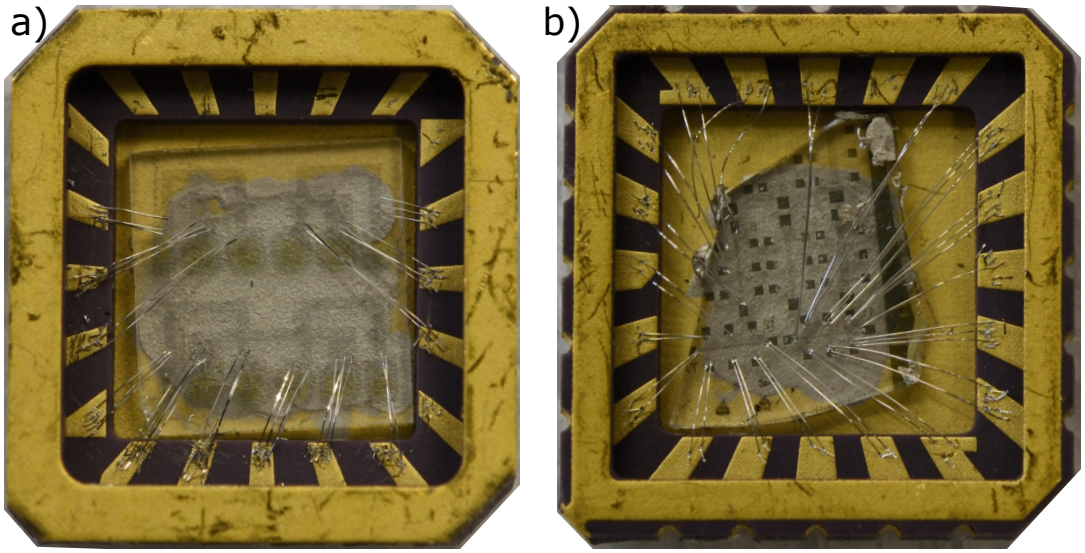

Figure 4.6.: Optical images of a) Sample 091220 - S b) Sample 090720 - I prepared for measurements. They have been glued into the chipcarriers and bonded with aluminum bonds. The design of the hallbars is different for both samples. For sample S both hallbars are identical. The dimensions of the hallbars in b) for Sample I do vary in width.

optical images[1] of the two samples presented below. Both films were patterened in a hallbar geometry. The hallbar of Sample 091220, referred to as Sample S, has a width of 250-300μm (uncertainty in dimensions stem from mechanical mask for shadow evaporation and evaporation executed with a small angle; see appendix A.3). Sample 090720, referred to as Sample I, has a width of 50μm. Both hallbars are sketched again for clarity in Fig. 4.7. The wider hallbar in Fig. a) for Sample S should have been an upgrade to the design of b), where contact pads were very small. In addition, we encountered serious problems on numerous samples to establish (good) electrical contacts to the films. The bond wires did not stick to the granular film or if they did, there was a mechanical but no electrical contact. Some samples could be measured at room temperature, but after cooldown to low temperatures electrical connection was lost. The two samples measured in this thesis are the ones that had enough working contacts at room temperature to be measured in a standard four-point geometry and at least two properly working contacts at low temperature for a two-point characterization. That is why both samples had to

[1]Photographs taken by S. Feyrer

be measured in a two-point geometry at low temperatures. The current path increased to approx. 28 sheets for both samples. The room temperature resistances could be measured with a four-point measurement and are listed in the table below together with other important values.

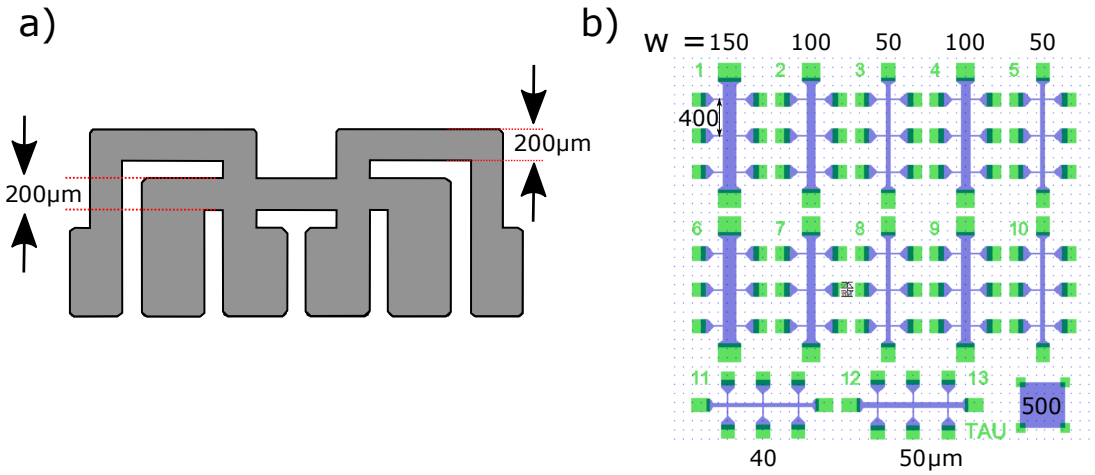

Figure 4.7.: Different hallbar designs: a) Current path designed to be 200μm, but increased to values between 250-300μm due to fabrication resolution and growth under a small angle. b) Design of various hallbars. Sample I corresponds to hallbar 12 with 50 μm width and 400μm between voltage probes. Due to fabrication the on-chip design is a mirror-image as seen in the optical image Fig. 4.6b). The design shown in b) was designed and provided by A. Glezer Moshe.

	Sample 091220 - S	**Sample 090720 - I**
width	300μm	50μm
thickness	5-6nm	9-10nm
N_{sheet}(2-point)	28	28
R_{sheet}(RT)	1.78kΩ	5.375kΩ
R_{sheet}(4K)	2.96kΩ	7.75kΩ
T_c	2.3-2.4K	1.8-2.4K

Morphology

The grain sizes, the size distribution as well as the critical temperature is known to depend on growth properties such as substrate temperature, vacuum pressure and oxygen concentration [165]. The film resistance may be tuned by the oxygen concentration during growth. But does the film thickness matter? What happens if the film is very thin, i.e. only a few nanometers? Does that impact the morphology and/or the shape of the granules?

To answer this question, both samples have been scanned with a scanning electron microscope[2] and checked for their average film thickness using a DekTak profilometer[3]. In addition a third unmeasured sample has been characterized with an atomic force microscope[4] for the thickness profile of the film A.2.

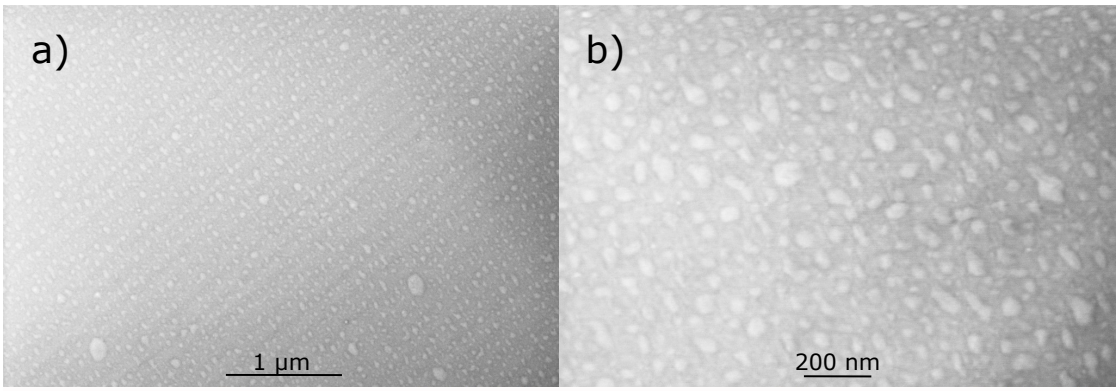

Figure 4.8.: Sample S - SEM Images: a) 24.000x low Zoom image b) 69.000x high Zoom image. The scale bars in a) and b) indicate 1μm and 200nm, respectively.

As Fig. 4.8 suggests, the reduction of thickness into the few atom layer limit does indeed strongly affect the granular morphology of the films. There is a strong inhomogeneity in the grain size distribution in contrast to films with thickness above 20nm. They show grain sizes of 2-3nm depending on growth properties. The ultra-thin films show a broad spectrum of grain size and distance. In Fig. 4.8a) only the large grains can be seen, while in b) after a further zoom in, we get grain sizes ranging between 2nm and 80nm. While the average distance between the grains is rather small, a few nm or less, the distance between the biggest grains is roughly the same as their size, up to 80nm.

A reference sample, designed for a thickness of 5nm, with actual thickness of roughly 10nm, and a room temperature resistance comparable to Sample S, was investigated for its thickness profile with an atomic force microscope.

[2]SEM by Zeiss
[3]DekTaK by Bruker
[4]AFM by Park

The AFM image in Fig. 4.9 has been analysed with the software Gwyddion[5].

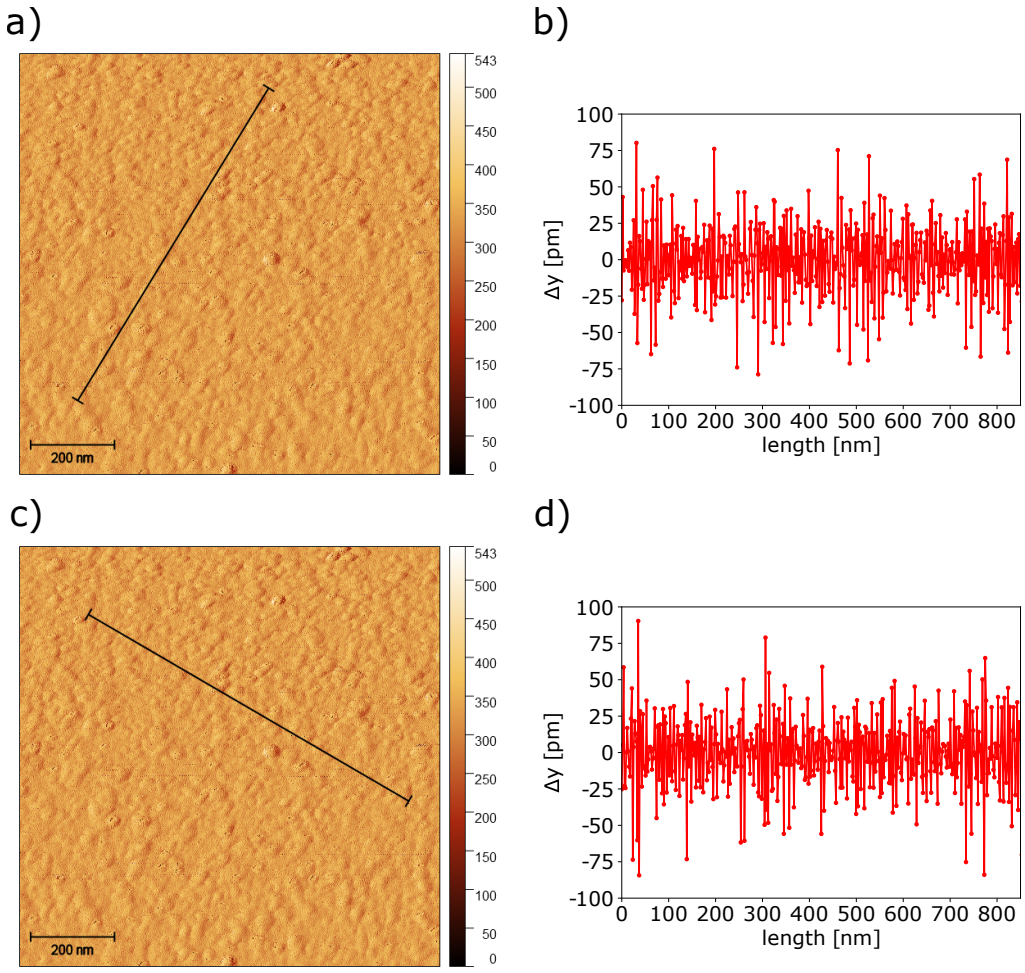

Figure 4.9.: Reference Sample - AFM Image: a) and c) show the same 1μm x 1μm wide window, where the scalebars indicate 200nm. The colorscale is in pm. The lowest value is 0 and the highest value is 543pm. The ticks indicate steps of 50pm.
The black line in a) corresponds to the linetrace shown in b) and the black line in c) to the linetrace in d). Both line traces show a thickness variation along its path below ±100pm.

The thickness in that 1 micron x 1 micron wide window varies only little around a random residual offset of approx. 0.3nm coming from the AFM (a big 3.74nm offset corresponding to the minimum in the original data has been removed). The deviation of thickness from the average value of ≈ 300pm is less than ± 100pm as shown by the line traces in Fig. 4.9 b) and d). The distribution of thickness across the total scanning area is shown in Fig. 4.10. The narrow distribution around the average thickness indicates a

[5]Free Software Gwyddion - gwyddion.net

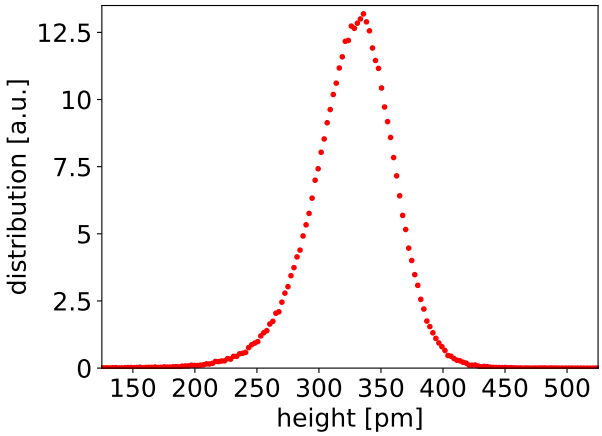

Figure 4.10.: Thickness distribution shown for the whole scanning area of 1μm x 1μm of Fig. 4.9a)/c). The maximum is at a random residual offset.

relatively flat surface and suggests that the aluminum grains are indeed encapsulated into an aluminum-oxide matrix, as expected from thicker films.

We will now return to the SEM images. They have been analysed using python's numpy and open-cv packages to evaluate the distribution of the grain areas and from that the distribution of the diameters. The processed SEM images of Fig. 4.8b) are shown in Fig. 4.11. From the scalebar we get a value of 1.63nm x 1.63nm per pixel, which is used in the image processing algorithm to calculate grain area and from that the grain diameter.

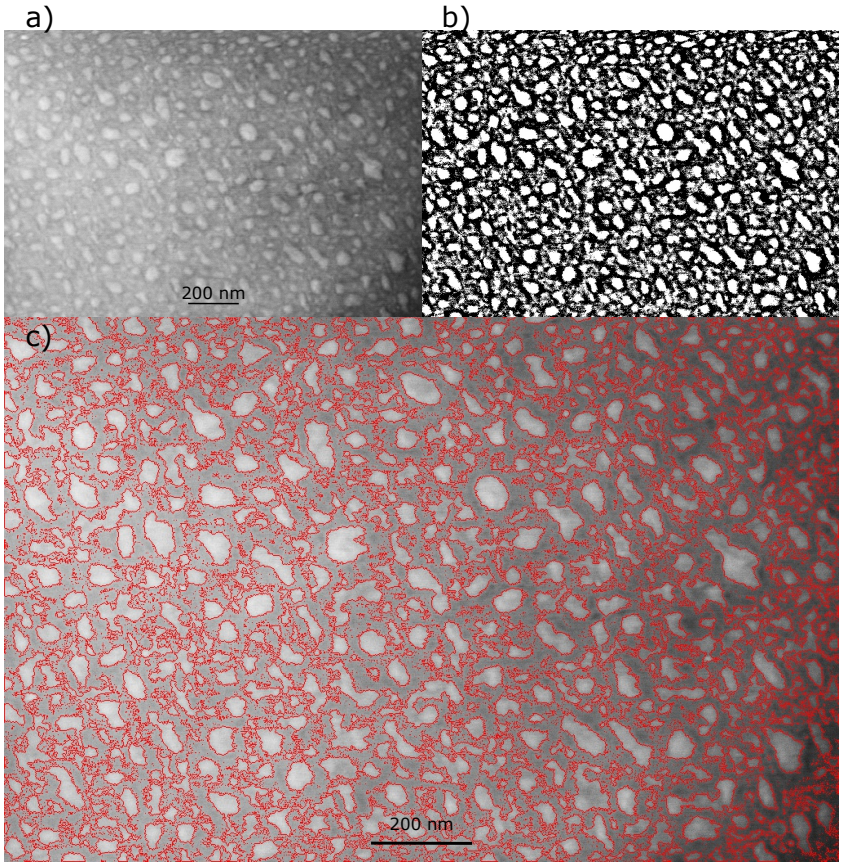

Figure 4.11.: Processed SEM image of Sample S: a) grayscale image of Fig. 4.8b). In b) the corresponding threshold image is shown. a) and b) have the same size and scalebar. c) shows the extracted contours from the threshold image projected onto original SEM image.

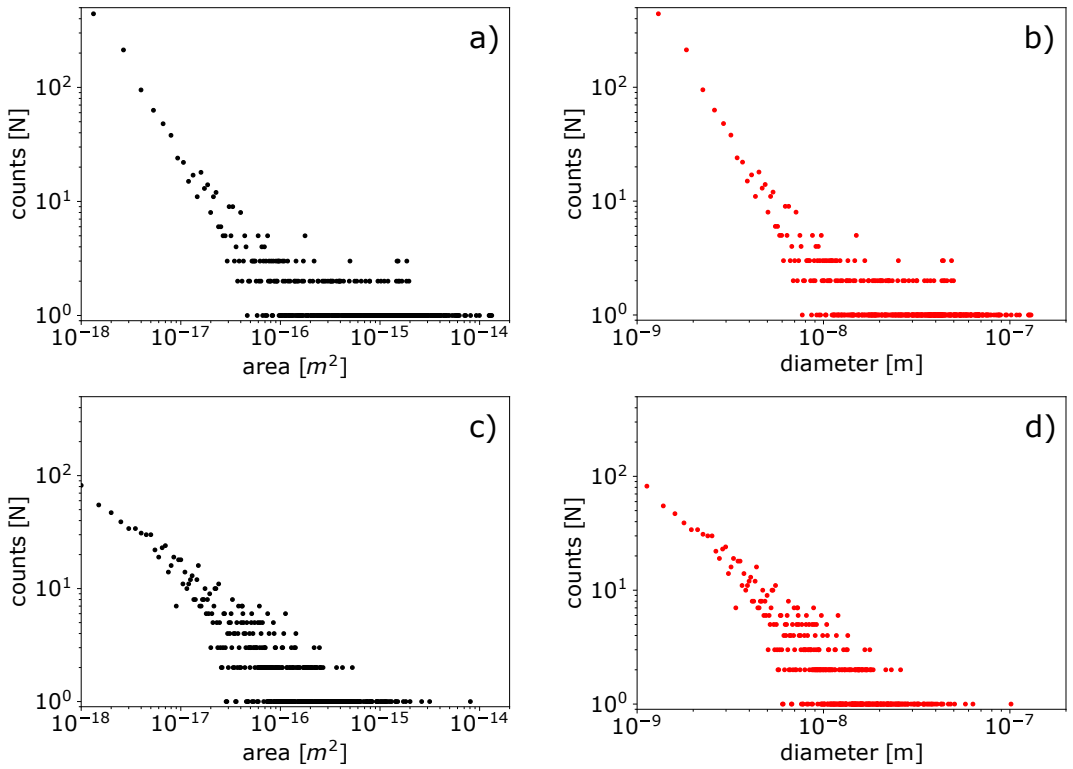

Figure 4.12.: Grain area and diameter distribution for circular grains of a), b) sample S and c), d) sample I on a double logarithmic scale. Plotted are the number N of counts versus area/diameter. Both samples exhibit a similar grain size distribution. The grain sizes vary between a few nm only up to ∼100nm. In both samples the number of small grains below 10nm dominate.

From the contour area distribution, we can deduce the diameter distribution by assuming a circular grain shape. The corresponding diameters lie in between a few nm and approx. 100nm.
Fig. 4.12 suggests, that sample S and sample I have approximately the same distribution of grains (area, diameter), where the small grains with d < 10nm dominate. Weighting the counts for the corresponding diameters by $d_{\mathrm{av}} = \sum(N_{\mathrm{i}} * d_{\mathrm{i}})/N_{\mathrm{tot}}$, we get average diameters of approximately 12nm for sample S and approx. 7nm for sample I.
The contour area algorithm rather underestimates the area for each grain. In addition, islands with diameter below 5nm are hard to detect or appear as parts of bigger grains due to image resolution. Due to the latter it is possible that a larger grain is shown as a pile of very small grains. That shifts the distribution towards smalle values. We apply a lower threshold to the grain diameter distribution and consider only grains with a diameter above 5nm. The deduced average grain diameter is approx. 28nm for Sample S and 13nm for Sample I.

In Ref. [8] Abeles proposed that the charging energy can be calculated by material and geometrical properties only.

$$E_{\mathrm{C}} = \frac{e^2}{4\pi\epsilon_0 d\kappa} \tag{4.1}$$

$$\kappa = \epsilon\left(1 + \frac{d}{2s}\right)$$

e is the electron charge, ϵ_0 the vacuum permittivity, ϵ the relative permittivity, d the grain size, and s the grain separation.

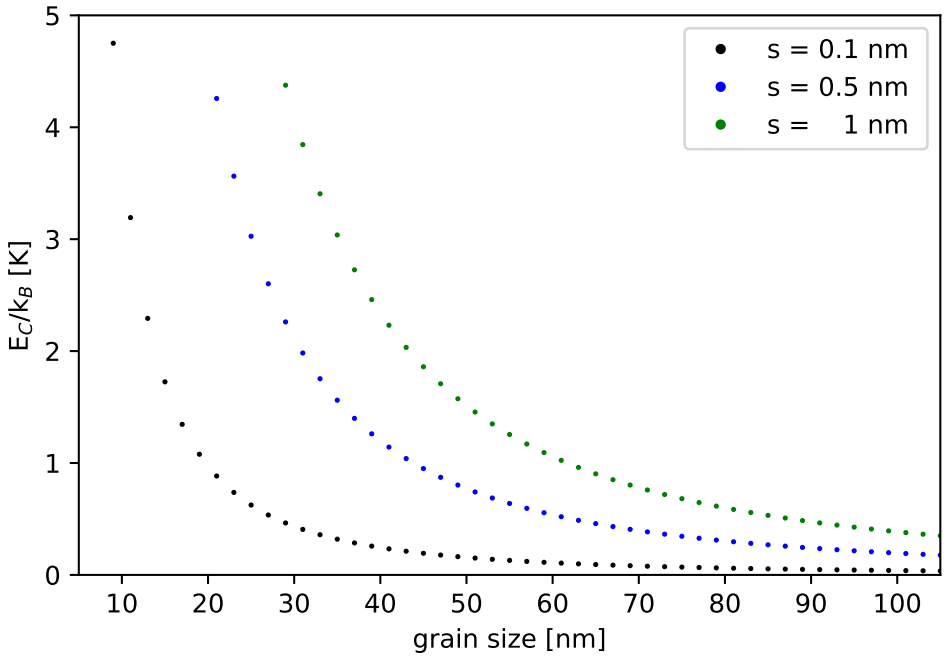

Figure 4.13.: Calculated charging energies using Eq. 4.1 for three different grain separation values.

Fig. 4.13 shows calculated charging energies using Eq. (4.1) for a grain size distribution as seen in Fig. 4.11 and for 3 different grain separations. The grain separation length s was chosen to be around 0.5nm as known for films with higher thickness and the relative permittivity for amorphous Al_2O_3 to be 8.5 [168].
Taking into account the average grain size to be in the order of 30nm for Sample S and the average grain separation to be approximetely 0.5nm or less, one expects the charging energy for single electrons to be a few hundred mK up to a few Kelvin. The same holds true for Sample I, where even higher charging energies are expected due to the smaller average diameter. In reality however, things are far more complex as the grain separation might as well vary locally. That leaves a random network of grain sizes and separations.

Nevertheless, those values should give an estimate for the order of the expected charging energies.
Assuming some grains turn superconducting below a certain temperature, then the transport would be composed by electrons and Cooper pairs. As the charge of a Cooper pair is $2e$, one expects a charging energy of $4E_{\mathrm{C}}^{(\mathrm{e})}$ for the same grain diameter and separation.

4.3. 2D Granular Aluminum with Normal Conducting Grains below T_c

As presented in section 4.2 our samples are two dimensional with thickness 5nm and 10nm and have a broad distribution of grain sizes from a few nm up to 100nm. In similar ultra thin films Goldman [10] found superconductivity and evaluated the influence of the film thickness. They found a sharp transition to an insulating state when decreasing the thickness below a critical value of a few nm (thickness induced SIT). We want to study the magnetic field induced superconductor to insulator transition and the behaviour of the insulating state. A granular metal, without superconductivity in the grains, may behave insulating with decreasing temperature, if the grains are weakly coupled [110] (see section 2.3). This has to be distinguished from an insulating state by decoupling the superconducting grains (see section 2.2.3). We therefore characterize our sample S without superconductivity in the grains and destroyed superconductivity by applying a magnetic field higher than the critical one.

In the high field regime ($B \gg B_c$) superconductivity is destroyed and the disordered system turns into a granular metal with weak coupling (see section 2.3). Transport in this regime is mediated by electron hopping between the grains. Due to weak coupling between the grains the system can be described by a Mott insulator, where the Mott gap is determined by the Coulomb energy E_C and the conductivity follows the activated form of Eq. 2.107. However, the Mott gap may be significantly reduced for finite tunneling conductances [112].
To study the low temperature behaviour of a granular metal in absence of superconductivity sample S was exposed to the maximum perpendicular magnetic field possible, 7T.

We can estimate an upper limit for the critical magnetic field needed to destroy superconductivity by assuming that the energy to break up the Cooper pairs is provided by the magnetic field only. The effect of pair breaking is a consequence of the effect of the external magnetic field on the electronic spins [18]. In the limit of neglected spin-orbit scattering the pair breaking energy equals the energy of the magnetic field, leading to $\mu_B B = \Delta_0$. However, as Clogston [119] and Chandrasekhar [120] pointed out, there will be a first-order transition to the normal conducting state when $\mu_B B = \frac{\Delta_0}{\sqrt{2}}$. This limits the upper critical field with negligible spin-orbit scattering to the Pauli limited field B_P given by

$$B_P = \frac{\Delta_0}{\sqrt{2}\mu_B} \tag{4.2}$$

Then for a critical temperature $T_c \approx 2.3$K and $\Delta_0 = 1.76 k_B T_{c0}$ we get a $\Delta_0 \approx 350\mu$eV. Using Eq. 4.2 the upper critical field is limited to $B_P \sim 4.23$T.

Activated Behaviour and Low Temperature Saturation

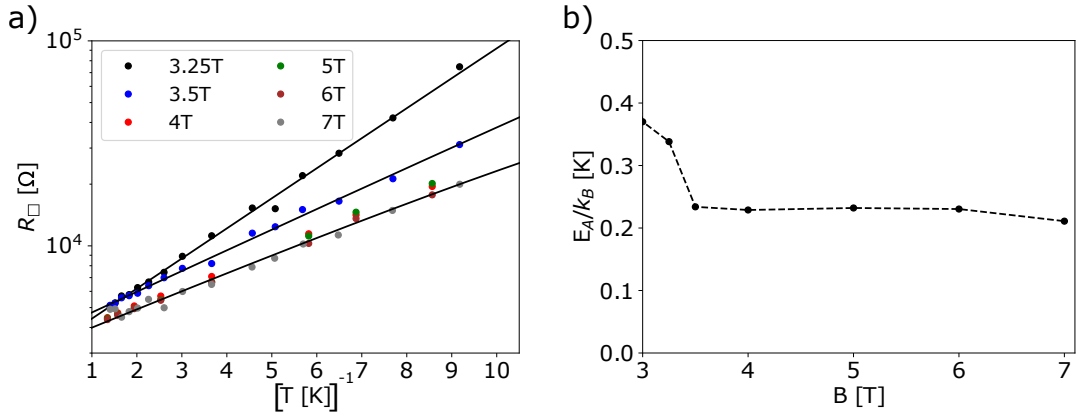

Figure 4.14.: Sample S: a) Arrhenius plot of the extracted zero bias resistances for magnetic fields $B > 3$T. The black lines correspond to fits by $R(T) = R_0 \exp\left(\frac{E_A}{k_B T}\right)$. For clarity only fits to $B = 3.25$T, $B = 3.5$T and $B = 7$T are shown. The extracted activation energies are plotted in b) versus the corresponding magnetic fields. While for $B < 3.5$T E_A shows an increase with decreasing magnetic field, it is independent for higher fields. The prefactor R_0 decreases for decreasing magnetic field below 3.5T. For $B > 3.5$T it is approximately constant around $R_0 \approx 3.25$kΩ and only slightly higher than the normal state resistance of $R_N = 3$kΩ. (see Fig. 5.15 for full $R_0(B)$)

Fig. 4.14b) shows the Arrhenius behaviour for magnetic fields $B > 3$T. In a broad temperature range 100mK $< T <$ 700mK the resistance follows a linear dependence in the Arrhenius graph, indicating an activated behaviour. The curves for 3.25T and 3.5T show a magnetic field dependence of the linear slope. This regime will be examined later and as for now it just means that for $B < 3.5$T the activation energy is given by $E_A(B)$. For magnetic fields $B > 3.5$T the slope is independent of magnetic field, which indicates that the superconducting gap has already vanished. In other words, $B = 7$T fulfills the condition $B \gg B_c$ and the high field Fermi insulator state may be examined.
The activation energy extracted from simple linear fits by Eq. 2.104 to the slopes in the Arrhenius graph is $E_A/k_B = 0.21$K +/- 0.01K for 3.5T $< B \leq 7$T.

In Fig. 4.14 we presented magnetic field dependence of the Arrhenius curves down to 100mK and saw an activated behaviour. We will now turn to the lowest temperatures. Therefore we remeasured the 7T dependence down to 15mK.
The IV curves of that measurement can be seen in Fig. 4.15a), while the Arrhenius behavior is shown in Fig. 4.15b). A linear increase of resistance for decreasing temperature is followed by a saturation at the lowest temperatures $T <$ 80mK.
A similar temperature dependence, a high temperature activated behaviour followed by a low temperature saturation, has been seen in Josephson junction arrays, where the

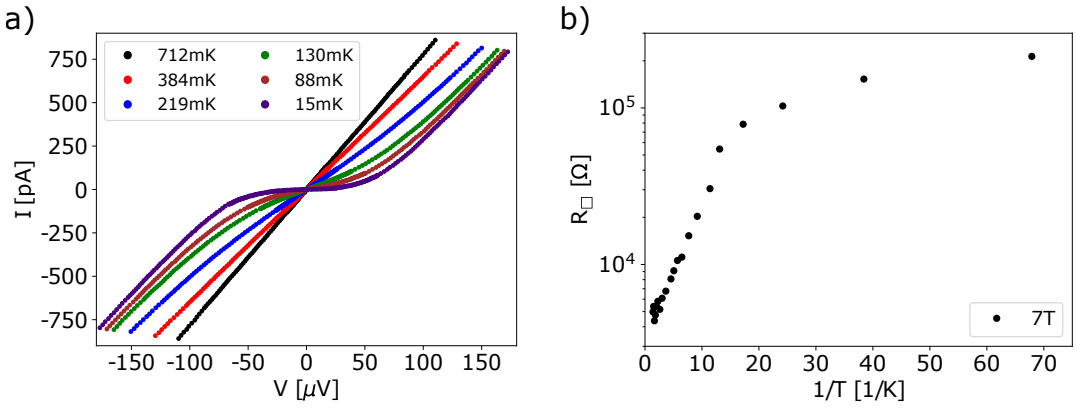

Figure 4.15.: Sample S at 7T: a) IVs of 6 selected temperatures ranging between 15mK and 712mK. At the lowest temperatures the IVs show a Coulomb blockade with a suppression of current flow. The extracted zero bias resistances are plotted in b) in an Arrhenius graph. At high temperatures the resistances fall onto a straight line for activated behaviour. However, below 80mK the resistance values start to saturate.

islands were in the normal conducting state. Superconductivity was destroyed in the same manner as in our case, i.e. by applying magnetic field above the critical B_c [80]. To explain their findings Ref.[80], it was suggested that there are two effects for charge transport. The first deals with the activated temperature dependence of the resistance and the second with the low temperature saturation.

The activated behaviour is attributed to the existence of charge solitons [188]. Adding a single charge to a (normal conducting) electrode in an electrically neutral array creates an electrostatical potential distribution, which is called soliton. Removing a single charge creates the counterpart, an antisoliton.
By tunneling events, the solitons can move freely in the array.
The fundamental, thermally activated, excitation is a soliton/antisoliton pair. In case, the charge is a single electron it is called single electron soliton (SES), in case it is a Cooper pair it is called Cooper pair soliton (CPS). In the case of superconducting electrodes both, SES and CPS can exist [80].

In this section we will only focus on SES, as the grains in our granular aluminum sample have been turned normal conducting by applying a magnetic field $B > B_c$.
At the lowest temperatures the resistance does not follow the activated form, but saturates. This is explained by taking quantum fluctuations into account. Ref. [80] investigated a series of JJAs with different normal state sheet resistances R_N. They found that the saturation resistance, which they call R_{QF} is critically dependent on the normal state resistance of the individual junctions in the array.

For arrays with $R_N \ll R_Q$ with normal conducting electrodes one does not expect insulating behaviour, because the energy uncertainty (lifetime uncertainty) of the state of defined charge, given by $\delta E \approx \hbar/R_N C$, is much larger than E_C [80, 189]. That means that quantum fluctuations of charge create a finite conductance in the array down to the lowest temperatures.
In the other extreme case $R_N \gg R_Q$ quantum fluctuations are negligible and the array behaves insulating due to Coulomb blockade [190]. The authors of Ref. [80] describe the crossover of the two extreme cases, taking into account both effects, i.e. thermal activation of single electron solitons and the low temperature saturation due to quantum fluctuations of charge. The empirical formula in Ref. [80] reads

$$G_0 = \frac{1}{R_0} = \left(\frac{1}{R_N} - \frac{1}{R_{QF}}\right) \exp\left(\frac{-E_A}{k_B T}\right) + \frac{1}{R_{QF}} \tag{4.3}$$

and is an adaption of Eq. 2.104 with R_{QF} as the temperature independent fluctuation resistance.
Our sample S, which is evaluated in this section, has a normal state sheet resistance of $R_N = 3\text{k}\Omega \approx R_Q$. That indicates that we are in the crossover regime and we therefore apply Eq. 4.3 to our $B = 7\text{T}$ data. The fit to the data is shown in Fig. 4.16.

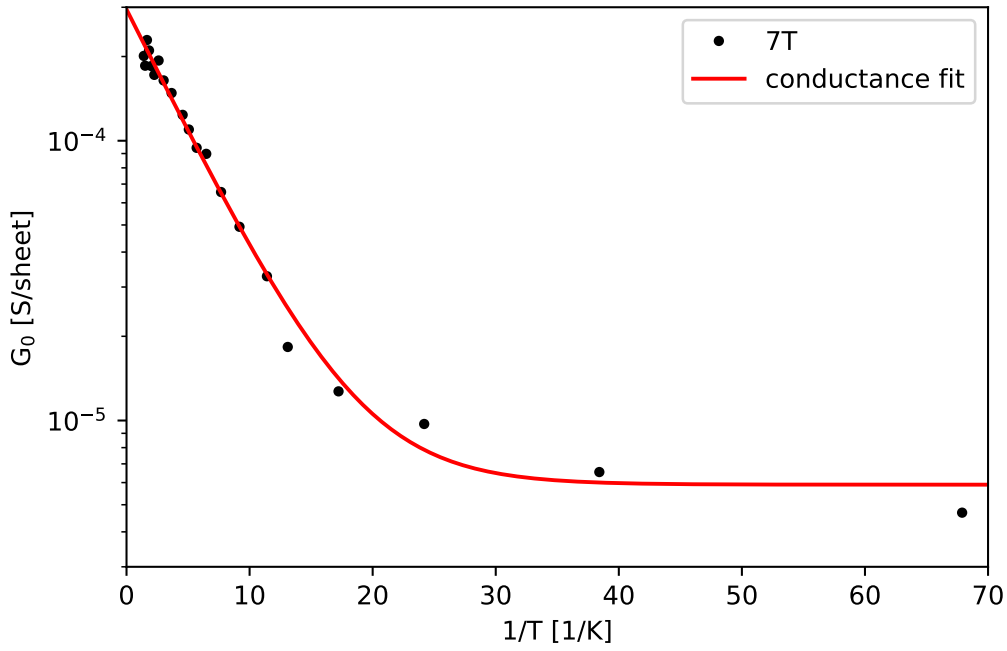

Figure 4.16.: Sheet conductance at 7T fitted to the formula given in Eq. 4.3. The fit nicely reproduces the activated behaviour at higher temperatures and takes the low temperature saturation into account.

The resulting activation energy of $E_A/k_B = 0.21K$ is in very good agreement with the value extracted by the linear fits in Fig. 4.14. To fit the data, a normal state sheet resistance of $R_N = 3.25k\Omega$ was used. That value only slightly exceeds the measured $R_N(T = 4K) = 3k\Omega$. The fit in addition gives a value of $R_{QF} = 152k\Omega$ per sheet.
Ref. [80] measured three JJAs with R_N ranging between $3.98k\Omega$ and $4.49k\Omega$, which is comparable to $R_N = 3k\Omega$ of our sample S. For these samples, with the electrodes in the normal conducting state, they extracted activation energies $E_{A,N} \sim 0.2K$-$0.266K$ in good agreement with our $E_{A,N} = 0.21K$.
For periodic JJAs with $R_N \gg R_Q$ [99], the authors found a relation between the activation energy E_A and the charging energy of a single junction E_C, $E_A = 1/4E_C$. That was confirmed by Ref. [80]. However, for JJAs with a $R_N \approx R_Q$ Ref. [80] found deviations from that ratio. The latter increases up to values of 0.7. In our sample the number of junctions is unknown and we cannot deduce the charging energy by an independent way. The ratio between the activation energy and the charging energy in our sample remains an open question.
However, the measured activation energies fall well into the lower part of the expected region for the single electron charging energies in the normal conducting state, $\approx$1K, as calculated in Fig. 4.13.
While in the three arrays of Ref. [80] the resistance in the normal state increased only slightly from its $R_N \sim 4k\Omega$ to $R_{QF} \sim 6$-$7k\Omega$, we find a higher increase by a factor $\sim$50 from $R_N = 3k\Omega$ to $R_{QF} = 152k\Omega$.

Threshold Voltage

In Fig. 4.15a) we have already shown the evolution of the Coulomb blockade with temperature. We now turn to the lowest temperature measured, $T = 15\text{mK}$. That curve is shown in Fig. 4.17. For clarification only the positive bias voltages of the IV curve are presented. The threshold voltage $V_{\text{T,N}}$ indicates the onset for the injection of SES.

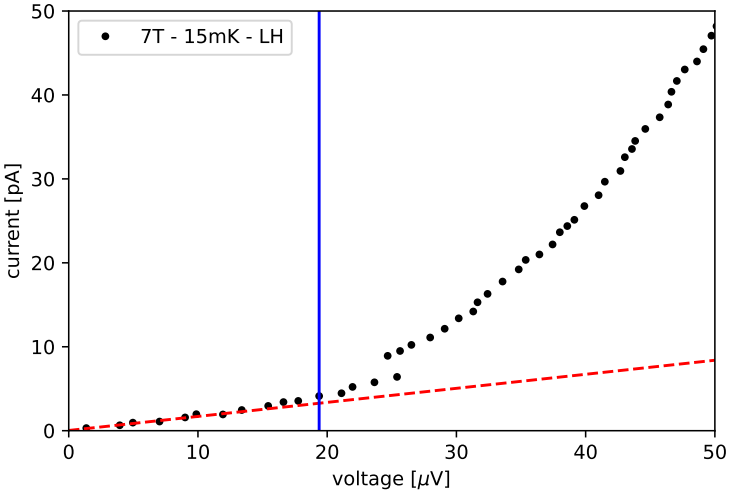

Figure 4.17.: Positive current/voltage branch of the IV measured at $B = 7\text{T}$ and $T = 15\text{mK}$. Onset of deviation from linear dependence at $V_{\text{T,N}}$ marked by the blue vertical line.

Similar to findings in JJAs with normal conducting electrodes by [80], we see a washed out Coulomb blockade. That is attributed to quantum fluctuations. Therefore, there is no sharp threshold voltage.
The red line is an extended linear fit around zero bias and the blue line indicates the deviation of linear behaviour. The deduced threshold voltage, using this method, in the normal state is $V_{\text{T,N}} = 19\mu\text{V}$. The three arrays of [80] with a comparable R_{N} as our sample S did show a superconducting behaviour, i.e. a decreasing resistance with decreasing temperature, but no threshold voltage in the state with normal conducting electrodes was considered. They mention an array with very high $R_{\text{N}} = 151\ \text{k}\Omega$, which did show a threshold voltage of $V_{\text{T,N}} = 250\mu\text{V}$. A theoretical calculated value for that array is $V_{\text{T,N,th}} = 2.3\text{mV}$. The authors argue that the deviation by a factor $\sim$10 is consistent with quantum fluctuations, which lower the threshold for the injection of SES.
Our small value of $V_{\text{T,N}} = 19\mu\text{V}$ can be attributed to the suppresion of the threshold voltage due to quantum fluctuations, too. This is in agreement with the washed out Coulomb blockade as seen in Fig. 4.15.

By comparing our measurements on granular aluminum to periodic JJAs, where the

grains and the electrodes have been turned normal conducting by a high magnetic field $B > B_c$, we find strong similarities. That includes an activated behaviour at temperatures $80\text{mK} < T < 700\text{mK}$ and a low temperature saturation below 80mK. A washed out Coulomb blockade without a sharp threshold voltage $V_{T,N}$ agrees with the explanation of quantum fluctuations of charge to be responsible for the low temperature saturation [80].

5. Measurement Results

Early studies on ultra-thin films revealed a morphological difference for films grown on Al_2O_3/glass-substrates [10, 61, 62, 191] and substrates with a predeposited amorphous germanium underlayer [63, 192]. The first revealed a granular nature associated with a disorder on length scales substantially larger than atomic level, but still smaller than sample size. The second were homogenously disordered and believed to have disorder in the atomic order. The difference has as well been noted in electron-tunneling studies by [162, 193]. For granular films the density of states does only weakly depend on R_N, but for homogenously disordered films the effective density of states decreases monotonically with increasing R_N.
The low temperature behaviour drastically differs for the two categories. Homogenous disordered samples either show a sharp transition to a zero resistive state or an insulating behaviour with an increasing resistance down to the lowest temperatures. The transition temperature T_c has been found to be well defined by the normal state sheet resistance, which in turn is controlled by the film thickness. The critical temperature monotonically decreases with increasing R_N. The resistance separating the superconducting from the insulating behaviour has been found to be material dependent.[192]
The ultra-thin granular films revealed a much more complex behaviour. The first noteable property is that the critical temperature T_c is independent on thickness or R_N. Secondly, the resistance separating superconducting and insulating behaviour seems to be independent on material. Global phase coherence and the resulting zero resistive state has only been found for resistance values of R_N smaller, but close to $R_Q = 6.45\text{k}\Omega$. In addition, granular films starting with insulating behaviour for $R_N \gg R_Q$ exhibit a reentrant behaviour, i.e. a local minimum in the $R(T)$ curve close, but below the critical temperature T_c, as R_N approaches R_Q. Further decreasing R_N leads to a low temperature flattening out of the local minimum. As the resistance did not vanish, this was attributed to a metallic behaviour. Finally, at values $R_N < R_Q$ global phase coherence is achieved and the resistance drops to an unmeasureable small value.[10]
A comparison between homogenous disordered Pb films and granular Pb films has been shown in Fig. 2.7. The evolution of the $R(T)$ curves by varying the thickness reveals a thickness/normal state resistance dependence of the critical temperature T_c for homogenous disordered films, while for granular films T_C is independent on thickness/normal state sheet resistance. The same behaviour has been found for other material systems including aluminum [10, 192]. The evolution of the $R(T)$s for ultra-thin granular aluminum can be seen in Fig. 2.17a). The transition temperature T_c does not depend on thickness/normal state sheet resistance.

However, for both classes the separation resistance was in the vicinity or close to the quantum resistance R_Q. Later studies on artificical Josephson junctions arrays [81] and homogenously disordered films, e.g. TiN [69, 83], showed that a SIT could well be induced by a magnetic field for $R_N \leq R_Q$. For details see section 2.2.3.

As introduced in section 2.2.3 thin films with a sheet resistance R_N close to the quantum resistance $R_Q = 6.45\text{k}\Omega$ may undergo a transition from a superconducting state to insulating behaviour (d-SIT). In that critical region and $R_N < R_Q$ a transition from superconducting to insulating can be induced by an external magnetic field as well (B-SIT).

After the studies on ultra-thin granular films by [10, 61, 62, 191] the focus shifted towards ultra-thin homogenous films [63, 192]. The development in microfabrication allowed to process artificial Josephson junction arrays, where the competing effects of Josephson coupling, charging and temperature could be studied in a defined and known geometry [80, 81]. Therefore there are only few explicit studies on the magnetic field dependence of ultra-thin granular films. In recent years granular systems received interest due to findings and theoretical explanations of an anomalous metallic state between the superconducting and the insulating phase of the SIT in two dimensions.

The main motivation for this thesis is to get a better understanding of the transport properties of ultra-thin superconducting granular aluminum films as literature lacks of a proper study of the impact of a magnetic field at low temperatures. Open questions are connected to a possible magnetic field induced superconductor to insulator transition, the nature of the insulating state and the mechanism driving the transition.

The sheet resistance of the two presented samples in this thesis is in the critical region $R_N \approx R_Q$ (see section 4). The first section 5.1 discusses the temperature dependence of the zero bias resistance in absence of magnetic field. After that we apply a perpendicular magnetic field to both samples and evaluate the influence on the $R(T)$ curves (see section 5.2). Here the temperature was swept and the magnetic field was fixed at certain values. For each magnetic field IV curves have been measured for a set of temperatures. We used the same approach for a set of parallel magnetic fields to see differences to the perpendicular orientation. In addition, to increase the number of magnetic field values in the evaluation for the $R(B)$, in section 5.3 temperatures have been fixed and the magnetic field was swept continuously.
In sections 5.1, 5.2 and 5.3 we will see a low temperature saturation of resistance in the vicinity of the magnetic field induced SIT. The results will be discussed in section 5.4.
Up to now we have only focused the zero bias resistance. In section 5.5 the differential resistance at bias voltages exceeding the dielectric breakdown will be evaluated and discussed.

5.1. Temperature Dependence of the Zero Bias Resistance R(T) across the Disorder-Induced SIT (B = 0T)

As shown in the previous pages at the start of chapter 5, ultra-thin granular films exhibit a very rich temperature dependence. In this section we will take a look at the evolution of the resistance of our two samples with temperature and we will for now focus on the zero magnetic field case. The sheet resistance has been extracted in the linear zero bias limit of current-voltage characteristics. The IV characteristics are measured across the complete sample length of N = 28 sheets. In the following the differential resistance corresponding to the slope of the IVs has been divided by a factor 28 to extract the sheet resistance $R_\square$. The shape of the IVs does as well drastically change for different temperature regimes and will be as well discussed.

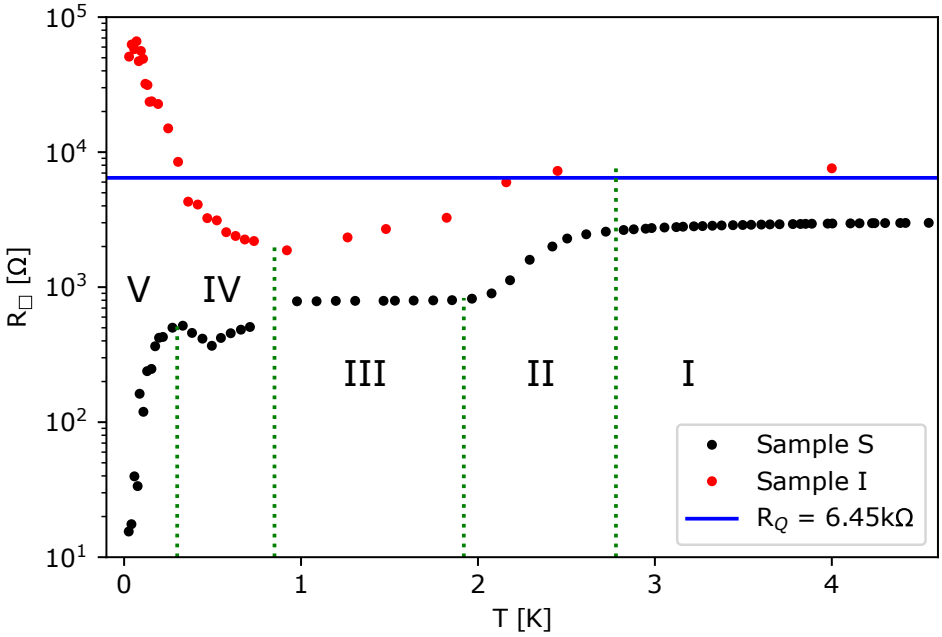

Figure 5.1.: SIT induced by disorder, where the sheet resistance at 4K is taken as a measure of disorder. The two presented samples cross the critical region around R_Q and show a completely different low temperature behaviour. Sample I has a $R_N(4K) = 7.8k\Omega$ and sample S $R_N(4K) = 3k\Omega$. Green dotted vertical lines indicate different temperature regimes labeled from I to V. The plateaus of region III and IV of sample S correspond to $R_\square \approx 750k\Omega$ and $R_\square \approx 500k\Omega$, respectively.

As shown in chapter 4, the two samples differ by a few kΩ per sheet at room temperature. The sheet resistances of both samples show an increase by cooling down from room temperature to 4K. Sample S starts at approx. 1.8kΩ and ends at 4K with a resistance of approx. 3kΩ. Sample I increases from approx. 5.4kΩ to approx. 7.8kΩ, a value slightly

above the quantum critical resistance. The resistance ratios comparing 4K and room temperature resistances are 1.66 and 1.44, respectively.

The $R(T)$ curves of both samples are presented in Fig. 5.1. As expected for granular films, both curves do not show a simple curvature, but are rich in detail. Similar to what has been explained in chapter 5, by decreasing R_N towards R_Q a pure insulating behaviour vanishes. Sample I (red) has a R_N only slightly exceeding R_Q at $T = 4$K. R_Q is indicated by the blue horizontal line. Below $T \sim$2K-2.3K the resistance decreases and forms a local minimum at $T \sim$1K. By further decreasing temperature the resistance starts to increase again.
Sample S (black) has a sheet resistance slightly below R_Q at 4K. Its $R(T)$ is even more complex. At approximately the same temperature as sample I the resistance starts to drop. Instead of a decrease to a zero resistance state, the resistance flattens out down to ∼1K. Further decreasing the temperature leads to a lower level of resistance, which has the shape of a broadened V. It is only at a temperature below ∼250mK, where the resistance finally drops down to zero, indicating the existance of global phase coherence.

Similar dependencies have been seen by Ref. [10, 61] in ultra-thin granular films of tin, lead, gallium and aluminum. It is important to note, that their lowest temperature was $T \sim 0.6$K, while in our measurements the lowest temperatures were either $T = 15$mK (sample S) or $T = 28$mK (sample I).
The reentrant behaviour and the plateaus in the $R(T)$ curves are connected to the three important energy scales E_J (Josephson coupling), E_C (charging/Coulomb energy) and k_BT (thermal energy). The first tries to align the phases of the wave functions on neighbouring grains for global phase coherence, while the second tries to localize charge carries onto the island. The latter corresponds to phase fluctuations of the order parameter in the individual islands. The third energy is given by the temperature. On the one hand E_J is directly coupled to the temperature dependent BCS energy gap $\Delta(T)$ and on the other hand thermally excited charge carriers may effectively limit the resistivity due to a finite conductivity when exceeding the charging energy.
The criterion for vanishing of phase fluctuations in a single junction [194] is given by

$$E_J > E_C + k_BT/2 \tag{5.1}$$

where $E_C = e^2/2C$ and E_J is given by $E_J = \frac{R_Q}{R_N}\frac{\Delta(T)}{2}\tanh\left(\Delta(T)/2k_BT\right)$, the standard expression for an ideal SIS junction as derived by Ambegaokar and Baratoff (see section 2.1.3). For $T = 0$ this reduces to the well known condition by Abeles [8]

$$E_J > E_C \tag{5.2}$$

with $E_{J,0} = \frac{R_Q}{R_N}\frac{\Delta_0}{2}$.
As has been shown a single Josephson junction can be modelled in the RCSJ-model (see section 2.1.3). The Hamiltonian for a single junction reads

$$H = \frac{1}{2}[(2e)^2/C]N^2 + E_J(1 - \cos(\theta)) \tag{5.3}$$

In this tilted-washboard potential small zero point fluctuations in the bottom of a potential well exist with energy

$$\hbar\omega_{\mathrm{p}} = (8E_{\mathrm{C}}E_{\mathrm{J}})^{(1/2)} \tag{5.4}$$

Particle number N and phase θ are conjugate variables, which implies an uncertainty relation of the form $\delta N\delta\theta > 1/2$. Large charging energies prohibit strong fluctuations of δN and lead to strong phase fluctuations $\delta\theta$. These strong fluctuations of phase destroy phase coherence up to the point, where condition Eq. 5.2 is fullfilled.[10]

Refs. [10, 61] explain the complex $R(T)$ curves measured on ultra-thin granular films with the existence of temperature dependent percolation paths forming from the tunneling junctions between single grains or clusters of grains. They argue that in an ordered square array of identical junctions the overall resistance ($R_{\Box}$) is given by the resistance of a single junction R_{single}. However, in ultra-thin granular films the individual junction resistances as well as the capacitances may drastically vary and result in a distribution of both. This is given by the randomness of the grain sizes, cluster sizes and grain separation distances.
Therefore, not all junctions may be phase-coupled at the same temperature, even if all grains turn superconducting at the same temperature T_{c}. Below the critical temperature there may exist clusters of phase-bonded grains. Any non-superconductive, i.e. non-Josephson-like, connection between such clusters along the current path will then dominate the measured resistance at $T < T_{\mathrm{c}}$. Global phase coherence, i.e. a zero resistive state, is approached once the percolation path spans across the total sample and effectively short-circuits the residual non-superconducting connections.
Early models by Refs. [135, 194, 195] could reproduce transitions from insulating behaviour to reentrant to superconducting behaviour by making the percolation fraction p_{J} depend on temperature and on tunnel distance. A more recent model by [92] predicts an inverse Arrhenius law $R \sim \exp(T/T_0)$ (see Section 2.2.3). This dependence has been found in a series of granular films, but does not explain our findings on ultra-thin films. However, low temperature saturation of resistance, reentrant behaviour and striking similarities to the data on ultra-thin granular films by [10, 61] have been found in microfabricated Josephson junction arrays with small aluminum tunnel junctions (C small, E_{C} large) by [196, 197]. A possible existence of percolation paths inside a random array might narrow down the distribution of size and separation distance of the grains participating in the charge transport. This effectively better ordered structure may then be modelled by periodic JJAs [10, 192].

Let us now take a closer look at the two $R(T)$ curves presented in Fig. 5.1 and separate them into different temperature regions, starting with sample S.

As seen in Fig. 5.1 in the temperature **region I ($T > 2.8$K)** the sheet resistances of both samples are in the vicinity of the quantum resistance of Cooper pairs R_{Q} indicated by the blue horizontal line.

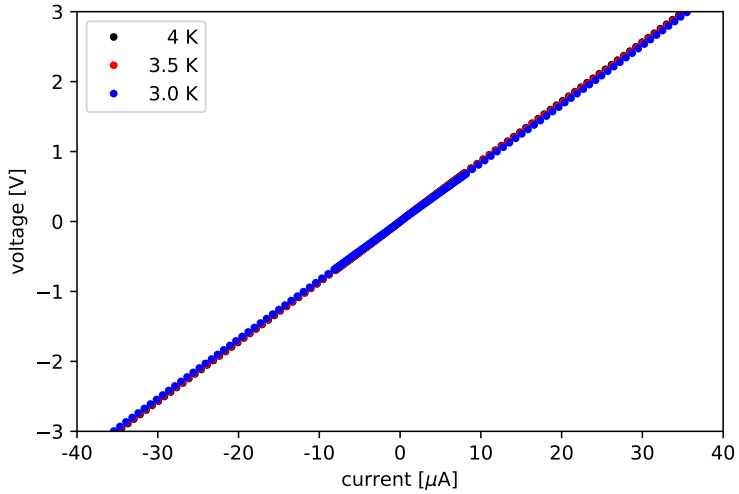

Figure 5.2.: Region I: IV characteristics for three selected temperatures above 2.5K. The 4K (black), 3.5K (red) and 3K (blue) curves are linear for all bias currents. The slope slightly decreases with decreasing temperature. This corresponds to the gradual decrease of the resistance for $T > 2.8$K in Fig. 5.1.

The IVs in this temperature region are linear over the total bias range, $I\pm$ 40 μA and $V\pm$ 3V (see Fig. 5.2). This indicates Ohmic behaviour, which is expected above the critical temperature. The slopes of the resistances slighty decrease with decreasing temperature, indicating a weak temperature dependence of the resistance as superconducting fluctuations (see section 2.2.2) increase the conductivity above T_{c}.

In **region II ($1.9\mathrm{K} < T < 2.8\mathrm{K}$)** both samples show a sharper decrease of resistance with decreasing temperature (compared to the decrease at higher temperature in region I). This can be associated with the onset of superconductivity on the grains. The corresponding critical temperature is $T_{\mathrm{c}} \sim 2.3$K, determined by the half-resistance criterion, i.e. the resistance $R_{\square}$ dropped to half of the normal state resistance $R_{\mathrm{N}}(4\mathrm{K})/2$. We find the onset of superconductivity in our two samples at approximately the same temperature. The independence of T_{c} on R_{N} has been linked to granular thin films by Ref. [10].
The IVs in Fig. 5.3 reveal a regime for small bias currents with a linear slope that decreases with decreasing temperature. That is directly linked with the decrease of the resistance with decreasing temperature in that temperature region in Fig. 5.1. At a fixed temperature, starting from zero current, in Fig. 5.3 an increasing bias current leads to an increase in the slope at a critical current $I_{\mathrm{c},2}$. This increase continuously goes over

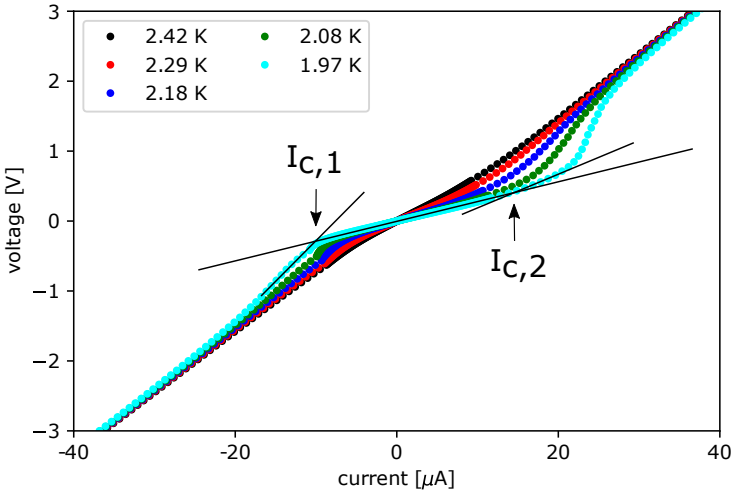

Figure 5.3.: Region II: IV characteristics for five selected temperatures between $T = 1.9$K and $T = 2.5$K. The linear resistance around zero bias decreases with decreasing temperature and smoothly connects to the normal state resistance at high bias currents. The deviation from linear resistance is denoted as $I_{c,1}$ for negative bias and $I_{c,2}$ for positive bias currents. This is shown examplarily for $T = 1.97$K. The black lines are a guide to the eye. With decreasing temperature both $|I_{c,1}|$ and $|I_{c,2}|$ increase.

into regime at high currents ($I \gg 30\mu$ A), where the differential resistance approaches the normal state sheet resistance $R_N(4K)$. The differential resistance in the high bias regime of the IVs is the same as the zero bias resistance in the temperature region I ($T > T_c$). That is a strong indicator for the existance of local superconductivity on the grains, which can be destroyed by either temperature or bias current.
For negative bias currents we find a critical current $|I_{c,1}|$ smaller than $|I_{c,2}|$ for positive bias currents. This is attributed to the sweep direction of the measurement. The curves in Fig. 5.3 have been measured from negative to positive bias currents. The suspicion, that the sweep direction influences the critical current will be verified in the next temperature region.

In **region III (0.85K $< T <$ 1.9K)**, i.e. below T_c, local superconductivity is present on the grains. However, the resistance saturates at a temperature independent plateau of $R_N/3$ as seen in Fig. 5.1. That indicates that phase fluctuations in some of the junctions lead to a reduced (with respect to R_N) but finite resistance. Using the arguments of Ref. [10], due to the randomness of inhomogenous granular films there may be percolation paths or clusters of superconducting grains with phase coherence. However, those can be separated by non-superconducting junctions. That junctions without phase coherence dominate the total measured resistance as they are in series with junctions having zero resistance (aligned phases).

The origin of the temperature independence in the broad range of $T = 1\text{K}$ up to $T = 1.9\text{K}$ seen in Fig. 5.1 is not fully understood. To create such a plateau the effects of $E_\text{J}(T)$ and $E_\text{C} + k_\text{B}T$ have to cancel out for a certain range of temperature. This means that for decreasing temperature the increasing effect of $E_\text{J}(T)$ is equal to the decreasing effects of $E_C + k_\text{B}T$ and therefore the sum of the effects is constant over that temperature interval.

Different effects may compete due to a broad distribution of grain sizes and probably grain separations. Charging effects given by E_C and tunneling effects of Cooper pairs for S-I-S junctions or S-N-S junctions, given by E_J and temperature dependent quasi-particle tunneling. While the Josephson effect tries to align the phases, the charging effect tries to disalign the phases of the superconducting wavefunctions over the grains (see sections 2.1.3 and 2.2.4).

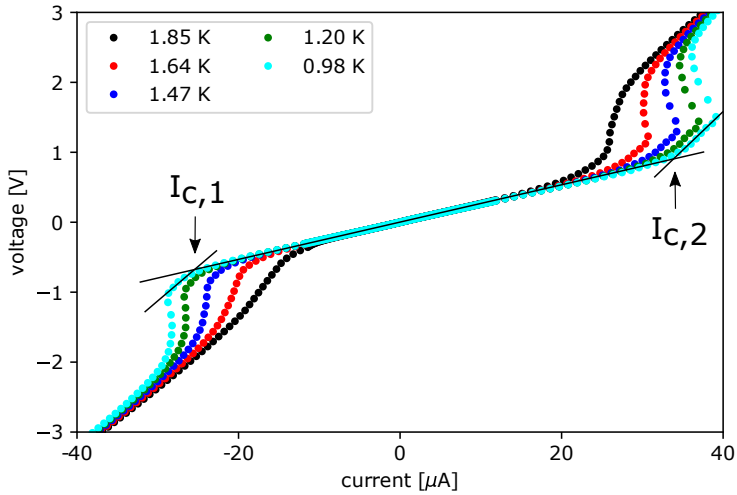

Figure 5.4.: Region III: IV characteristics for five selected temperatures between $T = 0.85\text{K}$ and $T = 1.9\text{K}$. The linear resistance around zero bias is temperature independent. The absolut values of the critical currents $I_{\text{c},1}$ and $I_{\text{c},2}$ marking the deviation from linear resistance still increases with decreasing temperature. This is examplarily shown for the curve $T = 0.98\text{K}$. The black lines are guides to the eye.

The slope around zero bias starts to be temperature independent, which results in a saturation of sheet resistance. Nevertheless, the critical currents $|I_{\text{c},1}|$ and $|I_{\text{c},2}|$ continue to increase with decreasing temperature. $|I_{\text{c},2}|$ exceeds $|I_{\text{c},1}|$ at all temperatures. The increase of the critical currents may be connected to an increase of the superconducting energy gap $\Delta(T)$ on the grains.

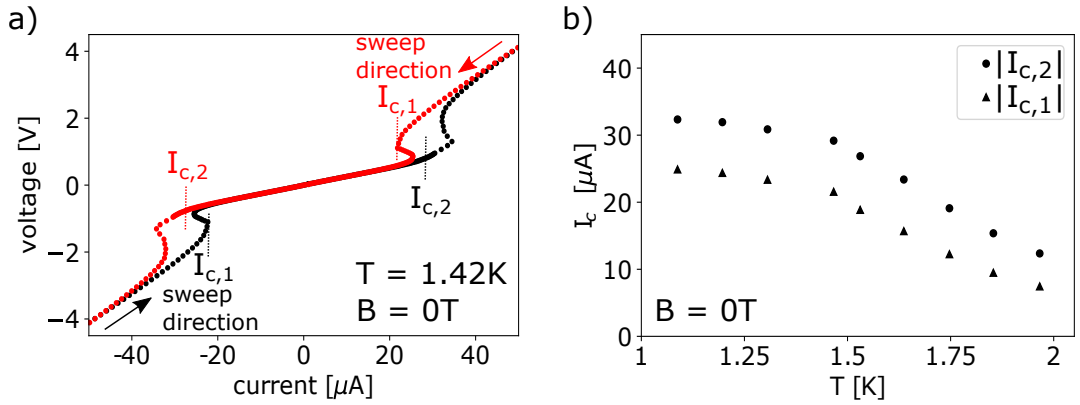

Figure 5.5.: Sample S: a) The sweep direction from negative to positive bias currents (black) and reverse (red) is presented to show symmetry around zero bias. In b) the temperature dependence of the extracted critical currents for the sweep direction from negative to positive currents is presented. For clarity the absolute value $|I_{c,1}|$ is depicted. As has been indicated in Figs. 5.3 and 5.4 the absolute values of the critical currents increase for decreasing temperature, even as the zero bias resistance has already saturated at a temperature $T \sim 1.8$K (see plateau for 1K $< T <$ 1.9K in Fig. 5.1).

We remeasured the IV at $T = 1.42$K for both sweep directions. The curves are presented in Fig. 5.5a). The curves are symmetric around zero. We therefore identify a retrapping current on the negative side and an escaping current for positive side. The retrapping current is associated with the jump from the high voltage branch down to the low voltage branch, while the escaping current is associated with the jump from the low voltage branch to the high voltage branch.

A possible explanation for the hysteresis could be a heating effect. At a fixed temperature $T = 1.42$K we ramp the current from zero to finite values and generate an increasing Joule power $P_1 = R_1 \cdot I^2$ as the finite linear slope around zero bias corresponds to a finite resistance R_1. The Joule power increases the electronic temperature and supresses the critical current. By exceeding the critical current superconductivity on the grains is destroyed and the resistance jumps up to a higher resistance $R_2 = R_N$ (linear slope at high currents).
By ramping down the current we start at the high resistance R_2 and therefore the Joule power $P_2 = R_2 \cdot I^2$ is high, meaning the critical current is even more suppressed. Therefore superconductivity arises at lower currents $I_{c,1}$ compared to currents $I_{c,2}$ destroying the superconductivity.
Another possible explanation for such a hysteresis is the effect of thermal fluctuations in underdamped Josephson junctions. This effect is discussed in section 6.3.3. in the book of Tinkham [18].

In b) the extracted temperature dependence of both critical currents are shown. As all the curves in Figs. 5.2 5.3 and 5.4 were measured from negativ to positive currents, we extracted the negative values of $I_{c,1}$ and plotted the absolute value. The values of both critical currents increase with decreasing temperature starting from 2K and saturate below a temperature of 1.5K. However, the zero bias resistance has already saturated at at temperature $T = 1.9$K.

In **region IV (0.3K $< T <$ 0.85K)** there is an approximate plateau with a resistance smaller than the plateau seen in region III. The average resistance of the plateau is $R_\square \approx 450\Omega$. The existance of that lower resistance plateau may be connected with the approach of percolation paths across the granular sample. By decreasing the temperature from region III to region IV two or more such percolation paths might get connected as a non-superconducting junction connecting them gets superconducting. This Josephson coupling leads to an overall decrease in resistance. However, as the resistance does not drop to zero, superconducting and normal conducting junctions exist along the current path.
Instead of being a flat plateau, the resistance seems to vary around that average value. It first decreases below the average value and then increases again. This indicates that in that temperature region, Josephson coupling and charging effects compete.

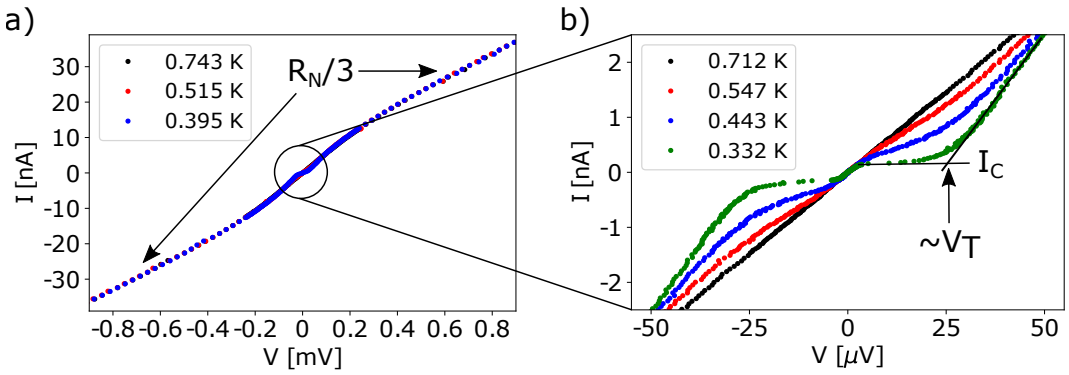

Figure 5.6.: IV characteristics of Sample S at low temperatures. a) Medium bias regime up to bias currents of 40nA and voltages of 1mV. b) Remeasured zero bias regime with higher resolution. Inside the Coulomb blockade for Cooper pairs $V < V_\mathrm{T}$ a zero bias feature arises, which could not be resolved in a). The zero bias feature exhibits critical current behaviour with a finite linear differential conductance. In addition, in that temperature interval the zero bias differential resistance of $R_\square \approx 450\Omega$ is approximately independent on temperature.

The IVs are linear for bias voltages $V > 0.5$mV (see Fig. 5.6a)). The differential resistance is $R_\mathrm{N}/3$ and is temperature independent for 0.4K $< T <$ 0.75K. The same resistance has been found in region III for even higher bias voltages and at higher temperatures $T >$ 1K. However, decreasing the bias voltage leads to a non-linearity in the IV. The curves

bend towards zero current indicating a smaller differential conductance. While for $T >$ 700mK the slope around zero bias is linear, it exhibits a blockade for current flow for lower temperature for $T = 395$mK (blue).

The very low bias regime has been remeasured and is presented in Fig. 5.6b). For T = 712mK (black) the curve is linear with a differential resistance smaller than $R_{\mathrm{N}}/3$. However, by further decreasing the temperature two features arise. First, at bias voltages around $V = 25\mu$V a Coulomb blockade for Cooper pairs is opening up with a thermally smeared out theshold voltage V_{T}. Secondly, instead of a zero current state below V_{T} the current smoothly crosses with a finite value over to a roughly temperature independent differential resistance around zero bias of about 0.5kΩ. The zero bias feature shows a critical current I_{c} below which the slope is linear and above which there is a jump to the threshold voltage of the Coulomb blockade. Both, I_{c} of the zero bias feature and V_{T} of the Coulomb blockade are examplarily shown in Fig. 5.6b) for the green curve $T =$ 332mK.
The plateau in temperature regime IV is directly connected with the temperature independent slope around zero bias.

In **region V ($T < 0.3$K)** Sample S shows another downturn of resistance towards a zero resistive state. The downturn can be interpreted as the onset of global phase coherence as the last non-superconducting junction along a percolation path spanning across the complete length of the sample turns into a Josephson junction. This completely superconducting path effectively shortens all other non-superconductive junctions and leads to a sharp decrease of the measured resistance as seen in Fig. 5.1.

Fig. 5.7a) shows the temperature dependence of the medium scale IVs for zero applied magnetic field at temperatures $T < 300$mK. The differential resistance in the higher bias range is independent of temperature and has the same value as in region IV and III, $R_N/3$.
In the low bias regime Coulomb blockade is coming up for the lowest temperatures. The low bias regime has been remeasured down to a temperature $T = 15$mK (see Fig. 5.7b)).

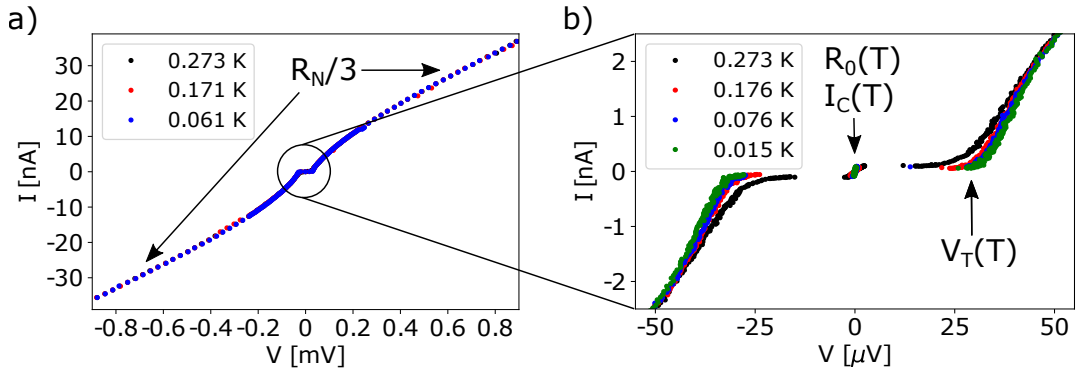

Figure 5.7.: IV characteristics of Sample S in region V. a) Medium bias regime up to bias currents of 40nA and voltages of 1mV. b) Remeasured zero bias regime with higher resolution. With decreasing temperature the Coulomb blockade shows a sharp onset of current flow at V_T. The zero bias feature exhibits a temperature dependent differential resistance $R_0(T)$ as well as a temperature dependent critical current $I_c(T)$. With decreasing temperature the smooth connection from the zero bias feature above I_c to V_T transforms into a discontinuous jump at the lowest temperatures.

Similar IV characteristics have been seen in Josephson junction arrays, including linear behaviour in the high bias regime, a threshold voltage $V_{T,S}$ connected to a Coulomb blockade and a supercurrent feature around zero bias. The role of vortices and charges in Josephson junction arrays as well as their duality has been discussed in section 2.2.4.
The large scale IVs for a superconducting array of Ref. [121] and an insulating array of Ref. [80] are shown in Fig. 5.8a) and b). In the high voltage regime IVs are linear with a resistance R_N for a single junction.
By decreasing the bias voltage for the superconducting array with $R_N < R_Q$ there is a sharp drop of current at a voltage $V_p = N \cdot 2\Delta_0/e$, where N is the number of junctions and Δ_0 is the BCS energy gap at $T = 0$K. The voltage V_p marks the onset of quasiparticle

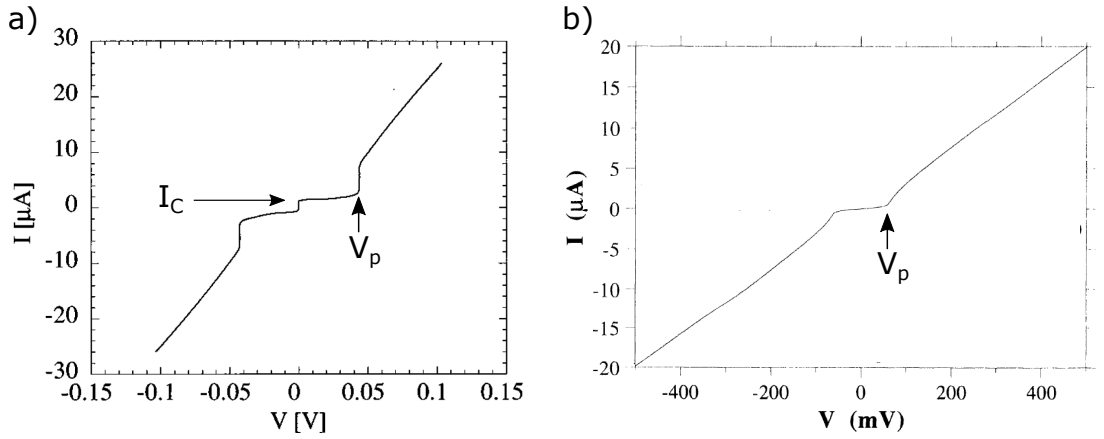

Figure 5.8.: Large scale IVs of a) a superconducting JJA with $R_N = 3.86k\Omega$ at $T = 15mK$ and b) an insulating JJA with $R_N = 24.4k\Omega$ at $T = 25mK$. The high bias parts are similar for superconducting and insulating arrays. It is the low bias part that differs. Figure a) adapted from [121] and b) from [80].

current flow at high bias. Below V_p there is a finite differential resistance, which goes over into critical current I_c around zero bias.
For an insulating array the current drops at V_p as well, but the transition is not as sharp as in a). Below V_p there is no vertical feature (supercurrent) around zero bias as seen for the superconducting array.
The small scale IVs for the arrays shown in Fig. 5.8 drastically differ not only from their large scale IVs (the small scale IVs are the low bias parts of the large scale IVs) but as well as by comparing a superconducting with an insulating array. In Fig. 5.9 we present the low bias part of the same arrays shown in Fig. 5.8. The small scale IV shown in Fig. 5.9a) for a superconducting array consists of both, vortex tunneling and flux flow behaviour. At higher bias there are collective jumps to a resistive state with V_p.

In a superconducting JJA, the Josephson coupling energy between the islands acts as a pinning for vortices. An applied bias current acts as a driving force for vortices as the Magnus force [198] counters the pinning from the Josephson coupling. The ratio of these two forces separates two classes of transport mechanisms [121].
In case the pinning force is larger than the Magnus force, then the vortex motion is due to tunneling of vortices through an energy barrier E_b. This energy barrier is connected to the Josephson energy for a single junction by $E_b = aE_J$. As the barrier may as well be overcome by thermal activation the temperature dependence in this case is thermally activated. As the tunneling is independent on bias current, the slope around zero bias is linear.
There is a depinning current I_d above which the Magnus force is larger than the pinning force. In this regime vortices are accelerated by the Magnus force. The IV characteristic becomes non-linear. For even higher bias currents there is a row by row switching where

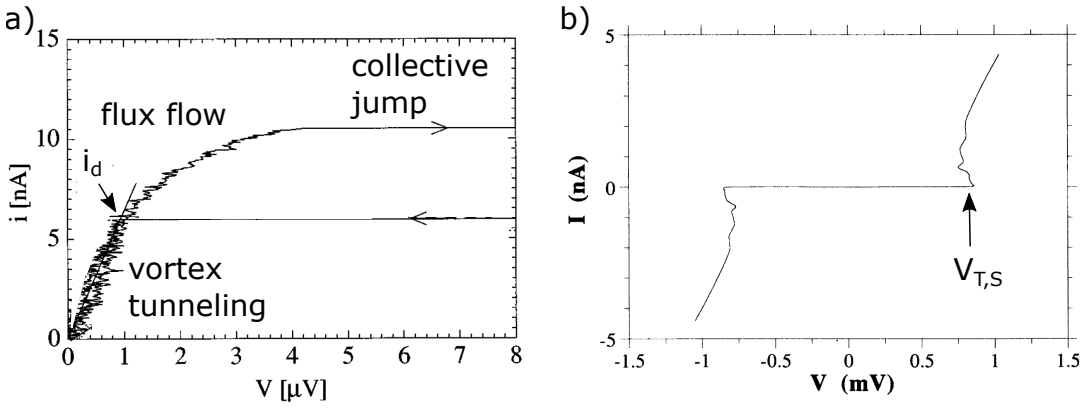

Figure 5.9.: Small scale IVs of the same arrays as presented in Fig. 5.8. a) Superconducting JJA with $R_N = 3.86k\Omega$: plotted is the current per junction $i = I/N$. The array consists of NxN junctions, therefore the measured current corresponds to N times the value of a single junction. i_d denotes the depinning current at which the low bias vortex tunneling regime crosses over to the flux flow regime. At a sufficiently high voltage $\sim 4\mu V$ the array exhibits a collective jump to V_p. The array shows a hysteresis for the different sweep directions, similar to underdamped Josephson junctions. b) Insulating JJA with $R_N = 24.4k\Omega$. A strong Coulomb blockade for Cooper pair solitons is visible. Below $V_{T,S}$ the current flow is mediated by thermally activated CPS only. $V_{T,S}$ marks the onset for the injection of CPS into the array. $V_{T,S}$ is much smaller than V_p associated with the destruction of superconductivity and the switching to quasiparticle dominated current flow. Figure a) adapted from [121] (curves of two other arrays with different R_N have been removed) and b) from [80].

for each jump the voltage increases by $2\Delta_0/e$ [199]. As all junctions, each with $2\Delta_0$, switch to the resistive state the voltage V_p is N times the value of a single junction.

The small scale IV, shown in Fig. 5.9b), for an insulating array is dominated by charge solitons (Cooper pair solitons (CPS) and single electron solitons (SES)), the dual to the vortices in the superconducting arrays (see section 4.3 for details). Below a threshold voltage $V_{T,S}$ the charge transport is mediated by thermally activated CPS following an Arrhenius behaviour. In the small scale IVs $V_{T,S}$ therefore marks the onset of current flow by the injection of CPS by an applied bias voltage. This voltage is significantly smaller than V_p at which the charge transport switches to quasiparticles.

To compare the low bias part of the IVs measured for our sample S with the low bias part of superconducting and insulating JJA Fig. 5.10 presents a further zoom around zero bias of the data shown in Fig. 5.7b).

The black curve measured at $T = 332$mK exhibits a linear slope around zero bias, which is smoothly connected to a higher voltage branch above a current I_c.

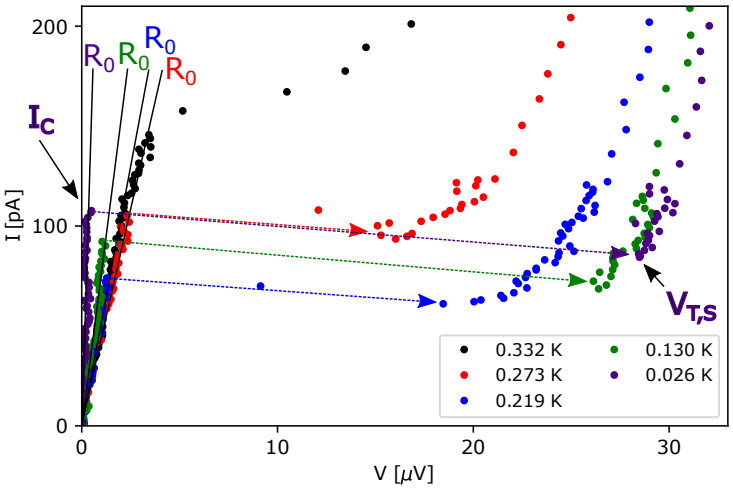

Figure 5.10.: Zoom to low bias regime of Sample S: around zero bias there is a finite linear slope. This is indicated by the black lines. The linear slope corresponds to a zero bias resistance. With decreasing temperature the slope increases and therefore the resistance decreases

By decreasing the temperature the linear slope around zero bias gradually increases for $T < 273$mK, implying that the zero bias resistance R_0 decreases with decreasing temperature. This is indicated by the solid lines labeled with R_0 in Fig. 5.10 and corresponds to the approach of the zero resistive state in region V in Fig. 5.1. The critical current I_c marks the deviation from the linear slope around zero bias. Following the analogy to Ref. [121], then the critical current I_c is the depinning current I_d below which the resistance is mediated by vortex tunneling. However, we do not see the flux flow regime above I_d. We find that by exceeding I_c there is a sharp jump to a high voltage branch with $V_{T,S}$ above which the current rapidly increases. I_c and $V_{T,S}$ have been denoted for $T = 26$mK examplarily in Fig. 5.10. Both, I_c and $V_{T,S}$, are temperature dependent. With decreasing temperature I_c first decreases (black, red, blue curves) and then starts to increase for even lower temperatures (blue, green, purple curves). $V_{T,S}$ increases with decreasing temperature and saturates at $V \sim 30\mu$V at the lowest temperatures. This voltage value is much smaller than $N \cdot \frac{2\Delta_0}{e} = N \cdot \frac{2 \cdot 350\mu V}{e}$, where $\Delta_0 = 350\mu$eV for $T_c = 2.3$K and N being the number of junctions along the current path. The threshold voltage $V_{T,S}$ is actually smaller than the average threshold voltage of a single junction assuming N identical junctions in series. We conclude that this voltage branch is the onset of current flow by Cooper pair solitons, $V_{T,S}$, as seen in insulating JJAs (see Fig. 5.9b)) instead of being the onset of quasiparticle flow at V_p for superconducting JJAs as shown in Fig. 5.8a).
The small scale IVs of Sample S therefore show features seen in superconducting (critical current I_c) and insulating (threshold voltage $V_{T,S}$) JJAs.

Ref. [121] found a hysteretic behaviour with sweeping direction in their IVs of superconducting JJAs as shown in Fig. 5.9. We therefore measured both sweep directions as well, i.e. from low to high bias and from high to low bias. We find a hysteresis and a sharp transition from a low resistance to a high resistance branch, too. Such a hysteresis and sharp transition is known for underdamped single Josephson junctions (see section 2.1.3).

Fig. 5.11a) shows the dependence of the critical current from the sweep direction at T = 15mK. Starting at zero current, we can identify an escaping current $I_{c,0}$ for which the voltage does abruptly jump from the low bias branch to the high bias branch and a retrapping current $I_{c,r}$ for which the voltage drops down abruptly to the low voltage branch when coming from high bias currents. The jumps are not vertical, but show a backshift. This is attributed to the measurement setup and the use of a preresistor.

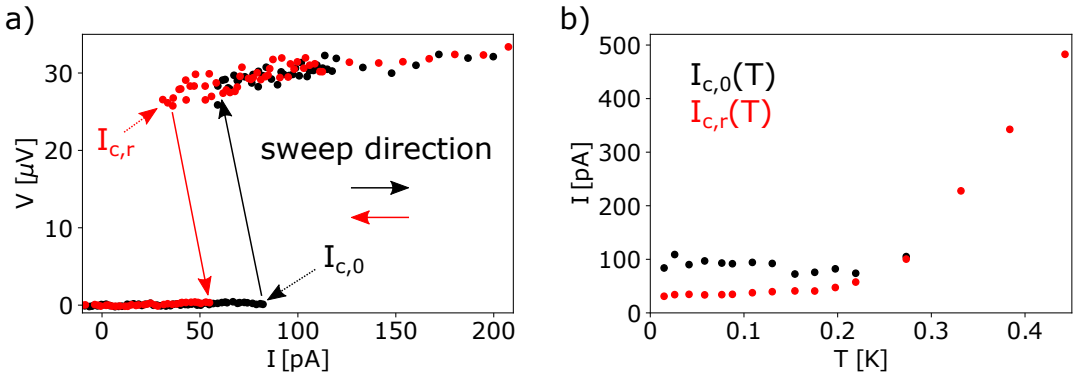

Figure 5.11.: Sample S in zero magnetic field: critical currents at T = 15mK.

The same measurement has been repeated for various temperatures and the resulting critical currents $I_{c,0}(T)$ and $I_{c,r}(T)$ are shown in Fig. 5.11b).
The separation of the critical currents into retrapping and escaping currents is clearly visible below $T \sim$ 200mK. For higher temperatures both critical currents approach each other until they are indistinguishable. This, according to theory section 2.1.3 and Ref. [18], is caused by increased thermal fluctuations at higher temperatures, which lead to a decrease of the escaping current and an increase of the retrapping current. In addition, we see an increase of I_c with increasing temperature. This can be seen in Fig. 5.6b). With increasing temperatures the localized Cooper pairs are delocalized by thermal activation and contribute to the supercurrent.

Sample S having a $R_N < R_Q$, but still $R_N \sim R_Q$, does show features of both, superconducting JJAs and insulating arrays. While around zero bias a supercurrent feature is found (probably connected to vortex motion) it displays a threshold voltage $V_{T,S}$ for the injection of Cooper pair solitons for finite bias voltages. As vortices and charges

do display duality around the SIT and the sample is close to the transition, it seems reasonable that there may be effects of both.

Sample I

Let us now have a look at $R(T)$ of sample I in Fig. 5.1. In contrast to sample S there is no clear distinction of temperature regions. The $T = 4$K resistance R_N is slightly larger than R_Q. As has been mentioned earlier, the onset of superconductivity on the grains is at approximately the same temperature as in sample S, as expected for granular thin films. However, region II, III and IV do not show a clear separation. Sample I exhibits a reentrant behaviour with a local minimum of resistance around $T = 1$K. For $T > 1$K the resistance smoothly connects to the normal state resistance $R_N(4K)$. For $T < 1$K the resistance increases with decreasing temperature. This insulating behaviour indicates that at $T < 1$K charging effects dominate. Instead of a global phase coherent state as seen for sample S, the fluctuations of phase connected with a large charging energy E_C effectively block the supercurrent between the grains and increase the resistance above the normal state value. At the lowest temperature the resistance has increased to a value of ∼60kΩ, which is a factor ∼8 higher than R_N and a factor ∼30 higher than the minimum resistance measured in the local minimum at $T = 1$K.

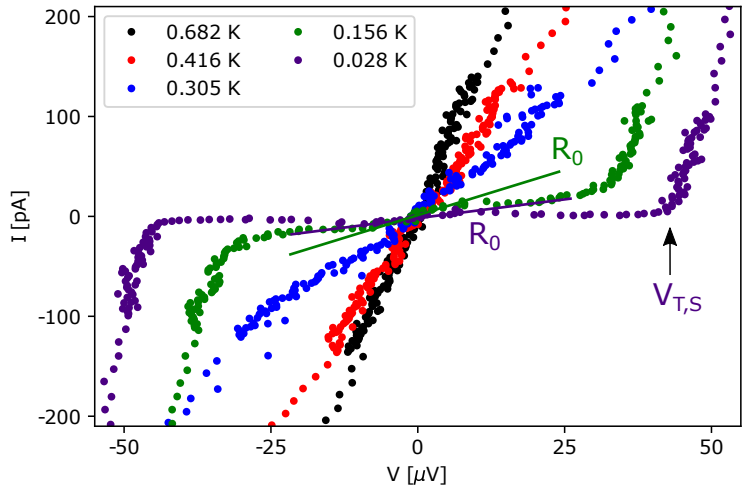

Figure 5.12.: Sample I: At high temperatures $T > 400$mK the slopes around zero bias are linear and decrease with decreasing temperature. That corresponds to an increase of resistance. Below $T = 400$mK the slope continues to decrease, however, at the lowest temperatures a Coulomb blockade with a threshold voltage $V_{T,S}$ opens up. Around zero bias there is a finite slope with R_0 and a much smaller I_c.

Fig. 5.12 shows the temperature dependence of the IV curves of Sample I below $T = 700$mK. Above $T = 400$mK the IVs are linear, but for lower temperatures the IV

characteristics show similarities to sample S. We see a Coulomb blockade opening with decreasing temperature. The threshold voltage increases up to $V_{T,S}$ of approx. 35-40 μV at the lowest temperatures $T \sim 28$mK (see Fig. 5.12). The threshold voltage for the injection of Cooper pair solitons is higher in sample I compared to sample S. In sample I, localization effects are stronger as E_C is larger and the ratio of E_J/E_C is smaller. As sample I lives on the insulating side of the disorder induced SIT ($R_N > R_Q$) for $B = 0$T one expects charging effects to dominate. Larger localization effects lead to larger values of $V_{T,S}$ as more voltage is needed to overcome the energy barrier.
In addition, there is no vertical feature around zero bias at the lowest temperatures. However, we find a feature with linear slope and very small residual critical current. The two green and purple linear lines denoted R_0 in Fig. 5.12 indicate that at low temperatures there is a large slope, i.e. a finite differential resistance. In Fig. 5.13 we present the data again with a smaller scaling on the current axis. There is a zero bias feature with a finite slope. The corresponding critical currents are very small, $I_c < 20$pA. Below $T = 83$mK I_c is temperature independent. The same is true for the differential zero bias resistance. The saturation value is approximately 60kΩ per sheet. In Fig. 5.13 the saturation resistance is indicated as $R_0(T = 42\text{mK})$ is larger than $R_0(T = 28\text{mK})$. The supression of the supercurrent is in agreement with large phase fluctuations due to a high E_C.

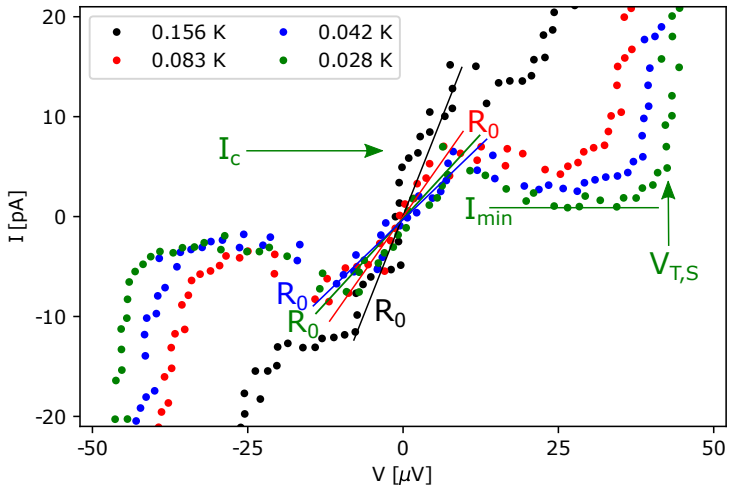

Figure 5.13.: Sample I: A further zoom in reaveals a linear regime around zero bias, where the resistance increases for decreasing temperatures. At the lowest temperatures R_0 saturates. Exceeding the corresponding critical current does not result in a jump to $V_{T,S}$. With increasing bias voltage the current first decreases to a non-zero minimum smaller than I_c. For bias voltages above the minimum, the current starts to increase slowly until it reached $V_{T,S}$. At $V_{T,S}$ there is a sharp onset of current flow. This behaviour is depicted for $T = 28$mK.

Summary

The presented findings are consistent with the bosonic theory of the superconductor to insulator transition, that is induced by disorder (d-SIT). In case of granular films, the sheet resistance at 4K has been taken as a reference value. The critical resistance for that transition has been found close to the quantum resistance $R_Q = 6.45k\Omega$ (see section 2.2.3) in ultra thin granular films. The sheet resistance at $T = 4K$ decides the low temperature behaviour of our two samples. Sample S with a $R_N < R_Q$ shows an decrease of resistance with decreasing temperature, while sample I with $R_N > R_Q$ shows an increase.
Especially below $T < 0.25K$ the samples behave very different in the temperature dependence of resistance. The temperature coefficient of the resistance is positive for sample S, indicating the existence of a global phase coherent state at the lowest temperatures, and negative for sample I, indicating insulating behaviour as phase fluctuations supress the supercurrent between the grains, leading to a high resistive state.

Both samples share strong similarities to already existing measurements on **ultra-thin granular films** by Refs. [10, 61]. This includes a critical temperature T_c, which marks the onset of local superconductivity on the grains, being independent on R_N. For decreasing temperature the $R(T)$ curves show a lot of details, e.g. a reentrant behaviour with a local minimum in resistance in sample I, plateaus in the $R(T)$ in sample S and a clear separation of positive or negative TCR at the lowest temperatures $T < 250mK$. Those properties are attributed to the competition of three energy scales, the Josephson coupling energy E_J, the charging energy E_C and the thermal energy $k_B T$ and the formation of percolation paths.

In addition, when taking a look at the current voltage characeristics at $T < 800mK$, the two samples do as well share similarities to **Josephson junction arrays** in the vicinity of the d-SIT ($E_J \sim E_C$). The overall shape, e.g. the bias independent differential resistance at high bias, a Coulomb blockade feature with a threshold voltage $V_{T,S}$ marking the onset of current flow, is quite similar to findings in insulating JJAs by [80]. In insulating Josephson junctions arrays $V_{T,S}$ relates to the injection of Cooper pair solitons.
For sample I and as well as for sample S we see a threshold voltage $V_{T,S} \sim 30\text{-}40\mu V$. As sample I is on the insulating side of the d-SIT ($R_N > R_Q$) for $B = 0T$ a threshold voltage for the onset of charge transport by Cooper pair solitons is expected, as has been seen in insulating JJAs (see Fig. 5.9b)). For sample S being on the superconducting side ($R_N < R_Q$) we would not expect to find such a threshold voltage, but we do.
In addition, also in both samples there is a feature in the zero bias limit (see Fig. 5.10 for sample S and Fig. 5.13 for sample I). This feature exhibits a supercurrent in sample S and a not expected finite voltage state in sample I.
Due to the fact that both samples are close ($R_N \sim R_Q$) to the d-SIT (one below and one above), there could be a competition of effects, which overlap near the critical point $R_N = R_Q$. That might be the reason why in both cases we see threshold and zero bias feature.

For sample S, we identify a supercurrent around zero bias, which is hysteretical for the different sweeping directions with an escaping and a retrapping current with a sharp jump. That is consistent with findings in superconducting JJAs by [121]. For currents exceeding the critical current [121] find a collective jump attributed to row-by-row switching with $2\Delta/e$ of each junciton. The total voltage after the jump is given by $V_\mathrm{p} = N \cdot \Delta/e$, where N is the number of junctions of the array. The same row-by-row switching and collcetive jumping has been observed by [199].
The sharp jump observed in our sample S ends at a voltage $V \sim 30\mu$V. This value is by far smaller than the theoretical value of $V_\mathrm{p} = N \cdot 2\Delta_0/e$ in a superconducting periodic array and the voltage is therefore attributed to the threshold voltage for Cooper pair solitons $V_\mathrm{T,S}$ as seen in insulating periodic JJAs [80].

The sharp jump from the low voltage/supercurrent branch to the high voltage branch is not expected for granular, inhomogenous films with a very broad distribution in grain sizes and separations. One would expect a smeared out, broad transition as different junctions do have different critical currents. The very sharp nature of the jump in our inhomogenous sample may be explained by the existence of a percolation path. This path consists of a chain of superconducting grains coupled by Josephson links, i.e. the phases of the superconducting wavefunctions are aligned. Due to the broad distribution of grain sizes and separation distances, the coupling strength $E_\mathrm{J}/E_\mathrm{C}$ between different sets of neighbouring grains may vary. By exceeding the critical current of the weakest link the junction resistance goes from zero to its normal value. As a Joule power is generated by the current and the normal resistance of the first destroyed link, the critical currents of the other junctions are suppressed by heating. This heating leads to an avalanche effect and the jump is very sharp. This transition effectively decouples the superconducting grains and the sample switches from a global phase coherent state with a supercurrent to an insulating state for $I > I_\mathrm{c}$. In that insulating state with $V_\mathrm{T,S}$ Cooper pair solitons are injected with increasing bias voltage.

Sample I shows a similar characteristic IV curve as sample S, but the supercurrent is suppressed due to the smaller ratio of the Josephson energy and charging energy. In addition, instead of a supercurrent (as seen in sample S) there is a finite resistance in the zero bias limit. The deviation of that finite slope starts at a current of $I_\mathrm{c} \sim 10$pA, which is a factor $\sim$10 smaller than the critical current in sample S. Above the I_c we find a continuous, but sharp connection to the threshold voltage $V_\mathrm{T,S}$.

The finite zero bias resistance found in our sample I is not in agreement with findings in insulating Josephson junction arrays by [80], where the resistance increased up to unmeasureable values of $\sim$1GΩ per sheet following activated behaviour. No saturation of resistance has been found by [80] as long as the islands of the arrays were superconducting. Our Sample I, however, does not diverge for $T \to 0$, but shows a saturation at value of 60kΩ per sheet. That low temperature saturation will be discussed in Section 5.4.

The emerging physical picture indicates that two dimensional granular aluminum can be modelled with periodic Josephson junction arrays, where Josephson coupling between the superconducting grains competes with charging effects. The two systems share strong similarities even if the geometric dimensions do vary by a factor 10-1000 (grain sizes in ultra-thin films are in the order of 1-100nm in width and length; the average area of a unit cell in a JJA by [80] is $\sim 1\mu\mathrm{m}^2$, i.e. a width and length of $\sim 1\mu$m). In addition, granular films are very inhomogenous, while periodic Josephson junction arrays are very homogenous. It is not surprising, that we also find deviations, when comparing granular films to periodic arrays (low temperature saturation of resistance, much smaller values of I_c,$V_\mathrm{T,S}$). Our samples lie in the transition regime, where R_N is very close to R_Q. The arrays of [121] had $R_\mathrm{N} < 4k\Omega$ and the arrays of [80] had $R_\mathrm{N} > 13k\Omega$. Sample S with R_N $\sim$ 3kΩ is comparable with the arrays by [121]. Sample I with a $R_\mathrm{N} \sim 7.75\mathrm{k}\Omega$ is right above R_Q. No array with similar R_N has been measured by [80].

5.2. Effect of Magnetic Field on the Resistance (B $\neq$ 0T)

As presented in sections 2.2.3 and 2.2.4 granular thin films can be modelled as a random Josephson junction array. In case the arrays have a sheet resistance close to R_Q and a Josephson energy comparable to the charging energy $E_J \sim E_C$, the superconductor to insulator transition may be induced by an applied magnetic field.

In section 5.1 it has already been shown that the sheet resistance at 4K of both samples is close to R_Q (see Fig. 5.1).
Sample S with $R_N < R_Q$ is on the superconducting side and sample I with $R_N > R_Q$ as presented in section 5.1.

5.2.1. The Differential Zero Bias Resistance in Perpendicular Magnetic Field

We now turn to the intermediate magnetic fields and deduce the zero bias resistance from the zero bias part of the measured IV curves.
In insulating artifical JJAs Ref. [80] found a temperature region 200mK $< T <$ 500mK, where the resistance could be described by activated behaviour expressed by

$$R(B,T) = R_0 e^{E_A(B)/k_B T} \tag{5.5}$$

The $R(T)$ curves of our granular films can be fitted to Eq. 5.5 in the same temperature region. For a better understanding we present the $R(T)$ curves in an Arrhenius form, where the resistance is shown in logarithmic scaling versus the inverse temperature $1/T$. By doing so the linear slope directly reveals E_A, while R_0 is the extrapolation of the linear curve for $T \to \infty$. We find the prefactor R_0 to be magnetic field dependent as well, $R_0(B)$.

Sample S

The fits of our data to Eq. 5.5 are presented in Fig. 5.14 in Arrhenius form.
Starting from $B = 0$T the slope increases up to a maximum at a magnetic field of ~2T. By further increasing the magnetic field the slope decreases. For better visualisation we separated the $R(T)$ curves into $B < 2$T and $B > 2$T.

In Fig. 5.14a) the $R(T)$ curves below $B = 2$T are shown. For $B = 0$T (lila) we see an overall decrease of resistance with decreasing temperature. The activation energy is negative and indicates a transition to a zero resistance state. By increasing the magnetic field to 50mT (green) the slope changes sign to positive, i.e. insulating behaviour. That means in sample S the SIT is induced by a magnetic field below 50mT. Further increasing the magnetic field leads to an overall increase of the slope. The dependence on B is non-monotonic. The slope of the blue 1T curve is smaller than the slopes of the curves with a smaller (50mT) and higher (1.6T) magnetic field in Fig. 5.14a).
Above 1.6T the slopes saturate up to the maximum of 2T (black).
For magnetic field values above this maximum the slopes decrease monotonously with

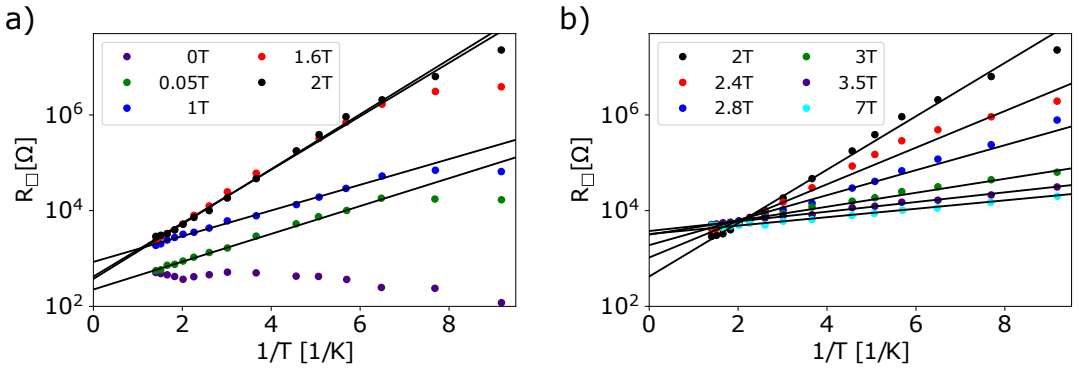

Figure 5.14.: Sample S: Magnetic field dependence of the $R(T)$ curves. a) shows magnetic field values smaller than $B_{\max}$, while b) shows values above $B_{\max}$. In the high temperature regime ($T > 500$mK, i.e. $1/T < 2$) of a) the presented curves show a jump in resistance between the lower two and upper three curves, i.e. between 50mT and 1T. In reality there is no jump, but a continuous transition. The apparent jump is attributed to the selection of magnetic fields. The continuous transition is seen in our complete set of magnetic fields.

increasing magnetic field (see Fig. 5.14b)) and saturate for $B > 3.5$T, i.e. the slope is independent on magnetic field. The evaluation of the high magnetic fields ($B > 3.5$T) is presented in Section 4.3. The independence of the slope is attributed to the destruction of superconductivity in the grains. This results in a random array of N-I-N-junctions.
It is supported by the magnetic field evolution of the prefactor R_0, presented in Fig. 5.15a). For magnetic fields above $B = 3.5$T the extrapolation of the linear slope is very close to the normal state sheet resistance $R_{\mathrm{N}}(4\mathrm{K}) \sim 3\mathrm{k}\Omega$. However, for smaller magnetic fields R_0 decreases to an approximately constant value of $\sim 400\Omega$ below $B = 2$T. This indicates that below $B = 3.5$T local superconductivity on the grains and the openening of the superconducting gap Δ influences the resistance for $T < T_{\mathrm{c}}$. Therefore the high temperature extrapolation of the activation fit does not correspond to the normal state for $T > 4$K, but to a state with a local minimum in resistance for $0.8\mathrm{K} < T < T_{\mathrm{c}}$ $R_{\mathrm{loc}} < R_{\mathrm{N}}$. This R_{loc} can be interpreted as the minimum resistance of a reentrant feature. The high temperature extrapolation and the increase of R_0 with increasing B is shown in Fig. 5.15b), where the $R(T)$ for $B = 0$T (black curve) is the reference with $R_{\mathrm{N}}(4\mathrm{K})$. The plateaus for $0.3\mathrm{K} < T < T_{\mathrm{c}}$ have been discussed in section 5.1. With increasing magnetic field the plateau for $B = 0$T is transformed into a local minimum.

In Fig. 5.14b) $R(T)$ curves apparently intersect in a single point at $T \sim 475$mK and $R \sim 6\mathrm{k}\Omega$. However, due to our stepsizes in magnetic field and temperature, i.e. a relative small number of points in that region, we can not distinguish between a true single crossing point or a region where the different $R(T)$s intersect. Such an intersection region can be caused by the increasing $R_0(B)$ and the decreasing $E_{\mathrm{A}}(B)$ with increasing magnetic field B. The magnetic field dependence of $R_0(B)$ can seen in Fig. 5.15a) and

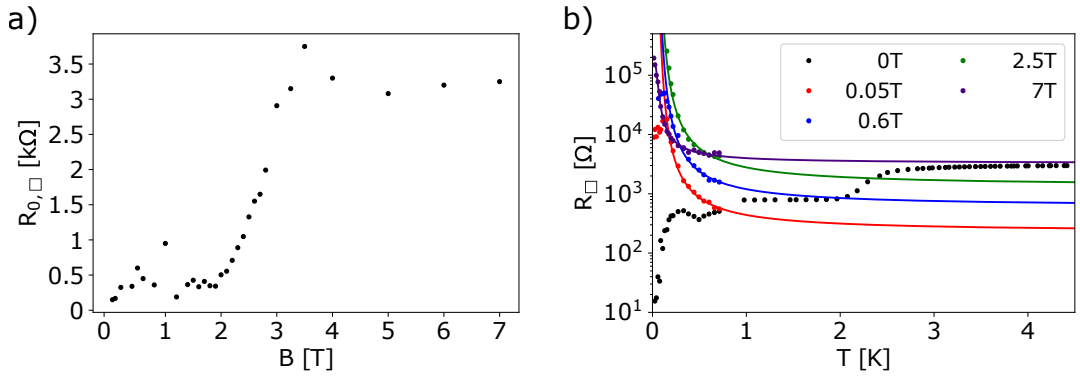

Figure 5.15.: a) Magnetic field dependence of prefactor R_0. b) $R(T)$ curves for five selected magnetic fields. The high temperature extrapolation of the corresponding fits are $R_0(B)$. With increasing magnetic field R_0 increases from a low value of ∼400Ω to $R_\mathrm{N}(4\mathrm{K})$ at high fields.

$E_\mathrm{A}(B)$ in Fig. 5.17. To verify either a single crossing point or an intersection region a measurement with very small stepsizes in temperature and magnetic field is necessary.

Now we turn to the magnetic field dependence of the slopes, which represent the activation energy E_A given by Eq. 5.5.
The above mentioned dependence has been studied by Delsing [80] in Josephson junction arrays. For magnetic fields above B_c superconductivity is destroyed and the charge transport is purely due to single electron solitons. The activation energy is magnetic field independent and found to be $E_\mathrm{A,N} = \frac{1}{4}E_\mathrm{C}^{(\mathrm{e})}$. The high magnetic field case has been discussed in section 4.3, where the concept of solitons (SES and CPS) was introduced [80, 188].
In case of superconducting islands there is a competition on transport between Cooper pair solitons and single electron solitons.
For insulating arrays in zero magetic field, one could think about two possible scenarios. The first describes the transport by SES only. That means that Cooper pairs have to be broken up. The activation energy reads

$$E_\mathrm{A,SES}(0) = \Delta_0 + \frac{1}{4}E_\mathrm{C}^{(\mathrm{e})} \tag{5.6}$$

where the first term is the BCS energy gap, which has to be overcome to break up the Cooper pairs and generate the single electrons. The second term is the charging energy for single electrons.
If the charge transport would be due to Cooper pair solitons only then one would expect an activation energy of four times of the activation energy of single electron solitons due to the doubled charge.

$$E_\mathrm{A,CPS}(0) = 4 \cdot E_\mathrm{A,N} = 4 \cdot \frac{1}{4}E_\mathrm{C}^{(\mathrm{e})} = E_\mathrm{C}^{(\mathrm{e})} \tag{5.7}$$

Ref. [99] found the ratio of Δ_0/E_C important. If $\Delta_0/E_C < 3/4$ the charge transport is dominated by SES, that are created by breaking up Cooper pairs. The magnetic field dependence follows

$$E_A(B) = \Delta(B) + \frac{1}{4}E_C^{(e)} \tag{5.8}$$

where the first term is the magnetic field dependent BCS energy gap.
However, if the ratio $\Delta_0/E_C > 3/4$ they find that a part of the charge transport is given by CPS, which leads to a deviation from the above formula Eq. 5.8. Ref. [80] found the critical value to be 2 instead of 3/4. For their arrays having $\Delta_0/E_C > 2$ the activation energy deviate from Eq. 5.8 as well and the activation energy is lower than this formula predicts. This behaviour is shown in Fig. 5.16. Another important finding of arrays fullfilling the condition $\Delta_0/E_C > 2$ is, that they show oscillations of $E_A(B)$.
In our sample S (see Fig. 5.17) we see a similar dependence of the activation energy

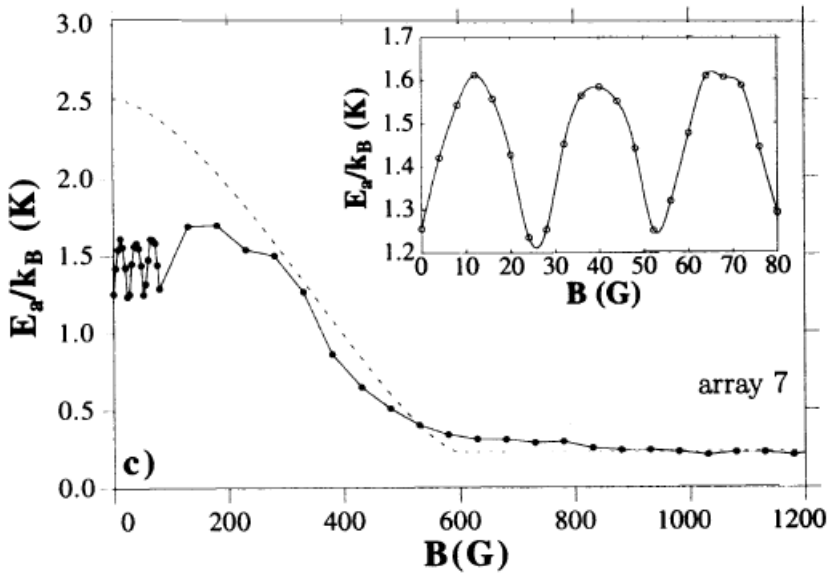

Figure 5.16.: Dotted line correspond to $E_A(B) = \Delta(B) + 1/4E_C^{(e)}$ with $E_A(0) = \Delta_0 + 1/4E_C^{(e)}$. Inset shows oscillations of E_A with magnetic field in the small magnetic field range. The ratio of $\Delta_0/E_C^{(e)}$ for that array is 2.49. Adapted from [80].

with magnetic field as Ref. [80]. These activation energies correspond to the slopes of the curves in Fig. 5.14.

Below $B = 2$T the activation energy shows oscillations. Above 2T up to $B = 3.5$T the activation energy monotonically decreases to a constant value for even higher magnetic fields. This is attributed to the crossover from CPS to SES charge transport. Due to the random nature of our film the ratio between E_A and E_C is unknown. We therefore substituted the saturation value of $E_A = 1/4\ E_C$ with $E_{A,N}$ in Eq. 5.10. The fit to our

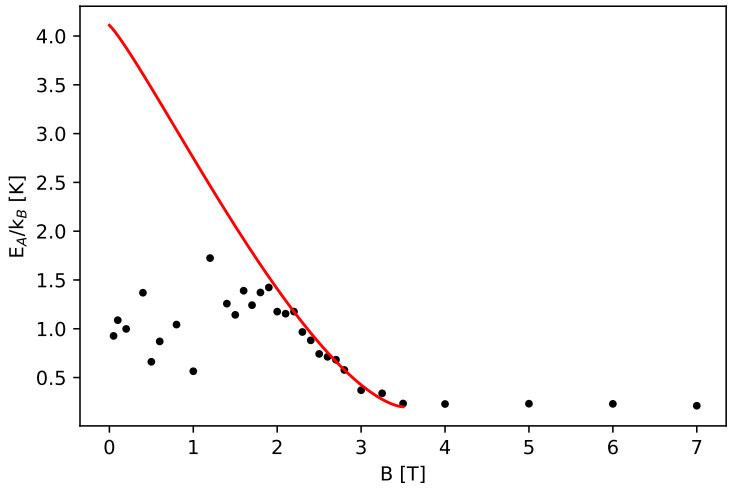

Figure 5.17.: Sample S: Fit corresponds to $E_{\mathrm{A}}(B) = \Delta(B) + E_{\mathrm{A,N}}$ with $E_{\mathrm{A}}(0) = \Delta_0 + E_{\mathrm{A,N}}$ and $B_{\mathrm{c}} = 3.5\mathrm{T}$.

$E_{\mathrm{A}}(B)$ data for pure single electron soliton transport is shown in Fig. 5.17. Our step size in magnetic field is too large to resolve oscillations in detail. In section 5.3 we present measurements with much smaller stepsize in magnetic field and discuss oscillations in the $R(B)$ curves.

Similar to what has been found in JJAs with $\Delta_0/E_{\mathrm{C}} > 2$, there is a transition from Cooper pair dominated transport at low magnetic fields to single electron transport at higher fields. The activation energy for the single electron transport follows Eq. 5.8. In our sample above $B = 2\mathrm{T}$ we expect that the transport is dominated by single electrons as Δ decreases with magnetic field. To fit our data to Eq. 5.8 the magnetic field dependence $\Delta(B)$ is necessary, but unkown for our samples. We therefore adapt the empiric approach of [80], where the energy gap follows

$$\Delta(B) \approx \Delta_0 \left(1 - \left(\frac{B}{B_{\mathrm{c}}}\right)^{1.6}\right)^{1.5} \tag{5.9}$$

The red curve in Fig. 5.17 is a fit of the data to

$$E_{\mathrm{A}} = \Delta_0 \left(1 - \left(\frac{B}{B_{\mathrm{c}}}\right)^{\alpha}\right)^{\beta} + E_{\mathrm{A,N}} \tag{5.10}$$

with α and β as free parameters. $\Delta_0 = 1.76 k_{\mathrm{B}} T_{\mathrm{c}}$ with T_{c}= 2.3K. The critical magnetic field value $B_{\mathrm{c}} = 3.5\mathrm{T}$ as it marks the onset of magnetic field independence of E_{A}. The saturation value is $E_{\mathrm{A}}/k_{\mathrm{B}} = 200\mathrm{mK}$. The fit describes the data best for $\alpha = 1.143$ and $\beta = 1.565$.

The activation energy is magnetic field independent as long as there is no superconductivity. This is seen in our sample for $B > 3.5$T, where the transport is purely due to single electrons. By decreasing the magnetic field the grains get superconducting with an energy gap $\Delta(B)$ that increases with decreasing magnetic field. There is a competition between Cooper pair and single electron transport. As we see that crossover from CPS to SES the ratio of Δ_0/E_C has to be higher than 3/4 [80, 99].

Sample I

In the same manner as presented for sample S, we fitted the $R(T)$ curves of sample I to the formula for activated behaviour Eq. 5.5. The curves are shown in Fig. 5.18. We see the same dependence on magnetic field. Starting from $B = 0$T, the slopes increase to a maximum around $B = 2$T (see Fig. 5.18a)) and decrease with further increase of magnetic field (see Fig. 5.18b)). The $B = 0$T curve shows an upturn in resistance with

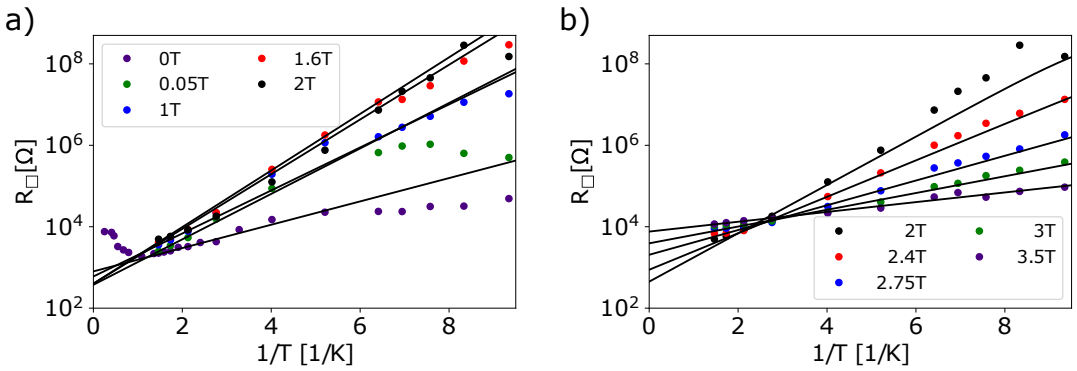

Figure 5.18.: Sample I: Linear fits in the Arrhenius graphs indicate non-monotonic behaviour with B and a deviation from activated behaviour at low temperatures.

decreasing temperature. That has already been shown in section 5.1 and attributed to the fact, that this sample is on the insulating side of the disorder induced superconductor to insulator transition, having a $R_N(4K) > R_Q$. The temperature dependence of the resistance, the magnetic field dependence of the activation energy and a crossing point in the $R(T)$ curves for magnetic fields above the maximum is very similar to what has been shown for Sample S. However, in contrast to Sample S there is no transition to a zero resistance state as the grains are superconducting, but no global phase coherence is achieved.

The extracted activation energies are shown in Fig. 5.19. Compared to sample S the magnetic field dependence of the activation energy is very similar. Coming from high fields we see a monotonic increase of E_A with decreasing magnetic field as explained for single electron transport. Between 2T and 3.5T Eq. 5.10 fits our data for $\alpha = 1.155$ and $\beta = 1.45$. The deviation at lower magnetic fields, $B < 2$T, comes from the increasing

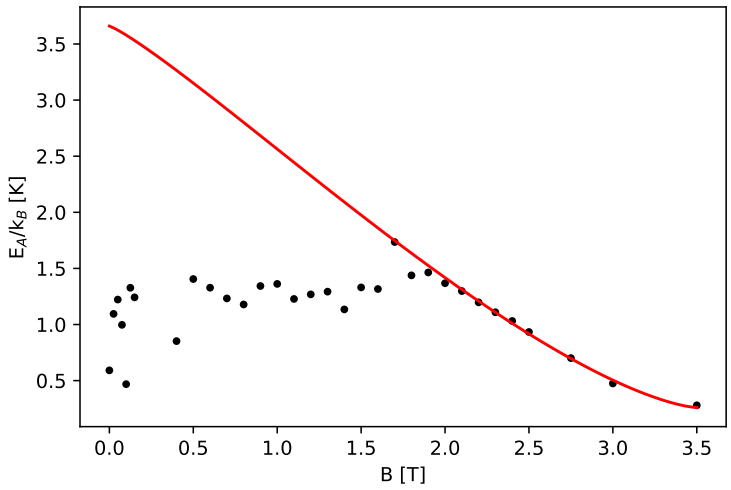

Figure 5.19.: Sample I: Fits correspond to $E_{\mathrm{A}}(B) = \Delta(B) + E_{\mathrm{A,N}}$ with $E_{\mathrm{A}}(0) = \Delta_0 + E_{\mathrm{A,N}}$ and $B_{\mathrm{c}} = 3.5\mathrm{T}$

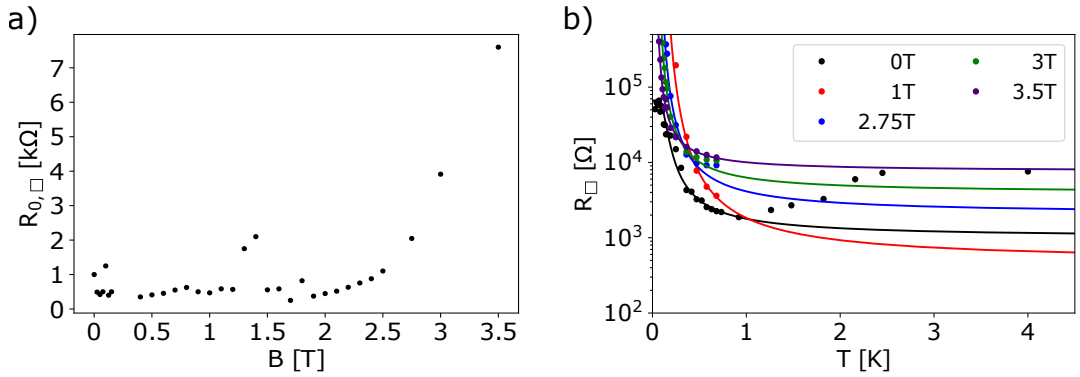

Figure 5.20.: Sample I: a) Magnetic field dependence of prefactor R_0. b) $R(T)$ curves for five selected magnetic fields. The high temperature extrapolation of the corresponding fits are $R_0(B)$. Similar as for sample S, $R_0(B)$ increases with increasing magnetic fields to $R_{\mathrm{N}}(4\mathrm{K})$ at high fields.

contribution of Cooper pair solitons to the transport.

The prefactor $R_{0,\square}$ is approximately constant below $B = 2$T and increases to R_N above 3.5T as superconductivity is destroyed. This is similar to sample S (see 5.15a).
The increase of $R_{0,\square}$ with magnetic field is attributed to the existence of the reentrant feature (see Fig 5.20b) for sample I), which is present for $B < 2$T and vanishes for higher B. Therefore $R_{0,\square}$ approaches R_N at high fields.

Summary

Our two granular films have been modelled by periodic JJAs to investigate the temperature dependence of the zero bias resistance for different magnetic field values. Sample S, being on the superconducting side of the d-SIT, can be driven across the SIT with an applied perpendicular magnetic field $B_\perp$ ∼50mT (B-SIT). Sample I, being on the insulating side of the d-SIT, shows the same magnetic field dependence as Sample S on the insulating side of the B-SIT. On the insulating side for both samples the $R(T)$ curves follow activated behaviour in a temperature region 200mK $< T <$ 500mK. This is in good agreement with findings in insulating JJAs by [80].

From the fits of eq. 5.5 to the $R(T, B)$ curves we extract the activation energy E_A and the prefactor R_0. The activation energy is attributed to the thermal activation of Cooper pair solitons below the threshold voltage $V_{T,S}$. The magnetic field dependence of the extracted activation energies can be separated into two regions by a magnetic field $B_{max} \sim 2$T. Above $B = 2$T charge transport is dominated by single electron solitons and at lower fields by Cooper pair solitons. Ref. [80] found the crossover for $\Delta_0/E_C > 2$. As we see that crossover, we expect our ratio to be $\Delta_0/E_C > 2$, as well.
With increasing magnetic field the resistance at the lowest temperatures $T < 30$mK reaches very high values of $R_\square > 10^7\Omega$ in sample S and $R_\square > 10^8\Omega$ in sample I. The increase from normal conducting resistance R_N to the highest observed resistances is a factor of $10^4 - 10^5$. Such an increase has been observed by [9, 192] in ultra-thin granular films by decreasing the film thickness. However, their experimental setup did not allow to study the magnetic field dependence of their films for $B > 210$mT.

5.2.2. The IV Characteristics in Perpendicular Magnetic Field

In the previous section 5.2.1 we extracted the temperature and magnetic field dependence of the differential resistance in the zero bias limit. We now turn to the non-linear resistance, i.e. the differential resistance for non-zero bias voltages. That has been done with IV characteristics.
In Fig. 5.21 a selection of IVs for a set of magnetic fields is presented at the lowest temperature measured for sample S and I.

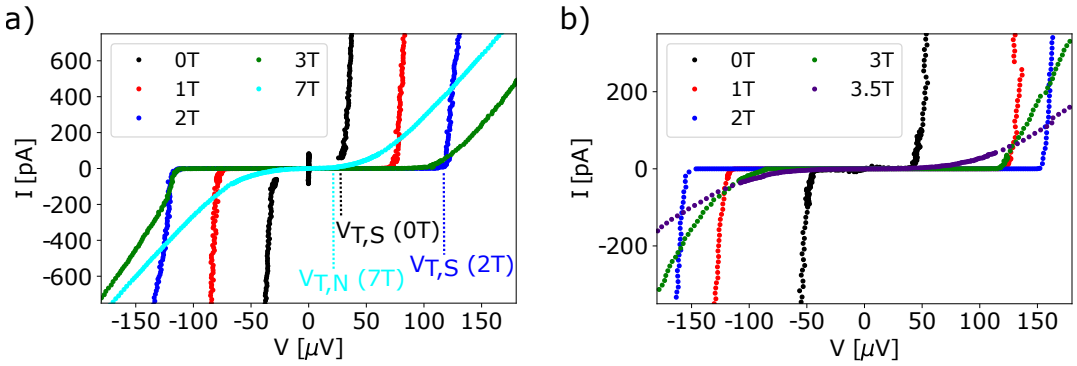

Figure 5.21.: Overview of current voltage characteristics measured for different magnetic fields for both samples. Temperature for sample S in a) is $T = 15$mK, for sample I in b) $T = 28$mK. Note the different scaling of the y-axis. Above the threshold voltage V_T there is a change of slope at $B \approx 2$T attributed to the change from Cooper pair soliton dominated transport at $B < 2$T to single electron soliton dominated transport at $B > 2$T.

In Fig. 5.21a) the evolution of the IV curves with magnetic field for sample S is shown. Sample I is presented in the same way in b).
In sample S in zero magnetic field (black curve) there is an insulating feature with a threshold voltage $V_{T,S}$ of approx. 30μV. Near zero voltage there is a supercurrent peak with $I_c \approx 100$pA. The $B = 0$T curve of sample I shows a finite differential resistance around zero bias voltage of about $R_\square \approx 60\text{k}\Omega$. Both $B = 0$T curves have been discussed in section 5.1.
The zero bias feature in both samples is supressed by applying a perpendicular magnetic field as can be seen in Fig. 5.21a) and b) for $B = 1$T (red curve). With an applied magnetic field $B > 50$mT both samples are beyond the magnetic field driven SIT, where the charge transport is mediated by thermally activated CPS below a threshold voltage $V_{T,S}$. Above the threshold voltage CPS are injected due to the bias voltage, hence there is a sharp increase of current with a low differential resistance. The bosonic scenario for the magnetic field driven SIT has been presented in section 2.2.3 and further discussed for periodic JJAs in section 2.2.4. The most plausible picture for the B-SIT is the duality between vortex/anti-vortex pairs and Cooper/anti-Cooper pairs on the superconducting and insulating side, which undergo a thermally driven unbinding transition.

Increasing the magnetic field leads to a weakening of the Josephson coupling E_J. The injection of CPS is therefore shifted to higher voltage values $V_{T,S}$. This effect can be seen in Fig. 5.21a) for sample S and b) for sample I. This increase has a maximum for B ∼2-3T in sample S and B ∼2T in sample I. The corresponding threshold voltages are $V_{T,S}$ ∼125µV and $V_{T,S}$ ∼150µV, respectively. As shown in section 5.2.1 at that magnetic field $B \sim B_{max}$ the charge transport switches from CPS dominated to SES dominated. The generated single electron solitons have a lower charging barrier to overcome compared to the CPS. Therefore a higher magnetic field leads to a decrease of the threshold voltage until it reaches $V_{T,N}$, the threshold voltage for the case of normal conducting grains.

In addition we find that the onset of charge flow is washed out in the SES dominated magnetic field range ($B > B_{max}$). This can be attributed to quantum fluctuations of charge with a higher impact on SES, due to their smaller E_C, than on CPS [80].

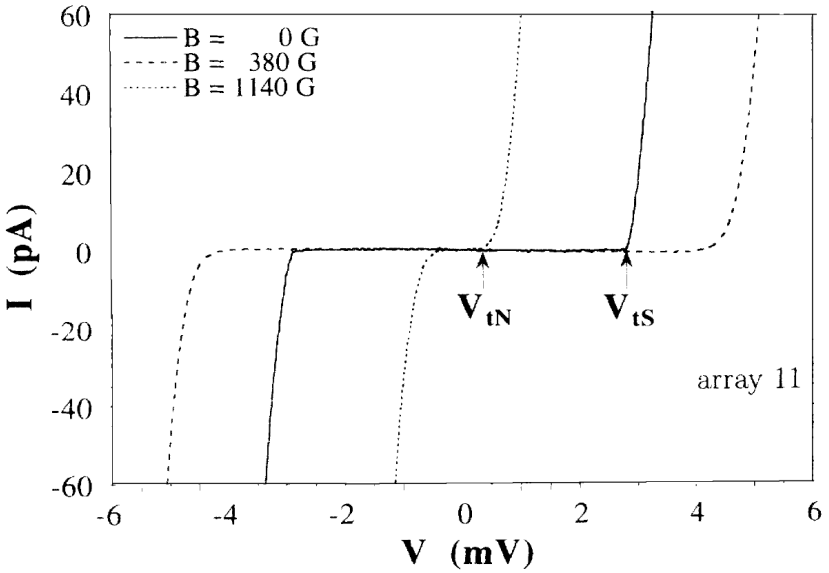

Figure 5.22.: Current voltage characteristics of a highly insulating JJA with $R_N \gg R_Q$. The threshold voltage $V_{T,S}$ increases from $B = 0T$ (black line) to intermediate magnetic fields ($B = 380G$, dashed line). Further increasing the magnetic field leads to a decrease of V_T. At high fields ($B = 1140G$, dotted line) the threshold voltage is smaller than the starting value at $B = 0$. It is denoted as $V_{T,N}$ as the magnetic field is high enough to destroy local superconductivity in the array islands, effectively turning the S-I-S junctions into N-I-N junctions with single electron soliton transport only. Figure taken from [80].

A similar dependence of the threshold voltage $V_{T,S}$ has been observed in periodic Josephson junction arrays by [80]. The array presented in Fig. 5.22 is insulating for $B = 0T$ with a high normal state sheet resistance $R_N = 151k\Omega$.

For both of our samples we find $V_{\mathrm{T,S}}$ to be approximately the same value as the normal state threshold $V_{\mathrm{T,N}}$. This may be attributed to the proximity to the SIT with $R_{\mathrm{N}} \sim R_{\mathrm{Q}}$. Quantum fluctuations may effectively decrease the threshold for the injection of CPS in the vicinity of the SIT.
The insulating array of Ref. [80] is far from the SIT and hence quantum fluctuations are negligible. Therefore the threshold voltage is not suppressed and higher than in the normal state $V_{\mathrm{T,S}}(B = 0\mathrm{T}) > V_{\mathrm{T,N}}$.

The differential resistance at $V > V_{\mathrm{T,S}}$ is very small below B_{max}, which supports the approach of CPS injection. After the crossover to SES dominated transport above B_{max} the differential resistance above $V_{\mathrm{T,S}}$ is shifted to higher values indicating a combination of non-superconducting charge flow by SES and superconducting charge flow by CPS. For magnetic field values $B > B_{\mathrm{c}}$ the charge flow is purely given by SES and hence the differential resistance is magnetic field independent.

5.2.3. Absence of Highly Insulating State in Parallel Magnetic Field

Up to now, we have only focused on perpendicular magnetic fields and attributed the existence of the highly resistive state to magnetic flux lines penetrating the thin film through normal areas in a random network of normal and superconducting regions. In the perpendicular magnetic field configuration we have a length and width that exceeds the thickness by orders of magnitude ($l_\perp$ = 28x300μm = 8.4mm, $w_\perp$ = 300μm and $d_\perp$ ~6nm). By switching the orientation to parallel magnetic field this configuration changes drastically. Then $d_\parallel$ is either $l_\perp$ or $w_\perp$ and by orders of magnitude thicker than the other remaining dimensions.

To see whether there are similar or different effects compared to the perpendicular magnetic field orientation, we measured 5 parallel magnetic fields ranging from 0.5T to 2.5T for temperatures between 15mK and 712mK. For each magnetic field $B_\parallel$ and temperature T an IV has been measured. An effective perpendicular magnetic field due to misalignement was compensated (see section A.4). The evolution with temperature of the current voltage characteristics is the same for all parallel fields. This is examplarily shown for B = 0T in Fig. 5.23.

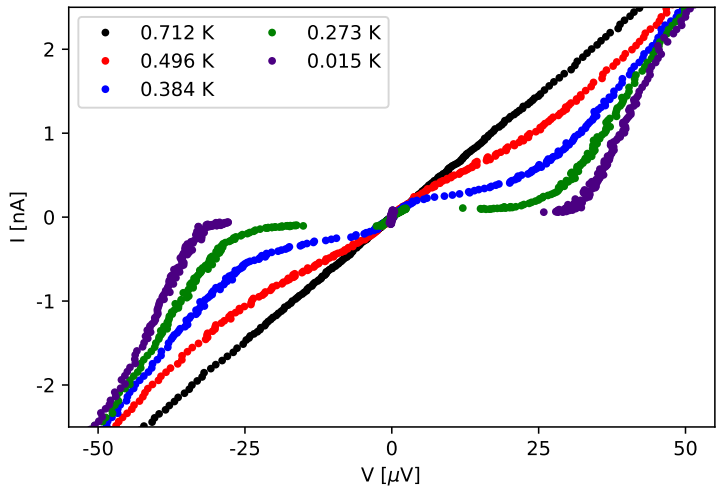

Figure 5.23.: Sample S in zero field. Shown are the IVs for different temperatures. They have been separated into different temperature ranges and discussed in section 5.1. With decreasing temperature thermal effects vanish and the Coulomb blockade and the zero bias feature become more pronounced.

With decreasing temperature the Coulomb blockade for Cooper pair solitons becomes more pronounced as the impact of thermal effects (hopping) is significantly reduced. Around zero bias a feature arises resembling a critical current. The temperature dependence and the overall shape of the IVs in zero magnetic field have been discussed in

section 5.1.

We will focus on the magnetic field dependence of the IV curves at the lowest temperature in parallel field configuration. The IV curves for the lowest temperature $T = 15$mK are presented in Fig. 5.24. The threshold voltage decreases from $V_{\mathrm{T,S}} \approx 30\mu$V to $\approx$

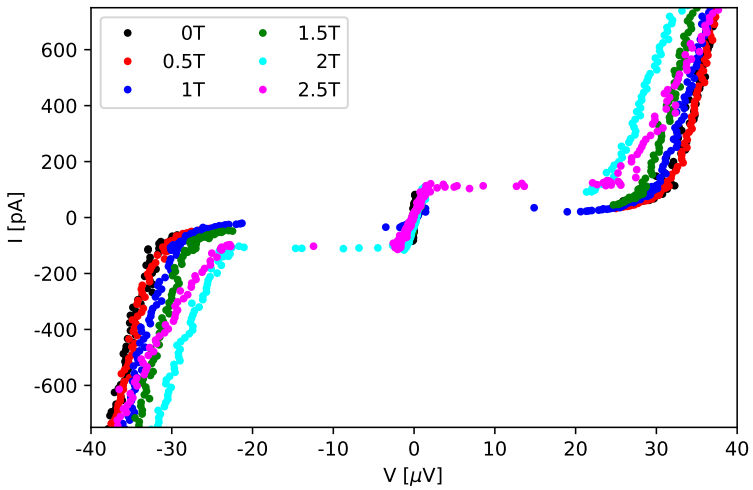

Figure 5.24.: Sample S in **parallel magnetic field** orientation. The IVs have been measured at $T = 15$mK for a set of magnetic fields. The overall shape does not change up to a magnetic field $B_{||} = 2.5$T. The linear slopes for $B = 0$T, 0.5T, 1T and 1.5T around zero bias are covered by the $B = 2$T and $B = 2.5$T curves.

20μV with increasing parallel fields up to $B_{||} \sim$2T. This is different to the findings in perpendicular magnetic fields, where an increasing magnetic field leads to an increase of the threshold voltage (see Fig. 5.25). The zero bias resistance, as well as the critical current, slightly depend on parallel magnetic fields (see Fig. 5.26).
While in perpendicular magnetic field configuration (see Fig. 5.25) the slope between $B_{\perp} = 25$mT and $B_{\perp} = 50$mT changes from vertical to almost horizontal, for parallel magnetic fields up to $B_{||} = 2.5$T the slope only slightly changes (see Fig. 5.24). For $T =$ 26mK the corresponding sheet resistances are presented in Fig. 5.26a).
A change in the slope from vertical to horizontal is associated with the suppression of the zero bias supercurrent. In parallel fields this change is not seen and therefore the supercurrent is not affected by the parallel magnetic field up to $B_{||} = 2.5$T.

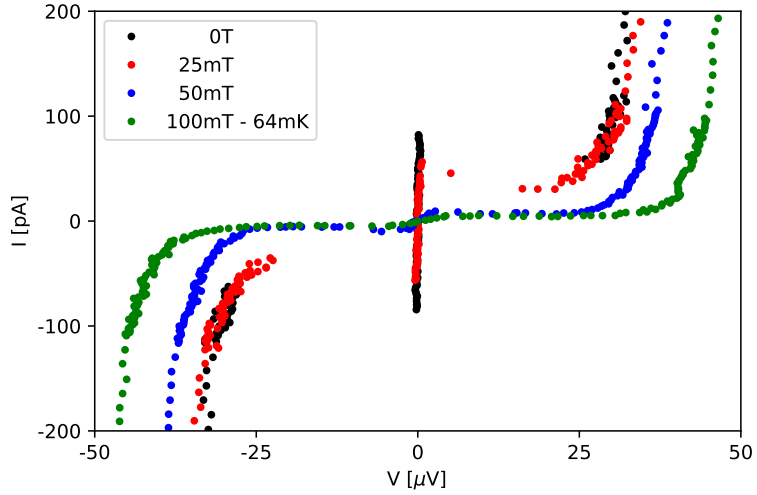

Figure 5.25.: Sample S in **perpendicular magnetic field** at $T = 15$mK: black (0T) and red (25mT) curve show a supercurrent feature, while blue (50mT) and green (100mT) show a finite slope around zero bias. For perpendicular magnetic fields $B > 50$mT the critical current I_c is significantly reduced. Note: green curve for $B_\perp = 100$mT is measured at $T = 64$mK.

We extracted the zero bias resistance from the IV curves measured at $T = 26$mK in parallel magnetic field orientation. The zero bias resistance is shown in the top panel of Fig. 5.26, where we can see a positive magnetoresistance. The sheet resistance increases from a zero resistive state to a sheet resistance of $R_{\square,||} \sim 1$kΩ. In perpendicular magnetic field orientation and at the lowest temperatures we see a magnetoresistance dome with a maximum at $B_\perp \sim 2$T with a sheet resistance $R_{\square,\perp} > 100$MΩ (see Fig. 5.29 in the next section 5.3).
The escape currents extracted at $T = 15$mK, i.e. bias voltage is swept from zero to finite values, are presented in the bottom panel of Fig. 5.26. The critical current decreases for an increasing magnetic field to minimum at $B = 1$T. Further increasing the magnetic field leads to an increase of critical current and a saturation for $B > 2$ T. To extract a magnetic field dependence of either resistance or critical current more data points are essential. If the additional measurement confirms our maximum for parallel magnetic fields at $B_{\mathrm{max},||} = 1$T, it is smaller than the maximum found for perpendicular fields at $B_{\mathrm{max},\perp} = \sim 2$T.

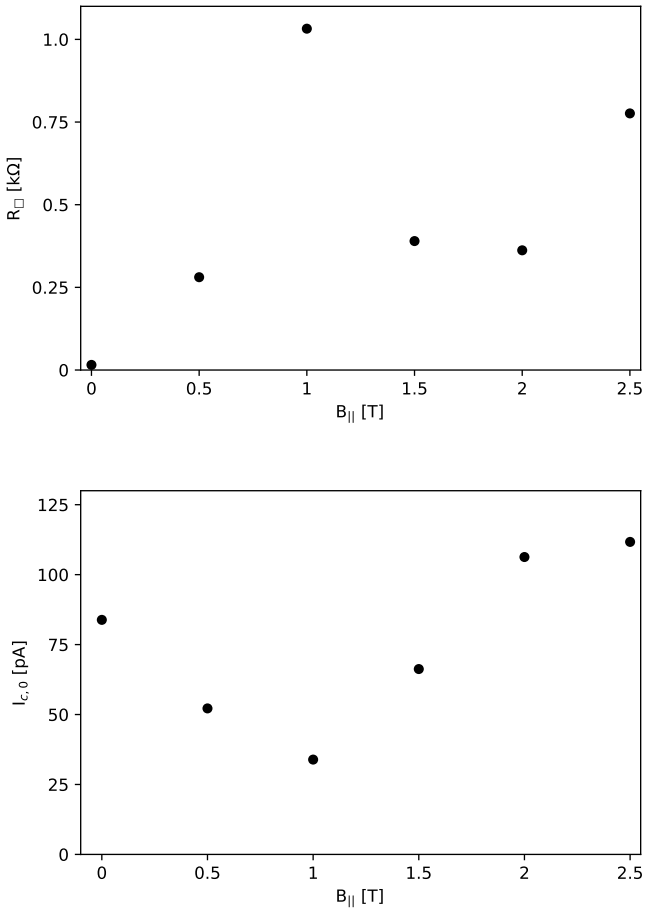

Figure 5.26.: Sample S: Top panel shows extracted zero bias resistances at a temperature $T = 26$mK. Bottom panel shows extracted critical escaping currents $I_{c,0}$ at a temperature $T = 15$mK. While the zero bias resistance shows an increase with increasing magnetic field, the critical current first decreases up to 1T and then starts to increase again.

After having discussed the shape of the IV characteristics in dependence of temperature and magnetic field, we now turn to the temperature dependence of the zero bias resistance $R_{\square}$.
The deduced values of each IV is presented in Fig. 5.27. a) presents the $R(T)$ curves for $B < 1$T, which exhibits a maximum in resistance at $B = 1$T, $T \approx 200$mK. For higher magnetic fields the $R(T)$ curves start to drop in resistance. That can be seen in b).

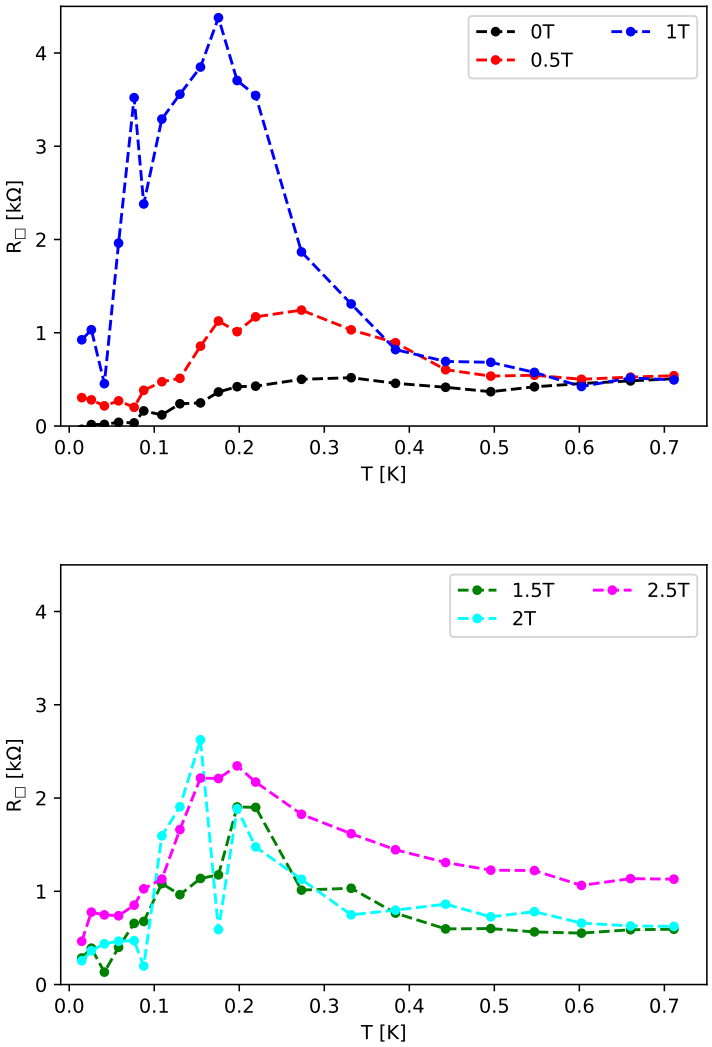

Figure 5.27.: Sample S: a) $R(T)$s for $B_{\parallel} < 1$T and b) $B_{\parallel} > 1$T indicating a maximum of magnetoresistance at $B_{\parallel} = 1$T.

While the $B_{\parallel} = 0$T curve shows a non-monotonic behaviour, the curves for $B_{\parallel} > 0$T show an upturn in resistance for decreasing temperatures in the temperature region $\approx$ 200mK $< T <\approx$ 600mK. However, below a crossover temperature T_{cross} (temperature of the maximum resistance) the resistance does not increase for decreasing temperatures, but starts to decrease. This decrease of resistance has been already shown for the $B =$ 0T case (see section 5.1). Due to a too large step size for the lowest temperatures we can not assign the low temperature behaviour to a saturation in resistance nor to a vanishing resistance at temperature below our minimum of $T = 15$mK.
The crossover temperature is shown in Fig. 5.28. With increasing parallel magnetic field, the crossover is shifted towards lower temperatures and seems to saturate for $B_{\parallel} > 1.5$T.

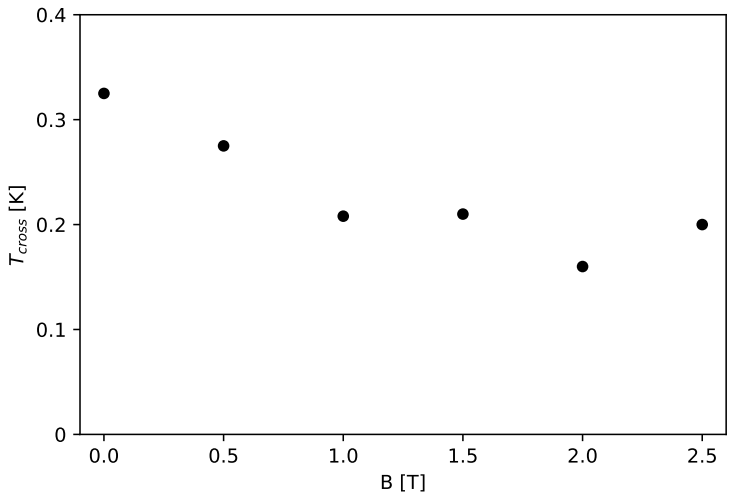

Figure 5.28.: Sample S: Temperature T_{cross} presented for parallel magnetic fields $B_{||}$. For $T > T_{\text{cross}}$ the resistance increases with decreasing temperature, while for $T < T_{\text{cross}}$ the resistance decreases with decreasing temperatures.

Summary

For parallel magnetic field orientations (up to $B_{||} = 2.5$T) we find that the overall shape of the IV curves is unaffected and resambles the curvature of the $B = 0$T curve. This is very different to the perpendicular magnetic field orietation, where a $B_{\perp} \sim$50mT has been found to be sufficient for a B-SIT.
The threshold voltage in parallel slightly decreases with increasing magnetic field $B_{||}$, while in perpendicular $V_{\text{T,S}}$ increases with increasing magnetic field $B_{\perp}$. The deduced zero bias resistance $R_{\square}(B)$ at $T = 26$mK exhibits a small increase, but stays below 1kΩ. This value is smaller than the normal state resistance $R_{\text{N}} = 3$kΩ.
The temperature dependence of $R_{\square}(T)$ follows an insulating trend for
$T > T_{\text{cross}} \sim 200$mK. Below the crossover temperature the resistance decreases with

decreasing temperature. This behaviour is the same as for the $B = 0$T curve. The maximum resistance value found in parallel orientation is $\sim$4kΩ, while the maximum resistance in perpendicular magnetic field exceeds $\sim$100MΩ.
We see a critical current with values between 50pA and 100pA up to the maximum applied parallel magentic field of $B_{||} = 2.5$T. This and the fact, that we do not observe resistance values above the normal state sheet resistance $R_{\mathrm{N}} = 3\mathrm{k}\Omega$, leads to the conclusion that there is no B-SIT up to a parallel magnetic field of $B_{||} = 2.5$T in our granular ultra-thin film.

However, we see effects (dome-like $R(T)$, increase/decrease of R with B) in the $R(T)$ by an applied parallel magnetic field. These effects might be explained by a small residual perpendicular magnetic field due to insufficient compensation as well as due to tolerances in the compensation curves for different parallel magnetic fields. A better alignment of sample to the parallel field orientation and an increased resolution of the compensating field is necessary.

5.3. Oscillatory Magnetoresistance

We will now turn back to the behaviour in perpendicular magnetic fields. In section 5.2 we presented $R(T)$ curves for fixed values of magnetic fields. We found insulating behaviour in sample S for magnetic fields above $B \sim 50$mT and in sample I for all magnetic fields including zero field. The magnetic field dependence of the $R(T)$ on the insulating side of the SIT can be separated into three regimes. For magnetic fields below a maximum $B_{\max}$ the resistance values increase with magnetic field and above they decrease. This positive and negative magnetoresistance (PMR, NMR) resembles a dome like shape centered around $B_{\max}$. For very high fields, exceeding the critical magnetic field B_c of the grains, $R(T)$ is magnetic field independent.
A magnetic field dependence of the resistance as described above, including a positive magnetoresistance followed by a negative magnetoresistance and a high field independence, has been found, e.g. in homogeneously disordered TiN thin films (see Fig. 2.8).
From the linear slopes of the $R(T)$ in an Arrhenius plot we extracted the corresponding activation energies (see Fig. 5.17). Comparing our $E_A(B)$ with periodic Josephson junction arrays we find similarities in the overall shape. The oscillations in E_A seen in the low magnetic fields (see Fig. 5.16) could not be reproduced. Due to our large magnetic field steps in the initial data in section 5.2 it is unclear whether there are no oscillations or if they are not observed due to a lack of data points. In addition, due to the randomness of our granular films it is an open question, whether oscillations of E_A or $R_\square$ do exist at all. In this section we therefore fix the temperature and sweep the magnetic field continuously.

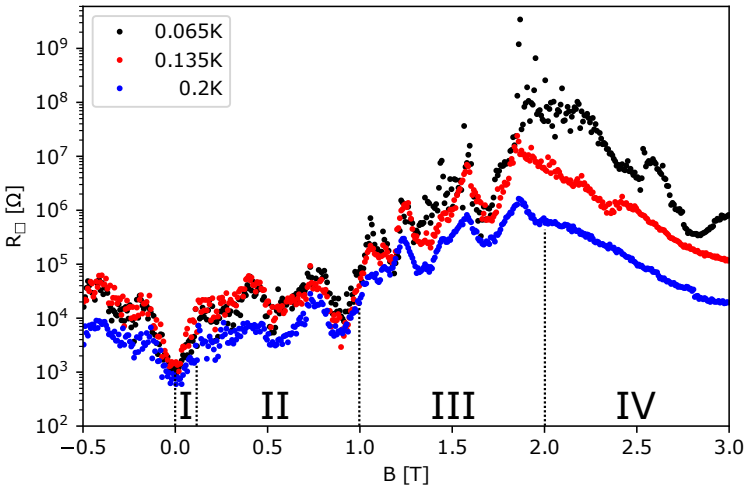

Figure 5.29.: $R(B)$ curves of **sample S** for three temperatures 65mK, 135mK and 200mK. The shape of the $R(B)$ is dome-like, i.e. for lower fields exhibits a positive magnetoresistance and for higher fields a negative magnetoresistance. The $R(B)$ has been further separated into four magnetic field regions.

In Fig. 5.29 we present $R_{\square}(B)$ for three temperatures below $T = 200$mK measured in sample S. The magnetic field ranges from B = -0.5T to $B = 3$T. We labeled the individual sections in the $R(B)$ from I to IV.
The low field ($|B| < 0.5$T) $R(B)$s are symmetric around $B = 0$T. In region I there is a sharp increase in resistance from $B = 0$T to $B = \pm$ 100mT, that becomes even more pronounced for lower temperatures. This increase is sketched in Fig. 5.31 with a black line and reveals an exponential increase in resistance by applying a perpendicular magnetic field. The resistance value of $R_{\square} \sim$ 600-800Ω is higher than the extracted value from the $R(T)$ with fixed magnetic fields. The $T = 200$mK value is comparable, but with decreasing temperature we do not find the sharp drop of resistance as seen in Fig. 5.1 for $B = 0$T. This difference of the resistances can be attributed to the different measurement methods. While in the previously presented data, IV curves have been recorded at a fixed temperature and magnetic field, for the $R(B)$s temperature is fixed, however the magnetic field is ramped continously. In addition, while sweeping from negative to positive magnetic fields two point IVs are ramped up and down continuously. The combination of the magnetic field sweeprate and the time for each IV defines the magnetic field stepwidth for the points in the $R(B)$ curves. This leads to a further increase of the minimum resistance observable with this method.
In the magnetic field range 100mT $< B <$ 1T, we see two effects (region II). First, with decreasing temperature the resistance saturates (curves for $T = 65$mK and $T = 135$mK match). This low temperature saturation of resistance has already been pointed out in section 5.2 and will be further discussed in section 5.4. Second, the $R(B)$ curves exhibit oscillations in magnetic field around an average resistance value which, at least for the two lower temperatures, seems to be magnetic field independent.
By increasing the magnetic field above $B = 1$T (region III) the resistance values start to increase. The positive magnetoresistance is superimposed with oscillations. The resistance increases up to values $R_{\square} \sim 10^7 - 10^8\Omega$ at the magnetic field $B_{\max}$.
At higher magnetic fields $B > B_{\max}$ (region IV) there is a negative magnetoresistance. The $R(B)$s at the two lowest temperatures seem to exhibit oscillations on the NMR side of the magnetoresistance dome as well.
The overall shape of the $R(B)$ is in agreement with the findings in section 5.2. Below $B_{\max}$ there is a positive magnetoresistance, as with increasing magnetic field the Josephson energy $E_{\mathrm{J},0}$ is decreased. Cooper pairs get localized, which leads to an increasing resistance. When approaching $B_{\max}$ the BCS energy gap starts to be supressed by the external magnetic field. Increasing B leads to the formation of single electron solitons due to the breaking up of Cooper pairs. The transport switches from Cooper pair to single electron transport. The resistance decreases as single electrons experience a lower threshold energy, $E_{\mathrm{C,SES}}$, for transport than Cooper pairs, $E_{\mathrm{C,CPS}}$ (see section 4.3 for the introduction of SES and CPS). That increases the conductivity with increasing magnetic field up to the critical magnetic field B_{c}, where all Cooper pairs are broken up.

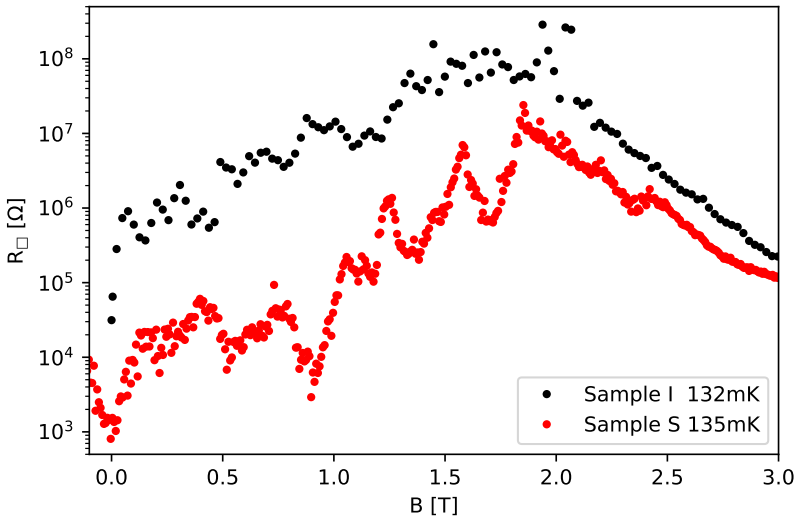

Figure 5.30.: $R(B)$s for sample S (red) and sample I (black) at ∼135mK. At magnetic fields around $B = 0$T both samples exhibit a sharp increase in resistance with increasing magnetic field (region I). The overall resistance values of sample I are higher than for sample S, which agrees with sample S being on the superconducting side of the disorder driven SIT for $B = 0$T and sample I being on the insulatng side. The field $B_{\max}$ is ~ 2T for both samples. Above $B_{\max}$ both samples show a negative magnetoresistance up to 3T.

Fig. 5.30 compares the magnetoresistances of sample S and sample I at a temperature T ∼135mK. The $R(B)$s of both samples (sample S as well as sample I) exhibit a dome like shape and show oscillations in magnetic field below their peak in resistance at $B_{\max}$. The overall resistance values of sample I are an order of magnitude higher at the same temperature and magnetic field compared to sample S. The $R(B)$s confirm the dependence of the resistance on magnetic field and the tendency of sample I being pushed further into the insulating regime as indicated in section 5.2. Considering the logarithmic scaling of the y-axis in Fig. 5.30, the amplitude of the oscillations is one order of magnitude samller for sample S than for sample I.

Let us now take a closer look at the oscillatory component in the $R(B)$s. The oscillations in the $R(B)$s (and $E_{\mathrm{A}}(B)$) are most likely a manifestation of the Aharonov-Bohm effect [200] and quantum interference [18]. For simplicity, we consider a periodic Josephson junction array as seen in Fig. 2.11a) of section 2.2.4. An applied external magnetic field B, perpendicular to the array plane, may penetrate through the normal regions and in our case through the superconducting areas of the islands as typically $\lambda >$ grain size. In the model of a JJA a unit cell is given by superconducting islands enclosing a normal conducting area A_{cell}. This enclosed normal area defines the period of the oscillation.

Charge carriers (Cooper pairs) experience a phase shift by the non-zero vector potential A [200]. The phase difference along a closed path encircling magnetic flux has to be 2π periodic [18, 201]. After summing up all phase differences across junctions and islands the gauge invariant phase difference is given by

$$\gamma = 2\pi \left(n - \frac{\Phi}{\Phi_0} \right) \tag{5.11}$$

The total gauge-invariant phase difference of the closed path around the unit cell is constrained to $2\pi n$ and for each physical situation the equilibrium value n will be the one which minimizes the free energy [201]. This gauge-invariant phase difference enters Eq. 2.53 and the Josephson energy is given by

$$E_{\mathrm{J}}(\Phi) = E_{\mathrm{J},0} \cos(\gamma) = E_{\mathrm{J},0} \cos\left(2\pi \frac{\Phi}{\Phi_0} \right) \tag{5.12}$$

The external magnetic field B needed to achieve one flux quantum per unit cell given by.

$$B_0 = \frac{\Phi_0}{A_{\mathrm{cell}}} \tag{5.13}$$

Eq. 5.12 can be rewritten in terms of the external magnetic field

$$E_{\mathrm{J}}(B) = E_{\mathrm{J},0} \cos\left(2\pi \frac{B}{B_0} \right) \tag{5.14}$$

Variations of external magnetic field lead to an oscillating Josephson coupling. The oscillation period $B_0 = \frac{\Phi_0}{A_{\mathrm{cell}}}$ is defined by the area in the unit cell A_{cell}, which is penetrated by the magnetic field.
In insulating Josephson junction arrays with $E_{\mathrm{C}} \gg E_{\mathrm{J}}$, where the charge transport is dominated by thermally activated Cooper pair solitons, this leads to oscillations in the $R(B)$ curves. The oscillating E_{J} increases/decreases the coupling strength between the superconducting islands. Ref. [80] found oscillations in E_{A} (see Fig. 5.16) with maxima at $B = (n + 1/2)B_0$. The extracted B_0 did well agree with the value calculated using their predefined A_{cell}. Oscillations in $R(B)$ and/or E_{A} with perpendicular magnetic field are taken as a strong indicator for a superconducting ground state, i.e. that Cooper pairs are localized onto superconducting grains separated by normal/insulating areas.
In the case of two dimensional granular aluminum the condition of superconducting islands separated by normal conducting regions is naturally given. However, due to the broad distribution of grain sizes, between a few nm and 100nm (see section 4.2), we might have a broad distribution of the normal regions A_{cell} between the grains as well. The change of E_{J} should therefore be different for the individual enclosed paths around unit cells with different geometry and average out over all unit cell of the granular array. Suprisingly we observe oscillations in the $R(B)$. In Fig. 5.31 we take a closer look at the $R(B)$ for $T = 135$mK. The maxima are indicated by blue lines and the minima by green lines. We find different oscillation periods B_0 for magnetic field region II and III. Region

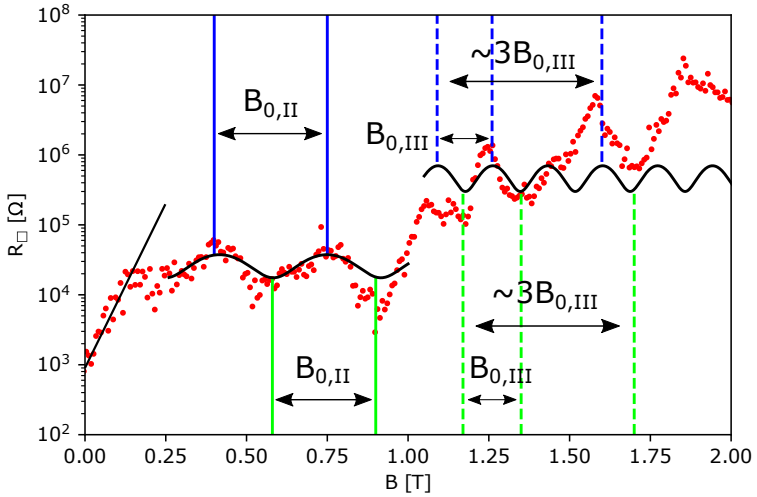

Figure 5.31.: Oscillatory components in the magnetoresistance of **sample S** for $T = 135$mK. The maxima and minima are highlighted by the blue and green vertical lines. The black sinusoidal curves are a guide to the eye. The oscillation period in region II is 330mT and in region III ∼170mT. The black linear curve below $B \sim 100$mT indicates the exponential increase of resistance with increasing magnetic field around $B = 0$T.

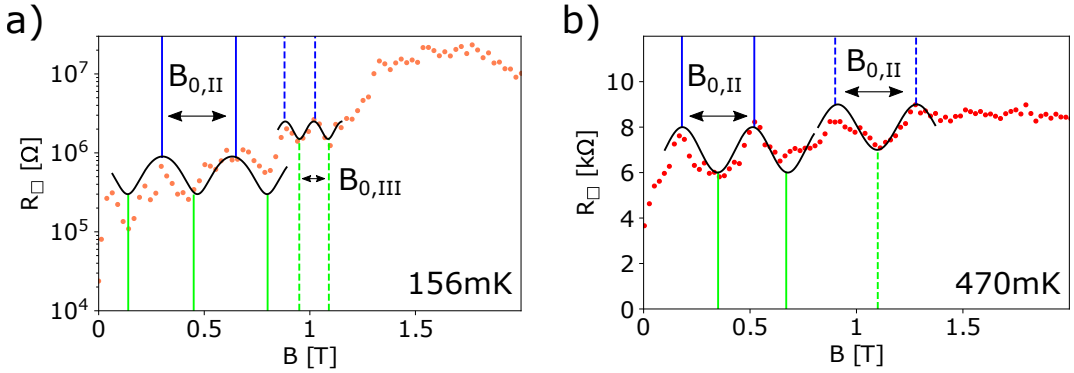

Figure 5.32.: Oscillatory components in the magnetoresistance of **sample I** for 156mK and 470mK. The oscillation period in the low fields is $B_{0,\mathrm{II}} \sim 330$mT as in sample S. The period changes for higher fields to $B_{0,\mathrm{III}} \sim 135$mT ($T = 156$mK) and $B_{0,\mathrm{III}} \sim 370$mT ($T = 470$mK)

II is shown with full lines and region III with dashed lines. Interestingly, the period of region II is approximately two times the period found in region III.
Assuming a simple naive picture of flux penetrating through periodic square shaped unit cells, then the oscillation period of $B_0 \sim 330$mT would correspond to unit cell with length and width of approx. 80nm. While that picture is way too simple for a true granular film, the length of 80nm is not too far off considering grain sizes between a few and ∼100nm.

In sample I we as well see oscillations with period ∼330-370mT in region II (see Fig. 5.32). In the simple picture that leads to the same length and width of unit cell, which is not surprising as both samples have approximately the same grain size distribution. The biggest grains are ∼100nm in both samples. For higher fields the oscillation period is changing. That may be attributed to a change of the average cell area A_{cell}. The trend is that for higher fields the period decreases $B_{0,\text{III}} < B_{0,\text{II}}$, and by Eq. 5.13 A_{cell} increases.

Summary

The magnetoresistance curves of both samples show a dome like shape with a positive magnetoresistance below a magnetic field B_{max} ∼2T and a negative magnetoresistance above. This behaviour is attributed to the effect of the magnetic field on E_J for low fields and on Δ_0 for high fields. This leads to a crossover from CPS transport to SES transport.
In addition, we find oscillations superimposed on the $R(B)$ curves. Such oscillations arise by a magnetic field penetrating a normal area surrounded by a ring of superconducting grains coupled by Josephson junctions. These oscillations are described in the theory for artifical periodic JJAs and have been experimentally observed [80]. In our samples we have a distribution in grain sizes and distances and therefore no periodic structure. Therefore, it is surprising, that we observe oscillations in $R(B)$. On top of this we see a change of the oscillation period at a magnetic field of $B \sim 1$T in both samples. The period shifts to smaller values at higher fields.
The explanation for the oscillations in the granular inhomogeous film remains an open question. The oscillation period is defined by the normal area A_{cell} between the superconducting grains. The distribution of A_{cell} for both of our samples is unknown. In chapter 4.2 we presented a broad grain size distribution and a random grain geometry. A correlation between grain size distribution and the distribution of the normal areas between them is therefor unknown as well. The observed oscillations indicate that the distribution of normal area is not random, but that a specific size is dominating. The extracted oscillation period of $B_0 \sim 330$mT corresponds to an area with width and length of ∼80nm in a periodic square shaped structure. The shift to smaller oscillation periods would require a change in size of the normal area as $B_0 = \frac{\Phi_0}{A_{\text{cell}}}$.

5.4. Anomalous Metallic State in the Vicinity of the Magnetic-Field-Induced SIT

In section 5.2 we discussed the magnetic field induced SIT and indicated that the $R(T)$ curves saturate at the lowest temperatures. Instead of following activated behaviour (Eq. 5.5) all the way to $T = 0$K, there is a crossover to another regime below a specific temperature, defined as T_{cross}. This can be seen in Figs. 5.14a) and 5.18a), for sample S and sample I, respectively.
The temperatures for which the deviation from activated behaviour is found is presented for some selected magnetic fields in Fig. 5.33.

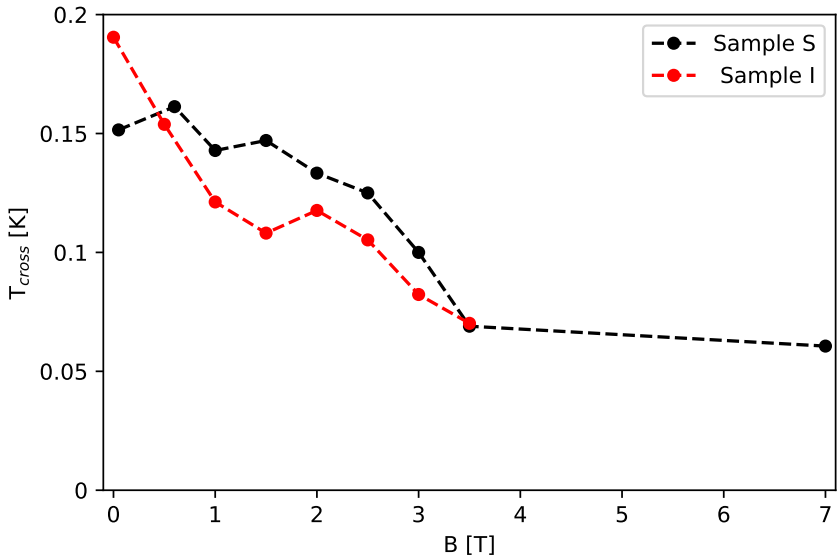

Figure 5.33.: Crossover temperature plotted versus applied perpendicular magnetic field for both samples. For temperatures below the crossover temperature the $R(T)$s do not follow activated behaviour as seen at higher temperatures. The overall tendency is that the crossover shifts to lower values for higher magnetic field values. For sample S the smallest magnetic field exhibiting a resistance increase at low temperatures across a wide temperature range is 50mT.

In Fig. 5.34 we present four $R(T)$ for sample S a) and sample I b) down to the lowest temperatures ∼20mK. Both samples show a deviation from activated behaviour and saturate at the lowest temperatures. The $R(T)$ curves are fitted with two modified activation formula Eq. 5.15 (red) and $R_\square = R_0 \exp\left(\frac{-E_{A,S}}{k_B T}\right) + R_{QF}$ (green). They take the low temperature saturation of resistance into account. The activation energies extracted from those fits are comparable with the activation energies shown in the section 5.2.

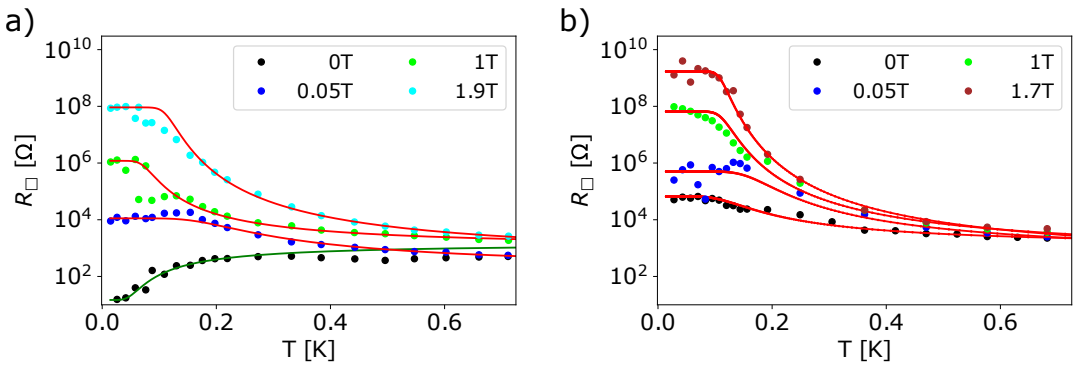

Figure 5.34.: $R(T)$ curves and the fits to the saturation formulas for conductivity (red) Eq. 5.15 and resistivity (green) $R_\square = R_0 \exp\left(\frac{-E_{A,S}}{k_B T}\right) + R_{QF}$. a) Sample S and b) Sample I. In a) the fitting curve for the 0T case indicates a low temperature saturation given only by a single point. This is not sufficient to be conclusive. In addition, a measurement performed at 25mT did show the same curvature but no low temperature saturation, see Fig. 5.35a).

To fit our $R(T)$ curves we follow Ref. [129] and apply the same duality of conductance and resistance saturation for the $R(T)$ curves in the vicinity of the magnetic field induced SIT. The basis is set by the saturation formula proposed by Ref. [80] for the low temperature saturation found in the high field limit of insulating JJAs, which was also used in Section 4.3. The saturation model consists of a temperature independent quantum fluctuation term and a temperature dependent term for the conductance due to thermal activation. On the insulating side, i.e. a saturation of the conductance, the activation energy $E_{A,I}$ and a proportionality prefactor G_0 are introduced. The latter replaces the prefactor $\frac{1}{R_N} - \frac{1}{R_{QF}}$ in Eq. 4.3.

$$G_\square = \frac{1}{R_\square} = G_0 \exp\left(\frac{-E_{A,I}}{k_B T}\right) + \frac{1}{R_{QF}} \tag{5.15}$$

While the data are consistent with a thermally activated resistance $R_\square \sim \exp\left(\frac{-E_{A,S}}{k_B T}\right)$ on the superconducting side, our sensitivity is insufficient to discriminate between superconductivity and a resistance saturation.

One sees in Fig. 5.34a) for sample S that at the lowest temperatures there is an indirect transition from a zero resistive state at $B = 0$T to an insulating state with $R_\square > 10^8\Omega$ at $B \sim 1.9$T with an intermediate metallic regime. Sample I (Fig. 5.34b)) shows a similar behaviour but starts with an insulating trend and the crossover to a metallic state for $B = 0$T already.

The data reveal an intermediate anomalous metallic state (AMS) in between the superconducting and insulating phases of the magnetic field driven superconductor to insulator transition. Such an anomalous metallic state has been seen in various two dimensional material systems, e.g. in two dimensional Josephson junctions arrays [121], gated two dimensional semiconductor-superconductor arrays [122], In-InOx composites [123], ultrathin amorphous gallium films [9] and in amorphous NbSi thin films [124].

The anomalous metallic state has been theoretically presented in section 2.3.3 and reviewed by Kapitulnik et al. [125]. Zhang et al. [129] further investigated the AMS in granular In/InOx composites and showed that the AMS consists of two phases, a failed superconducting and a failed insulating phase, both arising due to quantum fluctuations, i.e. phase and charge fluctuations, respectively. In addition, Zhang et al. [129] propose a phase diagram for granular superconductors, see Fig. 2.20.

As mentioned before, the low temperature resistance is proposed by Ref. [129] to be the sum of a temperature dependent activated term and a temperature independent term associated with quantum fluctuations. In summary, the latter lead to macroscopic quantum tunneling of the phase in case of the failed superconductor and of charge for the failed insulator. The transition from a superconductor to the anomalous metal state is referred to as Superconductor-to-Quantum-Metal Transition (SQMT) and is associated with the destruction of global phase coherence [125, 131, 132], while the transition from the anomalous metal to the insulating state as Quantum-Metal-to-Insulator Transition (QMIT), where the quantum charge fluctuations prevent a Coulomb-blockade-driven insulating state to be established [80, 96, 202]. In the following we present our data, measured in granular aluminum, which are fully consistent with the scenario as explained in section 2.3.3 and the resulting phase diagram for granular superconductors.

5.4.1. Field-induced Superconductor-to-Quantum-Metal Transition in grAl

In Fig. 5.35a) four $R(T)$ curves in the low magnetic field range of sample S are shown. The black horizontal line corresponds to the quantum resistance of Cooper pairs R_Q. We find a magnetic field driven SQMT transition for 25mT $< B <$ 50mT, as for low temperatures the resistance changes by factors and saturates at values larger than R_Q. In

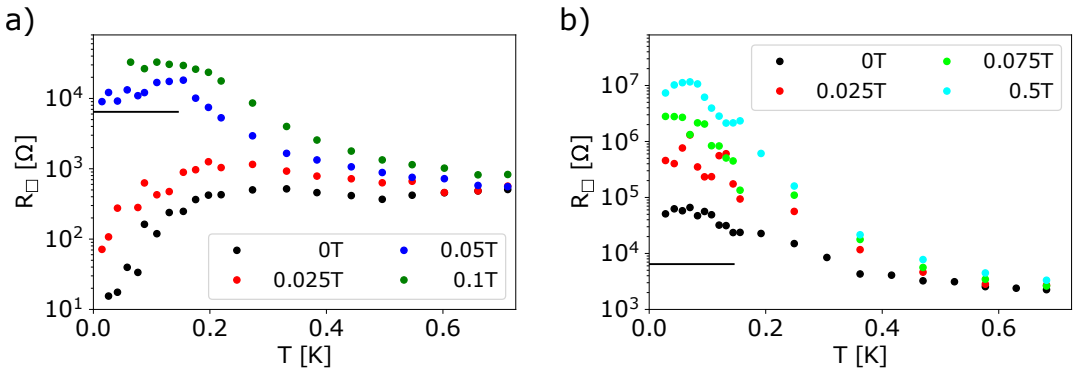

Figure 5.35.: $R(T)$ curves at very low B for Sample S a) and Sample I b). The black horizontal line corresponds to $R_Q = 6.45\text{k}\Omega$.

Fig. 5.35a) we see a downturn in resistance for magnetic fields of $B = 0$T and $B = 25$mT. The resistance value of the zero magnetic field curve is below our measurement resolution and indicates a zero resistive state. By applying 25mT the $R(T)$ as well shows a downturn. However, the resistance does not drop to zero above our lowest temperature. The $B =$ 50mT curve shows an upturn in resistance with a low temperature saturation at a value $R_{QF} \sim 10\text{k}\Omega > R_Q$. The low temperature extrapolation of the green curve for 100mT, shows an even higher R_{QF}. That findings indicate a transition from a superconducting zero resistive state to a quantum metal state by applying 50mT perpendicular. In the magnetic field range between 25mT and 50mT we do not have a data set to show the failed superconducting state with $R_{QF} < R_Q$. Above $B = 50$mT the values of $R_{QF} > R_Q$ indicate that we are in the failed insulating regime.
Sample I is in the failed insulator state for $B = 0$T as the resistance increases with decreasing temperature and saturates at a value $R_{QF} > R_Q$, Fig. 5.35b).

5.4.2. Field-induced Quantum-Metal-to-Insulator Transition in grAl

In Fig. 5.35b) sample I has been investigated down to 28mK for magnetic fields below $B = 0.5$T and found to be in the failed insulating state. In Fig. 5.36 we increase the magnetic field up to $B = 3.5$T for sample I. As there is a peak in resistance around $B = 2.1$T, we separated the data into two plots. Fig. 5.36a) shows the $R(T)$ curves from 0.4T to 2.1T, while 5.36b) shows the curves for $B > 2.1$T.

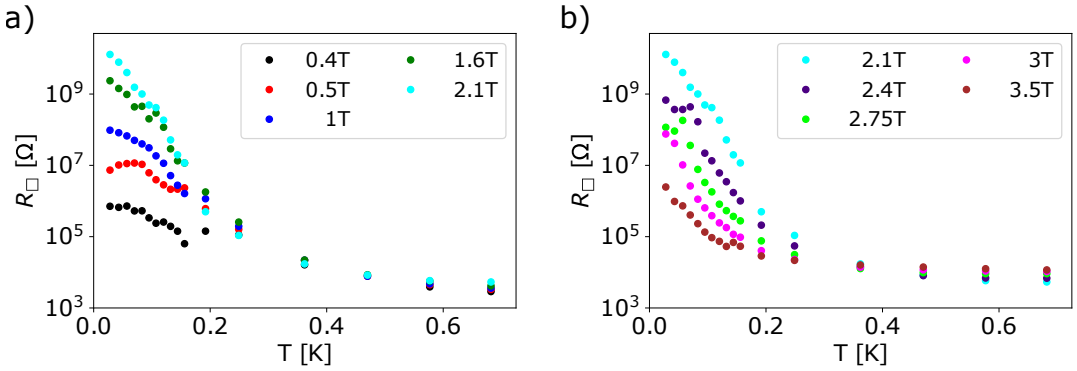

Figure 5.36.: Sample I: a) $R(T)$ curves for magnetic field values below $B_{\max}$ and b) for magnetic fields above $B_{\max}$. The crossover from the anomalous metal state to a Bose insulator is indictated by the vanishing of the saturation in the magnetic field range 0.5T - 2.1T. The resistance continuously increases for decreasing temperatures, however, it does not follow activated behaviour as seen at higher temperatures.

In Fig. 5.36a), for better visualization, we have only shown five magnetic fields out of more than 20. In addition to Fig. 5.34b), where we presented a resistance saturation at low temperatures up to $B = 1.7$T, we here show curves above $B = 0.5$T which do not saturate. A possible explanation could be the oscillating behaviour of the magnetoresistance seen in both samples and shown in Fig. 5.32 for sample I. To resolve this issue the magnetic field stepsize for the $R(T)$ measurements has to be decreased in a future experiment to a value much smaller than the oscillation period $B_0 \sim 330$mT.
Even those $R(T)$ curves without saturation deviate from activated behaviour at the lowest temperatures and show a lower resistance than predicted by $R_\square \sim \exp\left(\frac{-E_{\mathrm{A,I}}}{k_{\mathrm{B}}T}\right)$. That crossover from curves with saturation to those without can be interpreted as the crossover from failed insulating anomalous metal state to a true Bose insulating state with increasing magnetic field.

By further increasing the magnetic field from $B_{\max} \sim$2T to $B \sim 2.75$T, no saturation is found and the overall resistance values decrease again (see Fig. 5.36b). The low temperature data, $T < 100$mK, does as well deviate from activated behaviour below $B < 2.5$T.

Above $B = 2.75$T the sample approaches the normal state, i.e. the grains gradually become normal conducting. By applying the proposed activation formula by [80], Eq. 5.15, for the normal conducting state, we expect the $R(T)$ curves to saturate at the lowest temperatures for $B > B_c$ due to quantum fluctuations of charge. This has been shown for sample S at 7T in Fig. 4.15b). The fit to the data by Eq. 5.15 is presented in Fig. 4.16.
For sample I, the R(T) curve, at the maximum applied magnetic field of $B = 3.5$T, follows activated behaviour down to $T = 26$mK and we do not observe a low temperature saturation. The saturation may either set in for higher magnetic fields or at temperatures below our minimum temperature of $T = 26$mK in this measurement.

Summary

By evaluating the insulating $R(T)$ curves of our samples in section 5.2 we find, that below a magnetic field dependent temperature T_{cross} the curves deviate from activated behaviour. The curves show lower $R_\square$ values than expected from activated behaviour and we find a saturation of resistance in the vicinity of the B-SIT.
This behaviour demonstrates the existence of an anomalous metal state (see Ref. [125]), which may be separated into a failed superconducting state and a failed insulating state [129]. For low magnetic fields we see a transition from the superconducting state of sample S to a quantum metal state with $B = 50$mT (SQMT). For higher fields we see another transition from the quantum metal state to a Bose-insulating state in a broad range of magnetic fields (QMIT). At even higher fields superconductivity is destroyed in the grains and the granular film turns into a Fermi-insulator ($B > 3$T in both samples). Our findings are in agreement with the proposed phase diagram for granular superconductors by [129] presented in Fig. 2.20 after a study in granular In-InOx composites.

5.5. The Differential Resistance at Bias Voltages ≫ Threshold Voltage

Up to now we have focused mainly on the zero bias resistance. We will now turn to the differential resistance measured at bias voltages $V_{\mathrm{bias}} \gg V_{\mathrm{T}}$, to see how the charge transport is mediated in that regime.

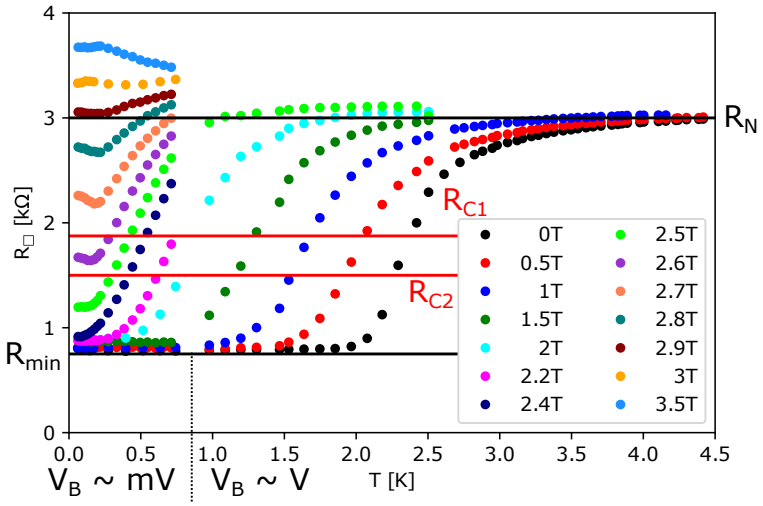

Figure 5.37.: Sample S above V_{T}. The $R(T)$s are shown for a set of magnetic fields between B = 0T and B = 3.5T. For B < 2T, the $R(T)$s saturate at R_{min}. The temperature at which the resistance approaches R_{min} decreases with increasing magnetic field. Magnetic fields above 2T increase the resistance from R_{min} to higher values. The lowest temperature part of the $R(T)$s crosses R_{N} for $B \sim$ 2.8-2.9T. In the magnetic field range 2.9T < B < 3.5T the TCR switches sign from positive to negative, indicating an increase of resistance with decreasing temperature above $B \sim$ 3T. The 3T curve is more or less temperature independent. R_{c1} = 1.875kΩ and R_{c2} = 1.5kΩ are the resistances used for the extraction of $B_{\mathrm{c}}(T)$ (see Fig. 5.40 below) using the half-resistance criterion $R_{\mathrm{c}} = (R_{\mathrm{N}}+R_{\mathrm{ref}})/2$ (see text below). The vertical dotted line at $T \sim$ 800mK separates the low temperature, V_{B} ∼mV, from the high temperature, V_{B} ∼V, region.

Fig. 5.37 presents the temperature dependence of the differential resistance measured with voltages higher than the threshold voltage V_{T}. While the low temperature part of the $R(T)$, T < 800mK, was measured with a voltage bias at ≈ 1mV, the high temperature part T > 800mK was measured with a voltage in the order of volts. The corresponding currents were ≈ 20nA and ≈ 5μA. The smooth transition of the low temperature $R(T)$s into the high temperature curves indicates, that the differential resistance above the threshold voltage $V_{\mathrm{T}} \leq 150\mu$V is roughly independent on bias voltage/current, i.e. follows ohmic behavior. There is an offset of 85Ω between the low temperature part of the $R(T)$s

and the high temperature part of the $R(T)$s, that has been removed to match the zero magnetic field $R(T)$s. In zero field the resistance exhibits a plateau of $R_{\mathrm{min}} \sim 750\Omega$ down to the lowest temperatures $T = 61\mathrm{mK}$. That plateau has already been presented for $T > 1\mathrm{K}$ in section 5.1. By increasing the perpendicular magnetic field we see a decrease of the critical temperature T_{c} with increasing magnetic field. The low temperature part of the $R(T)$s smoothly crosses over from R_{min}, above R_{N} to a maximum in resistance at $B \sim 4\mathrm{T}$ and saturates at values close, but below this maximum for higher magnetic fields up to 7T (curves for $B > 3.5\mathrm{T}$ are not shown in this plot). Interestingly, the lowest temperature parts of the $R(T)$ in the transition regime $2\mathrm{T} < B < 3\mathrm{T}$ show magnetic field dependent saturation values and the $R(T)$s for $B = 2.6\mathrm{T}$, 2.7T and 2.8T even show an upturn in resistance for very low temperatures. The minima in the $R(T)$s occur at $R = 1620\Omega$ and $T = 0.15\mathrm{K}$ at $B = 2.6\mathrm{T}$, $R = 2175\Omega$ and $T = 0.185\mathrm{K}$ at $B = 2.7\mathrm{T}$ and $R = 2650\Omega$ and $T = 0.215\mathrm{K}$ at $B = 2.8\mathrm{T}$. The $R(T)$ curves in Fig. 5.37 strongly resembles $R(T)$ curves measured in 3D granular aluminum (see section 4.1), for which minima have been found in the $R(T)$s at temperatures, which correspond to maxima in the $B_{\mathrm{c}}(T)$. We present the low temperature part of the $R(T)$s in Fig. 5.38 to compare it to Fig. 4.4b).

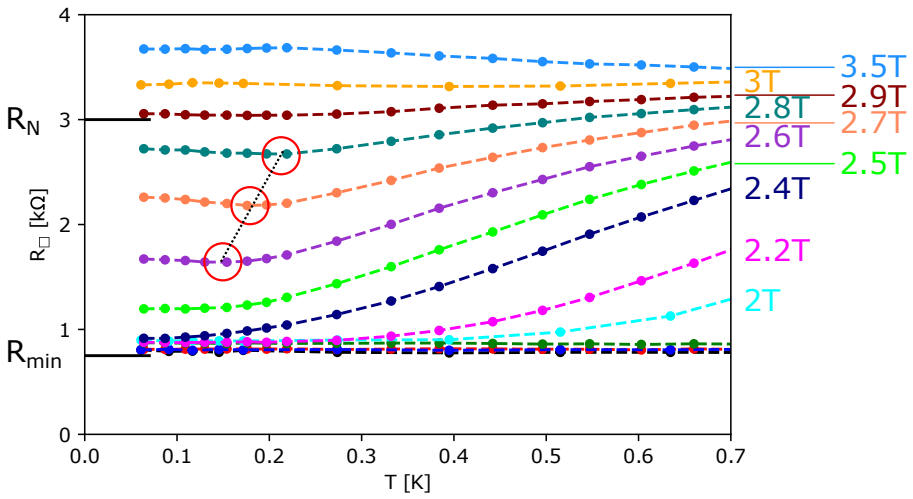

Figure 5.38.: Sample S above V_{T}. The low temperature part of the $R(T)$s reveal the crossover from $R(T)$s with positive TCR to $R(T)$s with negative TCR. In the intermediate magnetic field range we find a low temperature saturation arising from the plateau of R_{min} for $B = 2\mathrm{T}$, 2.2T, 2.4T and 2.5T. The curves for $B = 2.6\mathrm{T}$, 2.7T, and 2.8T show a high temperature positive TCR, which switches to a low temperature negative TCR. The corresponding minima are marked with red circles. The black dotted line indicates the approximately linear increase of the minima temperature with magnetic field. The non-labelled low magnetic fields follow the same colour coding as shown in Fig. 5.37.

We replot some selected temperatures in the $R(B)$ configuration in Fig. 5.39. With decreasing temperature we find the broad transition from the low resistive state to the normal state to become very sharp below $T \sim 250$mK. The same behaviour has been found in Fig. 4.4a).

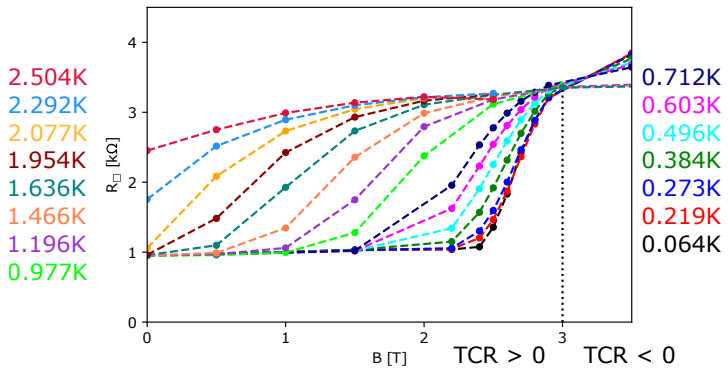

Figure 5.39.: Resistive state above V_T - $R(B)$ curves for a set of temperatures listed left and right to the plot. With decreasing temperature the transition becomes very sharp and at $B = 3$T the TCR switches sign from positive to negative.

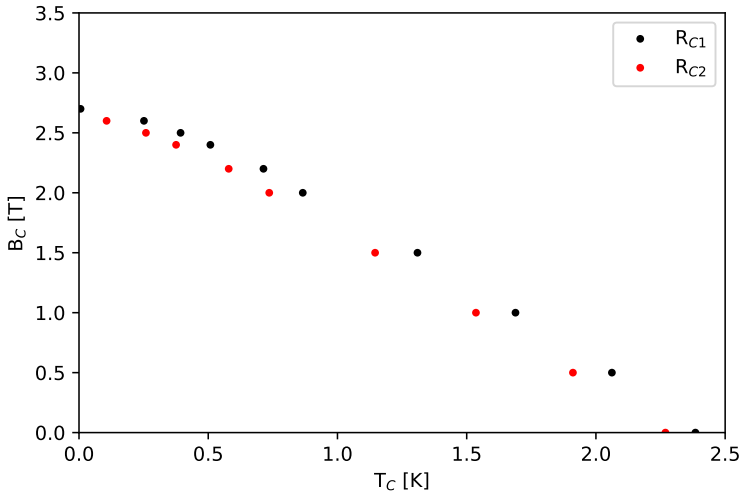

Figure 5.40.: $B_c(T)$: R_{c1} and R_{c2} correspond to the criteria as explained in the text.

For a superconducting sample with zero resistance below T_c the half-resistance criterion reads $R_c = R_N/2$. However, in our data the resistance does not drop to zero, but saturates at a value R_{min}. To deduce the temperature dependence of the upper critical magnetic two options may be applied, $R_{c1} = (R_N+R_{min})/2$ or $R_{c2} = R_N/2$. The resistance values

of the two criteria are shown as red horizontal lines in Fig. 5.37. The temperature dependence of the upper critical field $B_c(T)$ for both criteria is shown in Fig. 5.40.
The critical temperature for $B = 0$T is $T_{c,0} \sim 2.3 - 2.4$K and the critical magnetic field at $T = 0$K $B_c \sim 2.6 - 2.7$T. The temperature dependence of the critical magnetic field follows a linear increase with decreasing temperatures with a slight decrease of the slope below a temperature $T \sim 0.5$K.

In a future experiment the transition from the "anomalous" $R_N/3$ state to R_N should be measured with a much smaller stepsize or in a continuous magnetic field sweep.

Summary

In this section we studied the magnetic field dependence of the $R(T)$ curves extracted at a bias voltage far above the zero bias limit. Instead of a drop to a zero resistive state, as seen for 3D granular aluminum (see section 4.1), we find a temperature independent R_{min} $\sim 750\ \Omega$. This may be attributed to the reduced thickness of our samples compared to the 3D samples. In section 4.2 we have shown that the morphology (grain size distribution, grain separation distances) of a granular aluminum 2D film is dramatically different to a 3D film.
Besides the saturation of resistance at R_{min} for low magnetic fields, the magnetic field dependence is similar to the findings for thick grAl in Ref. [171]. With increasing magnetic field we see a shift of the critical temperature T_c of the anomalous state R_{min} to lower values. For magnetic fields $B > 1.5$T R_{min} increases up to values of $R_{min} \sim 3.8\text{k}\Omega > R_N$. This increase is attributed to the suppression of the local superconducting energy gap $\Delta(B)$ on the grains. This transition with magnetic field becomes sharp for the lowest temperatures.
For three $R(T)$s with magnetic fields in the transition we find minima for the temperature coefficient resistance. The TCR switches from positive at the higher temperature side to negative at lower temperatures side of the minima. Such minima in the $R(T)$ have also been found in Ref. [171]. There the temperature of the minima was consistent with a maximum found in their $B_{c2}(T)$ curves. To verify this for our sample we would need to measure more $R(T)$ curves inside the transition with magnetic field.
The evalution of our $B_{c2}(T)$ gives a critical temperature of $T_{c,0}$ ∼2.3-2.4K and an upper critical field $B_{c2}(T = 0) \sim 2.6$-2.7T. Our film has a sheet resistance of $R_N = 3\text{k}\Omega$. R_N can be converted into a three dimensional resistivity $\rho = R_N \cdot d$. With $d \sim 6$nm our ρ_N $\sim 1800\mu\Omega$cm. A 3D film with comparable resistivity at 4K, $\rho_{4.2K} = 1687\mu\Omega$cm, has a critical temperature $T_c = 2.62$K and a upper critical magnetic field of $B_{c2} = 3.98$T. The critical temperature is comparable to our value and higher critical magnetic field value may be attributed to the change of morphology.

6. Niobium-Silicon in Perpendicular Magnetic Field

In this chapter we report low temperature magnetic field properties of two amorphous niobium-silicon thin film alloys. Due to its high tunability, e.g. varying the niobium concentration, film thickness or heat treatment, Nb_xSi_{1-x} is a good model to study the SIT in homogenously disordered thin films. In strongly disordered superconductors the electronic ground state is determined by the competition between Coulomb interaction, disorder and superconductivity as has been shown for granular aluminum in chapter 5. In contrast to granular aluminum thin films, NbSi thin films have been shown to be continuous, amorphous and structurally non-granular down to a thickness of 2.5nm. The electron mean free path is estimated to be comparable to the interatomic distance [72].

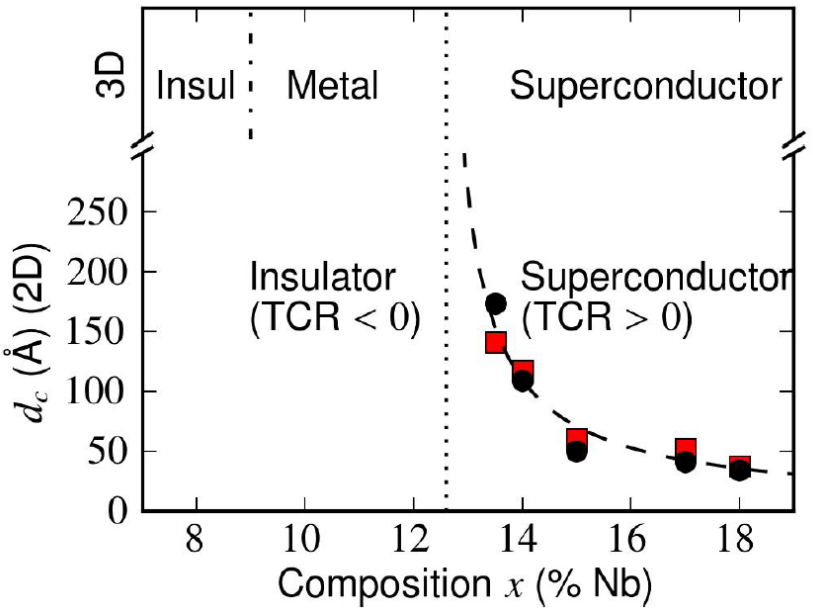

Figure 6.1.: Phase diagram as a function of niobium concentration and film thickness. The black dots and red squares correspond to two different methods to determine the critical thickness (see Ref. [203] for details). The dashed line is the best fit to $d_c = d_0 \left(\frac{x-x_c}{x_c}\right)^{\alpha}$ and the dotted vertical line corresponds to the critical composition x_c. Picture taken from [203].

Ref. [203] studied the thickness-tuned SIT for different niobium concentrations ranging from $x = 13,5\%$ to $x = 18\%$ and thicknesses between 20Å and 500Å. The reduction of thickness progressively drives the system from the superconducting state towards an insulating state. The relation between the critical temperature T_c and the film thickness is found to be linear and scale with $T_c \sim 1/d$. Ref. [203] presents a phase diagram for a function of niobium concentration x and film thickness d (see Fig. 6.1).
The phase diagram reveals, that the critical thickness d_c, separating the superconducting regime from the insulating one, can be tuned by the film composition. With decreasing niobium concentration d_c seems to diverge with a power law given by $d_c = d_0 \left(\frac{x-x_c}{x_c}\right)^{\alpha}$. The critical concentration was found to be $x_c \sim 12.4\%$, $d_0 \sim 17 \pm 7$Å and $\alpha \sim -0.9$. Interestingly, the critical thicknesses may be as large as a few hundred of Å. This is much larger than what has been found in pure metal films (a few monolayers), e.g. [63], or other alloys (few tens of Å), e.g. [204].

The two samples presented in this chapter have been provided by C. Marrache-Kikuchi[1] and have a composition of 13,5% niobium and 86,5% silicon. For a niobium concentration of $x = 13,5\%$ we expect a transition to a superconducting, zero resistance, state at low temperatures for films with a thickness above a critical thickness of $d_c \sim 15$nm and an insulating behaviour for thinner films (see Fig. 6.1).
Sample one, a 23nm film, shows a transition to a superconducting state. It will be referred to as **NbSi-Superconducting (NbSi-S)**. The second sample was grown to a film thickness of 5nm only and shows an insulating behavior with a low temperature saturation at the lowest temperatures. As the saturation resistance is in the kΩ range, the latter will be therefore named **NbSi-Metallic (NbSi-M)**. The evolution of the resistance with temperature in the zero magnetic field case can be seen in Fig. 6.5.

The samples consist of the following layers:

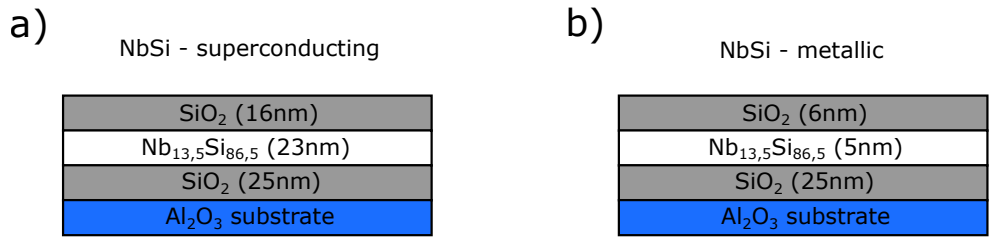

Figure 6.2.: Composition of both NbSi samples a) NbSi-Superconducting, b) NbSi-Metallic.

Both samples have been grown onto Al_2O_3 substrate with a 25nm thick SiO_2 underlayer. To protect the thin NbSi film both samples have been capped with a SiO_2 overlayer.

[1] Université Paris-Saclay, CNRS/IN2P3, IJCLab, 91405, Orsay, France

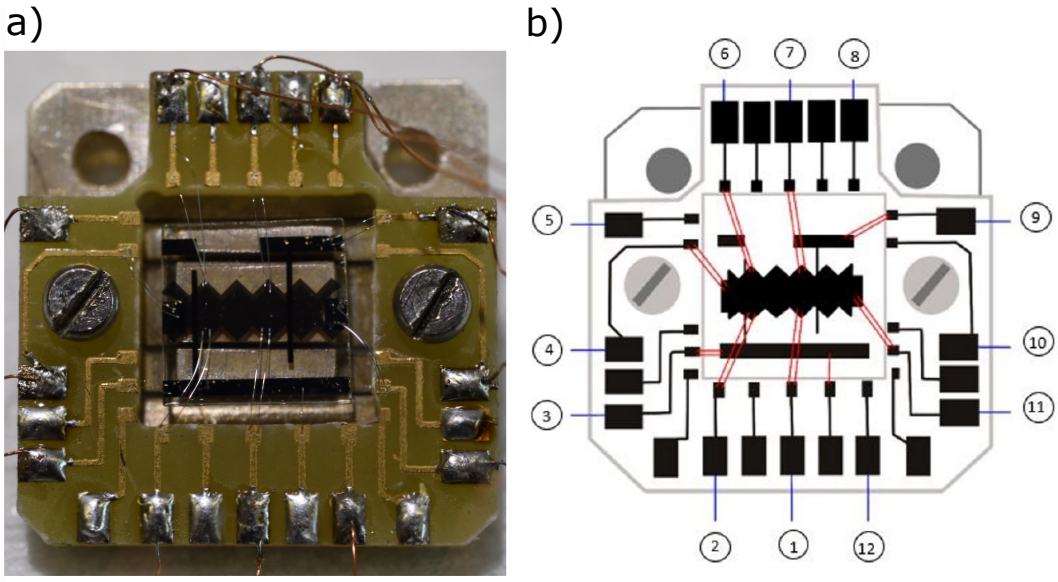

Figure 6.3.: a) Optical image of the sawtooth structured NbSi sample glued onto the silver sample holder for good thermal connection. The sample holder consists of a PCB onto which the mesurement lines are soldered. The final connection between PCB and sample is done with aluminum bond wires. The image was taken by S. Feyrer. b) Sketch of a): The pin layout is shown, where the red lines are the aluminum bondwires. Image and figure taken from [151].

Both samples were provided with a sawtooth structure as seen in Fig. 6.3a). The sawtooth pattern serves the purpose of supressing edge effects in co-deposition of Nb and Si. They have been glued onto the same silver sample holder with PMMA-glue. The pin configuration on the PCB board is presented in b) and is the same for both samples. The measurements were performed in a four-point geometry, where the current was sent through two outer contacts (4 and 11) and the voltage was measured over two inner contacts (6 and 7) spanning over 2 sheets. The data on the superconducting sample was collected together with two bachelor students [151, 152]. The metallic sample has been measured after those thesis works together with A. Weitzel.

A first characterization for sample NbSi-S in zero magnetic field was done by measuring DC current voltage characteristics at $T = 6$K and at the lowest temperature of $T \sim 11$mK. Both curves can be seen in Fig. 6.4.

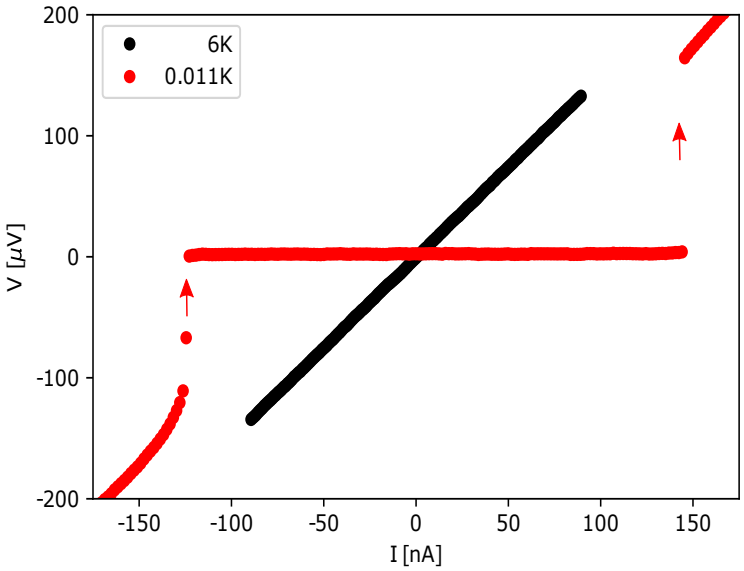

Figure 6.4.: NbSi-S: Comparison of base temperature IV (red) and normal state IV at 6K in zero magnetic field. The IV in the normal conducting state above the critical temperature is linear with a sheet resistance $R_\square \sim 750\Omega$. At base temperature $T < T_c$ the IVs reveal a zero voltage state below a critical current of $I_c \sim 125 - 150$nA.

At 6K the zero bias differential resistance is $R_\square(6\text{K}) = 750\Omega$, while the red curve at $T = 11$mK shows a horizontal line around zero bias indicating a zero voltage state, hence a zero resistive state for $R_\square(11\text{mK})$. The IVs are measured from negative bias currents to positive bias currents. The asymmetry is attributed to electron heating effects. The corresponding critical current is $I_c = 150$nA.
From this point on the measurements were performed by standard AC lock-in measurements. For sample NbSi-S we use a current excitation of 10nA to stay in the zero bias limit ($I < I_c$). The current excitation for the AC measurements of sample NbSi-M is $I \sim 0.5$nA. For AC currents with amplitude $I > 1$nA, we saw an impact in the $R(T)$ curves. To avoid this electron heating effect we reduced our amplitude to 0.5nA.
In Fig. 6.5 both $B = 0$T $R(T)$ curves are presented. While the resistance of the superconducting sample drops from $R_\square(350\text{mK})$ approx. 640Ω down to a very small resistance around the measurement resolution of 0.1Ω below $T \approx 70$mK, the metallic sample shows an upturn from $R_\square(350\text{mK}) \approx 8.5\text{k}\Omega$ to a $R_\square$ of $12.5\text{k}\Omega$ at the lowest temperatures $T <$ 35-40mK. The behaviour in zero field is as expected for a thickness induced SIT for a niobium concentration of $x = 13,5\%$, where Ref. [72] found a critical thickness $d_c \sim 15$nm.

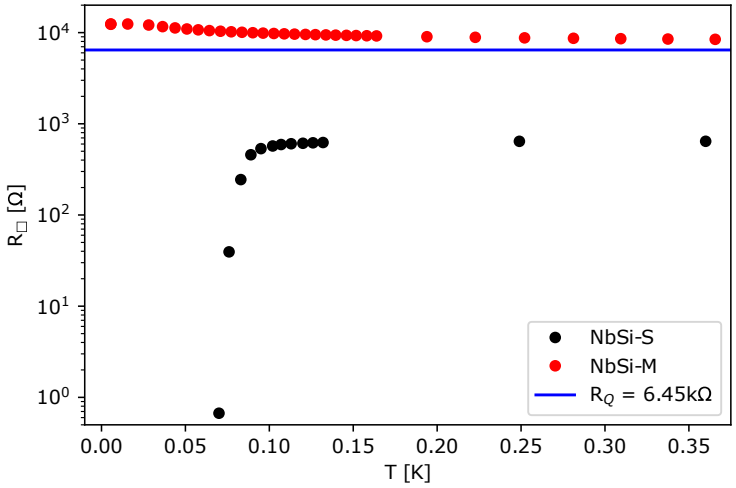

Figure 6.5.: Comparison of low temperature behaviour of the sheet resistance $R_\square$ in zero magnetic field for sample NbSi-S (black data points) and NbSi-M (red data points). The blue line indicates the resistance quantum for Cooper pairs $R_Q = 6.45\text{k}\Omega$. Sample NbSi-S shows a sharp transition to a zero resistive state with $T_c \sim 86\text{mK}$. For NbSi-M the resistance increases with decreasing temperature but saturates at the lowest temperatures.

The dependence of the two $R(T)$ curves on disorder (i.e. given by the sheet resistance at $T > T_c$) as well as the absolute values of $R_\square$ presented in Fig. 6.5 agree well with the data of Couëdo et al. [124] shown in Fig. 6.6. The authors of Ref. [124] focused on the SIT in zero magnetic field, where the disorder has been tuned by thermal heat treatment at various temperatures θ_{ht}. The heat treatment was performed under a flowing nitrogen atmosphere for one hour. The as-deposited films have experienced $\theta_{ht} = 70°\text{C}$ due to heating during the deposition process.

The authors of Ref. [124] found dissipative metallic phases, when tuning NbSi samples across the superconductor to insulator transition. They find that all of their films fall into one of four categories. Each has been identified in a 23nm thick amorphous $Nb_{13,5}Si_{86,5}$ sample, which is shown in Fig. 6.6a). The as-deposited film exhibits a zero resistive, superconducting state below a well defined critical temperature T_c. The temperature coefficient of resistance (TCR) is positive. Thermal treatment decreases the normal state conductivity σ_N, i.e. increases disorder and hence R_N. For heat treatments between 110°C and 140°C the low temperature TCR stays positive, but the sheet resistance is finite at the lowest temperatures $T = 10\text{mK}$. In this regime they find a low temperature saturation of resistance. The dissipative phase with positive TCR and a finite resistance at the lowest temperature is referred to as metal 1.

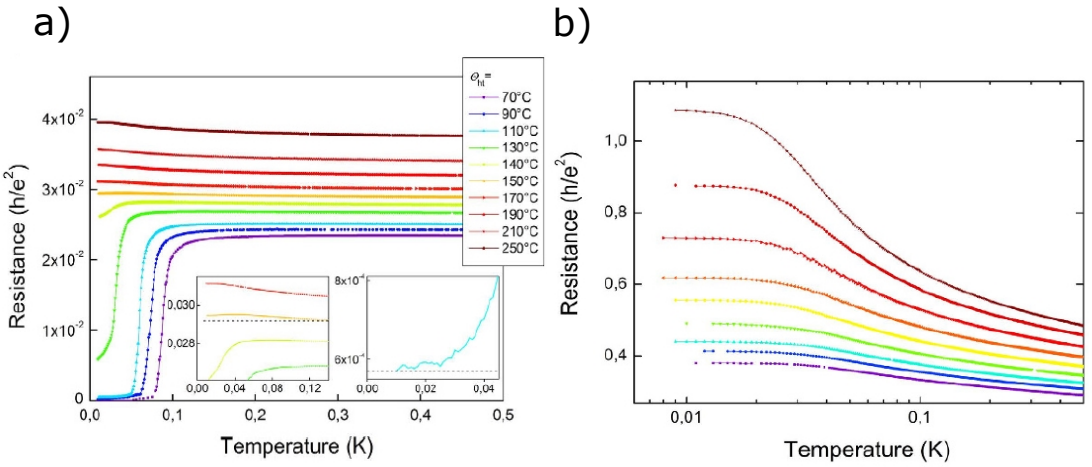

Figure 6.6.: a) Set of $R(T)$ curves for different thermal treatments for a 23nm thin a-$Nb_{13,5}Si_{86,5}$. The two insets show the transition from positive to negativ TCR with increasing temperature of thermal treatment and the non-vanishing resistance at low temperatures for a heat treatment of 110°. b) Set of $R(T)$ curves for different thermal treatments for a 5nm thin a-$Nb_{13,5}Si_{86,5}$. The resistance increases as expected for insulating behaviour due to $d < d_c$, but saturates at the lowest temperatures. The resistance is measured in units of h/e^2. Figures taken from [124].

Further increasing the temperature θ_{ht} above 140°C leads to a change of sign of the TCR. The resistance increases with decreasing temperature. This is a signature of an insulating behaviour. However, the resistance does not diverge in this regime, but saturates at a finite resistance at the lowest temperatures. This regime is called metal 2.

The dependence of the shape of the $R(T)$ curves on disorder (given by thermal heat treatment) of Ref. [124] shown in Fig. 6.6a) as well as the low temperature saturation of resistance shown in Fig. 6.6a) and depicted in more detail on the insulating side of the SIT in Fig. 6.6b) resembles the findings of an anomalous metallic state [125, 129] in the vicinity of a magnetic field driven SIT in granular superconductors. Such an anomalous metallic state and its two corresponding phases (failed superconductor and failed insulator) have been shown by Ref. [129] in thin granular In/InOx composites. In addition, the data for our ultra-thin granular aluminum films, presented in section 5.4, match well with the proposed anomalous metallic state. In case of the presented NbSi data, following the notation of Ref. [129], metal 1 is comparable to a failed superconducting state and metal 2 to a failed insulating state.

At even larger disorder the sample may become insulating with a diverging resistance at the lowest temperatures. This behaviour has been seen by Ref. [124] in other insulating NbSi samples with $\sigma_N < \frac{e^2}{h}$, where the resistance follows the Arrhenius law for activated behaviour $R(T) = R_0 \exp(T_0/T)$ down to the lowest temperatures. For the sample

presented in Fig. 6.6 this regime was not reached. Ref. [124] closer investigated the metal 2 phase in a 5nm thin $Nb_{13,5\%}Si_{86,5\%}$ sample. The curves for different heat treatments are shown in Fig. 6.6b). As has been explained in that regime, the $R(T)$ shows an insulating-like behaviour with a increasing resistance with decreasing temperature and a low temperature saturation of resistance. Ref. [124] hypothesises that the metal 1

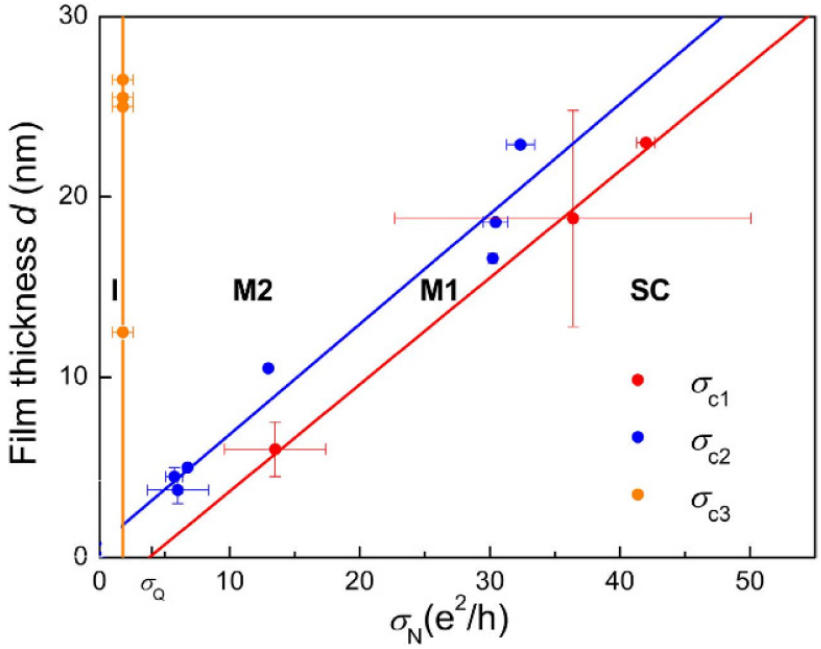

Figure 6.7.: Phase diagram as a function of thickness and normal state conductivity. The red line separates the superconducting state from the metal 1/failed superconducting state, while the blue line separates the metal 1/failed superconducting state from the metal 2/failed insulating state. At lower normal state conductivities, i.e. at higher normal state sheet resistances, there is another transition marked by the vertical orange line to a true insulating state with activated behaviour down to the lowest temperatures. σ_{c1}, σ_{c2} and σ_{c3} represent the critical conductivities for the corresponding transitions between the different phases in different samples. Figure taken from [124].

corresponds to a phase where short living Cooper pairs survive locally, but global phase coherence is lost due to superconducting fluctuations. The importance of superconducting fluctuations is explained by the continuous evolution of the critical temperature to smaller values during the transition form the superconducting state into the metal 1 state. However, it is argued that such a behaviour requires built in inhomogeneities, which have not been found in NbSi and is morphologically homogenous. In the metal 2 phase the transport is governed by the normal state conductivity σ_N only. Therefore, it is argued that there might be a crossover to a quasi-particle dominated regime, where the saturation of resistance may be explained by a parallel channel of conduction, which short-circuits localized fermions. The second metallic regime is found to terminate at

$\sigma_N \sim e^2/h$, below which the transport shows activated behaviour down to the lowest temperatures. The proposed phase diagram by [124] is shown in Fig. 6.7. It reveals the two metallic phases in between the superconducting phase and the insulating phase of NbSi. By approaching $d \to 0$, the metal 2 phase vanishes, while the metal 1 phase persists even for $d \to 0$. The conductivity, which separates the superconducting state from the metal 1 phase extrapolates to $\sigma_Q = 4e^2/h$.

In section 5.4 we focused on metallic phases in the vicinity of the magnetic field induced SIT in ultra-thin granular aluminum. The evaluation and theoretical explanation of this anomalous metallic state followed Ref. [125] and [129]. By increasing a perpendicular magnetic field, Ref. [129] showed that in natural granular In-InOx composites two intermediate metallic phases arise in the vicinity of the magnetic field driven SIT, which are governed by either phase or charge fluctuations and lead to a low temperature saturation of resistance on the superconducting and insulating side of the SIT, respectively. The used model consists of superconducting grains coupled by Josephson weak links, where the interplay between E_J and E_C is the tuning parameter.
NbSi is morphologically homogenous therefore the model of superconducting grains inside an insulating matrix is not applicable. Nevertheless, the great similarity to granular systems indicates an emergent electronic granularity [64, 65]. The underlying mechanism of the superconductor to insulator transition in a-NbSi is still a controversial issue. While both, fermionic as well as bosonic scenario, may lead to an insulating state, the nature of the insulating ground state is an open question.
The strong similarities to granular films and hence the indication of an electronic granularity agrees with a bosonic scenario, where superconducting grains are coupled by Josephson links. The activated behaviour found on the insulating side of the SIT is therefore determined by charging energies. In a homogenously disordered system, like NbSi, an effective electronic granularity may arise due to a diverging localization length ξ_{loc} (self-induced granularity). However, until 2021 no signs of a bosonic insulating state had been found. [205]
Humbert et al. [205] studied high resistive NbSi samples and found an overactivated behaviour by approaching the SIT from the insulating side. The term overactivation refers to an increase of the activation energy at the lowest temperatures. In an Arrhenius plot, the linear slope (E_A) at relatively high temperatures shows an upturn to a higher activation energy at the lowest temperatures (see Fig. 6.8). Since the overactivated behaviour is only found close to the SIT, Ref. [205] argues that this is connected to superconductivity, which sets in locally in some effective grains. As the behaviour is insulating, no global phase coherence is achieved. The authors conclude that the increase of the activation energy at the lowest temperatures is due to the formation of Cooper pairs. The existence of Cooper pairs on the insulating side of the SIT in NbSi is surprising, because there has not yet been any evidence for a bosonic insulating state in that material system and indicates a possible bosonic scenario for the SIT in a-NbSi [205].

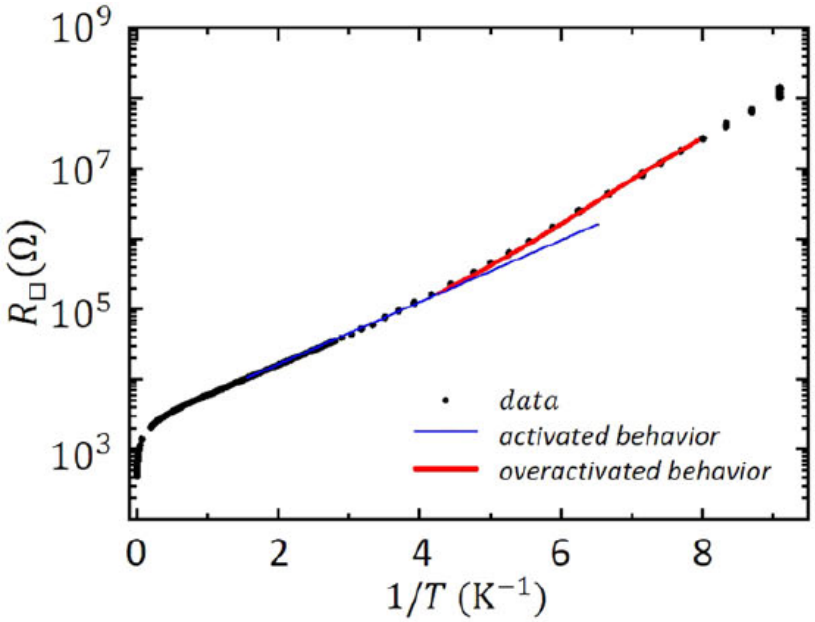

Figure 6.8.: Activated behaviour on the insulating side, but close to the SIT. The Arrhenius plot shows a crossover from a high temperature activation to a low temperature overactiation. The activation energy in the overactivated regime is higher than the activation energy in the activation regime. Figure taken from [205].

In this thesis two NbSi samples have been exposed to a perpendicular magnetic field. All above mentioned transitions from the superconducting to the insulating state in NbSi have been performed in zero field. The response to an external magnetic field may add another turning knob and reveal the nature of the electronic groundstate.
The superconducting sample is in its initial state, as-deposited (compare to Fig. 6.6a) (purple curve)). The metallic sample had seen a heat treatment at a temperature of 90°C for one hour (compare to Fig. 6.6b) (dark blue curve)) for $B = 0$T.

6.1. Superconductor-Metal Transition

Sample NbSi-S is exposed to perpendicular magnetic fields up to 0.4T for temperatures below $T = 0.15$K. In Fig. 6.9a) the magnetoresistance isotherms are shown, while in b) the same data is presented in a $R(T)$ configuration. In b) the $B = 0$T curve is substituted with the higher resolution $R(T)$ as shown in Fig. 6.5. We evaluate the upper critical magnetic field $B_{c2}(0)$ from the flux flow approach for the $R(B)$ curves in Fig. 6.9a) and from the $R(T)$ curves in Fig. 6.9b) using the half resistance criterion.

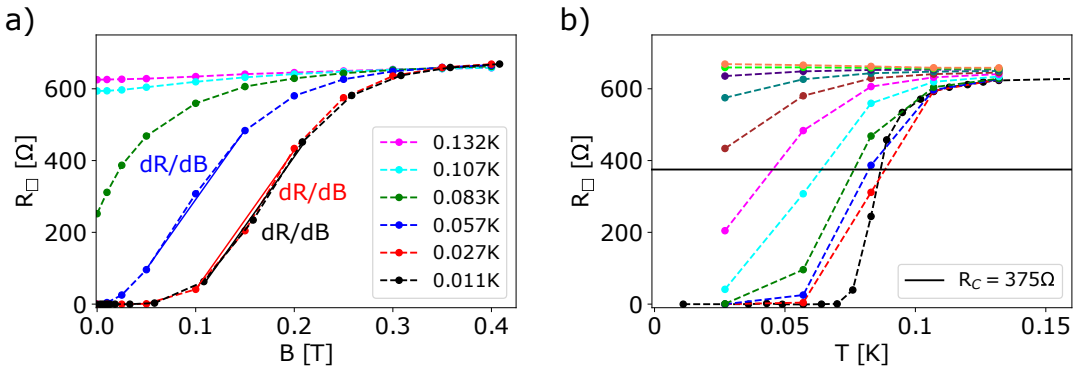

Figure 6.9.: NbSi-S: a) $R(B)$ for the different temperatures listed in the figure. The full lines denoted as $\mathrm{d}R/\mathrm{d}B$ are the slope in the corresponding $R(B)$ curve used for the flux flow criterion.
b) The same data points presented in a $R(T)$ configuration. The magnetic fields presented are 0T(black), 10mT(red), 25mT(blue), 50mT(green), 100mT(cyan), 150mT(magneta), 200mT(brown), 250mT(teal), 300mT(indigo), 350mT(lime) and 400mT(coral). The black horizontal line corresponds to the critical resistance for the half-resistance criterion, $R_c = R_N(6\mathrm{K})/2$.

Upper critical field

By following the model of Bardeen-Stephen for flux flow resistance [18], presented in section 2.1.2, we can extract the viscous drag coefficient η and the upper critical field B_{c2} at $T = 0$.
As it is only possible to extract a linear slope $\mathrm{d}R/\mathrm{d}B$ for three temperatures (11mK, 27mK and 57mK) (see Fig. 6.9a)) and their values vary only little around ∼3.9kΩ/T, unexpectedly no temperature dependence is found. Therefore, in the following we focus on the $T = 0$K case only by taking the temperature independent average of the three measured values.

A film thickness of $d = 23$nm leads to

$$\eta(T=0) = \frac{\Phi_0}{d(\mathrm{d}R/\mathrm{d}B)} \sim 2.3 \cdot 10^{-11} \frac{\mathrm{T^2 m}}{\Omega} \tag{6.1}$$

using the $\mathrm{d}R/\mathrm{d}B$ ∼3.9kΩ/T. The upper critical field is given by

$$B_{c2}(T=0) = \frac{\eta\rho_N}{\Phi_0} = \frac{\eta R_{N,\square} d}{\Phi_0} \sim 192\mathrm{mT} \tag{6.2}$$

Another criterion for the upper critical field is the half resistance criterion, which is applied to the $R(T)(B)$s, shown in Fig. 6.9b). The criterion reads $R_c = R_\square(6\mathrm{K})/2$ and in our case $R_c = 375\Omega$. From the $R(T)(B = 0\mathrm{T})$ curve one can extract the critical temperature $T_c = 86.3\mathrm{mK}$, while the resistance vanishes completely below a temperature of 70mK.
A BCS fit by Eq. 2.34 applied to the $B_{c2}(T)$ curve extracted for the criterion $R_c = 375\Omega$ in the $R(T)$ curves for different magnetic fields gives: $T_c(0) = 88.74\mathrm{mK}$ and $B_{c2}(0) = 195.8\mathrm{mT}$. The extracted $B_{c2}(T)$ values and the corresponding BCS fit by Eq. 2.34 are shown in Fig. 6.10. The critical temperature value T_{c0} from the extrapolation of the fit to $B_{c2}(T)$ is in good agreement to the extracted 86.3mK from the single $R(T)$ curve value with zero magnetic field.

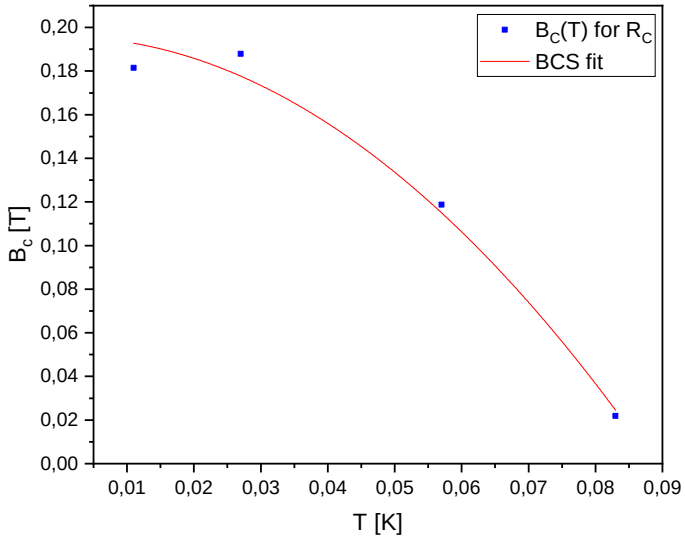

Figure 6.10.: NbSi-S: $B_{c2}(T)$ extracted from the half resistance criterion, $R_c = R_N(6K)/2$, applied to the $R(T)$s in Fig. 6.9b). The upper critical field B_{c2} is denoted as B_c. The red curve is a BCS fit to the data by Eq. 2.34.

The such determined upper critical magnetic field value is consistent with the value extracted using the flux flow approach.

From the upper critical field value a coherence length $\xi(0)$ can be calculated with Eq. 2.44, which is $\xi_{\mathrm{exp}}(0) \sim 41$nm for both cases, flux flow and BCS, respectively. The extracted value for the coherence length is in good agreement with previous measurements of $\xi_{\mathrm{exp}}(0)$ = 30nm by the group of D. Shahar[2] (private communication with C. Marrache-Kikuchi). The extracted values of $\xi(0)$ ∼30-40 nm are in good agreement with an upper boundary of $\xi_{\mathrm{exp}}(0) = 50$nm. That value has been calculated using the dirty limit expression [18] $\xi(T=0) = 0.855\sqrt{\frac{\hbar\nu_{\mathrm{F}}l}{\pi\Delta}}$ with $\Delta(T=0) = 1.76k_{\mathrm{B}}T_{\mathrm{c}}$, $T_{\mathrm{c}} = 0.1$K, $\nu_{\mathrm{F}} = 5 \cdot 10^5$m/s and $l = 0.5$nm (private communication with C. Marrache-Kikuchi).

In addition, we see in Fig. 6.9a), that the two curves measured at the lowest temperatures $T = 11$mK and $T = 27$mK match. That indicates a low temperature saturation of resistance similar to what has been seen by Ref. [124] in NbSi for different temperatures used for heat treatment and by Ref. [129] in granular In/InOx by applying an external magnetic field. In both cases, failed superconducting and failed insulating regimes have been observed connected with an anomalous metalic state.
Our data (Fig. 6.9) exhibits a low temperature saturation at resistance values smaller than the normal state resistance $R_{\square}(350\mathrm{mK}) \sim 640\Omega$ with a TCR > 0. This indicates a failed superconducting behaviour. However, at $B \sim 300 - 350$mT the TCR switches sign to TCR < 0 and the saturation resistance is larger than $R_{\square}(350\mathrm{mK})$. The 300mT curve (indigo) has a TCR > 0, while the next larger magnetic field 350mT (lime) shows a negative TCR < 0. This can be interpreted as a transition to a failed insulating state. These findings indicate an anomalous metallic state in the vicinity of the magnetic field driven SIT in NbSi.
Following arguments of Ref. [124] (see section 6) and Ref. [125] (see section 5.4) the failed superconducting phase can be attributed to superconducting fluctuations.
Below 50mT the sample is superconducting. The failed superconducting phase ranges from $B = 50$mT, where the saturation resistance becomes finite, to 300mT-350mT. In that magnetic field range the TCR switches sign. As shown above, the critical perpendicular magentic field is $B_{\mathrm{c}} \approx 195$mT. In a magnetic field range slightly above the critical magnetic field superconducting fluctuations may still persist. For $B > 350$mT (approx. 1.5 times the critical field) the fluctuations vanish completely and there should be a crossover to the failed insulating phase. As no perpendicular magnetic field above $B =$ 400mT was applied to that sample, there is not enough data for the failed insulating phase in this sample. However, the failed insulating phase is further investigated in sample NbSi-M, which is already in a state with TCR < 0 for $B = 0$T, in the next section.

[2]Department of Condensed Matter Physics, The Weizmann Institute of Science, Rehovot 7610001, Israel

6.2. Failed Insulating Phase: Effect of Magnetic Field

In Fig. 6.11a) we show the temperature dependence of the resistance for a set of perpendicular magnetic fields. The corresponding $R(B)$ curves are presented in b). The overall resistance values increase with increasing magnetic field up to $B = 1$T. By further increasing B the resistance values start to saturate up to 3T, above which it is roughly independent on magnetic field.

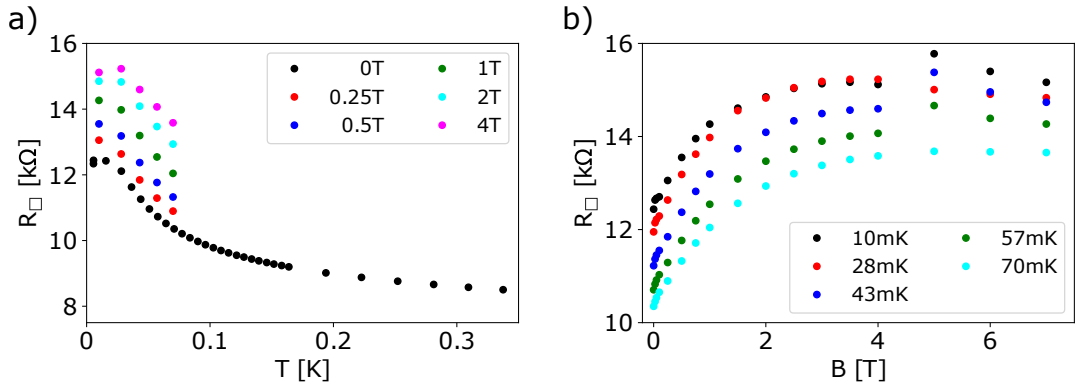

Figure 6.11.: NbSi-M: a) $R(T)$s for the magnetic fields denoted in the figure. b) The same data points presented in a $R(B)$ configuration together with additional magnetic fields and for temperatures denoted in the figure. The low temperature data points at $B = 5$T and 6T are unreliable, as the sample temperature deviated from thermal equilibrium with bath temperature. The chosen thermalization times were to short.

We now take a look at the $R(T)$ curves in Fig. 6.11a). We find an insulating trend of the resistance down to a temperature of $T \sim 40 - 50$mK followed by a low temperature saturation for $T < 30$mK. We fit the data to Eq. 5.15, proposed by Ref. [129] for the failed insulating state of the anomalous metallic state, which includes a high temperature activated behaviour and a low temperature saturation of resistance. The fits to our data are presented in Fig. 6.12.

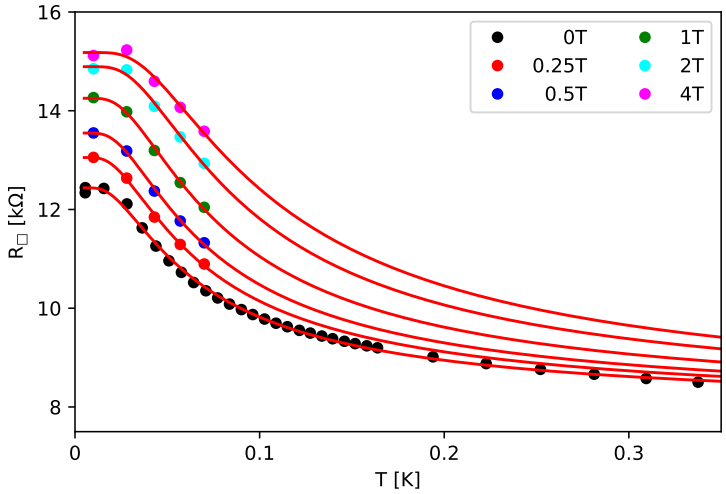

Figure 6.12.: NbSi-M: Activated behaviour with low temperature saturation of resistance. Presented are some selected $R(T)$ curves including the fits to Eq. 5.15.

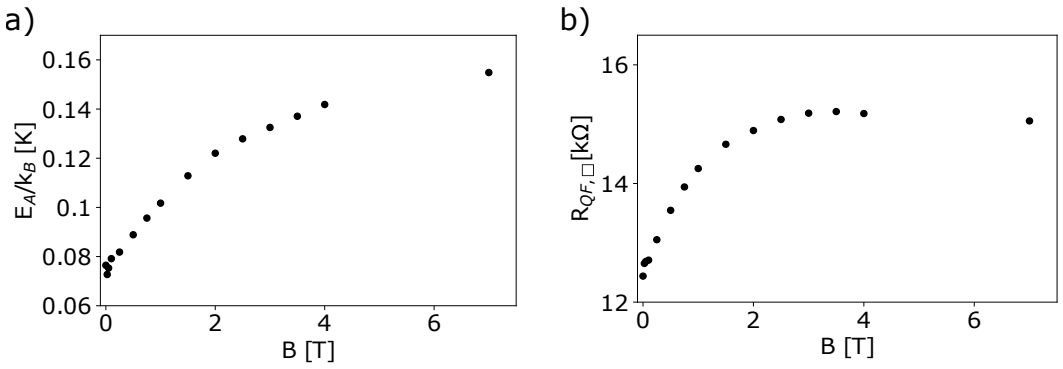

Figure 6.13.: NbSi-M: Evaluation of the fitting parameters for activated behaviour with low temperature saturation of resistance. a) and b) show the extracted activation temperatures $E_\mathrm{A}/k_\mathrm{B}$ and the low temperature saturation resistances denoted as R_QF as it resembles the saturation in the failed insulating state, where the saturation is attributed to quantum fluctuation of charge.

As the $R(T)$ curves for $B > 0$T consist of very few points (see Fig. 6.11a)), we first fit the $B = 0$T curve to the proposed formula Eq. 5.15. We keep the high temperature R_N constant for the fits of $B \neq 0$T. R_N enters Eq. 5.15 as $G_0 = \frac{1}{R_N} - \frac{1}{R_{QF}}$. That assumes that the resistance at temperatures of at least 10 times the measurement interval does not respond to an external perpendicular magnetic field.

The extracted activation energies are shown in Fig. 6.13a) and the corresponding saturation resistance R_{QF} in b).
At $B = 0$T the activation energy has a value of $E_A/k_B \sim 75$mK and continuously increases up $E_A/k_B \sim 150$mK. We do not observe a saturation or a dome-like behaviour up to our maximum magnetic field of 7T. The saturation resistance R_{QF} increases more rapidly for magnetic fields between 0T and 1T, then starts to slow down its increase and saturates for $B > 3$T.

Summary

We investigated the temperature and magnetic field dependence of the zero bias resistance in two niobium silicon samples. One sample shows a transition to a zero resistance state below a critical temperature (NbSi-S) and the other sample shows an insulating behaviour with a low temperature saturation (NbSi-M). Sample NbSi-S could be tuned continuously into a metallic state by applying a perpendicular magnetic field. We find a saturation of resistance for $T < 30$mK.
By applying a magnetic field to sample NbSi-M we find a positive magnetoresistance up to $B = 3$T, above which the resistance saturates. The increase of resistance at the lowest temperatures is about ∼25%. The $R(T)$ curves follow activated behaviour with activation energies increasing from $E_A/k_B \sim 0.075$K to $E_A/k_B \sim 0.15$K. The saturation resistance R_{QF} follows approximately the same curvature as the $R(B)$ at the lowest temperature $T = 10$mK.

We see a transition from a superconducting state to a metallic state with a low temperature saturation in NbSi-S, where the saturation resistance increases continuously with increasing perpendicular magnetic field. At $B = 400$mT, the maximum applied magnetic field, the resistance is approximately constant down to the lowest temperatures. Higher magnetic fields than our maximum have to be applied to distinguish between a persisting metallic state with a magnetic field independent resistance or a possible B-SIT leading to an insulating state. In case of a magnetic field driven SIT the transition from the superconducting state to the failed superconducting state is explained with phase fluctuations (see Ref. [124] for fermionic scenario in NbSi and Ref. [129] for bosonic scenario in granular In/InOx).
The origin of the failed insulating phase, as seen in sample NbSi-M, is still debated whether it arises from a fermionic groundstate or a bosonic one.
In a fermionic scenario the insulating behaviour of sample with $R_N > R_Q$ is attributed to localized electrons as superconductivity is not present. The low temperature saturation

following this model is still an open issue.
In case of a bosonic scenario, the insulating behaviour is attributed to localized Cooper pairs on either physical grains (grAl, In-InOx) or on electronical, self-induced grains (TiN). Ref. [129] gives an explanation for the low temperature saturation on the insulating side, which bases on the duality of charge and phase. The Cooper pairs are localized and quantum fluctuations of charge, which generate a temperature independent finite conductivity, limit the increase of resistance to a finite value at the lowest temperatures. The magnetic field dependence of the $R(T)$s in the insulating phase observed in NbSi-M as well as the persisting low temperature saturation up to the highest magnetic field applied, $B = 7\mathrm{T}$, indicate that the groundstate of the failed insulating phase may be of bosonic nature.

7. Summary

This thesis presents measurements on ultra-thin granular aluminum films. The findings are compared to periodic JJAs and measurements on other granular thin films. We find agreements as well as surprising effects. This is also valid for niobium-silicon. The field of granular and electronically disordered superconductors, especially with focus on the magnetic field driven SIT, is an interesting field for future research.

The focus has been set on the low temperature transport properties of **ultra-thin granular aluminum films** ($d < 10$nm). We have measured current voltage characteristics for perpendicular and parallel magnetic fields at different temperatures ($T < 4$K) and extracted the corresponding zero bias resistances $R_{\square}$.

For pre-characterization scanning electron and atomic force microscopy was used. The **film morphology** dramatically differs from that of thicker films (d ∼40-100nm) [170, 171]. As our films have been grown using the same growth process as for the thicker 3D films [5, 164], we surprisingly find a broader distribution of grain sizes (∼1nm - ∼100nm) compared to 3D films with 2-3nm. That indicates that the film thickness has an impact on film morphology. It would be an interesting study to investigate the evolution of the morphology with film thickness for the growth process used for granular aluminum. A change in morphology from granular to homogenous films has been found by Jaeger et al. [10] with film thickness. However, they used a different growth process.

We measured two samples with different normal state sheet resistances $R_{\mathrm{N}}(T = 4\mathrm{K})$. One sample has a $R_{\mathrm{N}} = 7.75\mathrm{k}\Omega$, i.e. above $R_{\mathrm{Q}} = 6.45$ kΩ, (Sample I) and the other a $R_{\mathrm{N}} = 3\mathrm{k}\Omega$, i.e. below $R_{\mathrm{Q}} = 6.45$ kΩ, (Sample S). In ultra-thin granular [10] and homogenous films [63], as well as in artificial, periodic JJAs [80, 81], a normal state R_{N} value in the vicinity of R_{Q} determines the low temperature dependence. The normal state sheet resistance of our samples has been tuned to values $R_{\mathrm{N}} \sim R_{\mathrm{Q}}$.
Due to the granular nature, our films consist of superconducting grains below T_{c}, which are coupled by Josephson junctions in a random array. For periodic JJAs theory as well as experimental results are available and can be compared to our findings.

At the lowest temperatures and **zero magnetic field**, we find that sample I ($R_{\mathrm{N}} > R_{\mathrm{Q}}$) behaves insulating (for $T < 1$K) and sample S ($R_{\mathrm{N}} < R_{\mathrm{Q}}$) (for $T < 0.3$K) exhibits a transition to a zero resistive state. This is consistent with the theory of a disorder induced superconductor to insulator transition (d-SIT).
However, for temperatures $0.3\mathrm{K} < T < 1.9\mathrm{K}$ both samples deviate from either insulating behaviour or from a zero resistive state. Sample I exhibits a reentrant feature, a local

minimum in resistance, at a temperature $T < T_c$. Similar behaviour has been found in various granular thin films. The reentrance can be attributed to the competition of the charging energy E_C, the Josephson energy E_J and the thermal energy $k_B T$.
Sample S does not show a vanishing resistance in the temperature range $0.3\text{K} < T < 1.9\text{K}$, smaller than T_c, but two temperature independent plateaus, meaning the sum of the effects of E_C, E_J and $k_B T$ has to be constant. As the temperature continuously decreases it is unexpected that the effects of E_C and E_J exactly compensate the decreasing $k_B T$ over such a large temperature range. A further investigation of the plateaus in dependence of e.g. sheet resistance or gate voltage could reveal more details on their origin.

By examining the **current voltage characteristics** (B = 0T) of sample I, we find a threshold voltage marking the onset of current flow. In insulating periodic JJAs [80] this is attributed to the injection of Cooper pair solitons. Nevertheless, we see a finite differential resistance in the zero bias regime, whereas in insulating periodic JJAs with $R_N \gg R_Q$ such a behaviour in the zero bias limit has not been observed.
Sample S shows a threshold voltage with a similar value as sample I, which indicates insulating behaviour. However, in the zero bias limit, we find a small temperature dependent supercurrent with $I_c \sim$100pA at the lowest temperature.
Therefore we see insulating and superconducting effects in both samples, but with different distinctness. That can be attributed to the vicinity to the d-SIT ($R_N \sim R_Q$).
In sample S at $T = 15\text{mK}$ we find a sharp jump in the IV curve from the supercurrent branch to the higher branch with finite voltage by exceeding the critical current. For granular, inhomogenous films with a very broad distribution in grain sizes and separations we would expect a smeared out, broad transition due to the different critical currents of each individual junction. The origin for the sharp jump, as a signature of a single junction, may be explained by e.g. a collective jump of all junctions in the array or the breakdown of a junction in a percolation path. To distinguish the origin theoretical models have to be discussed followed by appropriate high resolution measurements.

By applying a **perpendicular magnetic field** ($R(T)$s for different Bs) to sample S we find a transition from the superconducting state to an insulating state (B-SIT). We examined the temperature dependence of the zero bias resistance for a set of magnetic fields in both samples. In a temperature interval $200\text{mK} < T < 500\text{mK}$ the curves can be modelled by activated behaviour. The extracted activation energy $E_A(B)$ is separated into a low magnetic field range dominated by Cooper pair solitons and a high magnetic field range dominated by single electron solitons. Such a crossover has also been found in insulating JJAs with superconducting electrodes [80] and supports a bosonic scenario for the B-SIT. The activated behaviour leads to high resistances $R_\square > 100\text{M}\Omega$ at intermediate magnetic fields $B \sim 2\text{T}$ and is caused by the suppression of the Josephson coupling between the superconducting grains. The magnetic field dependence of the threshold voltage follows the same trend as seen in insulating JJAs. With increasing magnetic field $V_{T,S}$ increases to a maximum and then decreases to a magnetic field independent value $V_{T,N}$ associated with the Coulomb blockade for single electron solitons only.

In **parallel magnetic field** orientation the shape of the IV curves does not change with increasing $B_{||}$ and are comparable to the $B = 0$T curve. However, the zero bias resistance slightly varies with temperature and magnetic field ($R(T)$s for different Bs). We do not find highly resistive states up to $B_{||} = 2.5$T. The maximum measured resistance in parallel configuration is $R_{\square} \sim 4\text{k}\Omega$. This is in the same order of magnitude as the normal state sheet resistance at 4K of $R_{\text{N}} = 3\text{k}\Omega$ and by several orders smaller than the maximum measured resistance in perpendicular configuration ($R_{\square} > 100\text{M}\Omega$). Therefore we conclude that by applying a parallel magnetic field there is no or almost no decoupling of the superconducting grains. The measured effects (dome-like $R(T)$, increase/decrease of R with B) in the $R(T)$ by an applied parallel magnetic field might be explained by a small residual perpendicular magnetic field due to insufficient compensation (offset by misalignment) or due to tolerances in the compensation curves for different parallel magnetic fields. A clarification may be achieved by a more detailed (decreasing stepsizes of measured temperatures and magnetic fields as well as increasing the absolute value of the magnetic field) and precise (better alignment and compensation) measurement.

To get a deeper insight in the fine structure of the $R(B_{\perp})$ curve, we reduced the stepsize of the magnetic field down to $\sim$7mT in sample S and $\sim$25mT in sample I. The **magnetic field dependence** $R(B_{\perp})$ reveals oscillations.
In periodic Josephson junction arrays such oscillations are connected to the existence of equally large normal conducting areas, enclosed by superconducting electrodes coupled by Josephson junctions. Magnetic flux penetrates the normal area, which determines the oscillation period. Therefore in periodic JJAs oscillations in the $R(B)$ are expected.
In our granular and inhomogenous system, there is a broad distribution in the size of the normal areas. Therefore we expect a very broad distribution in the oscillation periods. Oscillations with a fixed, single valued period should not be observable in our granular system. In addition, the SEM and AFM pictures do not reveal any signs of holes (macroscopic voids in the film structure) in our films. To understand our surprising result further experiments and a theoretical model is necessary.

At low temperatures we find that our $R(T)$ curves deviate from activated behaviour. In the vicinity of the B-SIT, on the insulating side, the resistance saturates at $R > R_{\text{Q}}$. This can be attributed to an **anomalous metallic state** (AMS). Our findings are in agreement with a study on granular In-InOx composites [129] and the proposed phase diagramm for granular superconductors. With increasing magnetic field we observe a transition from the superconducting state to the failed insulating state of an anomalous metallic state. A possible failed superconductor has not been seen. This can be attributed to the magnetic field stepsize in our experiment. Further increasing the magnetic field leads to a broad crossover from the anomalous metallic state to a Bose-insulating state. To verify the existence of a proposed failed superconductor on the superconducting side and a failed insulator on the insulating side of the B-SIT in ultra-thin granular aluminum, a further experiment should focus on the temperature dependence of the zero bias resistance close to the magnetic field driven SIT.

The evaluation of the **differential resistance** at voltages far above the zero bias limit ($\boldsymbol{V \gg V_T}$) shows that for $B = 0$T the resistance saturates for $T < 1.8$K at a temperature independent value $R_{\min} \sim 750\Omega$. With increasing magnetic field ($B > 1.5$T) the resistance continuously increases from that minimum to a value slightly above the normal state sheet resistance R_N at $B = 3.5$T. This is drastically different to the very high sheet resistances found in the zero bias limit for the same temperatures and magnetic fields. The high applied voltage induces a current higher than the critical current of the individual Josephson junctions, but smaller than the critical current for the superconducting state on the grains. This leads to a regime, where the charge transport is conducted by Cooper pair solitons as well as single electron solitons. While Cooper pair solitons carry charge without resistance, single electron solitons generate a finite resistance. The ratio of Cooper pair solitons and single electron solitons is shifted towards the latter with increasing magnetic field. This leads to an increase of resistance until superconductivity is destroyed and the normal conducting state is reached.
The $R(T)$ and $R(B)$ curves of our 2D film reveal strong similarities with resistance measurements in the zero bias limit in 3D granular films.

In addition, we investigated two samples of **niobium-silicon thin films**. One sample (NbSI-S) shows a transition to a state with zero resistance and the other (NbSi-M) shows insulating behaviour with a low temperature saturation.
With increasing magnetic field NbSi-S can be tuned continuously from the zero resistive state to a metallic phase. For magnetic fields, $50\text{mT} < B < 350\text{mT}$, the resistance decreases with decreasing temperature and saturates at values below R_N at low temperatures. This can be attributed to a failed superconductor arising by superconducting fluctuations. This is agreement with a fermionic as well as a bosonic scenario for a possible SIT. For $B > 350$mT the resistance is approximately constant with decreasing temperature. To distinguish betweeen a persisting metallic state or a possibly started B-SIT, leading to an insulating state, magnetic fields higher than our maximum of $B = 400$mT have to be applied.
Sample NbSi-M is in a failed insulating state without magnetic field with a low temperature saturation value $R_\square \sim 12\text{k}\Omega > R_Q$. By applying up to $B = 7$T the shape of the $R(T)$ curves does not change. However, we observe a magnetoresistance of $\sim$25% and an increase of the activation energy by a factor of 2. While the fermionic scenario does not give an explanation for the low temperature saturation in the $R(T)$, in case of a bosonic scenario, connected to an anomalous metallic state in the vicinity of the B-SIT, the low temperature saturation is explained by quantum fluctuations of charge. For a B-SIT with a bosonic groundstate, one would expect a positive magnetoresistance at low field (localization of Cooper pairs) and a negative one at high fields (breaking up of Cooper pairs for $B > B_c$). We find a positive magnetoresistance up to 3T, followed by a possible high magnetic field saturation of resistance. To distinguish between a persisting magnetic field independence (fermionic case) or a negative magnetoresistance (bosonic case) measurements at higher magnetic fields than our maximum of $B = 7$T are necessary.

In a nutshell, the morphology of our ultra-thin (2D) granular aluminum films dramatically differs from the morphology of thicker films (3D). In case of zero magnetic field our findings are consistent with the theory of a disorder induced SIT. By applying a small perpendicular magnetic field to sample S a SIT is induced, which is followed by a high resistive state. The high resistive state vanishes once the magnetic field exceeds the critical magnetic field B_c. The transport properties (R(T) and R(B)) show similarities to inhomogenous ultra-thin films (complex R(T), reentrant behaviour and an anomalous metallic state), to homogenous disordered films, e.g. TiN, (R(B)-magnetoresistance) as well as to periodic insulating Josephson junction arrays (oscillating component in the magnetoresistance and the activated temperature dependence of the resistance). Those findings are a strong indication for the bosonic nature of the magnetic field driven SIT in ultra-thin granular aluminum.

A. Appendix

A.1. Building Process for Ag-Epoxy Filters

The Ag-epoxy filters are home made following the ideas of Ref. [153] and show high frequency damping combined with very good thermal properties. See section 3.1 for details.

The filters are made out of a silver epoxy (EpoTeK E4110) rod around which an insulated copper wire is wound. The electrical conductivity of the epoxy is $\sigma_{\text{Ag-epoxy}} \geq 2 \cdot 10^5$ S/m. The wire is made of 100μm copper and a 8μm polyurethan layer. The conductivities are $\sigma_{\text{Cu}} = 5.95 \cdot 10^7$ S/m and $\sigma_{\text{Pu}} < 9.3 \cdot 10^{-14}$ S/m. The dielectric constant of polyurethan is $\epsilon_{\text{ins}} \approx 4.6$. [154]

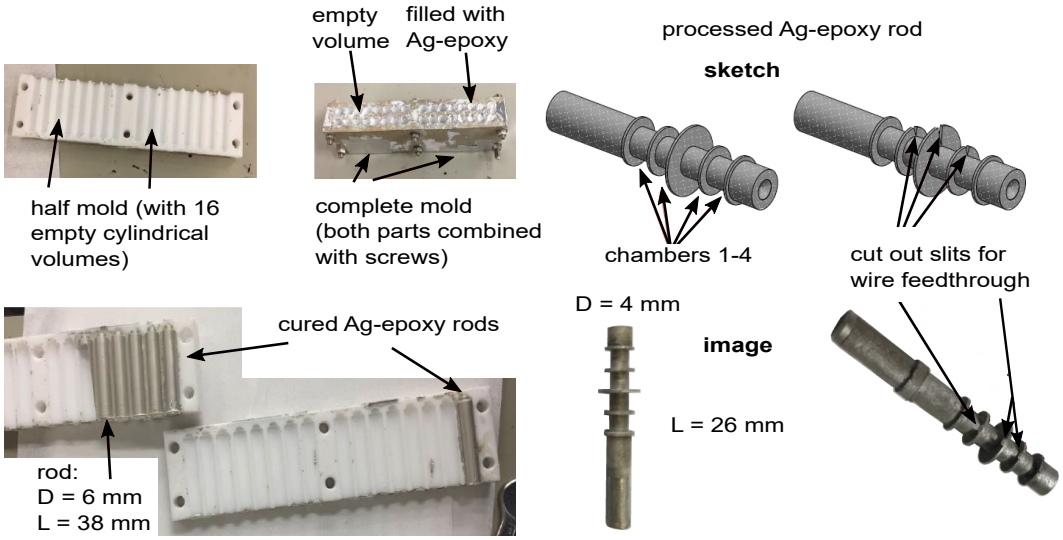

Figure A.1.: Ag-epoxy rod: a) mold in different states of casting. b) processed rod prepared for winding. Figures adapted from [155].

The first step is to fabricate the silver epoxy rods. Therefore a cylindrical mold was used. The liquid Ag-epoxy was filled into the mold, then shaken heavily for approx. 15 minutes to ensure there are no air bubbles encapsulated. After that the Ag-epoxy has to dry for 3-7 days at room temperature or 3 hours at a 80 degree celsius hot plate. Once cured the chambers are routed by the mechanical workshop using the design shown in Fig. A.1b). The chambers with length 3mm are separated by 0.3mm discs. The disc in the middle is

slightly wider than the other two as it has to hold the filter in the filter box.
Each barrier separating two chambers has a slit cut into it serving as a feedtrough for the wire and as a fixation while switching winding direction. The winding direction was changed for each chamber so the generated magnetic fields by the current passing through the coil-like wire is minimized. The slit was carfully carved by hand using a scalpel.
The winding of the filters was carried out together with M. Simmel and K. Lehar in the electronics workshop.

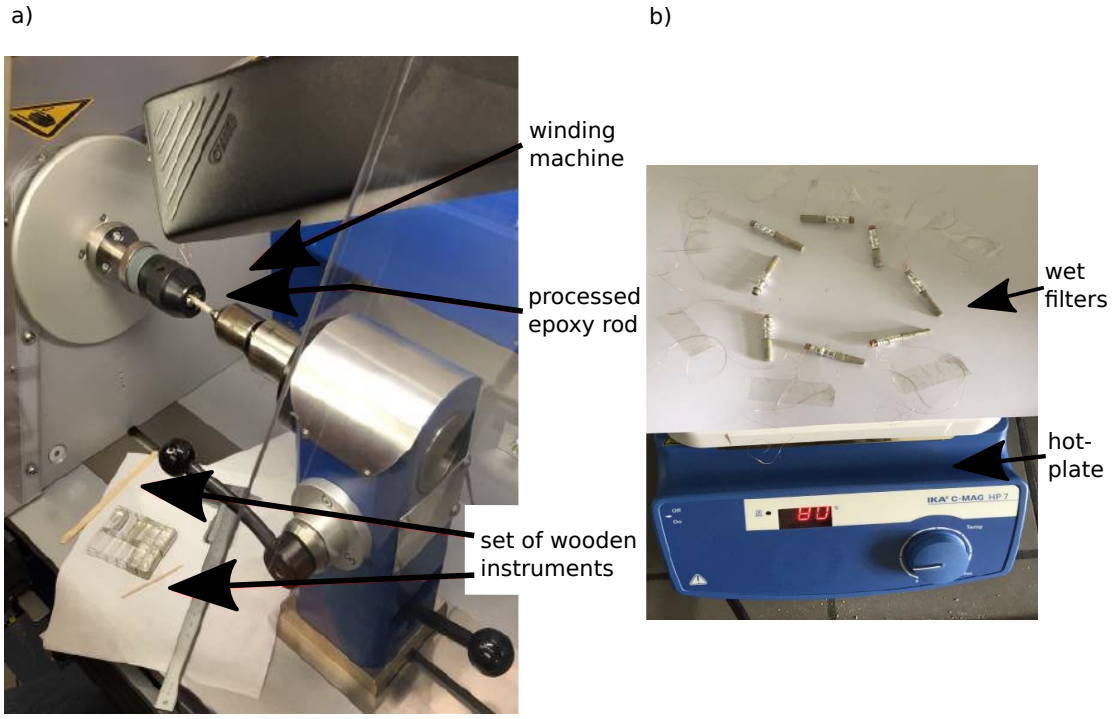

Figure A.2.: a) Image of a processed epoxy rod placed into the winding machine. We used wooden intruments only to guide the wire while the machine is rotating. Wooden instruments reduce the probability of damaging the wire insulation. b) After the winding process, the wet filters are heated up to 80 degree celsius on a hotplate until they are dry. We used a thick paper to prevent the hotplate from being in direct contact with the wet Ag-epoxy. Figures adapted from [155].

The rod is placed into a winding machine by RUFF GmbH. A length of approx. 4m of wire is used. Each chamber consists of 5 layers of 21 windings. The segmentation reduces impact of stray capacitances. To ensure good electrical and thermal contact the rod and the wire are constantly covered with liquid Ag-epoxy while winding. After another 3 hours of curing at 80 degree the filters finally can be tested for their electrical properties, e.g. resistance of the copper, shorts between inner conductor and "outer"/Ag-epoxy-conductor and the high frequency damping. The DC resistance of the filter is approx. 10-12Ω.

To check the high frequency damping, one filter was tested in a electrically shielded environment (closed metal box). To further improve the filtering properties different options were tested that could be used for low temperature purpose. The tests included Ag-epoxy sealing of the metallic interlayer, sealing the lid of the box and filling Eccosorb (high frequency damping material) into the output volume, which can be seen in Fig. 3.5. For all tests the output side was closed with a metallic lid.

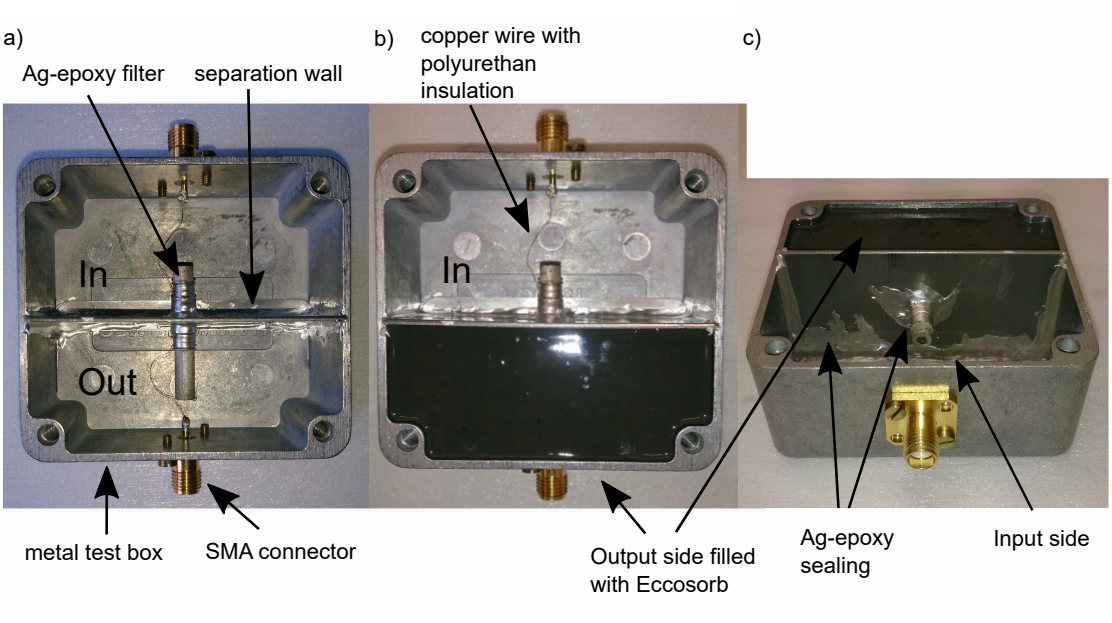

Figure A.3.: Ag-epoxy filter test box: a) Filter with Ag-Epoxy sealed metallic interlayer. b) Filter with Ag-Epoxy sealed metallic interlayer and Eccosorb filled into output side. c) side view of b), where the Ag-Epoxy sealing is better visible.

The filter was then characterized by measuring the transmission coefficient S_{21} with a Vector Network Analyzer by Rohde und Schwartz. The damping behaviour can be seen in Fig. 3.5b) in Sec. 3.1. Test I corresponds to a closed box as seen in a). Test II corresponds to a closed box as seen in b) and in test III the lid was sealed in the same form as seen in c) for the slits between box and separation wall.

A.2. Shielded Measurement Environment for mK-Purpose

As the filters were supposed to be located at the lowest temperature stage inside a He3/He4-dilution refrigerator, the design of the electrically shielded volume had to take into account very good thermal coupling in addition to very good electrical coupling of the outer conductor to ground. This reduces relaxation times after temperature changes, but also stops the incoming heat from higher temperature stages to reach measurement volume.

To achieve those requirements we used the design as for the testbox. A sketch can be seen in Fig. 3.6.
A brass plate separates the volume into an input side and an output side and provides holes, where the filters are located. The filters are designed in such a way, that one-half is in the input-side and the other is in the output side, sitting on the brass-plate by its middle ring with a diameter larger than the diameter of the hole. To fix the position of the filters we covered them with silver epoxy (see Tab. A.3) on both sides. This also secures very good thermal coupling of the outer conductor to the brass plate. To hermetically seal the output side the slits between the brass plate and the brass box were also covered with silver epoxy, further improving thermal coupling. The top part of the box is then in contact with the mixing chamber plate using screws for pressure. To further reduce high frequency noise, the output side is filled with Eccosorb (see Tab. A.3).

This idea was used in two different filter boxes. One was designed for calibration of low-temperature resistance thermometers right at the mixing chamber, the other for continuously filtering the measurement/thermometry lines reaching down into sample space with homogenous magnetic field.

Box 1: Thermometer Calibration

This box is designed to be in good thermal contact with the mixing chamber plate. It is screwed to it from the bottom and is electrically shielded using brass overlappings. The images can be seen in Fig. A.4. The box contains 5 Ag-epoxy filters going through a brass plate from input (unfiltered) to output (filtered) side. The input is connected with a Micro-D connector (see Tab. A.3) to which the filters are soldered to. From this dead space the lines enter the real input volume through a small hole. To provide the insulation to be scratched a heat shrink tubing was placed in the hole. The slits connecting the input/output are covered with silver epoxy. The output side has a 5mm thick layer of Eccosorb further increasing the high frequency damping, strip lines to solder leads of a resistance thermometer onto as well as a metal cube with a thread. The metal cube's purpose is two-fold: first it acts as a fixation point for the thermometer, secondly it increases the thermalisation of the thermometer to the surrounding temperature.

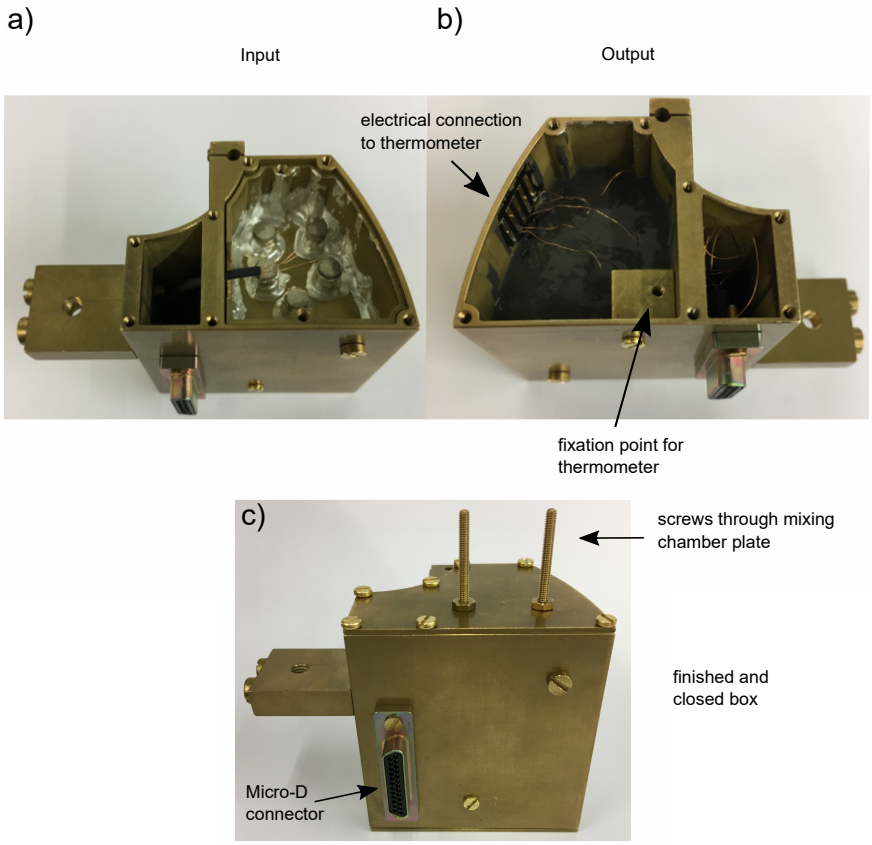

Figure A.4.: Thermometer Calibration box: a) Input including Micro-D connector to dead space, feedthrough with heat sink tubing to input space and filters glued into brass plate with Ag-epoxy. b) Output including other half of filters covered with Eccosorb. Striplines on the inner side of the box, denoted as electrical connection, are used to solder the four leads of the thermometer to the insert wiring. The thermometer (usually a small SMD encapsulated in Stycast inside a silver foil) is fixed by a screw to a brass square, which is in good thermal contact to the box and the mixing chamber. c) Finished, closed box.

A thick brass projection is added. It has 3 threads and can be used as optional positions for thermalization of other/future parts. Another possibility is to add a calibrated thermometer to check the real temperature of the box and hence of the thermometer to be calibrated.

Box 2: Filtering Measurement and Thermometry Lines

As presented in section 3.1 to match the requirements for filtered lines, which extend a shielded environment down to the sample space, the metal filterbox located at the mixing chamber is connected to the sample space, located at the bottom of the coldfinger, with shielded CuNi cables (see Tab. A.3). This section will first cover the implementation of the filters into the filterbox. The second part focuses on the coldfinger buildt to contain sample space in the central magnetic field of the Oxford Instruments dewar and the cabling connecting filterbox with sample space.

The idea of the filterbox follows the one of the calibration box shown above, where the two volumes (input and output) are separated by a metal layer including holes for the filters. The signal therefore has to go through the filters rather than bypassing them. To minimize bypassing the slits are covered with electrical conducting Ag-epoxy and the output side is partly-filled with Eccosorb (see sketch in Fig. 3.6).

Input

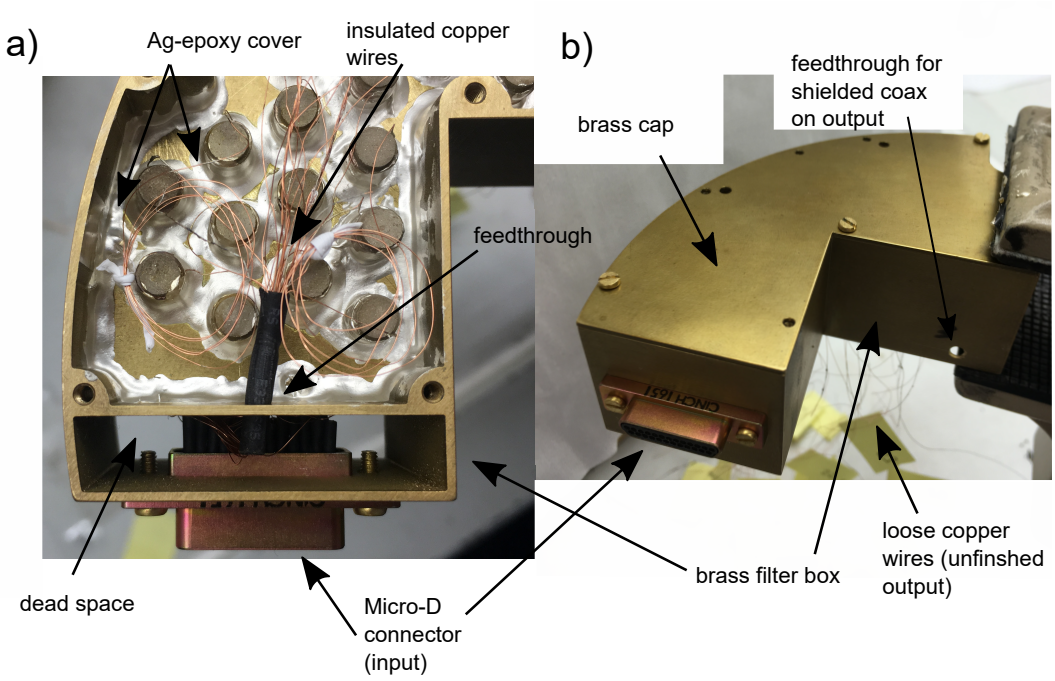

Figure A.5.: Input of Ag-Epoxy filterbox: a) The measurement lines are connected to the filter box with a Micro-D connection. The connector reaches into a dead space, where the insulated copper wires of the filters are soldered to the rear side. The feedthorugh is done with a heat shrink tubing. b) shows the box in a state, where the input was finished and closed, but the output side remained to be dealt with.

The unfiltered input side can be seen in Fig. 3.6. A zoom can be seen in Fig. A.5a). This box is bigger than the box designed for thermometer calibration and contains 31 filters, where each of the filters is glued with Ag-epoxy separately. The Ag-epoxy covering on the edges of the box can be seen as well. As the Micro-D connector has 25 pins only, 6 filters are used as reserve in case one filter has a short to ground or does not work as intended. The free lines of the reserves were wound up and can be see best in Fig. A.5a), while b) shows the closed input side.

Output

The output side resembles a mirror of the input, but with an addition of a thick Eccosorb layer completely covering the Ag-epoxy filters. Fig. A.6a) shows the output side after the Eccosorb is hardened. The wires from the filters are soldered to strip lines on small PCB boards. The strip lines were glued using a drop of Eccosorb in a way that the lines are in a parallel configuration to the output feedthroughs. The inner conductors are very weak and might break easily. The final connection can be seen in Fig. A.6b).

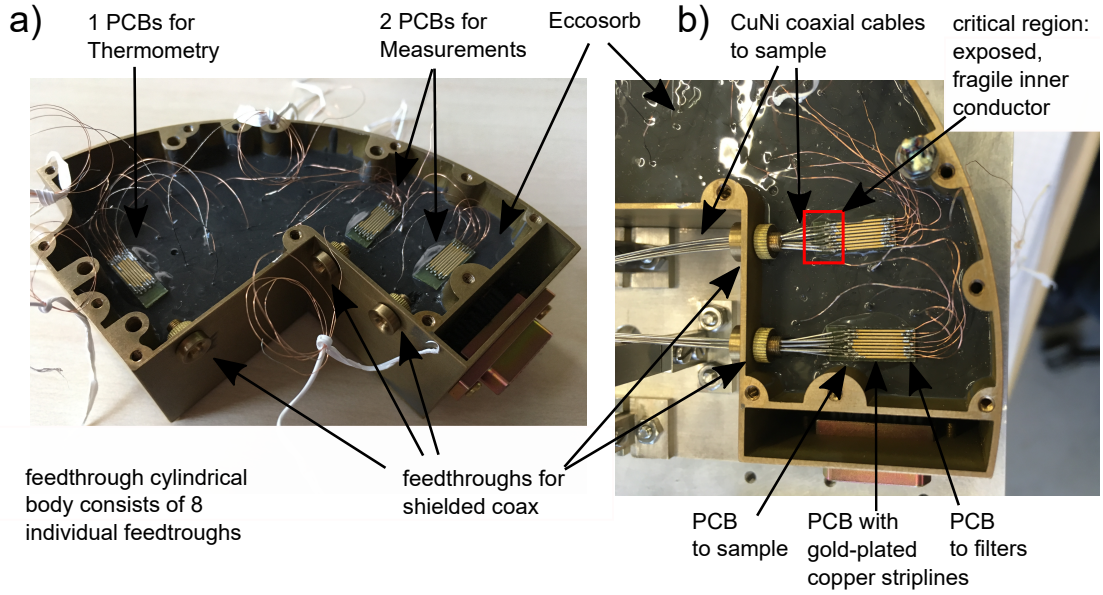

Figure A.6.: Output side of Ag-epoxy filter box: a) Unconnected output wiring ending with solder connections on PCBs located on the hardened Eccosorb. b) A zoom shows how the connection between filter side (insulated coper wire) and sample side (shielded CuNi coaxial cable) via striplines is achieved. Special care has to be taken by soldering the fragile inner conductor of the coaxial cable to the stripline (red square). Bending, pushing or pulling on the coaxial cable rapidly leads to a disruption of the inner conductor.

Coldfinger and shielded sample space

As seen in Fig. A.6 the output side of the filterbox directly leads into shielded cables (soldered, slits in box covered with Ag-epoxy). The connection of the filterbox and the samples space in a distance of approx. 30cm was achieved by designing a coldfinger with a high thermal conductivity. At its end a metal cyclinder defines the shielded sample volume. The coaxial cables are fed through the top part of the metal cylinder using the same cylindrical feedthrough body as seen in Fig. A.6. As thermometry and measurement lines need to reach into sample space, the body has 25 individual feedthroughs. The Ag-epoxy filter box and the coldfinger (including the shielded lines) were produced in parallel. In the last step both were connected by soldering the ends of the coaxial cable onto the striplines in the output side of the filterbox.

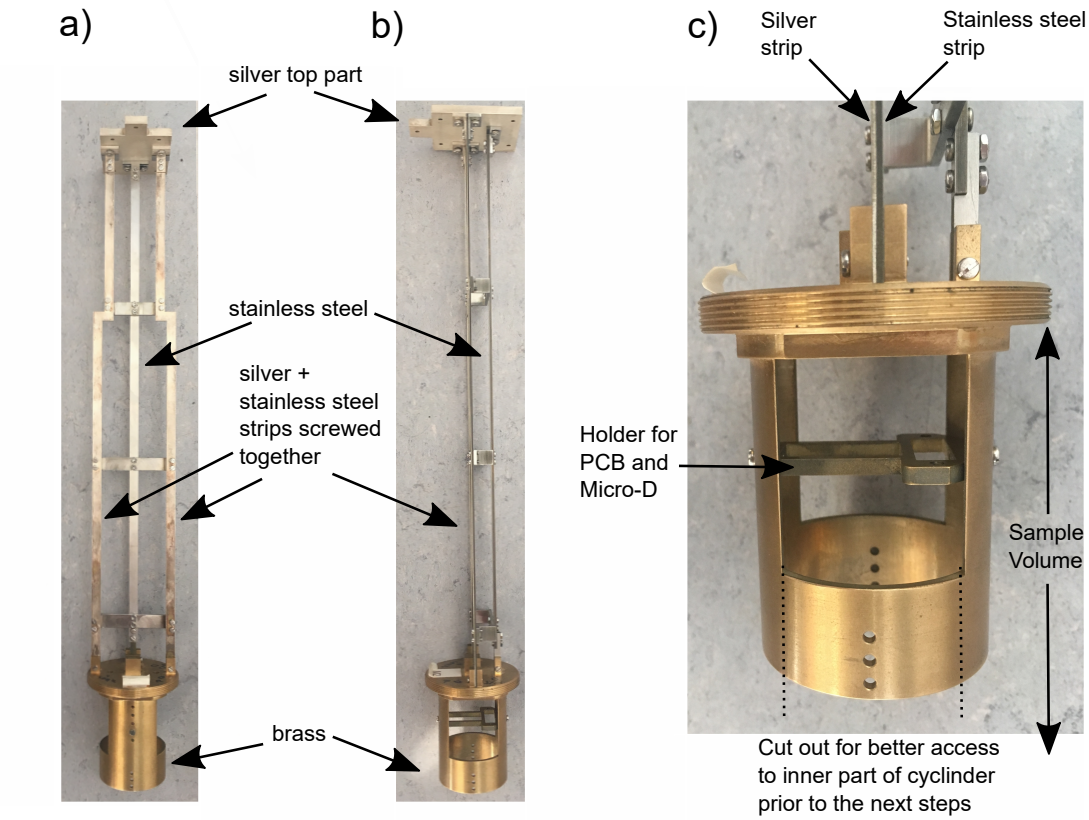

Figure A.7.: Coldfinger: a) Top view and b) side view. Some parts originally designed to be made out of stainless steel have been replaced by silver parts to further increase thermal contact between sample volume and mixing chamber. c) Bottom part of coldfinger, where the connection between silver/stainless steel parts and brass cylinder can be seen. The big threat is used to close the sample volume with a brass can.

In Fig. A.7 the raw coldfinger can be seen. The materials chosen are silver for its good thermal conductance, stainless steel for its stiffness and brass for its good thermal conductance, but higher resistivity than silver. The idea was to reduce effects of currents induced by the external magnetic field. To further decrease heating effects by induced currents we cut out a quarter of the bottom part as indicated in Fig. A.7c).
The top end of the coldfinger is a pure silver plate, which is screwed directly to the bottom of the mixing chamber plate. Three sets of strips connect the top part with the bottom part. The first design consisted of one main strip being thicker than the other two and made out of pure stainless steel to act as stabilization. The other two were a combination of a silver strip and a stainless steel strip. To further increase thermal contact high purity copper braids were added. For the final setup all three metal connections were replaced by thicker pure silver only ones. In addition, the design of the brass bottom part was reshaped. The mass was reduced and the previously closed bottom loop was opened on one side. This was done to further reduce thermalization times and minimize currents due to magnet field changed, as well as gaining easier access to the sample space. The

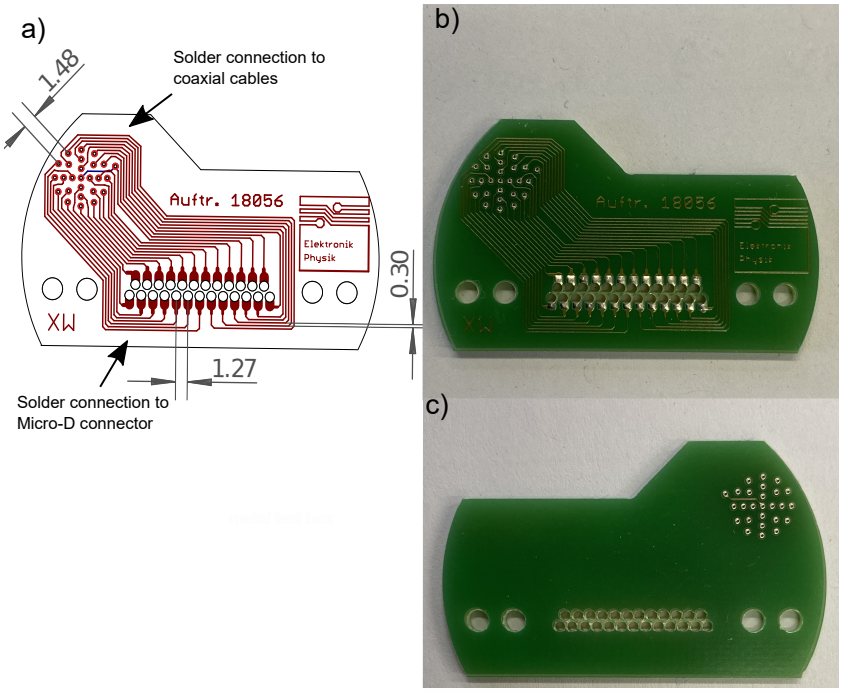

Figure A.8.: Coldfinger - printed circuit board: a) Design including scales in mm. b) Front side and c) back side. The walls of the holes for the soldering of the inner conductor of the coaxial cables are covered with metal. The inner conductors were fed through from the top to the back. Soldering happened on the backside.

inner conductor of the shielded lines are soldered to a printed circuit board (PCB) inside the sample space. The PCB-board was designed by Dieter Riedl (electronics workshop) and manufactured by Fischer Leiterplatten GmbH. The board consisted of strips lines

connecting soldering feedtroughs for the incoming measurement lines on the one side and soldering cups for a micro-D connector. The design of the PCB can be seen in Fig. A.8. After all lines were soldered into the PCB we covered a small volume with Stycast to prevent the fragile inner conductor from being damaged or disrupted.
Fig. A.9 covers the most important steps for the coldfinger. At first the cables were fed through the brass feedtroughs. To keep them parallel distance keeper were used as seen in a). Secondly, they were soldered into the soldering-feedthroughs of the PCB board in b). To ensure the soldering connections to be stable and to minimize the risk for the

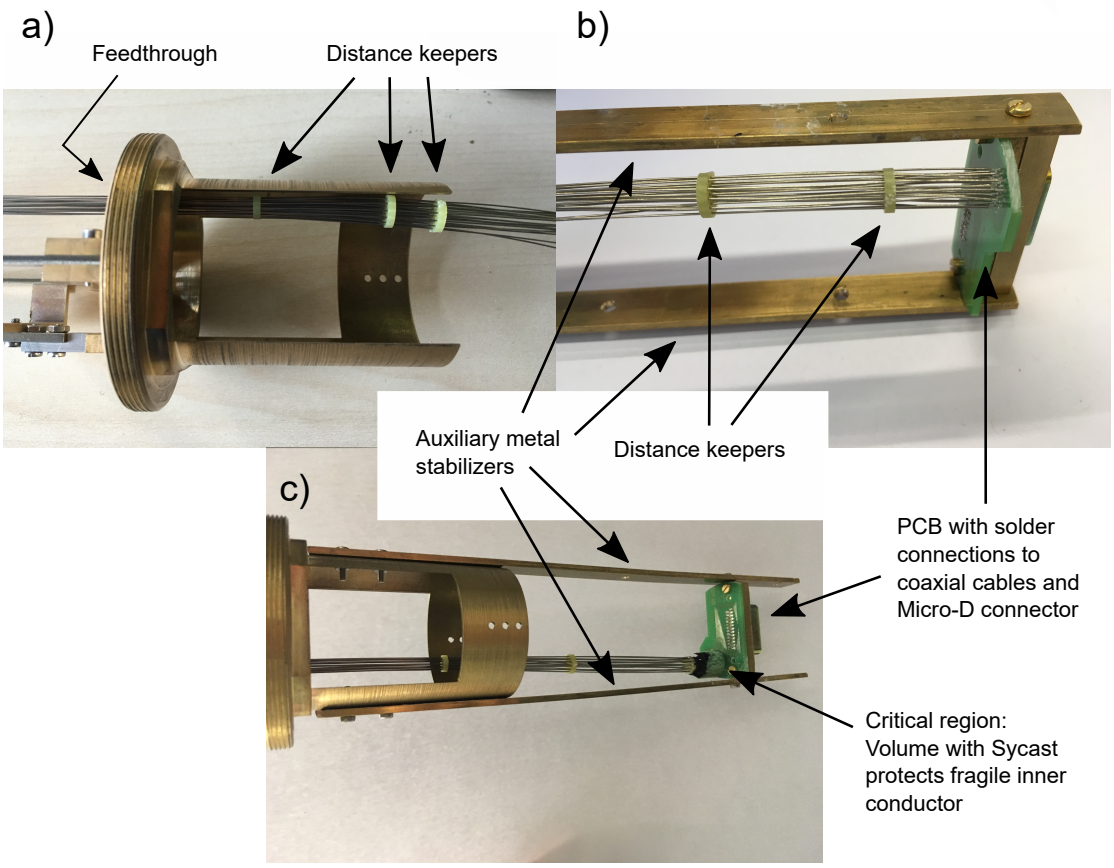

Figure A.9.: Distance keepers not only keep the cables alinged in parallel configuration, it prevents them from rotation as well. The auxiliary metal stabilizers are important to have a fixed geometry while soldering into the PCB. They are removed after the Stycast is cured. The PCB is carefully pushed up to its final position.

inner conductor of the cable to break, a cyclindrical volume was filled with Stycast (see Tab. A.1). This can be seen in c). The material used is electrically non-conducting (no short between inner conductor and cold ground), but thermally conducting (heat can be transferred away). Then the metal stabilizers were removed and the PCB-board was pushed up to its final position. The last step connects the finished filterbox to the open

ends of the shielded measurement lines. This connection can be seen in Fig. A.6b). The bottom part of the insert in its final version can be seen in Fig 3.7.

A.3. Metal Mask for Shadow Evaporation

The shadow mask was designed to evaporate granular aluminum into a predefined structure (Hallbar like) under a small angle. Due to problems with bonding/contacting the material the goal was to increase the number of working contacts while decreasing the contact resistances. To do so, the idea was to grow gold contact pads in Step 1 and then cover those with granular aluminum in Step 2. Ideally, one would first grow the granular aluminum film and then put contacts on top. An in situ growth of gold onto the grAl was not possible in Tel Aviv. The sample has to be taken out of the growth chamber exposing it to air as it it transported to a second chamber. The surface immediately starts to oxidize resulting in an oxide tunneling barrier between the gold-contacts and the grAl.
The work-around is to first make gold contact and then evaporate the grAl. However, as the gold contacts should be 10nm or more (for wedge bonding) their thickness exceeded the thickness of the film (5nm), probabably leaving behind a gap at the edges. To have a continuous film which covers the contact pad across the edge the growth is done under a small angle of approx. 1 degree.
In Fig. A.10 the four different main components are shown, i.e. a) chip holder, b) wedge, c) mask 1 for gold contact pads and d) mask 2 for granular aluminum hallbars on top of gold contacts.

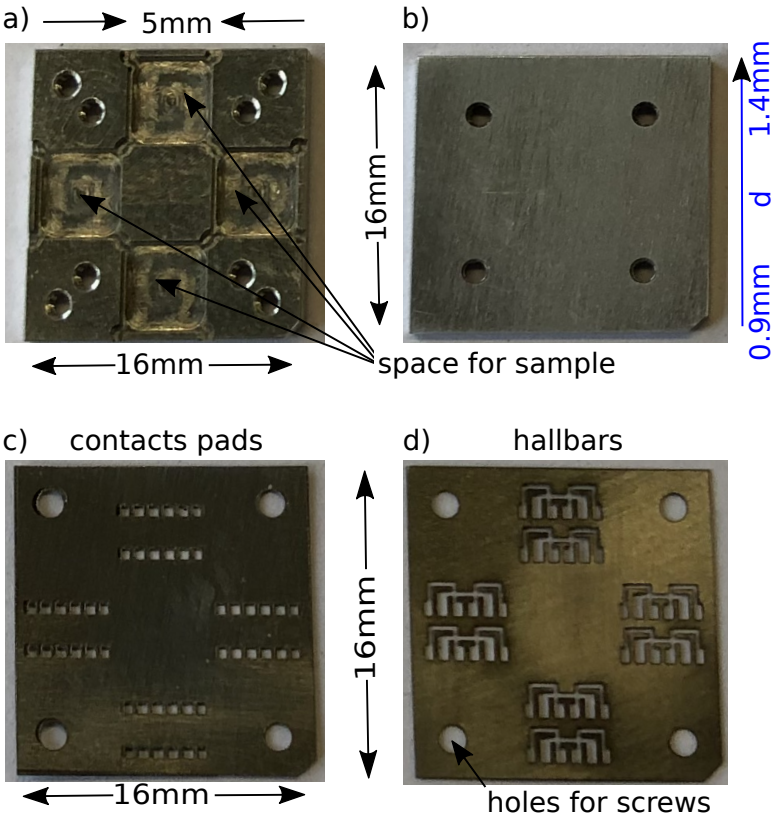

Figure A.10.: All four components are 16mm in length and width. a) Chip holder (aluminum) with 4 sample spaces with 5mm in length and width. b) Wedge (aluminum) with increasing thickness starting from 0.9mm to 1.4mm indicated by the blue arrow. The corresponding angle is 1.79°. c) Mask 1 (brass) with 4 sets structure. Each structures consists of two rows with 6 squares. The squares have a length and width of 0.5mm. The width of outermost squares is only 0.4mm. The squares are separated by 0.3mm. d) Mask 2 (brass) for hallbars. The additional structures, in reference to mask 1, which connects the contact pads/area, has a designed width of 0.2mm. The width increased to $\sim$ 0.25-0.3mm in the manufacturing process.

The chip holder contains four sample spaces. Therefore up to 4 samples may be grown in the same run. The wegde defines the tilt of the substrate. The top side is slightly thicker than the lower side, i.e. thickness d increases (see Fig. A.10). It defines an angle of 1.79°. Mask 1 is the shadow mask for step 1 defining the gold contacts, while mask 2 is used to put the Hallbar geometry in Step 2.

Fig. A.11a) and b) shows the components combined for Step 1 (Sample Holder + Mask 1), while c) and d) show Step 2 (Wedge, Sample Holder + Mask 2).

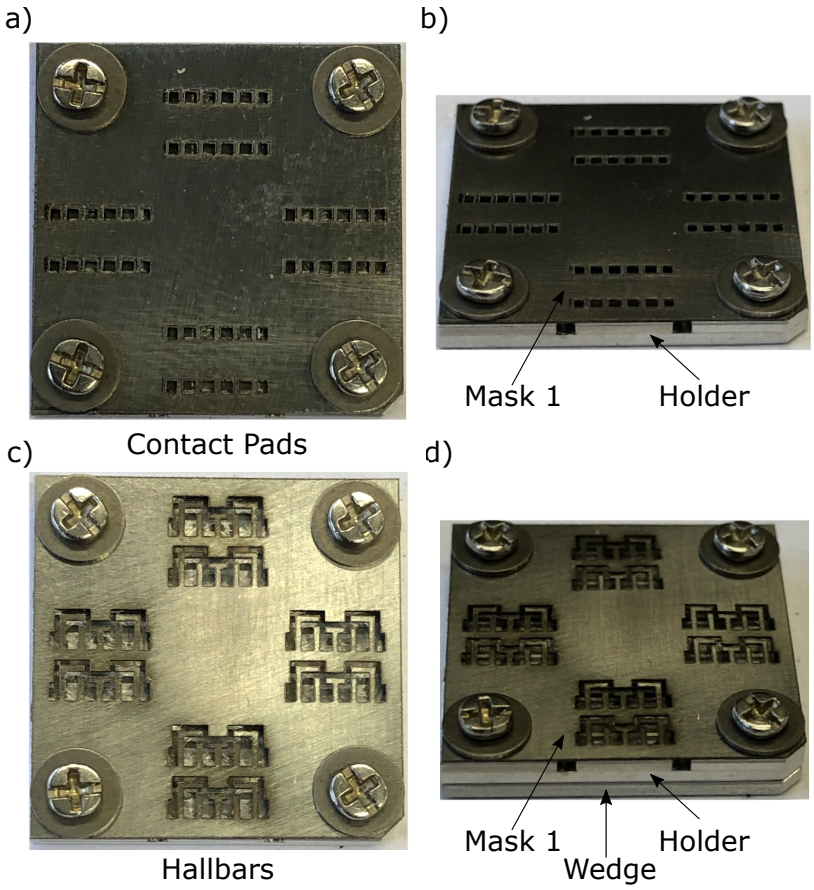

Figure A.11.: Combination of the components for Step 1 (contact pads) shown as a top view in a) and side view in b). The combination for Step 2 (Hallbar-like structure) for deposition of the granular aluminum film is presented in c) and d).

A.4. Add-on to Section 5.2.3: Compensation of Residual Perpendicular Magnetic Field in Parallel Magnetic Field Configuration

For the parallel magnetic field configuration it is important to compensate a perpendicular magnetic field (Z-axis), which is generated by a slight tilt of the sample in respect to the X-axis of the 2D vector magnet. The response of the sample to an applied perpedicular magnetic field has been shown in section 5.2. Even small perpendicular fields in the range of tens of mT do have a dramatic effect.

The used approach is to set the B_X field of the 2D vector magnet to a fixed value and sweep the B_Z magnetic field component to find a minimum in $R(B_Z)$. That $B_{Z,min}$, denoted as compensation field, is exactly the magnetic field needed to cancel out the residual B_{perp} generated by the tilt of the sample in the X-Y plane.

All of the presented measurements with parallel magnetic fields in section 5.2.3 have been compensated using this method.

The impact of an uncompensated residual perpendicular magnetic field can be seen in Fig. A.12 in the temperature evolution of the current voltage characteristics. Fig. A.13

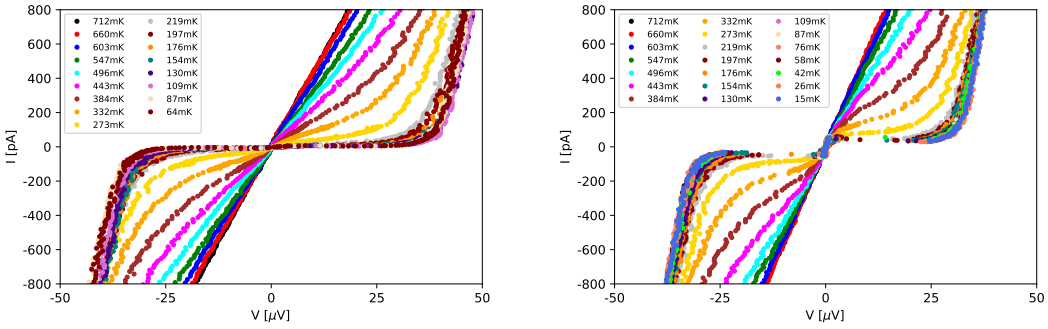

Figure A.12.: $B_{\parallel} = 0.5$T: a) Set of uncompensated IVs(T). b) Set of compensated IVs(T). The temperature ranges from $T = 712$mK down to $T = 64$mK in a) and from $T = 712$mK down to $T = 15$mK in b). The Coulomb blockade with threshold voltage is seen in both measurements. However, the zero bias supercurrent feature is only present in b), when using the compensation method.

presents the measurements at $B_X = 500$mT at $T = 87$mK in a uncompensated a) and compensated b) configuration and indicates the suppression of the zero bias anomaly with residual perpendicular magnetc field. The compensated data is similar to the $B = 0$T curve.

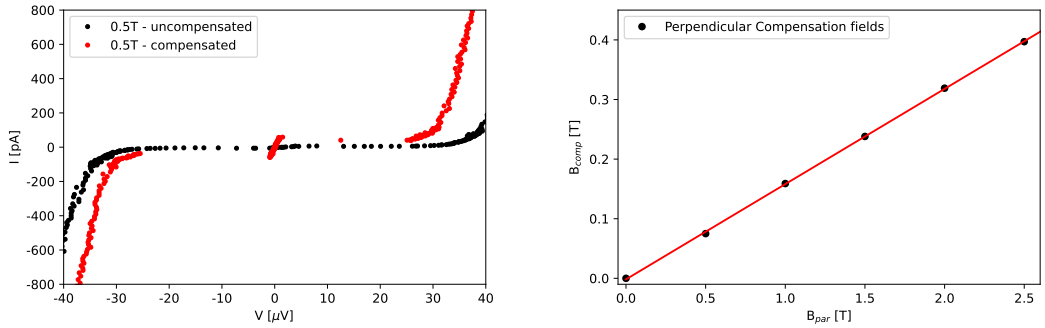

Figure A.13.: $B_{\parallel} = 0.5$T: a) Comparison of compensated and uncompensated IVs at $T = 87$mK. The black curve is the uncompensated measurement and the red curve is the compensated measurement. The deviation around zero bias is visible. In addition, the uncompensated perpendicular field shifted the threshold voltage to higher values. b) Compensation field B_{Comp} along the Z-axis for parallel magentic fields. The red curve is a linear fit to the data. The slope is used to calculate the angle α corresponding to the tilt of the sample in respect to the X-Y plane.

The corresponding tilt of the sample plane compared to the X-Y plane can be calculated by evaluating the slope of compensation fields in respect to the applied B_{X} fields. The B_{Z} values to find a minimum were 75mT for 0.5T, 159mT for 1T, 238mT for 1.5T, 319mT for 2T and 397mT for 2.5T. This is shown in Fig. A.13b), where the data is fitted to a linear slope. The tilt of the sample in the X-Y-plane is given by $\alpha = \tan^{-1}(\mathrm{slope}) = \tan^{-1}(0.15977143) \approx 9°$.

A.5. Devices and Materials

Name	Company	Description
Kelvinox HA 400	Oxford Instruments	dilution refrigerator and superconducting magnet system
Model 372	Lake Shore Cryotronics, Inc.	AC-resistance bridge and temperature controller
Model 3726	Lake Shore Cryotronics, Inc.	scanner
low-loss dewar including 2-axes magnet	Oxford Instruments	superconducting magnet (Z - 7T, X - 3T)
Mercury IPM	Oxford Instruments	magnet powersupply
Mercury IPS	Oxford Instruments	magnet powersupply
model Gr-200A-20-0,05A	Lake Shore Cryotronics, Inc.	calibrated germanium resistor, thermometry
model RX-102B-RS	Lake Shore Cryotronics, Inc.	initially uncalibrated RuOx resistor, calibrated against calibrated germanium thermometer and Magnicon MFFT
MFFT noise thermometer	Magnicon GmbH	SQUID thermometer

Table A.1.: Devices for the low temperature system and thermometry.

Name	**Company**	**Description**
GS200	Yokogawa Test and Measurement Corporation	DC voltage/current source
3458A	Agilent Technologies, Inc.	8 1/2 digit multimeter
SR830 DSP	Stanford Research Systems	lock-in amplifier
DDPCA-S	FEMTO Messtechnik GmbH	current-to-voltage transducer
DLPVA	FEMTO Messtechnik GmbH	voltage amplifier
SEM Auriga	Carl Zeiss GmbH	scanning electron microscope
AFM Park	Park Systems	atomic force microscope

Table A.2.: Devices used for measurement setups and sample characterization.

Name	Company	Description
EPO-TEK E4110	Epoxy Technology	electrically conductive silver epoxy
Eccosorb CRS 117	Laird / Emerson and Cuming	high-loss material for microwave frequency range
STYCAST 2850FT	Henkel Loctite / Emerson and Cuming	thermally conductive, electrically insulative epoxy
LW-30	Ruff GmbH	winding machine
Lackdraht 0.1 200GR - CUL200/0.1	Bürklin/Distrelec	copper wire with PU-insulation
A2427	GVL Cryoengeneering	semi-rigid coaxial cable, cupronnickel inner and outer conductor, PTFE insulation, low noise
25-MDM	CINCH / Oxford Instruments	25-way Micro-D connector
copper clamps, gold-plated	Mechanical Workshop, Electronical Workshop	thermalization of Magnicon cabling
copper anchors, gold-plated	Mechanical Workshop, Electronical Workshop	forms: cylindrical including threads or 90 degree angle; fixation points for copper-braids and RC-filters
copper braids, gold-plated	Electronical Workshop	purpose: thermal shortcut

Table A.3.: Devices and materials used for filtering and thermalization.

Name	Company	Description
Mouser Electronics-Nr.: 71-TNPW0805820RBEEA	Vishay	820Ω resistance, TNPW thin-film, 0805-inch for surface mounting
Mouser Electronics-Nr.: 71-TNPW08051K20BEEA	Vishay	1.2kΩ resistance, TNPW thin-film, 0805-inch for surface mounting
Mouser Electronics-Nr.: 81-GRM21BC1H183FA1L	Murata	9.1nF capacitor, GRM-series, layered ceramics, 0603-inch for surface mounting
Mouser Electronics-Nr.: 81-GRM1885C1H912JA1D	Murata	18nF capacitor, GRM-series, layered ceramics, 0805-inch for surface mounting
Mouser Electronics-Nr.: 800-420153LF	Tusonix	EMI-Pi-filters, 5500pF, feed through

Table A.4.: Devices for RC-filtering and Pi-filtering.

Bibliography

[1] J. Bardeen, L. N. Cooper, and J. R. Schrieffer. "Theory of superconductivity". In: *Physical review* 108.5 (1957), p. 1175.

[2] V. L. Ginzburg and L. D. Landau. "Zh. Eksp. Teor. Fiz." In: *SSSR 20* 1063 (1950).

[3] B. Abeles, R. W. Cohen, and W. R. Stowell. "Critical magnetic fields of granular superconductors". In: *Physical Review Letters* 18.21 (1967), p. 902.

[4] G. Deutscher et al. "Transition to zero dimensionality in granular aluminum superconducting films". In: *Journal of Low Temperature Physics* 10.1 (1973), pp. 231–243.

[5] G. Deutscher et al. "Granular superconducting films". In: *Journal of Vacuum Science and Technology* 10.5 (1973), pp. 697–701.

[6] G. Deutscher. *Granular Superconductivity: a Playground for Josephson, Anderson, Kondo, and Mott*. 2021.

[7] T. I. Baturina and V. M. Vinokur. "Superinsulator–superconductor duality in two dimensions". In: *Annals of Physics* 331 (2013), pp. 236–257. ISSN: 0003-4916. DOI: https://doi.org/10.1016/j.aop.2012.12.007. URL: https://www.sciencedirect.com/science/article/pii/S0003491612002229.

[8] B. Abeles. "Effect of charging energy on superconductivity in granular metal films". In: *Physical Review B* 15.5 (1977), p. 2828.

[9] H. M. Jaeger et al. "Threshold for superconductivity in ultrathin amorphous gallium films". In: *Physical Review B* 34.7 (1986), p. 4920.

[10] H. M. Jaeger et al. "Onset of superconductivity in ultrathin granular metal films". In: *Physical Review B* 40.1 (1989), p. 182.

[11] H. Kamerlingh Onnes. "The resistance of pure mercury at helium temperatures". In: *Commun. Phys. Lab. Univ. Leiden, b* 120 (1911).

[12] H. Kamerlingh Onnes. "Further experiments with Liquid Helium. G. On the Electrical Resistance of Pure Metals, etc. VI. On the Sudden Change in the Rate at which the Resistance of Mercury Disappears." In: *Through Measurement to Knowledge*. Springer, 1991, pp. 267–272.

[13] W. Meissner and R. Ochsenfeld. "Ein neuer Effekt bei Eintritt der Supraleitfähigkeit". In: *Naturwissenschaften* 21.44 (1933), pp. 787–788.

[14] F. London and H. London. "The electromagnetic equations of the supraconductor". In: *Proceedings of the Royal Society of London. Series A-Mathematical and Physical Sciences* 149.866 (1935), pp. 71–88.

[15] C. J. Gorter and H. B. J. Casimir. In: *Phys. Z. 35, 963* (1934).

[16] C. Enss and S. Hunklinger. *Low-temperature physics*. Springer Science & Business Media, 2005.

[17] F. B. Silsbee. "A note on electrical conduction in metals at low temperatures". In: *Journal of the Washington Academy of Sciences* 6.17 (1916), pp. 597–602.

[18] M. Tinkham. *Introduction to superconductivity, Second Edition*. Dover Publications, 2004.

[19] V. L. Ginzburg and L. D. Landau. "On the theory of superconductivity". In: *On superconductivity and superfluidity*. Springer, 2009, pp. 113–137.

[20] J. G. Bednorz and K. A. Müller. "Possible high Tc superconductivity in the Ba-La- Cu- O system". In: *Zeitschrift für Physik B Condensed Matter* 64.2 (1986), pp. 189–193.

[21] L. N. Cooper. "Bound electron pairs in a degenerate Fermi gas". In: *Physical Review* 104.4 (1956), p. 1189.

[22] H. Fröhlich. "Theory of the superconducting state. I. The ground state at the absolute zero of temperature". In: *Physical Review* 79.5 (1950), p. 845.

[23] J. Bardeen. "Wave functions for superconducting electrons". In: *Physical Review* 80.4 (1950), p. 567.

[24] A. A. Abrikosov. In: *Sov. Phys. JETP* 5 (1957), p. 1174.

[25] A. A. Abrikosov. "Concerning surface superconductivity in strong magnetic fields". In: *Sov. Phys. JETP* 20.2 (1965), p. 480.

[26] U. Essmann and H. Träuble. "The direct observation of individual flux lines in type II superconductors". In: *Physics letters A* 24.10 (1967), pp. 526–527.

[27] H. F. Hess et al. "Scanning-tunneling-microscope observation of the Abrikosov flux lattice and the density of states near and inside a fluxoid". In: *Physical review letters* 62.2 (1989), p. 214.

[28] H. F. Hess, R. B. Robinson, and J. V. Waszczak. "Vortex-core structure observed with a scanning tunneling microscope". In: *Physical review letters* 64.22 (1990), p. 2711.

[29] L. P. Gor'kov. "Microscopic derivation of the Ginzburg-Landau equations in the theory of superconductivity". In: *Sov. Phys. JETP* 9.6 (1959), pp. 1364–1367.

[30] A. B. Pippard and W. L. Bragg. "An experimental and theoretical study of the relation between magnetic field and current in a superconductor". In: *Proceedings of the Royal Society of London. Series A. Mathematical and Physical Sciences* 216.1127 (1953), pp. 547–568.

[31] B. D. Josephson. "Possible new effects in superconductive tunnelling". In: *Physics letters* 1.7 (1962), pp. 251–253.

[32] V. Ambegaokar and A. Baratoff. "Tunneling Between Superconductors". In: *Phys. Rev. Lett.* 10 (11 June 1963), pp. 486–489. DOI: 10.1103/PhysRevLett.10.486. URL: https://link.aps.org/doi/10.1103/PhysRevLett.10.486.

[33] M. H. Devoret, A. Wallraff, and J. M. Martinis. *Superconducting Qubits: A Short Review*. 2004. DOI: 10.48550/ARXIV.COND-MAT/0411174. URL: https://arxiv.org/abs/cond-mat/0411174.

[34] R. Gross and A. Marx. *Festkörperphysik*. De Gruyter Oldenbourg, 2014. ISBN: 9783110358704. DOI: doi:10.1524/9783110358704. URL: https://doi.org/10.1524/9783110358704.

[35] R. Gross and A. Marx. *Applied Superconductivity: Josephson Effect and Superconducting Electronics*. 2005. URL: https://www.wmi.badw.de/fileadmin/WMI/Lecturenotes/Applied_Superconductivity/AS_Chapter3.pdf.

[36] J. Pearl. "Current distribution in superconducting films carrying quantized fluxoids". In: *Appl. Phys. Lett. 5, 65* (1964).

[37] J. M. Kosterlitz and D. J. Thouless. "Long range order and metastability in two dimensional solids and superfluids. (Application of dislocation theory)". In: *Journal of Physics C: Solid State Physics* 5.11 (June 1972), pp. L124–L126. DOI: 10.1088/0022-3719/5/11/002. URL: https://doi.org/10.1088/0022-3719/5/11/002.

[38] J. M. Kosterlitz and D. J. Thouless. "Ordering, metastability and phase transitions in two-dimensional systems". In: *Journal of Physics C: Solid State Physics* 6.7 (Apr. 1973), pp. 1181–1203. DOI: 10.1088/0022-3719/6/7/010. URL: https://doi.org/10.1088/0022-3719/6/7/010.

[39] V. L. Berezinskii. "Destruction of long-range order in one-dimensional and two-dimensional systems having a continuous symmetry group I. Classical systems". In: *Sov. Phys. JETP* 32.3 (1971), pp. 493–500.

[40] V. L. Berezinskii. "Destruction of long-range order in one-dimensional and two-dimensional systems possessing a continuous symmetry group. II. Quantum systems". In: *Sov. Phys. JETP* 34.3 (1972), pp. 610–616.

[41] B. I. Halperin and D. R. Nelson. "Resistive transition in superconducting films". In: *Journal of low temperature physics* 36.5 (1979), pp. 599–616.

[42] The Royal Swedish Academy of Science. *Press release: The Nobel Prize in Physics 2016*. 2016. URL: https://www.nobelprize.org/prizes/physics/2016/press-release/.

[43] S. V. Postolova, A. Y. Mironov, and T. I. Baturina. "Nonequilibrium transport near the superconducting transition in TiN films". In: *JETP letters* 100.10 (2015), pp. 635–641.

[44] D. J. Resnick et al. "Kosterlitz-Thouless Transition in Proximity-Coupled Superconducting Arrays". In: *Phys. Rev. Lett.* 47 (21 Nov. 1981), pp. 1542–1545. DOI: 10.1103/PhysRevLett.47.1542. URL: https://link.aps.org/doi/10.1103/PhysRevLett.47.1542.

[45] T. I. Baturina et al. "Superconducting phase transitions in ultrathin TiN films". In: *EPL (Europhysics Letters)* 97.1 (Jan. 2012), p. 17012. DOI: 10.1209/0295-5075/97/17012. URL: https://doi.org/10.1209/0295-5075/97/17012.

[46] B. L. Altshuler and A. G. Aronov. "Electron–electron interaction in disordered conductors". In: *Modern Problems in condensed matter sciences*. Vol. 10. Elsevier, 1985, pp. 1–153.

[47] L. G. Aslamasov and A. I. Larkin. "The influence of fluctuation pairing of electrons on the conductivity of normal metal". In: *Physics Letters A* 26.6 (1968), pp. 238–239. ISSN: 0375-9601. DOI: https://doi.org/10.1016/0375-9601(68)90623-3. URL: https://www.sciencedirect.com/science/article/pii/0375960168906233.

[48] E. Abrahams, M. Redi, and J. W. F. Woo. "Effect of Fluctuations on Electronic Properties above the Superconducting Transition". In: *Phys. Rev. B* 1 (1 Jan. 1970), pp. 208–213. DOI: 10.1103/PhysRevB.1.208. URL: https://link.aps.org/doi/10.1103/PhysRevB.1.208.

[49] K. Maki. "The Critical Fluctuation of the Order Parameter in Type-II Superconductors". In: *Progress of Theoretical Physics* 39.4 (Apr. 1968), pp. 897–906. ISSN: 0033-068X. DOI: 10.1143/PTP.39.897. eprint: https://academic.oup.com/ptp/article-pdf/39/4/897/5475903/39-4-897.pdf. URL: https://doi.org/10.1143/PTP.39.897.

[50] K. Maki. "Critical Fluctuation of the Order Parameter in a Superconductor. I". In: *Progress of Theoretical Physics* 40.2 (Aug. 1968), pp. 193–200. ISSN: 0033-068X. DOI: 10.1143/PTP.40.193. eprint: https://academic.oup.com/ptp/article-pdf/40/2/193/5304634/40-2-193.pdf. URL: https://doi.org/10.1143/PTP.40.193.

[51] R. S. Thompson. "Microwave, Flux Flow, and Fluctuation Resistance of Dirty Type-II Superconductors". In: *Phys. Rev. B* 1 (1 Jan. 1970), pp. 327–333. DOI: 10.1103/PhysRevB.1.327. URL: https://link.aps.org/doi/10.1103/PhysRevB.1.327.

[52] V. M. Galitski and A. I. Larkin. "Superconducting fluctuations at low temperature". In: *Phys. Rev. B* 63 (17 Apr. 2001), p. 174506. DOI: 10.1103/PhysRevB.63.174506. URL: https://link.aps.org/doi/10.1103/PhysRevB.63.174506.

[53] K. Kronfeldner. "Transport properties of critically disordered TiN films". PhD thesis. 2017.

[54] T. I. Baturina et al. "From quantum corrections to magnetic-field-tuned superconductor–insulator quantum phase transition in TiN films". In: *Physica B: Condensed Matter* 359-361 (2005). Proceedings of the International Conference on Strongly Correlated Electron Systems, pp. 500–502. ISSN: 0921-4526. DOI: https://doi.org/10.1016/j.physb.2005.01.127. URL: https://www.sciencedirect.com/science/article/pii/S0921452605001523.

[55] D. Belitz and T. R. Kirkpatrick. "The Anderson-Mott transition". In: *Rev. Mod. Phys.* 66 (2 Apr. 1994), pp. 261–380. DOI: 10.1103/RevModPhys.66.261. URL: https://link.aps.org/doi/10.1103/RevModPhys.66.261.

[56] F. Evers and A. D. Mirlin. "Anderson transitions". In: *Rev. Mod. Phys.* 80 (4 Oct. 2008), pp. 1355–1417. DOI: 10.1103/RevModPhys.80.1355. URL: https://link.aps.org/doi/10.1103/RevModPhys.80.1355.

[57] V. F. Gantmakher and V. T. Dolgopolov. "Superconductor–insulator quantum phase transition". In: *Physics-Uspekhi* 53.1 (Jan. 2010), pp. 1–49. DOI: 10.3367/ufne.0180.201001a.0003. URL: https://doi.org/10.3367/ufne.0180.201001a.0003.

[58] Y.-H. Lin, J. Nelson, and A. M. Goldman. "Superconductivity of very thin films: The superconductor–insulator transition". In: *Physica C: Superconductivity and its Applications* 514 (2015). Superconducting Materials: Conventional, Unconventional and Undetermined, pp. 130–141. ISSN: 0921-4534. DOI: https://doi.org/10.1016/j.physc.2015.01.005. URL: https://www.sciencedirect.com/science/article/pii/S0921453415000143.

[59] K. B. Efetov. "Phase transition in granulated superconductors". In: *Sov. Phys. - JETP (Engl. Transl.); (United States)* 51:5 (May 1980). URL: https://www.osti.gov/biblio/7061039.

[60] M. P. A. Fisher. "Quantum Phase Slips and Superconductivity in Granular Films". In: *Phys. Rev. Lett.* 57 (7 Aug. 1986), pp. 885–888. DOI: 10.1103/PhysRevLett.57.885. URL: https://link.aps.org/doi/10.1103/PhysRevLett.57.885.

[61] B. G. Orr et al. "Global phase coherence in two-dimensional granular superconductors". In: *Phys. Rev. Lett.* 56 (4 Jan. 1986), pp. 378–381. DOI: 10.1103/PhysRevLett.56.378. URL: https://link.aps.org/doi/10.1103/PhysRevLett.56.378.

[62] B. G. Orr et al. "Global Phase Coherence in Two-Dimensional Granular Superconductors - Erratum". In: *Phys. Rev. Lett.* 56 (9 Mar. 1986), pp. 996–997. DOI: 10.1103/PhysRevLett.56.996.3. URL: https://link.aps.org/doi/10.1103/PhysRevLett.56.996.3.

[63] D. B. Haviland, Y. Liu, and A. M. Goldman. "Onset of superconductivity in the two-dimensional limit". In: *Phys. Rev. Lett.* 62 (18 May 1989), pp. 2180–2183. DOI: 10.1103/PhysRevLett.62.2180. URL: https://link.aps.org/doi/10.1103/PhysRevLett.62.2180.

[64] D. Kowal and Z. Ovadyahu. "Disorder induced granularity in an amorphous superconductor". In: *Solid State Communications* 90.12 (1994), pp. 783–786. ISSN: 0038-1098. DOI: https://doi.org/10.1016/0038-1098(94)90242-9. URL: https://www.sciencedirect.com/science/article/pii/0038109894902429.

[65] V. F. Gantmakher et al. "Giant negative magnetoresistance of semi-insulating amorphous indium oxide films in strong magnetic fields". In: *Zh. Eksp. Teor. Fiz* 109.5 (1996), p. 1765.

[66] Y. Dubi, Y. Meir, and Y. Avishai. "Nature of the superconductor–insulator transition in disordered superconductors". In: *Nature* 449.7164 (2007), pp. 876–880.

[67] B. Sacépé et al. "Disorder-Induced Inhomogeneities of the Superconducting State Close to the Superconductor-Insulator Transition". In: *Phys. Rev. Lett.* 101 (15 Oct. 2008), p. 157006. DOI: 10.1103/PhysRevLett.101.157006. URL: https://link.aps.org/doi/10.1103/PhysRevLett.101.157006.

[68] D. Shahar and Z. Ovadyahu. "Superconductivity near the mobility edge". In: *Phys. Rev. B* 46 (17 Nov. 1992), pp. 10917–10922. DOI: 10.1103/PhysRevB.46.10917. URL: https://link.aps.org/doi/10.1103/PhysRevB.46.10917.

[69] T. I. Baturina et al. "Localized superconductivity in the quantum-critical region of the disorder-driven superconductor-insulator transition in TiN thin films". In: *Physical review letters* 99.25 (2007), p. 257003.

[70] S. R. Khan et al. "Superconductor-insulator transition in granular Pb films near a superconducting ground plane". In: *Phys. Rev. B* 61 (9 Mar. 2000), pp. 5909–5912. DOI: 10.1103/PhysRevB.61.5909. URL: https://link.aps.org/doi/10.1103/PhysRevB.61.5909.

[71] A. Frydman. "The superconductor insulator transition in systems of ultrasmall grains". In: *Physica C: Superconductivity* 391.2 (2003), pp. 189–195. ISSN: 0921-4534. DOI: https://doi.org/10.1016/S0921-4534(03)00895-5. URL: https://www.sciencedirect.com/science/article/pii/S0921453403008955.

[72] O. Crauste et al. "Effect of annealing on the superconducting properties of a-Nb_xSi_{1-x} thin films". In: *Phys. Rev. B* 87 (14 Apr. 2013), p. 144514. DOI: 10.1103/PhysRevB.87.144514. URL: https://link.aps.org/doi/10.1103/PhysRevB.87.144514.

[73] B. J. Bishop, E. G. Spencer, and R. C. Dynes. "The metal-insulator transition in amorphous Nb:Si". In: *Solid-State Electronics* 28.1 (1985), pp. 73–79. ISSN: 0038-1101. DOI: https://doi.org/10.1016/0038-1101(85)90212-6. URL: https://www.sciencedirect.com/science/article/pii/0038110185902126.

[74] A. M. Finkel'stein. "Suppression of superconductivity in homogeneously disordered systems". In: *Physica B: Condensed Matter* 197.1 (1994), pp. 636–648. ISSN: 0921-4526. DOI: https://doi.org/10.1016/0921-4526(94)90267-4. URL: https://www.sciencedirect.com/science/article/pii/0921452694902674.

[75] E. Abrahams, S. V. Kravchenko, and M. P. Sarachik. "Metallic behavior and related phenomena in two dimensions". In: *Rev. Mod. Phys.* 73 (2 Mar. 2001), pp. 251–266. DOI: 10.1103/RevModPhys.73.251. URL: https://link.aps.org/doi/10.1103/RevModPhys.73.251.

[76] M. V. Feigel'man et al. "Eigenfunction Fractality and Pseudogap State near the Superconductor-Insulator Transition". In: *Phys. Rev. Lett.* 98 (2 Jan. 2007), p. 027001. DOI: 10.1103/PhysRevLett.98.027001. URL: https://link.aps.org/doi/10.1103/PhysRevLett.98.027001.

[77] V. L. Pokrovsky, G. M. Falco, and T. Nattermann. "Phase Diagram of Electron Systems near the Superconductor-Insulator Transition". In: *Phys. Rev. Lett.* 105 (26 Dec. 2010), p. 267001. DOI: 10.1103/PhysRevLett.105.267001. URL: https://link.aps.org/doi/10.1103/PhysRevLett.105.267001.

[78] S. Sachdev. "Quantum phase transitions". In: *Physics World* 12.4 (Apr. 1999), pp. 33–38. DOI: 10.1088/2058-7058/12/4/23. URL: https://doi.org/10.1088/2058-7058/12/4/23.

[79] A. Larkin. "Superconductor-insulator transitions in films and bulk materials". In: *Annalen der Physik* 511.7-9 (1999), pp. 785–794.

[80] P. Delsing et al. "Charge solitons and quantum fluctuations in two-dimensional arrays of small Josephson junctions". In: *Physical Review B* 50.6 (1994), p. 3959.

[81] P. Delsing et al. "Two-dimensional arrays of low capacitance tunnel junctions: general properties, phase transitions and Hall effect". In: *AIP Conference Proceedings*. Vol. 427. 1. American Institute of Physics. 1998, pp. 313–340.

[82] H. Q. Nguyen et al. "Observation of giant positive magnetoresistance in a cooper pair insulator". In: *Physical review letters* 103.15 (2009), p. 157001.

[83] T. I. Baturina et al. "Quantum metallicity on the high-field side of the superconductor-insulator transition". In: *Physical review letters* 98.12 (2007), p. 127003.

[84] M. P. A. Fisher. "Quantum phase transitions in disordered two-dimensional superconductors". In: *Physical Review Letters* 65.7 (1990), p. 923.

[85] M. P. A. Fisher, G. Grinstein, and S. M. Girvin. "Presence of quantum diffusion in two dimensions: Universal resistance at the superconductor-insulator transition". In: *Phys. Rev. Lett.* 64 (5 Jan. 1990), pp. 587–590. DOI: 10.1103/PhysRevLett.64.587. URL: https://link.aps.org/doi/10.1103/PhysRevLett.64.587.

[86] S. L. Sondhi et al. "Continuous quantum phase transitions". In: *Rev. Mod. Phys.* 69 (1 Jan. 1997), pp. 315–333. DOI: 10.1103/RevModPhys.69.315. URL: https://link.aps.org/doi/10.1103/RevModPhys.69.315.

[87] V. F. Gantmakher et al. "Suppression of 2D superconductivity by the magnetic field: quantum corrections vs. the superconductor-insulator transition". In: *Journal of Experimental and Theoretical Physics Letters* 77.8 (2003), pp. 424–428.

[88] K. Kronfeldner, T. I. Baturina, and C. Strunk. "Multiple crossing points and possible quantum criticality in the magnetoresistance of thin TiN films". In: *Physical Review B* 103.18 (2021), p. 184512.

[89] E. Shimshoni, A. Auerbach, and A. Kapitulnik. "Transport through quantum melts". In: *Physical review letters* 80.15 (1998), p. 3352.

[90] K. Sheshadri et al. "Percolation-Enhanced Localization in the Disordered Bosonic Hubbard Model". In: *Phys. Rev. Lett.* 75 (22 Nov. 1995), pp. 4075–4078. DOI: 10.1103/PhysRevLett.75.4075. URL: https://link.aps.org/doi/10.1103/PhysRevLett.75.4075.

[91] A. Ghosal, M. Randeria, and N. Trivedi. "Inhomogeneous pairing in highly disordered s-wave superconductors". In: *Phys. Rev. B* 65 (1 Nov. 2001), p. 014501. DOI: 10.1103/PhysRevB.65.014501. URL: https://link.aps.org/doi/10.1103/PhysRevB.65.014501.

[92] Y. M. Strelniker, A. Frydman, and S. Havlin. "Percolation model for the superconductor-insulator transition in granular films". In: *Phys. Rev. B* 76 (22 Dec. 2007), p. 224528. DOI: 10.1103/PhysRevB.76.224528. URL: https://link.aps.org/doi/10.1103/PhysRevB.76.224528.

[93] L. Merchant et al. "Crossover from phase fluctuation to amplitude-dominated superconductivity: A model system". In: *Physical Review B* 63.13 (2001), p. 134508.

[94] S.-Y. Hsu and J. M. Valles. "Magnetic-field-induced pair-breaking effects in granular Pb films near the superconductor-to-insulator transition". In: *Phys. Rev. B* 48 (6 Aug. 1993), pp. 4164–4167. DOI: 10.1103/PhysRevB.48.4164. URL: https://link.aps.org/doi/10.1103/PhysRevB.48.4164.

[95] R. Fazio and H. van der Zant. "Quantum phase transitions and vortex dynamics in superconducting networks". In: *Physics Reports* 355.4 (2001), pp. 235–334. ISSN: 0370-1573. DOI: https://doi.org/10.1016/S0370-1573(01)00022-9. URL: https://www.sciencedirect.com/science/article/pii/S0370157301000229.

[96] R. Fazio and G. Schön. "Charge and vortex dynamics in arrays of tunnel junctions". In: *Phys. Rev. B* 43 (7 Mar. 1991), pp. 5307–5320. DOI: 10.1103/PhysRevB.43.5307. URL: https://link.aps.org/doi/10.1103/PhysRevB.43.5307.

[97] J. V. José and C. Rojas. "Superconducting to normal state phase boundary in arrays of ultrasmall Josephson junctions". In: *Physica B: Condensed Matter* 203.3 (1994), pp. 481–489. ISSN: 0921-4526. DOI: https://doi.org/10.1016/0921-4526(94)90100-7. URL: https://www.sciencedirect.com/science/article/pii/0921452694901007.

[98] J. E. Mooij et al. "Unbinding of charge-anticharge pairs in two-dimensional arrays of small tunnel junctions". In: *Phys. Rev. Lett.* 65 (5 July 1990), pp. 645–648. DOI: 10.1103/PhysRevLett.65.645. URL: https://link.aps.org/doi/10.1103/PhysRevLett.65.645.

[99] T. S. Tighe et al. "Measurements of charge soliton motion in two-dimensional arrays of ultrasmall Josephson junctions". In: *Physical Review B* 47.2 (1993), p. 1145.

[100] M. Pollak, M. Ortuño, and A. Frydman. *The electron glass*. Cambridge University Press, 2013.

[101] N. F. Mott. "ON THE TRANSITION TO METALLIC CONDUCTION IN SEMICONDUCTORS". In: *Canadian Journal of Physics* 34.12A (1956), pp. 1356–1368. DOI: 10.1139/p56-151. eprint: https://doi.org/10.1139/p56-151. URL: https://doi.org/10.1139/p56-151.

[102] E. M. Conwell. "Impurity Band Conduction in Germanium and Silicon". In: *Phys. Rev.* 103 (1 July 1956), pp. 51–61. DOI: 10.1103/PhysRev.103.51. URL: https://link.aps.org/doi/10.1103/PhysRev.103.51.

[103] A. Miller and E. Abrahams. "Impurity Conduction at Low Concentrations". In: *Phys. Rev.* 120 (3 Nov. 1960), pp. 745–755. DOI: 10.1103/PhysRev.120.745. URL: https://link.aps.org/doi/10.1103/PhysRev.120.745.

[104] P. W. Anderson. "Absence of Diffusion in Certain Random Lattices". In: *Phys. Rev.* 109 (5 Mar. 1958), pp. 1492–1505. DOI: 10.1103/PhysRev.109.1492. URL: https://link.aps.org/doi/10.1103/PhysRev.109.1492.

[105] N. F. Mott and W. D. Twose. "The theory of impurity conduction". In: *Advances in Physics, 10:38, 107-163,* (1961). DOI: 10.1080/00018736100101271.

[106] N. F. Mott. "Conduction in glasses containing transition metal ions". In: *Journal of Non-Crystalline Solids* 1.1 (1968), pp. 1–17. ISSN: 0022-3093. DOI: https://doi.org/10.1016/0022-3093(68)90002-1. URL: https://www.sciencedirect.com/science/article/pii/0022309368900021.

[107] A. L. Efros and B. I. Shklovskii. "Coulomb gap and low temperature conductivity of disordered systems". In: *Journal of Physics C: Solid State Physics* 8.4 (Feb. 1975), pp. L49–L51. DOI: 10.1088/0022-3719/8/4/003. URL: https://doi.org/10.1088/0022-3719/8/4/003.

[108] P. Sheng, B. Abeles, and Y. Arie. "Hopping Conductivity in Granular Metals". In: *Phys. Rev. Lett.* 31 (1 July 1973), pp. 44–47. DOI: 10.1103/PhysRevLett.31.44. URL: https://link.aps.org/doi/10.1103/PhysRevLett.31.44.

[109] J. Delahaye, T. Grenet, and F. Gay. "Coexistence of anomalous field effects and mesoscopic conductance fluctuations in granular aluminum". In: *Eur. Phys. J. B 65, 5-19* (2008). DOI: https://doi.org/10.1140/epjb/e2008-00317-4.

[110] I. S. Beloborodov et al. "Granular electronic systems". In: *Reviews of Modern Physics* 79.2 (2007), p. 469.

[111] D. V. Averin and Y. V. Nazarov. "Virtual electron diffusion during quantum tunneling of the electric charge". In: *Phys. Rev. Lett.* 65 (19 Nov. 1990), pp. 2446–2449. DOI: 10.1103/PhysRevLett.65.2446. URL: https://link.aps.org/doi/10.1103/PhysRevLett.65.2446.

[112] I. S. Beloborodov, A. V. Lopatin, and V. M. Vinokur. "Coulomb effects and hopping transport in granular metals". In: *Physical Review B* 72.12 (2005), p. 125121.

[113] M. V. Feigel'man and A. S. Ioselevich. "Variable-range cotunneling and conductivity of a granular metal". In: *Jetp. Lett. 81, 277-283* (2005). DOI: https://doi.org/10.1134/1.1931015.

[114] P. W. Anderson. "Theory of dirty superconductors". In: *Journal of Physics and Chemistry of Solids* 11.1 (1959), pp. 26–30. ISSN: 0022-3697. DOI: https://doi.org/10.1016/0022-3697(59)90036-8. URL: https://www.sciencedirect.com/science/article/pii/0022369759900368.

[115] C. T. Black, D. C. Ralph, and M. Tinkham. "Spectroscopy of the Superconducting Gap in Individual Nanometer-Scale Aluminum Particles". In: *Phys. Rev. Lett.* 76 (4 Jan. 1996), pp. 688–691. DOI: 10.1103/PhysRevLett.76.688. URL: https://link.aps.org/doi/10.1103/PhysRevLett.76.688.

[116] Y. Shapira and G. Deutscher. "Semiconductor-superconductor transition in granular Al-Ge". In: *Phys. Rev. B* 27 (7 Apr. 1983), pp. 4463–4466. DOI: 10.1103/PhysRevB.27.4463. URL: https://link.aps.org/doi/10.1103/PhysRevB.27.4463.

[117] A. I. Larkin. "Superconductor of small dimensions in a strong magnetic field". In: *Sov. Phys. JETP* 21 (1965), p. 153.

[118] I. S. Beloborodov, K. B. Efetov, and A. I. Larkin. "Magnetoresistance of granular superconducting metals in a strong magnetic field". In: *Phys. Rev. B* 61 (13 Apr. 2000), pp. 9145–9161. DOI: 10.1103/PhysRevB.61.9145. URL: https://link.aps.org/doi/10.1103/PhysRevB.61.9145.

[119] A. M. Clogston. "Upper Limit for the Critical Field in Hard Superconductors". In: *Phys. Rev. Lett.* 9 (6 Sept. 1962), pp. 266–267. DOI: 10.1103/PhysRevLett.9.266. URL: https://link.aps.org/doi/10.1103/PhysRevLett.9.266.

[120] B. S. Chandrasekhar. "A note on the maximum critical field of high-field superconductors". In: *Applied Physics Letters* 1.1 (1962), pp. 7–8.

[121] C. D. Chen et al. "Flux flow and vortex tunneling in two-dimensional arrays of small Josephson junctions". In: *Physical Review B* 54.13 (1996), p. 9449.

[122] C. G. L. Bøttcher et al. "Superconducting, insulating and anomalous metallic regimes in a gated two-dimensional semiconductor–superconductor array". In: *Nature Physics* 14.11 (2018), pp. 1138–1144.

[123] X. Zhang et al. "Robust anomalous metallic states and vestiges of self-duality in two-dimensional granular In-InOx composites". In: *npj Quantum Materials* 6.1 (2021), pp. 1–8.

[124] F. Couëdo et al. "Dissipative phases across the superconductor-to-insulator transition". In: *Scientific reports* 6.1 (2016), pp. 1–6.

[125] A. Kapitulnik, S. A. Kivelson, and B. Spivak. "Colloquium: anomalous metals: failed superconductors". In: *Reviews of Modern Physics* 91.1 (2019), p. 011002.

[126] D. Ephron et al. “Observation of quantum dissipation in the vortex state of a highly disordered superconducting thin film”. In: *Physical review letters* 76.9 (1996), p. 1529.

[127] N. Mason and A. Kapitulnik. “Dissipation effects on the superconductor-insulator transition in 2D superconductors”. In: *Physical review letters* 82.26 (1999), p. 5341.

[128] N. Mason and A. Kapitulnik. “True superconductivity in a two-dimensional superconducting-insulating system”. In: *Physical Review B* 64.6 (2001), p. 060504.

[129] X. Zhang, A. Palevski, and A. Kapitulnik. *Anomalous metals: from "failed superconductor" to "failed insulator"*. 2022. DOI: 10.48550/ARXIV.2201.08801. URL: https://arxiv.org/abs/2201.08801.

[130] B. Hen et al. “Superconductor–insulator transition in two-dimensional indium–indium-oxide composite”. In: *Proceedings of the National Academy of Sciences* 118.2 (2021).

[131] B. Spivak, A. Zyuzin, and M. Hruska. “Quantum superconductor-metal transition”. In: *Physical Review B* 64.13 (2001), p. 132502.

[132] B. Spivak, P. Oreto, and S. A. Kivelson. “Theory of quantum metal to superconductor transitions in highly conducting systems”. In: *Physical Review B* 77.21 (2008), p. 214523.

[133] M. V. Feigel’man and A. I. Larkin. “Quantum superconductor–metal transition in a 2D proximity-coupled array”. In: *Chemical physics* 235.1-3 (1998), pp. 107–114.

[134] B. Mühlschlegel, D. J. Scalapino, and R. Denton. “Thermodynamic properties of small superconducting particles”. In: *Physical Review B* 6.5 (1972), p. 1767.

[135] O. Entin-Wohlman, A. Kapitulnik, and Y. Shapira. “Dependence of T c on the normal-state resistivity in granular superconductors”. In: *Physical Review B* 24.11 (1981), p. 6464.

[136] Y. Imry and M. Strongin. “Destruction of superconductivity in granular and highly disordered metals”. In: *Physical Review B* 24.11 (1981), p. 6353.

[137] L. B. Ioffe and A. I. Larkin. “Properties of superconductors with a smeared transition temperature”. In: *Sov. Phys.-JETP (Engl. Transl.);(United States)* 54.2 (1981).

[138] A. O. Caldeira and A. J. Leggett. “Quantum tunnelling in a dissipative system”. In: *Annals of Physics* 149.2 (1983), pp. 374–456. ISSN: 0003-4916. DOI: https://doi.org/10.1016/0003-4916(83)90202-6. URL: https://www.sciencedirect.com/science/article/pii/0003491683902026.

[139] D. B. Schwartz et al. “Quantitative Study of the Effect of the Environment on Macroscopic Quantum Tunneling”. In: *Phys. Rev. Lett.* 55 (15 Oct. 1985), pp. 1547–1550. DOI: 10.1103/PhysRevLett.55.1547. URL: https://link.aps.org/doi/10.1103/PhysRevLett.55.1547.

[140] John M. Martinis, Michel H. Devoret, and John Clarke. "Experimental tests for the quantum behavior of a macroscopic degree of freedom: The phase difference across a Josephson junction". In: *Phys. Rev. B* 35 (10 Apr. 1987), pp. 4682–4698. DOI: 10.1103/PhysRevB.35.4682. URL: https://link.aps.org/doi/10.1103/PhysRevB.35.4682.

[141] G. Schön and A. D. Zaikin. "Quantum coherent effects, phase transitions, and the dissipative dynamics of ultra small tunnel junctions". In: *Physics Reports* 198.5 (1990), pp. 237–412. ISSN: 0370-1573. DOI: https://doi.org/10.1016/0370-1573(90)90156-V. URL: https://www.sciencedirect.com/science/article/pii/037015739090156V.

[142] J. M. Hergenrother et al. "Photon-activated switch behavior in the single-electron transistor with a superconducting island". In: *Phys. Rev. B* 51 (14 Apr. 1995), pp. 9407–9410. DOI: 10.1103/PhysRevB.51.9407. URL: https://link.aps.org/doi/10.1103/PhysRevB.51.9407.

[143] J. P. Pekola et al. "Environment-Assisted Tunneling as an Origin of the Dynes Density of States". In: *Phys. Rev. Lett.* 105 (2 July 2010), p. 026803. DOI: 10.1103/PhysRevLett.105.026803. URL: https://link.aps.org/doi/10.1103/PhysRevLett.105.026803.

[144] W. Pan et al. "Exact Quantization of the Even-Denominator Fractional Quantum Hall State at $\nu = 5/2$ Landau Level Filling Factor". In: *Phys. Rev. Lett.* 83 (17 Oct. 1999), pp. 3530–3533. DOI: 10.1103/PhysRevLett.83.3530. URL: https://link.aps.org/doi/10.1103/PhysRevLett.83.3530.

[145] F. Pobell. *Matter and methods at low temperatures*. Vol. 2. Springer, 2007.

[146] C. D. Motchenbacher and J. A. Connelly. *Low-noise electronic system design*. Vol. 269. Wiley New York, 1993.

[147] J. B. Johnson. "Thermal Agitation of Electricity in Conductors". In: *Phys. Rev.* 32 (1 July 1928), pp. 97–109. DOI: 10.1103/PhysRev.32.97. URL: https://link.aps.org/doi/10.1103/PhysRev.32.97.

[148] H. Nyquist. "Thermal Agitation of Electric Charge in Conductors". In: *Phys. Rev.* 32 (1 July 1928), pp. 110–113. DOI: 10.1103/PhysRev.32.110. URL: https://link.aps.org/doi/10.1103/PhysRev.32.110.

[149] D. M. Pozar. *Microwave engineering*. John wiley & sons, 2011.

[150] K. Bladh et al. "Comparison of cryogenic filters for use in single electronics experiments". In: *Review of Scientific Instruments* 74.3 (2003), pp. 1323–1327.

[151] S. Feyrer. *Magnetwiderstand und Hall-Effekt in dünnen NbSi-Schichten*. 2019.

[152] S. Holmer. *Supraleitung in schwach dotierten NbSi-Filmen*. 2020.

[153] C. P. Scheller et al. "Silver-epoxy microwave filters and thermalizers for millikelvin experiments". In: *Applied physics letters* 104.21 (2014), p. 211106.

[154] C. P. Scheller et al. "Silver-epoxy microwave filters and thermalizers for millikelvin experiments - Supplementary Material". In: *Applied physics letters* 104.21 (2014), p. 211106.

[155] W. Wittl. *Herstellung eines Tieftemperaturfilters zur Messung von Supraleiter/Topologische-Isolator Strukturen*. 2018.

[156] LakeShore Cryotronics. *Manual for Model 372 AC Resistance and Temperature Controller*. downloaded 03.06.2022. URL: https://www.lakeshore.com/products/categories/downloads/temperature-products/ac-resistance-bridges/model-372-ac-resistance-bridge-temperature-controller.

[157] J. Engert et al. "Practical noise thermometers for low temperatures". In: *Journal of Physics: Conference Series* 150.1 (Feb. 2009), p. 012012. DOI: 10.1088/1742-6596/150/1/012012. URL: https://doi.org/10.1088/1742-6596/150/1/012012.

[158] J. Beyer et al. "A Magnetic-Field-Fluctuation Thermometer for the mK Range Based on SQUID-Magnetometry". In: *IEEE Transactions on Applied Superconductivity* 17.2 (2007), pp. 760–763. DOI: 10.1109/TASC.2007.898265.

[159] J. Engert et al. "A noise thermometer for practical thermometry at low temperatures". In: *International Journal of Thermophysics* 28.6 (2007), pp. 1800–1811.

[160] A. Kirste et al. "Optimization of SQUID magnetometers and gradiometers for magnetic-field-fluctuation thermometers". In: *Journal of Physics: Conference Series* 97 (Feb. 2008), p. 012320. DOI: 10.1088/1742-6596/97/1/012320. URL: https://doi.org/10.1088/1742-6596/97/1/012320.

[161] S. Reinhardt et al. "Lab::Measurement—A portable and extensible framework for controlling lab equipment and conducting measurements". In: *Computer Physics Communications* 234 (2019), pp. 216–222. ISSN: 0010-4655. DOI: https://doi.org/10.1016/j.cpc.2018.07.024. URL: https://www.sciencedirect.com/science/article/pii/S0010465518302819.

[162] R. C. Dynes et al. "Tunneling Study of Superconductivity near the Metal-Insulator Transition". In: *Phys. Rev. Lett.* 53 (25 Dec. 1984), pp. 2437–2440. DOI: 10.1103/PhysRevLett.53.2437. URL: https://link.aps.org/doi/10.1103/PhysRevLett.53.2437.

[163] F. Levy-Bertrand et al. "Electrodynamics of granular aluminum from superconductor to insulator: Observation of collective superconducting modes". In: *Phys. Rev. B* 99 (9 Mar. 2019), p. 094506. DOI: 10.1103/PhysRevB.99.094506. URL: https://link.aps.org/doi/10.1103/PhysRevB.99.094506.

[164] S. Lerer et al. "Nernst effect beyond the coherence critical field of a nanoscale granular superconductor". In: *Phys. Rev. B* 90 (21 Dec. 2014), p. 214521. DOI: 10.1103/PhysRevB.90.214521. URL: https://link.aps.org/doi/10.1103/PhysRevB.90.214521.

[165] A. G. Moshe, E. Farber, and G. Deutscher. "Optical conductivity of granular aluminum films near the Mott metal-to-insulator transition". In: *Physical Review B* 99.22 (2019), p. 224503.

[166] B. Abeles, Roger W. Cohen, and G. W. Cullen. "Enhancement of Superconductivity in Metal Films". In: *Phys. Rev. Lett.* 17 (12 Sept. 1966), pp. 632–634. DOI: 10.1103/PhysRevLett.17.632. URL: https://link.aps.org/doi/10.1103/PhysRevLett.17.632.

[167] N. Bachar et al. "Kondo-like behavior near the metal-to-insulator transition of nanoscale granular aluminum". In: *Phys. Rev. B* 87 (21 June 2013), p. 214512. DOI: 10.1103/PhysRevB.87.214512. URL: https://link.aps.org/doi/10.1103/PhysRevB.87.214512.

[168] N. Bachar and G. Deutscher. *Spin-flip scattering in superconducting granular aluminum films*. Tel-Aviv University, 2014.

[169] N. Bachar et al. "Mott transition in granular aluminum". In: *Phys. Rev. B* 91 (4 Jan. 2015), p. 041123. DOI: 10.1103/PhysRevB.91.041123. URL: https://link.aps.org/doi/10.1103/PhysRevB.91.041123.

[170] N. Bachar et al. "Signatures of Unconventional Superconductivity in Granular Aluminum". In: *Journal of Low temperature Physics, 179, 83-89* (2015).

[171] A. G. Moshe, E. Farber, and G. Deutscher. "From orbital to Pauli-limited critical fields in granular aluminum films". In: *Physical Review Research* 2.4 (2020), p. 043354.

[172] A. G. Moshe et al. "Tunneling study in granular aluminum near the Mott metal-to-insulator transition". In: *Physical Review B* 104.5 (2021), p. 054508.

[173] L. Grünhaupt et al. "Loss Mechanisms and Quasiparticle Dynamics in Superconducting Microwave Resonators Made of Thin-Film Granular Aluminum". In: *Phys. Rev. Lett.* 121 (11 Sept. 2018), p. 117001. DOI: 10.1103/PhysRevLett.121.117001. URL: https://link.aps.org/doi/10.1103/PhysRevLett.121.117001.

[174] L. Grünhaupt et al. "Granular aluminium as a superconducting material for high-impedance quantum circuits". In: *Nature materials* 18.8 (2019), pp. 816–819.

[175] P. Monod. "Magnetic Field Dependence of the Kondo Resistivity Minimum in CuFe and CuMn Alloys". In: *Phys. Rev. Lett.* 19 (19 Nov. 1967), pp. 1113–1117. DOI: 10.1103/PhysRevLett.19.1113. URL: https://link.aps.org/doi/10.1103/PhysRevLett.19.1113.

[176] M.-T. Béal-Monod and R. A. Weiner. "Negative Magnetoresistivity in Dilute Alloys". In: *Phys. Rev.* 170 (2 June 1968), pp. 552–559. DOI: 10.1103/PhysRev.170.552. URL: https://link.aps.org/doi/10.1103/PhysRev.170.552.

[177] J. Kondo. "Resistance minimum in dilute magnetic alloys". In: *Progress of theoretical physics* 32.1 (1964), pp. 37–49.

[178] N. F. Mott. "The Basis of the Electron Theory of Metals, with Special Reference to the Transition Metals". In: *Proceedings of the Physical Society. Section A* 62.7 (July 1949), pp. 416–422. DOI: 10.1088/0370-1298/62/7/303. URL: https://doi.org/10.1088/0370-1298/62/7/303.

[179] N. F. Mott. "Metal-Insulator Transition". In: *Rev. Mod. Phys.* 40 (4 Oct. 1968), pp. 677–683. DOI: 10.1103/RevModPhys.40.677. URL: https://link.aps.org/doi/10.1103/RevModPhys.40.677.

[180] L. Pisani, P. Pieri, and G. Calvanese Strinati. "Gap equation with pairing correlations beyond the mean-field approximation and its equivalence to a Hugenholtz-Pines condition for fermion pairs". In: *Phys. Rev. B* 98 (10 Sept. 2018), p. 104507. DOI: 10.1103/PhysRevB.98.104507. URL: https://link.aps.org/doi/10.1103/PhysRevB.98.104507.

[181] L. Pisani et al. "Entanglement between pairing and screening in the Gorkov-Melik-Barkhudarov correction to the critical temperature throughout the BCS-BEC crossover". In: *Phys. Rev. B* 97 (1 Jan. 2018), p. 014528. DOI: 10.1103/PhysRevB.97.014528. URL: https://link.aps.org/doi/10.1103/PhysRevB.97.014528.

[182] D. C. Mattis and J. Bardeen. "Theory of the Anomalous Skin Effect in Normal and Superconducting Metals". In: *Phys. Rev.* 111 (2 July 1958), pp. 412–417. DOI: 10.1103/PhysRev.111.412. URL: https://link.aps.org/doi/10.1103/PhysRev.111.412.

[183] P. Fulde and R. A. Ferrell. "Superconductivity in a Strong Spin-Exchange Field". In: *Phys. Rev.* 135 (3A Aug. 1964), A550–A563. DOI: 10.1103/PhysRev.135.A550. URL: https://link.aps.org/doi/10.1103/PhysRev.135.A550.

[184] A. I. Larkin and Y. N. Ovchinnikov. "Nonuniform state of superconductors". In: *Zh. Eksp. Teor. Fiz. 47, 1136 (1964) [Sov. Phys. JETP 20, 762 (1965)]* (1965).

[185] N. R. Werthamer, E. Helfand, and P. C. Hohenberg. "Temperature and Purity Dependence of the Superconducting Critical Field, H_{c2}. III. Electron Spin and Spin-Orbit Effects". In: *Phys. Rev.* 147 (1 July 1966), pp. 295–302. DOI: 10.1103/PhysRev.147.295. URL: https://link.aps.org/doi/10.1103/PhysRev.147.295.

[186] P. Fulde and K. Maki. "Fluctuations in high field superconductors". In: *Zeitschrift für Physik A Hadrons and nuclei* 238.3 (1970), pp. 233–248.

[187] A. Spuntarelli, P. Pieri, and G. Calvanese Strinati. "Solution of the Bogoliubov–de Gennes equations at zero temperature throughout the BCS–BEC crossover: Josephson and related effects". In: *Physics Reports* 488.4-5 (2010), pp. 111–167.

[188] N. S. Bakhvalov et al. "Statics and dynamics of single-electron solitons in two-dimensional arrays of ultrasmall tunnel junctions". In: *Physica B: Condensed Matter* 173.3 (1991), pp. 319–328.

[189] D. V. Averin and K. K. Likharev. *Averin, D. V. and Likharev, K. K. in Mesoscopic Phenomena in Solids, edited by Al'tshuler, B. L. and Lee, P. A. and Webb, R. A.* 1991.

[190] H. Grabert and M. H. Devoret. *Single charge tunneling: Coulomb blockade phenomena in nanostructures*. Vol. 294. Springer Science & Business Media, 2013.

[191] D. B. Haviland et al. "Local superconducting coupling in the strong-localization limit of ultrathin granular metal films". In: *Phys. Rev. B* 40 (1 July 1989), pp. 719–722. DOI: 10.1103/PhysRevB.40.719. URL: https://link.aps.org/doi/10.1103/PhysRevB.40.719.

[192] Y. Liu et al. "Insulator-to-superconductor transition in ultrathin films". In: *Phys. Rev. B* 47 (10 Mar. 1993), pp. 5931–5946. DOI: 10.1103/PhysRevB.47.5931. URL: https://link.aps.org/doi/10.1103/PhysRevB.47.5931.

[193] R. C. Dynes, J. P. Garno, and J. M. Rowell. "Two-Dimensional Electrical Conductivity in Quench-Condensed Metal Films". In: *Phys. Rev. Lett.* 40 (7 Feb. 1978), pp. 479–482. DOI: 10.1103/PhysRevLett.40.479. URL: https://link.aps.org/doi/10.1103/PhysRevLett.40.479.

[194] G. Deutscher et al. "Percolation description of granular superconductors". In: *Phys. Rev. B* 21 (11 June 1980), pp. 5041–5047. DOI: 10.1103/PhysRevB.21.5041. URL: https://link.aps.org/doi/10.1103/PhysRevB.21.5041.

[195] E. Šimánek. "Origin of the resistivity minima in granular superconductors". In: *Phys. Rev. B* 25 (1 Jan. 1982), pp. 237–244. DOI: 10.1103/PhysRevB.25.237. URL: https://link.aps.org/doi/10.1103/PhysRevB.25.237.

[196] L. J. Geerligs and J. E. Mooij. "Charge quantization and dissipation in arrays of small Josephson junctions". In: *Physica B: Condensed Matter* 152.1 (1988), pp. 212–217. ISSN: 0921-4526. DOI: https://doi.org/10.1016/0921-4526(88)90090-7. URL: https://www.sciencedirect.com/science/article/pii/0921452688900907.

[197] L. J. Geerligs et al. "Charging effects and quantum coherence in regular Josephson junction arrays". In: *Phys. Rev. Lett.* 63 (3 July 1989), pp. 326–329. DOI: 10.1103/PhysRevLett.63.326. URL: https://link.aps.org/doi/10.1103/PhysRevLett.63.326.

[198] P. Ao and D. J. Thouless. "Berry's phase and the Magnus force for a vortex line in a superconductor". In: *Phys. Rev. Lett.* 70 (14 Apr. 1993), pp. 2158–2161. DOI: 10.1103/PhysRevLett.70.2158. URL: https://link.aps.org/doi/10.1103/PhysRevLett.70.2158.

[199] T. S. Tighe, A. T. Johnson, and M. Tinkham. "Vortex motion in two-dimensional arrays of small, underdamped Josephson junctions". In: *Phys. Rev. B* 44 (18 Nov. 1991), pp. 10286–10290. DOI: 10.1103/PhysRevB.44.10286. URL: https://link.aps.org/doi/10.1103/PhysRevB.44.10286.

[200] Y. Aharonov and D. Bohm. "Significance of Electromagnetic Potentials in the Quantum Theory". In: *Phys. Rev.* 115 (3 Aug. 1959), pp. 485–491. DOI: 10.1103/PhysRev.115.485. URL: https://link.aps.org/doi/10.1103/PhysRev.115.485.

[201] R. S. Newrock et al. "The two-dimensional physics of Josephson-junction arrays". In: *SOLID STATE PHYSICS-NEW YORK-ACADEMIC PRESS-* 54 (2000), pp. 266–512.

[202] D. V. Averin and K. K. Likharev. "Coulomb blockade of single-electron tunneling, and coherent oscillations in small tunnel junctions". In: *Journal of low temperature physics* 62.3 (1986), pp. 345–373.

[203] O. Crauste et al. "Destruction of superconductivity in disordered materials: A dimensional crossover". In: *Phys. Rev. B* 90 (6 Aug. 2014), p. 060203. DOI: 10.1103/PhysRevB.90.060203. URL: https://link.aps.org/doi/10.1103/PhysRevB.90.060203.

[204] S. J. Lee and J. B. Ketterson. "Critical sheet resistance for the suppression of superconductivity in thin Mo-C films". In: *Phys. Rev. Lett.* 64 (25 June 1990), pp. 3078–3081. DOI: 10.1103/PhysRevLett.64.3078. URL: https://link.aps.org/doi/10.1103/PhysRevLett.64.3078.

[205] V. Humbert et al. "Overactivated transport in the localized phase of the superconductor-insulator transition". In: *Nature communications* 12.1 (2021), pp. 1–10.

Acknowledgements

At this point I would like to thank all those who have supported me during my work as a PhD student. This includes discussions on theory, help in the laboratory and in private.

My supervisor **Prof. Dr. C. Strunk**: Christoph gave me the opportunity to work in the field of disordered superconductors and to take care of a He3/He4 dilution refrigerator. To improve and upgrade that system to match the requirements necessary for low temperature measurements on various material systems has been one of the main tasks of my thesis. Christoph supported me constantly with new ideas and solutions, especially during my study in the challenging field of two dimensional granular aluminum. I was allowed to attend to several conferences. My two highlights have been the "28th International Conference on Low Temperature Physics" (LT28) in Gothenburg, Sweden, in 2016 and the "International Workshop on: The Superconductor-Insulator Transition and Low-Dimensional Superconductors", in Villard-de-Lans, France, in 2018. To meet and talk to leading scientists in the field of low temperatures, disordered superconducting systems and the superconductor-insulator transition during the first years of my thesis was very impressive.

Prof. Dr. D. Bougeard for being the second referee for my thesis.

Prof. G. Deutscher for providing us with ultra-thin granular aluminum films and for the discussion about the results.

Dr. A. Glezer Moshe for growing the thin granular aluminum films, for the time taken to tune the films to the desired thickness and sheet resistance and the good communication.

Dr. C. Marrache-Kikuchi for the possibility to measure two of her niobium-silicon samples.

Prof. Dr. D. Weiss for the infrastructure in the chair including the cleanroom and other equipment.

Dr. A. K. Hüttel: Thank you for all the fruitful discussions and inspirations including software, hardware and cryogenics. Your hints and tricks concerning dilution refrigerators were very helpful.

Christian Haimerl and **Thomas Solleder** for the endless support of liquid helium and nitrogen and the flexibility in case of emergency.

The **mechanical workshop** for all the produced parts needed for my experiments.

The **electronics workshop**: I would like to thank **Dieter Riedl** for designing and fullfilling my wishes on printed ciruit boards, **Max Simmel** and **Kurt Lehar** for the winding of the Ag-epoxy high frequency filters and **Josef Haberkorn** for gold-plating a lot of different metal pieces.

Our technicians **Michael Weigl**, **Cornelia Linz** and **Uli Gürster** for maintenence and constantly upgrading our equipment. I would like to thank **Thomas Haller** for all the work that was needed to design the drawings for my setup. We had a very good cooperation in the early time of the new "millikelvin lab" properly distributing measurement equipment and parts of the different low temperature systems locally. Especially i would like to thank you for the help in the lab after the "Sintflut 2016" to get the lab dry again. Thanks to **Daniel Pahl** for taking care of the gas warning system for the new lab and coordinating its implementation.

Our secretaries **Elke Haushalter** and **Claudia Moser** for all the administrative help, listening to every possible issue and the welcoming atmosphere. I always had a good time talking to you.

I would like to give credit to **Dr. Christian Baumgartner** and **Simon Reinhardt** for the help with the SEM. Both were my long term office colleagues together with **Dr. Lorenz Fuchs**. Thanks a lot for the good time we had.

Elisabeth Richter for the help with the AFM.

Dr. Stefan Blien and **Alexander Weitzel** for the help on the dilution refigerator and the good time we spent in the lab.

To the **AG Strunk** including my (former) colleagues **Dr. Nicola Paradiso**, **Dr. Christian Bäuml**, **Dr. Klaus Kronfeldner**, **Paul Linsmeier**, **Lea Pfaffinger**, **Johanna Berger**, **Jay Schmidt** and **Simon Feyrer** for all the discussions, the fun time in the labs and the good time we had outside of the world of physics. Thanks to all I forgot to mention that contributed to the collegial and welcoming atmosphere in our chair.

I would like to express my deepest gratitude to my parents, **Robert** and **Sonja**, as well as to my sister **Sandra**. Throughout my life you keep supporting me in every situation possible.

At the end I would like to thank all those I forgot to mention. It would have been hard to finish this thesis without you.